frontiers | Research Topics

Sedimentary evolution and hazardous geology during the Holocene in the Yangtze River and the Red River Deltas and the neighboring coastal areas

Edited by
Jian Liu, Alessandro Amorosi and Xiaoyong Duan

Published in
Frontiers in Earth Science

ISSN 1664-8714
ISBN 978-2-8325-4616-1
DOI 10.3389/978-2-8325-4616-1

About Frontiers

Frontiers is more than just an open access publisher of scholarly articles: it is a pioneering approach to the world of academia, radically improving the way scholarly research is managed. The grand vision of Frontiers is a world where all people have an equal opportunity to seek, share and generate knowledge. Frontiers provides immediate and permanent online open access to all its publications, but this alone is not enough to realize our grand goals.

Frontiers journal series

The Frontiers journal series is a multi-tier and interdisciplinary set of open-access, online journals, promising a paradigm shift from the current review, selection and dissemination processes in academic publishing. All Frontiers journals are driven by researchers for researchers; therefore, they constitute a service to the scholarly community. At the same time, the *Frontiers journal series* operates on a revolutionary invention, the tiered publishing system, initially addressing specific communities of scholars, and gradually climbing up to broader public understanding, thus serving the interests of the lay society, too.

Dedication to quality

Each Frontiers article is a landmark of the highest quality, thanks to genuinely collaborative interactions between authors and review editors, who include some of the world's best academicians. Research must be certified by peers before entering a stream of knowledge that may eventually reach the public - and shape society; therefore, Frontiers only applies the most rigorous and unbiased reviews. Frontiers revolutionizes research publishing by freely delivering the most outstanding research, evaluated with no bias from both the academic and social point of view. By applying the most advanced information technologies, Frontiers is catapulting scholarly publishing into a new generation.

What are Frontiers Research Topics?

Frontiers Research Topics are very popular trademarks of the *Frontiers journals series*: they are collections of at least ten articles, all centered on a particular subject. With their unique mix of varied contributions from Original Research to Review Articles, Frontiers Research Topics unify the most influential researchers, the latest key findings and historical advances in a hot research area.

Find out more on how to host your own Frontiers Research Topic or contribute to one as an author by contacting the Frontiers editorial office: frontiersin.org/about/contact

Sedimentary evolution and hazardous geology during the Holocene in the Yangtze River and the Red River Deltas and the neighboring coastal areas

Topic editors
Jian Liu — Qingdao Institute of Marine Geology (QIMG), China
Alessandro Amorosi — University of Bologna, Italy
Xiaoyong Duan — Qingdao Institute of Marine Geology (QIMG), China

Citation
Liu, J., Amorosi, A., Duan, X., eds. (2024). *Sedimentary evolution and hazardous geology during the Holocene in the Yangtze River and the Red River Deltas and the neighboring coastal areas*. Lausanne: Frontiers Media SA.
doi: 10.3389/978-2-8325-4616-1

Table of contents

frontiers | Frontiers in Earth Science

TYPE Editorial
PUBLISHED 06 March 2024
DOI 10.3389/feart.2024.1365009

OPEN ACCESS

EDITED AND REVIEWED BY
Steven L. Forman,
Baylor University, United States

*CORRESPONDENCE
Jian Liu,
✉ liujian0550@vip.sina.com

RECEIVED 03 January 2024
ACCEPTED 06 February 2024
PUBLISHED 06 March 2024

CITATION
Liu J, Amorosi A and Duan X (2024), Editorial: Sedimentary evolution and hazardous geology during the Holocene in the Yangtze River and the Red River Deltas and the neighboring coastal areas.
Front. Earth Sci. 12:1365009.
doi: 10.3389/feart.2024.1365009

Editorial: Sedimentary evolution and hazardous geology during the Holocene in the Yangtze River and the Red River Deltas and the neighboring coastal areas

Jian Liu[1,2]*, Alessandro Amorosi[3] and Xiaoyong Duan[1]

[1]Qingdao Institute of Marine Geology, Qingdao, China, [2]Laboratory for Marine Geology, Qingdao National Laboratory for Marine Science and Technology, Qingdao, China, [3]Department of Biological, Geological and Environmental Sciences, University of Bologna, Bologna, Italy

KEYWORDS

the Holocene, sedimentary evolution, hazardous geology, Yangtze River Delta, Red River Delta, source to sink processes, sediment dynamics

Editorial on the Research Topic
Sedimentary evolution and hazardous geology during the Holocene in the Yangtze River and the Red River Deltas and the neighboring coastal areas

The Yangtze River and Red River both originate from the Tibetan Plateau and are among the top ten rivers in Asia in terms of sediment discharge (Milliman and Meade, 1983). These rivers have a significant impact on the global carbon cycle (Gao et al., 2017). The Yangtze River Delta is located on the west coast of the East China Sea, while the Red River Delta occurs on the west coast of the Gulf of Tonkin in the South China Sea. Both deltas began forming during the early to middle Holocene with the stabilization of global sea level (Hori and Saito, 2007). There is a growing body of literature on the evolution of the deltas and the neighboring coastal areas (e.g., Tanabe et al., 2006; Liu et al., 2023; Song et al., 2013), yet further research is required to enhance our understanding of the intricate interplay between sea-level and climatic changes, hydrodynamic processes, and human activities for these delta areas. Fortunately, collaborative research on these delatic settings between geoscientists from China and Vietnam has increased understanding on the sedimentary record for the past ca. 10,000 years and potential geologic hazards.

The objective of this Research Topic is to explore new findings on sedimentary evolution and geologic hazards in the Yangtze River and Red River deltas and the adjacent coastal areas during the Holocene. This study is part of the collaborative research effort between China and Vietnam, and this collection of manuscripts focuses on the following aspects:

1) Studying the sedimentary evolution and stratigraphic records in the deltas and coastal areas under the influence of sea level changes, climate variations, sediment sources and dynamics, and human activities.
2) Investigating the source-to-sink processes in the deltas and coastal areas during the Holocene.
3) Analyzing the types, distribution, formative mechanisms, and trends of geohazards in the deltas and coastal areas.

We provide a summary and analysis of the nine papers associated with this Research Topic on the Sedimentary Evolution and Hazardous Geology during the Holocene in the Yangtze River and the Red River deltas and the Neighboring Coastal Areas.

Two articles by Chen et al. and He et al. discuss recent advancements in the study of the sedimentary evolution of the Jiangsu coast, which is located at the northern end of the modern Yangtze River Delta. Chen et al. conducted a comprehensive analysis of two cores obtained from the central North Jiangsu Plain (NJP) to reconstruct the sedimentary history of the area since MIS 2. They discovered a significant shift in sediment source from the Yangtze River to the Yellow River during the early Holocene in north central NJP. This change may be or is attributed to the transport of Yellow River sediments by strong tidal currents and waves or the southward migration of the Yellow River. He et al. investigated the formation and evolution of the radial tidal sand ridge (RTSR) off the Jiangsu coast in the South Yellow Sea, which is a remarkable and distinctive seabed formation. The analysis of sedimentological and paleoecological data from cores retrieved from the Jiangsu Plain and offshore from the sand ridges indicates that the RTSR originated 9,000 cal yr BP under transgressive conditions. These forms persisted throughout the Holocene but experienced significant development after 1128 AD, coinciding with the southward flow of the Yellow River into the Yellow Sea.

Sun et al. conducted a study on the formation of authigenic pyrites and gypsums in core JC-1, located offshore of Zhoushan Islands near the current delta of the Yangtze River. They discovered the presence of gypsum minerals or the coexistence of pyrite and gypsum in the enriched authigenic pyrites in different sedimentary facies. The results indicate that local environmental acidification leads to the formation of authigenic gypsums, with sulfate derived from overlying seawater and pyrite oxidation. This research provides important insights into the impact of sea level rise and climate change on different sedimentary environments.

Qiu et al. conducted an analysis of sediment thickness and source during the Holocene in Sanmen Bay, located on the Zhejiang coast. The study aimed to understand the sedimentary processess of the bay in relation to the transport of sediments from the Yangtze River. These results indicate that the fine-grained sediments in Sanmen Bay primarily originate from the Yangtze River and that the bay serves as a significant sink for these sediments. This study documented a high rate of sedimentation during the early and late Holocene, which decreased notably during the mid-Holocene. Thess changes in sedimentation rate are attributed to the southward transport processes of Yangtze River sediments under the influence of the East Asian Winter Monsoon. The study emphasizes the important role of coastal bays in Zhejiang coast for the source-sink process of Yangtze River sediments.

Tong et al. conducted a study of core G02 on the northwestern continental slope of the South China Sea (SCS) to investigate the variations in organic matter sources and distribution over the past ~8,600 years. Core G02 showed a significant increase in δ^{15}N values between 8.4 and 4.6 cal kyr BP, indicating the intrusion of low-oxygen subsurface water from the Kuroshio Current into the northern SCS. Furthermore, they found negative δ^{13}C values from 8.3 to 3.0 cal kyr BP, suggesting a weakening of the East Asian Monsoon. In turn, positive δ^{13}C values during 3.0–1.4 cal kyr BP may indicate the weakening of the Indian Summer Monsoon. The study also highlighted the increasing influence of human activities on organic carbon production and burial since 1.4 cal kyr BP. These findings contribute to our understanding of organic matter source-sink processes and the factors influencing these processes on continental slopes in low-latitude marginal seas.

Dong et al. used end member modeling analysis (EMMA) and grain size trend analysis (GSTA) to study the sediment transport in the nearshore seabed of Hai Hau, Nam Dinh Province, southwest of the Red River Delta. They found that sediments from the Hai Hau coast are eroded and deposited in the center of the study area due to various dynamic processes. The fine-grained components of transported sediments may originate from the Ba Lat River mouth, and the sand component from the Ba Lat River mouth which is partially transported to deeper water areas (below 28 m depth). This study provides new insights into the offshore sediment transportation for the Red River Delta.

Three articles in this issue focus on the research of geological hazards in the study region. The article by Jiang et al. investigates the type, distribution, and origin of geological hazards in the Oujiang estuary on the Zhejiang coast. Through analysis of shallow seismic profiles and boreholes, the authors identify various geological hazards, such as shallow gas pockets, active sand waves, shallow-buried irregular bedrock, erosion channels, steep submarine slopes, and buried paleochannels. Jiang et al. also provide maps of recoginzed geologic hazards. The formation of these hazards is influenced by the geological structure and external dynamic forces, including sea-level changes, modern hydrodynamics, and human activities. The other two articles explore the origin and hydrochemical characteristics of confined groundwater in coastal areas, enhancing our comprehension of the formation and evolution of saline groundwater in coastal areas. Zhan et al. analyze the hydrochemistry of 87 groundwater samples collected from five confined aquifers in the Yangtze River Delta. They propose that the groundwater samples have two different origins, marine-continental and continental, with distinct hydrochemical characteristics. These results indicate that human activities have caused the infiltration of saline water into the groundwater near surface aquifer over the past century. Gao et al. compare the hydrogeochemical characteristics and relationships between saline groundwater and the sedimentary environment in two representative muddy coastal zones, the Yellow Sea coast (YSC) and the Bohai Sea coast (BSC). The findings demonstrate that the enrichment of total dissolved solids (TDS) in the BSC and YSC is primarily caused by freshwater-seawater-brine and freshwater-seawater mixing, respectively. The salinity of groundwater is mainly due to saltwater intrusion, followed by water-rock interactions.

In summary, this Research Topic has brought together state-of-the-art studies on sedimentary evolution and hazardous geology during the Holocene in the Yangtze River and the Red River deltas and their nearby coastal areas, and sheds new light on the deeper understanding of the Holocene sedimentary history and geo-hazardous mechanism. It is our belief that a thorough and unbiased evaluation of the geological investigation and research results, in conjunction with the latest advancements and innovative findings, could potentially shed light on the most favorable ways for future research.

Author contributions

JL: Writing–original draft. AA: Writing–original draft. XD: Writing–original draft.

Conflict of interest

The authors declare that the research was conducted in the absence of any commercial or financial relationships that could be construed as a potential conflict of interest.

Publisher's note

References

Gao, Y., Yang, T., Wang, Y., and Yu, G. (2017). Fate of river-transported carbon in China: implications for carbon cycling in coastal ecosystems. *Ecosyst. Health Sustain.* 3 (3), e01265. doi:10.1002/ehs2.1265

Hori, K., and Saito, Y. (2007). An early Holocene sea-level jump and delta initiation. *Geophys. Res. Lett.* 34, L18401. doi:10.1029/2007gl031029

Liu, J., Qiu, J. D., Saito, Y., Zhang, Y., Wang, H., Wang, F. F., et al. (2023). Late pleistocene to Holocene facies architecture and sedimentary evolution of the Zhejiang coast, East China sea. *Mar. Geol.* 459, 107027. doi:10.1016/j.margeo.2023.107027

Milliman, J. D., and Meade, R. H. (1983). World-wide delivery of river sediment to the oceans. *J. Geol.* 91, 1–21. doi:10.1086/628741

Song, B., Li, Z., Saito, Y., Okuno, J., Li, Z., Lu, A., et al. (2013). Initiation of the Changjiang (Yangtze) delta and its response to the mid-Holocene Sea level change. *Palaeogeogr. Palaeoclimatol. Palaeoecol.* 388, 81–97. doi:10.1016/j.palaeo.2013.07.026

Tanabe, S., Satio, Y., Saito, Y., Vu, Q. l., Hanebuth, T. J. J., and Ngo, Q. L. (2006). Holocene evolution of the Song hong (Red River) delta system, northern Vietnam. *Sediment. Geol.* 197, 29–61. doi:10.1016/j.sedgeo.2005.12.004

frontiers | Frontiers in Earth Science

TYPE Original Research
PUBLISHED 05 January 2023
DOI 10.3389/feart.2022.1077484

OPEN ACCESS

EDITED BY
Jian Liu,
Qingdao Institute of Marine Geology (QIMG), China

REVIEWED BY
Fangjian Xu,
Hainan University, China
Xiaozhong Huang,
Lanzhou University, China

*CORRESPONDENCE
Zhenke Zhang,
✉ zhangzk@nju.edu.cn

SPECIALTY SECTION
This article was submitted to Quaternary Science, Geomorphology and Paleoenvironment, a section of the journal Frontiers in Earth Science

RECEIVED 23 October 2022
ACCEPTED 13 December 2022
PUBLISHED 05 January 2023

CITATION
Chen Y, Xia F, Zhang Z, Xu Q and Gui F (2023), Environmental and provenance change since MIS 2 recorded by two sediment cores in the central North Jiangsu Plain, East China.
Front. Earth Sci. 10:1077484.
doi: 10.3389/feart.2022.1077484

Environmental and provenance change since MIS 2 recorded by two sediment cores in the central North Jiangsu Plain, East China

Yingying Chen[1,2], Fei Xia[3], Zhenke Zhang[2]*, Qinmian Xu[4] and Feng Gui[5]

[1]School of Geography, Geomatics, and Planning, Jiangsu Normal University, Xuzhou, China, [2]The Key Laboratory of Coast and Island Development of Ministry of Education, School of Geography and Ocean Science, Nanjing University, Nanjing, China, [3]School of Geography, Jiangsu Second Normal University, Nanjing, China, [4]Tianjin Center, China Geological Survey, Tianjin, China, [5]Marine Science and Technology College, Zhejiang Ocean University, Zhoushan, China

In order to reveal the evolution of sediment provenance and paleoenvironment of the central North Jiangsu Plain (NJP) since marine isotope stage 2 (MIS 2), we analyzed lithology, accelerator mass spectrometry (AMS) ^{14}C dating, macrofossils and foraminifera, grain size, and geochemical compositions of sediments from two sediment cores (Core M and Core Y) recovered in the northern side of the Yangtze River. Our results show that fluvial environments prevailed in the central NJP during MIS 2, followed by alternations of coastal-marsh environments and shallow-bay environments in north central NJP and coastal-marsh environments in south central NJP during MIS 1. Provenance analysis suggests a major change in sediment provenance from the Yangtze River to the Yellow River at early MIS 1 in north central NJP; these Yellow River sediments might be transported from previously deposited sediments by strong tidal currents and intense waves to this area or be a reflection of a southward shift of the Yellow River during this period. However, the Yangtze River-derived sediments dominated the south central NJP since MIS 2. The depositional succession and sediment supplies since MIS 2 were dominantly controlled by sea-level fluctuations, regional geomorphic patterns, shift of the rivers, etc.

KEYWORDS

sedimentary environment, provenance, environmental evolution, Core Y, Core M, North Jiangsu Plain

1 Introduction

Coastal sedimentary records are important archives to understand the links between climate and sea levels. *In situ*-preserved sediments contain valuable information on marine–terrestrial interactions. Many studies have deciphered the sedimentary records from coastal areas worldwide to understand the history of relative sea-level changes (Hanebuth et al., 2000; Li et al., 2001; Shi et al., 2021), coastal stratigraphy, and environmental evolution on different spatial and temporal scales (Liu et al., 2016; Liu et al., 2018; Johnson et al., 2020; Zhou et al., 2021; Sun et al., 2022).

As a large sedimentary sink, the North Jiangsu Plain (NJP) is a key region connecting the land and ocean in the east of China, and it has preserved abundant environmental change information and provides a good medium for studying regional environmental change. In addition, the NJP is an important sediment reservoir for two globally large rivers: the Yellow River and the Yangtze

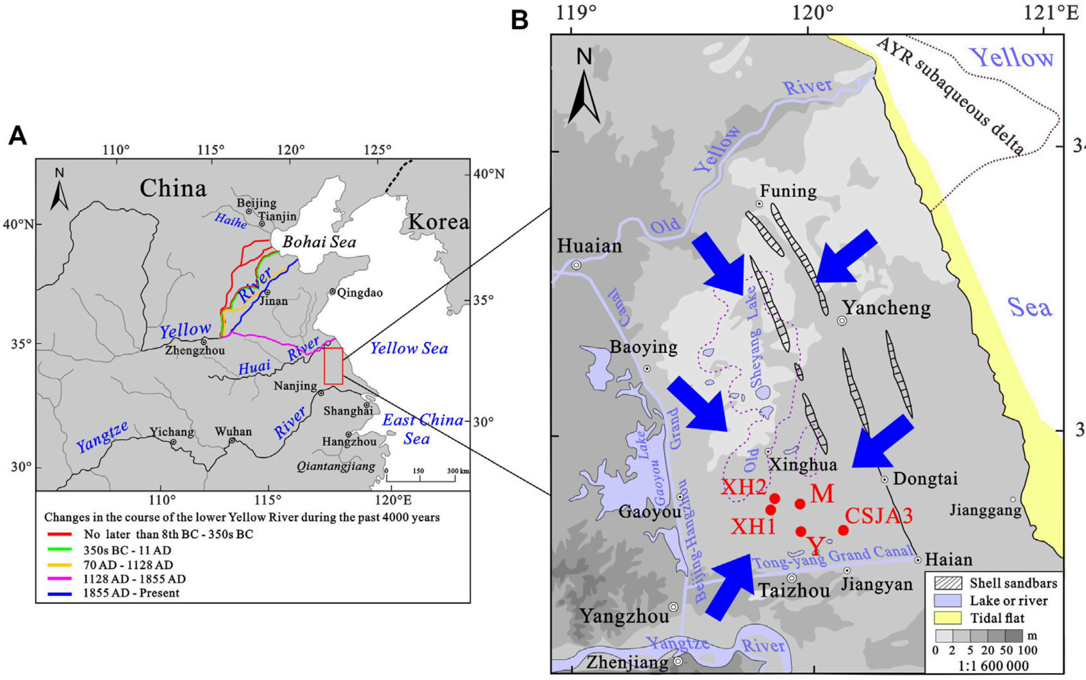

FIGURE 1
Left map **(A)** [modified after Yang et al. (2006)] showing the study area (the red rectangle area) and changes in the course of the lower Yellow River during the past 4000 years [Chen et al. (2012)]; right map **(B)** [modified after the Provincial Geomatics Center of Jiangsu Province (2004) and Gu et al. (1983)] showing the locations of the drill cores M and Y (M, Maoshan; Y, Yuduo), XH1 and XH2 (Zhang, 2009), and CSJA3 (Yu et al., 2016) in the northern part of the Yangtze River Delta; blue arrows denote the flow direction of possible sediment sources of the study area (AYR, Abandoned Yellow River).

(Changjiang) River. Therefore, sediments from the NJP will contain important paleoenvironmental information that is relevant to studying sea-level and tectonic variations, source-to-sink processes, etc. Great progress has been made in understanding the sedimentary evolution of the NJP since the Quaternary, especially over the Late Quaternary (e.g., Yang et al., 2002; Wang et al., 2006; Zhang, 2009; Zhang et al., 2010; Chen, 2016). Results have revealed that sedimentation in this region is characterized by the alternation of marine and terrestrial deposits. Comprehensive analyses of sediment cores from the central NJP reveal that sedimentary environmental changes since MIS 5 were strongly controlled by sea-level fluctuations, with most of the preserved sediments deposited in MIS 5, MIS 3, and MIS 1 (Chen, 2016). Using foraminifera abundances, one transgression layer has been identified in Core XH1 and Core XH2 (Figure 1B) (Zhang, 2009).

As the important sediment reservoir for the Yellow River and the Yangtze River, however, whether and to what extent the Yellow River and the Yangtze River supplied sediments to the central NJP is still controversial. Yang et al. (2002) noted that the Yangtze River had prevailed in the Jiangsu coastal plain sedimentation during the early stage of the Holocene, while the Yellow River dominated the area during the late Holocene. A study on the major, trace, and rare earth element characteristics of sediments in the Huaibei Plain demonstrated that the Yellow River may have migrated in the Huaihe River catchment during the last deglaciation (~13.2 ka) at least (Zhang et al., 2016). This result demonstrates that the influence of the Yellow River on the formation and shaping of the NJP may have been underestimated.

Given the complicated environment and provenance change, more case studies of sedimentary records from various locations around the NJP are needed, and investigations of high-resolution proxies of environmental changes will provide a better understanding of the sedimentary history in relation to the sea-level change. In this paper, two sediment cores (Core M and Core Y) with ~15 km apart in the northern side of the Yangtze River were obtained. Based on the lithology, AMS ^{14}C dating, grain size, and geochemical analyses of Core M and Core Y, changes in the sedimentary environment and provenance in the central NJP since MIS 2 were discussed. The results could provide important information for a better understanding of the formation and evolution of the NJP.

2 Study area

The central NJP is located between the Old Yellow River in the north and the Tongyang Grand Canal in the south (Figure 1). The topography of this area is dominated by lowland with a ground elevation below 5 m, and it declined from the Beijing–Hangzhou Grand Canal in the west toward the east along the Northern Jiangsu coast, with the lowest place around the Xinghua-Old Sheyang Lake area (Figure 1B). The Yangtze River and the Yellow River enter the East China Sea and the Bohai Sea, respectively. Although both rivers do not directly flow into the Yellow Sea at present, it was reported that they had frequently entered the Yellow Sea through the NJP during the Late Quaternary (Ren and Shi, 1986; Milliman et al., 1987; Chen and Stanley, 1995). For example, the deposition of huge amounts of sediment within the river channel and along the alluvial plain has caused frequent and extensive changes in the Yellow River's lower course (Figure 1A). The Yellow River shifted its river course from Shandong Province to the north Jiangsu coastal area in 1128 AD and delivered huge amounts of sediment to the coastal area and

TABLE 1 List of cores drilled from central NJP.

Core no.	Location		Elevation (m) (85 national datum)	Length (m)	Recovery (%)
	Latitude (°N)	Longitude (°E)			
M	32°45.051′	120°00.623′	~2	90	93.52
Y	32°38.713′	120°02.389′	~3	92	92.38

the Yellow Sea until 1855 AD; the coastline prograded rapidly, and the Abandoned Yellow River subaqueous delta was developed during this period (Ren and Shi, 1986; Milliman et al., 1987) (Figure 1). Following the capture in 1128–1855 AD by the Yellow River, the Huaihe River became a tributary of the Yellow River (Editorial Board on Records of Huaihe River, 1997). Abundant sediments supplied by the Yellow River also make the topography in the north NJP (near the Old Yellow River course) obviously higher than that in the south (Xinghua-Old Sheyang Lake area).

Sedimentary sequences of the Late Quaternary in the Jiangsu coastal plain and the northern Yangtze River Delta have been studied extensively on the basis of analysis of sediment cores (Li et al., 2001; Sun et al., 2015). The thickness of the Last Glacial Maximum (LGM) strata ranges from 2 m to 10 m, at a burial depth of 3–25 m, increasing eastward in burial depth and decreasing eastward in sedimentary thickness. This stiff clay layer was inferred to be compound ones resulting from alternating deposition and pedogenesis on the palaeo-interfluve of the Yangtze River, which became very hard after being exposed and dewatered (Li and Wang, 1998; Chen et al., 2008). At the end of the LGM, the topographic form in the area was tilted and uplifted from southeast to northwest, which significantly influenced the postglacial transgression (Chen et al., 1995). The paleo-coastline in the North Jiangsu Plain even reached the Huaiyin–Gaoyou–Yangzhou area (Pan, 1983), and a huge estuary of the Yangtze River with the apex at Zhenjiang and Yangzhou areas was formed when postglacial transgression reached the maximum (Li et al., 2000). After 7000 a BP, the sea level gradually tended to be stable, and this was evidenced by a series of shelly sandbars parallel to the present coastal line at the central part of the northern Jiangsu coastal plain area, which was developed at the Funing–Yancheng–Dongtai–Hai'an area with ~200 km long from north to south and ~60 km west of the present coastline (Figure 1B) (Gu et al., 1983).

3 Materials and methods

3.1 Core sampling

Two borehole cores (Core M and Core Y) were obtained in March 2014 from the back of the northern part of the Yangtze River Delta (Table 1; Figure 1). Core M and Core Y were split, descried, photographed, and subsampled in the laboratory immediately after the completion of drilling. In this study, we mainly focused on the upper 20 m of the whole core, where the age framework was effectively established by the AMS ^{14}C results.

3.2 Sediment grain-size analysis

Subsamples were generally taken at 10–50 cm intervals for grain-size analysis: intervals that, on visual inspection, appeared of relatively homogenous grain size were sampled less dense; intervals with more variations were sampled denser. A total of 75 and 46 samples were obtained from the upper 20 m of Core M and 10 m of Core Y, respectively. Each sample was 2 cm thick. The grain size was measured using a Malvern Mastersizer 2000 laser particle size analyzer. Before measuring grain size, samples were pretreated with 10% H_2O_2 and 0.1 N HCl to remove organic matter and biogenic carbonate, respectively. The results from the laser particle size analyzer were statistically processed using GRADISTAT software (Blott and Pye, 2001). The Folk and Ward (1957) classification scheme was adopted in this study. Analyses of grain size were carried out in the Key Laboratory of Coast and Island Development of the Ministry of Education, Nanjing University.

3.3 Elemental analysis

Bulk sediments were used in this study for chemical analysis. A measure of 0.1 g powdered samples of the sediment was digested with concentrated 1 ml HNO_3, 0.5 ml $HClO_4$, and 5 ml HF in a clean Teflon vessel at ~90°C for about 4 h until the digested solution was evaporated to dryness. Then, it was eluted with 1.5 ml aqua regia (3: 1 HCl: HNO_3) and 8.5 ml distilled water. Concentrations of major and trace elements were measured by ICP-AES (OPTIMA 5300DV, produced by PerkinElmer Company, United States of America). The contents of 17 elements (Al, Ca, Fe, K, Mg, Mn, Na, Ti, P, Ba, Cr, Cu, Li, Ni, Sr, V, and Zn) were tested. The detection limit was 0.00X-0. X mg/L, RSD≤2%. Chinese standard materials, GSS2 and GSS5, and several sandbank samples were analyzed with the sample sets in order to monitor the analytical precision and accuracy. The results show that relative deviations between measured and certified values are generally less than 10%, indicating satisfactory recoveries. Chemical analyses of all samples were carried out in the Center of Modern Analysis, Nanjing University.

3.4 Species identification of macrofossils and foraminifera

Four samples of macrofossils (i.e., bivalves and gastropods) were analyzed in the Nanjing Institute of Geology and Paleontology, Chinese Academy of Sciences. They were rinsed with clean water and dried thoroughly before being analyzed. Zheng (2013) and Zhang (2008) are the main references used in the species identification of macrofossils. Eight samples of foraminifera of Core M and five of Core Y were analyzed in the Marine Science and Technology College, Zhejiang Ocean University. Wang (1988) and Loeblich and Tappan (1988) are

TABLE 2 AMS ^{14}C dating results of Core M and Core Y.

Core	Sample no.	Depth (m)	Material	Measured^{14}C age (a BP)	^{13}C/ ^{12}C (‰)	Conventional age (a BP)	Laboratory no.	Comment
M	M1	1.40	Organic-rich mud	5190 ± 30	−20.7	5260 ± 30	Beta-379364	Reliable
	M3	3.89	Shell	6050 ± 30	−3.8	6400 ± 30	Beta-379365	Reliable
	M12	7.28	Organic-rich mud	9870 ± 40	−21.3	9930 ± 40	Beta-379366	Reliable
	M4	12.33	Organic-rich mud	30,510 ± 160	−21.5	30,570 ± 160	Beta-379367	Reliable
	M8	19.88	Plant debris	NA	−28.6	>43,500	Beta-379368	Unreliable
Y	Y2	3.56	Shell	6150 ± 30	−8.5	6420 ± 30	Beta-379371	Reliable
	Y4	5.30	Organic-rich mud	15,320 ± 50	−22	15,370 ± 50	Beta-379372	Reliable
	Y6	8.33	Organic-rich mud	26,440 ± 110	−21.7	26,490 ± 110	Beta-379373	Reliable

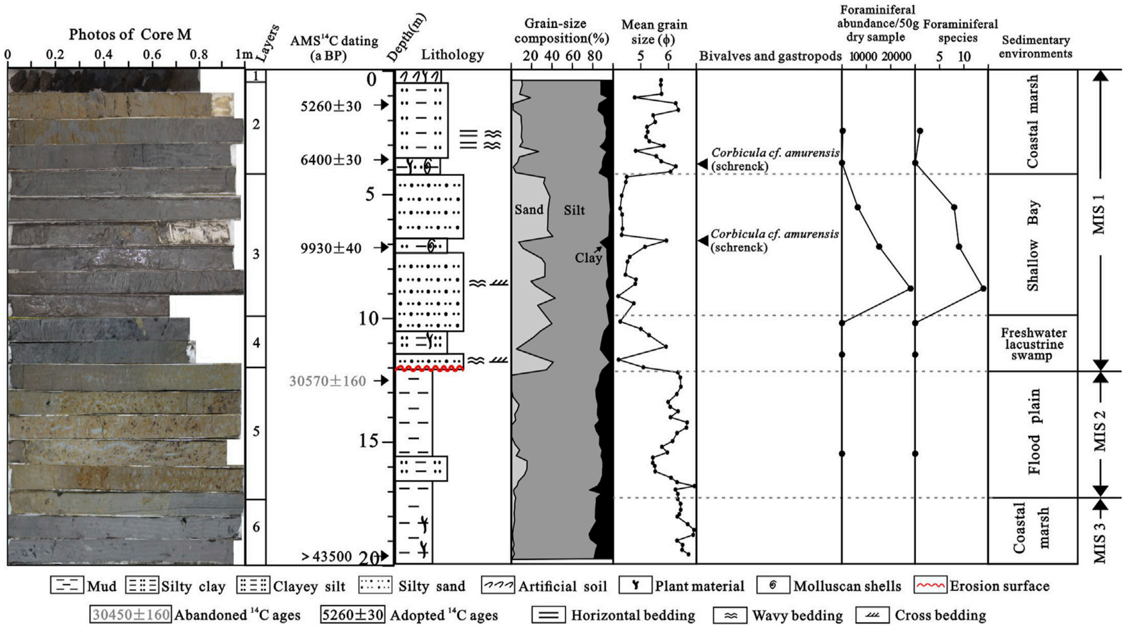

FIGURE 2
Comprehensive column of lithology, grain size, foraminiferal abundance, and species in Core M with AMS ^{14}C ages and interpreted sedimentary environments.

the main references used in the species identification of foraminifera.

3.5 AMS ^{14}C dating

Of the selected molluscan shells, plant debris, or organic-rich mud from these two cores, eight AMS ^{14}C ages were measured by Beta Analytic Inc. (Table 2). Age determinations were estimated based on a Libby half-life of 5568 years. To deal with the marine reservoir effect on the gastropod and shell samples, the ΔR value (135 ± 42) of a coastal sample from northwest Taiwan reported by Yoneda et al. (2007) was used.

4 Results

4.1 Sedimentary changes

Based on a comprehensive analysis of the testing results of Core M and Core Y, for example, sediment colors and components,

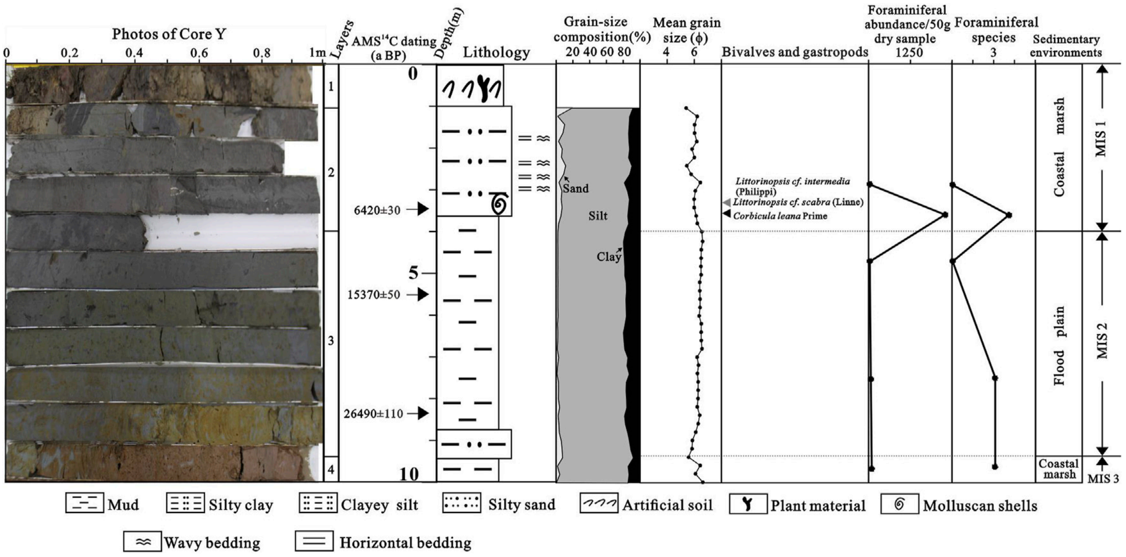

FIGURE 3
Comprehensive column of lithology, grain size, foraminiferal abundance, and species in Core Y with AMS ^{14}C ages and interpreted sedimentary environments.

sedimentary textures and structures, grain size, and macro- (i.e., bivalves and gastropods) and microfossils (i.e., foraminifer), the sediments in Core M and Core Y can be divided into five and three depositional units, respectively (Figure 2; Figure 3).

4.1.1 Sedimentary changes in Core M

Layer 5 (17.20–11.90 m): This layer is comprised of hardened or semi-hardened yellowish-brown stiff clayey silt, with abundant small black Fe-Mn nodules. The mean grain size is 5.09–6.93 ϕ, averaging 6.09 ϕ. No foraminifer was found in this layer. The contact relation between this layer and the underlying layer is transitional. This stiff mud layer is interpreted to be composed of river floodplain deposits that formed during MIS 2.

Layer 4 (11.90–9.94 m): Layer 4 is comprised of gray–black sandy silt with occasional wavy bedding, cross-bedding, and a few plant debris and mica pieces. The mean grain size ranges between 4.20 and 5.91ϕ, averaging 4.93ϕ. No foraminifer was found in this layer. The bottom contacts the underlying layer *via* an obvious erosion surface. Based on the aforementioned analyses, this section is interpreted as composed of freshwater lacustrine swamp deposits.

Layer 3 (9.94–4.10 m): Layer 3 is comprised of dark gray sandy silt, with occasional waving bedding, cross-bedding, and abundant mica pieces. A section of 6.71 m–7.00 m contained black mud, and plenty of intact or fragmentary shells were found. The mean grain size is 4.19–6.07ϕ, averaging 4.69ϕ. Foraminiferal abundances in this layer are extremely high, even reached to ~30,000/50 g dry sample, with 8–14 species. Within the foraminiferal assemblage, *Ammonia takanabensis* (Ishizaki) is the most abundant, followed by *Epistominella naraensis*, *Ammonia beccarii* (Linné) *var*, *Cribrononion vitreum*, *Astrononion tasmanensis*, *Brizalina striatula*, and *Florilus atlanticus*, all of them being the common benthic species in the present northern Jiangsu coastal area. Planktonic species *Globigerina* spp., which is both typical shallow marine and stenohaline species, was also identified in this layer, but all of them were young specimen fossils. All of the aforementioned foraminiferal species are attributed to the hyaline group. In addition, the porcelaneous group, with two specimens of *Quinqueloculina akneriana rotunda (Gerke)* and 12 specimens of *Quinqueloculina* spp, was observed in a sample at a burial depth of 8.85 m. Foraminiferal assemblage of benthic and planktonic species and euryhaline and stenohaline species, which are mixed with sandy silt, with high abundance and diversity, indicates that they might be transported by the tidal current for a long distance. *Corbicula cf. amurensis* (Schrenck), belonging to bivalves, was identified. The contact relation between this layer and the underlying layer is transitional. Based on the aforementioned analyses, this layer is interpreted as composed of shallow bay deposits.

Layer 2 (4.10–1.00 m): This layer is primarily comprised of gray–black and yellowish-brown clayey silt, with occasional wavy bedding and cross-bedding. At the bottom of the layer (3.45–4.00 m), plenty of plant debris, intact shells, and shell fragments were observed. The mean grain size ranges between 4.78 and 6.35ϕ, averaging 5.54ϕ. *Corbicula cf. amurensis* (Schrenck), belonging to bivalves, was identified, some of which had two valves hinged, indicating that they were *in situ* buried. Abundant foraminifera were observed in a sample at a burial depth of 2.45 m, but the foraminiferal assemblage is very monotonous; only *Ammonia beccarii* (Linné) var. was found. No foraminifer was found at 3.75 m. In addition, some of the foraminifers were etched and partially or wholly decalcified, presenting the antique white color. The contact relation between this layer and the underlying layer is transitional. This layer is interpreted as composed of coastal marsh deposits. Monotonous species and the one commonly dominating species of foraminifers are the most important characteristics of coastal marsh deposits (Wang et al., 1985). Results from Murray (1968) have shown that the diverse fields of hyposaline lagoons are very low, particularly for samples rich in silt and clay.

Layer 1 (1.00–0 m): This backfill soil layer is mainly comprised of gray–black and gray–yellow clayey silt, with a few rock dregs, plant roots, and debris.

4.1.2 Sedimentary changes in Core Y

Layer 3 (9.26–4.00 m): This layer is mainly comprised of hardened or semi-hardened yellowish-brown, olive green stiff clayey silt, with abundant small black Fe-Mn nodules. The mean grain size is 5.83–6.61ϕ, averaging 6.36ϕ. A total of 25, 4, and 2 specimens of *Quinqueloculina akneriana rotunda (Gerke)*, *Cribrononion vitreum*, and *Elphidium limpidum* were recognized in a sample at a burial depth of 7.53 m, respectively. The contact relation between this layer and the underlying layer is transitional. Based on the aforementioned analyses, this stiff mud layer is interpreted to be composed of river floodplain deposits that were formed during MIS 2. Foraminifers in this layer are very likely due to the reworking, transportation, and redeposition of sediments from the exposed marine strata, which were caused by paleo-storm during the LGM (Xia et al., 2013). Foraminifera are also found in the stiff clay mud of more than half of the sixteen cores, including cores T2, T4, T5, T6, T7, T9, T10, T13, and T15 (located in the Yangtze River Delta) (Chen et al., 2008). In addition, a few marine or estuarine shell fragments and calcareous nannofossils of core 07SR01 (located in the middle Jiangsu coast) and the marine shell fragment-mixed sand layers of core T9 were also found in the stiff muds (Zhao et al., 1997; Xia et al., 2013).

Layer 2 (4.10–1.00 m): This layer is primarily comprised of brownish-gray clayey silt, with occasional sand–mud thin layers. The mean grain size ranges between 5.40 and 6.45ϕ, averaging 5.98ϕ. At the bottom of the layer (3.3 m–3.7 m), plenty of intact shells and shell fragments were observed. *Littorinopsis cf. intermedia* (Philippi) and *Littorinopsis cf. scabra* (Linne), belonging to gastropods, were identified with one in each species, which usually inhabit near the high tide line. *Corbicula leana* Prime, belonging to bivalves, was present abundantly. Plenty of foraminifers were recognized at 3.64 m, and no foraminifer was found at 2.92 m in the core. The contact relation between this layer and the underlying layer is transitional. This layer is interpreted as coastal marsh deposits.

Layer 1 (1.00–0 m): This backfill soil layer is mainly comprised of gray–black and gray–yellow clayey silt, with a few rock dregs, plant roots, and debris.

4.2 Dating results

AMS ^{14}C dating results of Core M and Core Y indicated that the lower sections analyzed are older than 43,500 a BP and 26,490 ± 110 a BP (Table 2), respectively. Hence, they are considered to represent the Late Pleistocene.

4.3 Concentrations of major and trace elements in the core sediments

Elemental compositions of Core M and Core Y are given in Figure 4 and Figure 5. Major and trace elements show variable trends in concentrations of different depositional units of Core M (Table 3). Concentrations of most elements of sediments are generally higher in MIS 2 than in MIS 1 (Figure 4; Table 3). Except Na_2O and TiO_2, the rest of the elements all showed a decreasing trend (Figure 4), and concentrations of most elements (e.g., Al, Fe, K, Cr, Li, Ni, V, and Zn) are relatively close to the Yangtze River sediments (Table 3). Concentrations of most elements are slightly lower during MIS 1 but as a whole remain fairly stable; in spite of a sudden fluctuation at ~3.5 m, the average concentrations of most of the elements (e.g., Al, Fe, Mg, Ti, Cr, V, and Zn) are very close to the Yellow River sediments (Table 3).

Concentrations of most of the elements in sediments of Core Y show little variation since MIS 2 (Figure 5; Table 3), and the average concentrations of many elements (e.g., Fe, K, Ba, Cr, Ni, V, and Zn) are very similar to the Yangtze River sediments (Table 3).

5 Discussion

5.1 Chronostratigraphic framework

The establishment of a reliable chronostratigraphic framework is the foundation for studying and explaining many geological problems. Multiple layers of stiff clays, which are mottled dense argillaceous strata and easily distinguished due to their stiffness and abrupt contacts with overlying strata, have been found in the Late Quaternary sedimentary records of several major river deltas in the world, such as the Mississippi River Delta (Aslan and Autin, 1998) and the Yangtze River Delta (Li et al., 2002; Chen et al., 2008). For example, the first stiff clays that were found at depths of 3–28 m in the Yangtze River Delta possess a marked boundary with the overlying Holocene deposits and a diffuse boundary with underlying grayish-yellow littoral or fluvial silt and sandy clay (Chen et al., 2008). Therefore, the first stiff clays in the Yangtze Delta are useful and important regional markers in the stratigraphic framework of the eastern coastal areas of China. By using the AMS ^{14}C dating results, together with the first stiff clays for reference, a chronostratigraphic framework was established for the sedimentary succession of Core M and Core Y.

According to analyses of abundant ^{14}C dating results of a large number of drill cores in the Abandoned Yellow River Delta region of Jiangsu coastal plain, ^{14}C ages dated by organic carbon from clayey silt tend to be older owing to increased reworking and admixture of older carbon during transportation (Xia et al., 2015). Residues of the acid–alkali–acid extraction of the peaty layers and organic macrofossils such as larger wood fragments, *in situ* root remnants (Hanebuth et al., 2000), and shells (Xia et al., 2015) yielded the most reliable ages. For Core M, AMS ^{14}C age dated by plant debris from clayey silt at 19.88 m is >43,500 a BP, which could provide certain reference significance. AMS ^{14}C age dated by organic-rich mud from clayey silt at 12.33 m of Core M is 30,510 ± 160 a BP, which might be reliable. The material dated from the bottom of Layer 2 (3.89 m) was recognized as *in situ* buried marine shells that yielded an age of 6400 ± 30 a BP. AMS ^{14}C ages at 1.40 m and 7.28 m of peaty layers were also found to be reliable. For Core Y, AMS ^{14}C ages dated by organic carbon from clayey silt at the bottom (8.33 m) and the top (5.30 m) of Layer 3 are 15,370 ± 50 a BP and 26,490 ± 110 a BP, respectively. The material dated from the bottom of Layer 2 (3.56 m) was recognized as *in situ* buried marine shells that yielded a reliable age of 6420 ± 30 a BP.

Therefore, on the basis of the dates of global sea-level changes during the Late Quaternary (Waelbroeck et al., 2002), together with the AMS ^{14}C dates, and using the first stiff clays for reference, in Core M, Layer 6 (coastal marsh deposits), Layer 5 (floodplain deposits), Layer 4 (freshwater lacustrine swamp deposits), Layer 3 (shallow bay deposits), and Layers 2 and 1 (coastal marsh deposits) are interpreted to have been formed in the late MIS 3, MIS 2, early MIS 1, early to

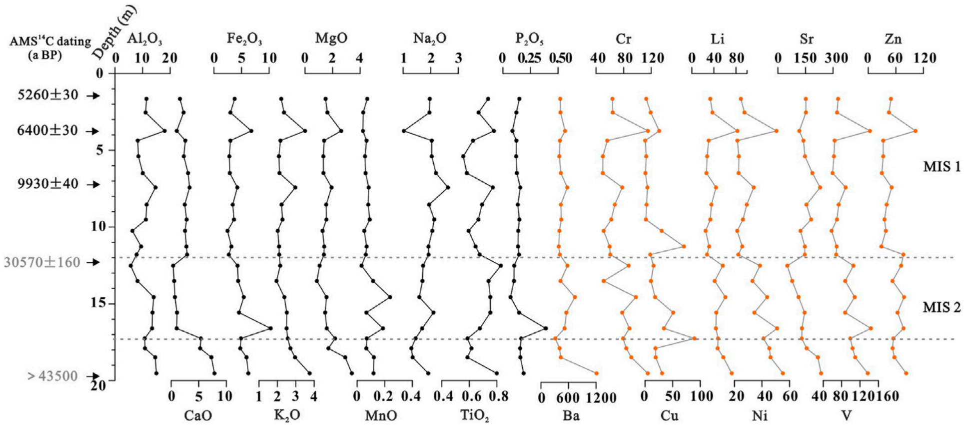

FIGURE 4
Elemental compositions of Core M sediments from the central North Jiangsu Plain (major elements in % and trace elements in μm/g).

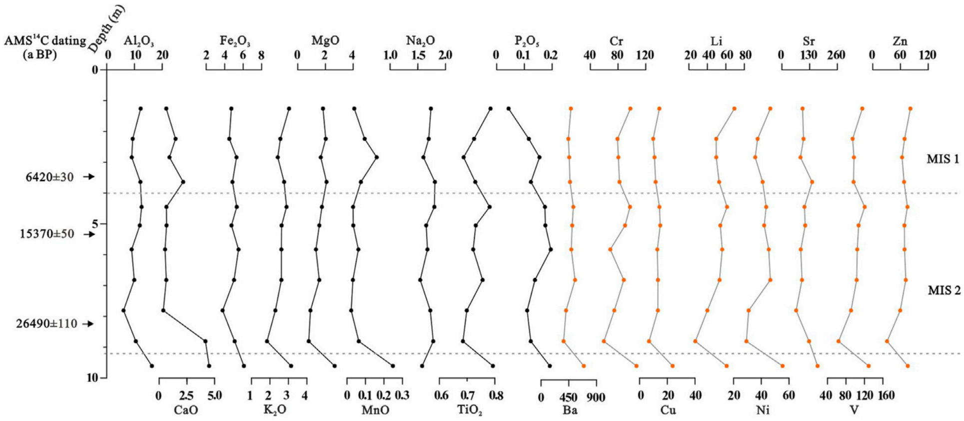

FIGURE 5
Elemental compositions of Core Y sediments from the central North Jiangsu Plain (major elements in % and trace elements in μm/g).

middle MIS 1, and middle-to-late MIS 1, respectively (Figure 2). In Core Y, Layer 4 (coastal marsh deposits), Layer 3 (floodplain deposits), and Layers 2 and 1 (coastal marsh deposits) are interpreted to have been formed in the late MIS 3, MIS 2, and middle-to-late MIS 1, respectively (Figure 3).

5.2 Evolution of sedimentary environments since MIS 2

The floodplain deposits suggest that in the area around the Core M and Core Y sites, a terrestrial environment prevailed during MIS 2. With the initiation of dramatic global cooling, the polar ice sheets advanced very quickly, and the sea level began to fall rapidly. The sea level of the Yellow Sea was situated at about −120 m during the LGM and later progressively rose to stabilize or slightly decrease at −100 m level and 16 cal ka BP (Figure 6) (Liu et al., 2004). Because of the extremely dry and cold climate during the LGM, a yellowish-brown-to/or-olive-green stiff clay mud was well developed in the northern side and southern side of the Yangtze River Delta with a buried depth of 3–25 m, which was the product of the ongoing accretion and pedogenesis on the floodplain during this period (Chen et al., 2008). This floodplain deposit was also well developed in the study area, and the stiff clay mud layer was recorded with a sedimentary thickness of 5.30 m in Core M and 5.26 m in Core Y. The burial depth in Core M and Core Y was 11.9–17.2 m (the depth of Core M and Core Y referred to in this study was the actual burial depth, not considering the compaction effect) and 4.0–9.3 m, respectively. As there was an erosion surface at the top of the MIS 2 deposit, the actual sedimentary thickness of this layer in Core M was certainly more than 5.3 m. The difference in sedimentary thickness of LGM deposits on the floodplain was a common phenomenon due to topographic fluctuations, distance from the river bed, and different water dynamic conditions in the Yangtze River Delta and the North Jiangsu Plain area (Chen et al., 2008).

The deglacial period began at ~15 cal ka BP as a result of global warming. The step-like and rapid rise of the postglacial sea level occurred as a result of global meltwater pulses (Figure 6) (Fairbanks, 1989; Liu et al., 2004). Freshwater lacustrine swamp, shallow bay, and coastal marsh deposits were developed in Core M during this period,

TABLE 3 Element concentrations in the sediments of Core M and Core Y (major element*: % and trace element: μm/g).

Element	Core M			Core Y			River	
	Mean	MIS 2-avg	MIS 1-avg	Mean	MIS 2-avg	MIS 1-avg	Yangtze	Yellow
Al_2O_3*	10.28	13.09	9.20	10.28	10.00	10.69	12.30	9.20
CaO*	1.91	2.97	1.51	1.23	1.18	1.31	4.00	4.61
Fe_2O_3*	3.75	4.80	3.35	4.88	4.90	4.84	5.50	3.14
K_2O*	2.27	2.53	2.16	2.57	2.48	2.70	2.21	1.94
MgO*	1.43	1.68	1.34	1.55	1.31	1.90	2.22	1.40
MnO*	0.07	0.09	0.06	0.06	0.04	0.09	0.11	0.06
Na_2O*	1.74	2.01	1.64	1.70	1.70	1.71	1.23	2.20
TiO_2*	0.66	0.73	0.63	0.73	0.73	0.73	0.92	0.60
P_2O_5*	0.13	0.15	0.12	0.14	0.15	0.11	0.15	0.14
Ba	474	562	440	470	474	464	512	540
Cr	70	81	66	82	80	85	82	60
Cu	17	26	13	12	13	12	35	13
Li	40	49	37	51	49	55	43	23
Ni	31	40	28	40	40	40	33	20
Sr	141	103	156	102	99	107	150	220
V	84	107	76	99	98	101	97	60
Zn	54	69	48	66	62	70	78	40

avg, average. The element compositions of the Yangtze River and Yellow River sediments are derived from Zhao and Yan (1992).

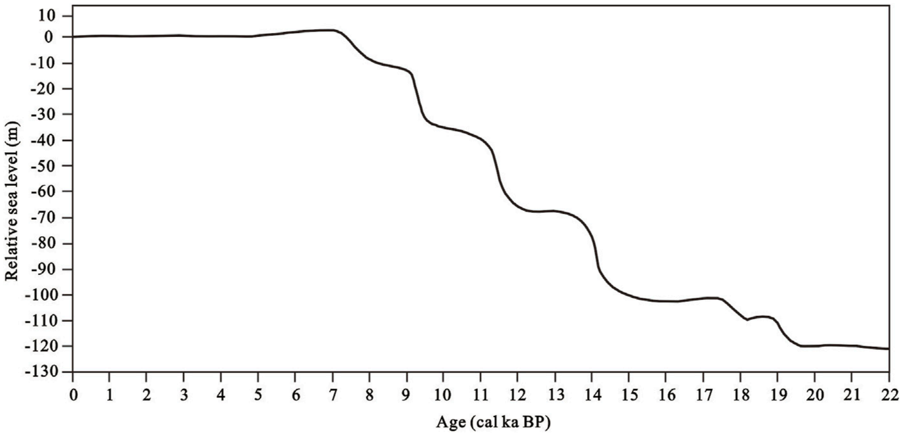

FIGURE 6
Stepwise postglacial sea-level rise in the western Pacific (after Liu et al., 2004).

and the corresponding grain size showed a coarse–coarse–fine pattern, indicating strong–strong–weak hydrodynamic conditions. The obvious erosion surface and sudden increase in grain size also demonstrated strong water dynamics during the postglacial period, which reflects that the top layer of the stiff clay mud formed during MIS 2 in Core M was eroded. Transgression layers with obvious erosion surfaces at the bottom were extensively distributed during the postglacial period in the continental shelves in eastern China (Li and Wang, 1998; Xia et al., 2013). The postglacial deposit thickness of Core Y is relatively small; only a 4 m coastal marsh deposit with fine grain size was developed, indicating relatively weak water dynamics.

Since the sea level reached a maximum at around 7000 a BP, the paleo-coastline at NJP even reached the Huaiyin–Gaoyou–Yangzhou area (Figure 1B), and a huge estuary of the Yangtze River with the apex at Zhenjiang and Yangzhou areas was formed when the postglacial transgression reached the maximum (Li et al., 2000). After 7000 a BP, the sea level gradually tended to be stable (Figure 6); this was evidenced by a series of shelly sandbars (formed at ~7 ka BP, 4.6 ka BP, and 3.8 ka BP from west to east, respectively) parallel to the present coastline in the NJP, which have been found in Funing–Yancheng–Dongtai–Hai'an area (Figure 1B, Gu et al., 1983). These shelly sandbars, together with the north sandbank of the Yangtze River and the south sandbank of the Huaihe River, surrounded the central NJP, making this area a big shallow coastal lagoon that was separated from the open sea by shelly sandbars, which were linked with the open sea by a number of inlets (Pan, 1983). Core M and Core Y sites all developed coastal marsh deposits after 7000 a BP. Few foraminifer assemblages in Core M and Core Y during this period might be a reflection of a relatively long distance from the open sea or could be due to the etch of the calcareous shell at a low pH. Results from Murray (1968) have shown that the foraminifer assemblage in hyposaline lagoons diminishes sharply with the increasing distance to the open sea as salinity decreases from the back to the mouth.

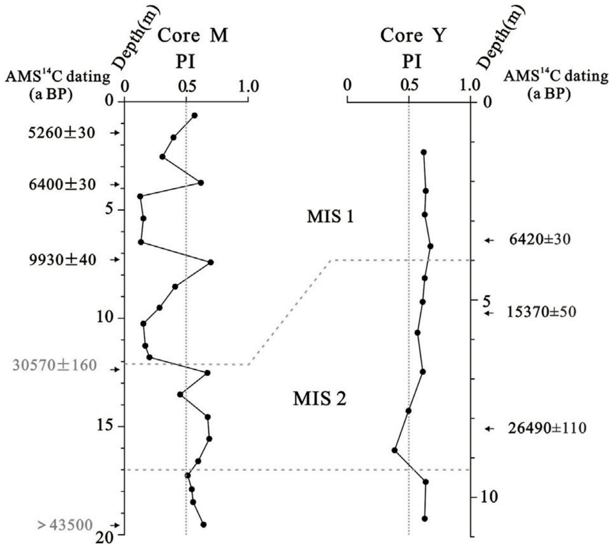

FIGURE 7
Depth profiles of PI values in Core M and Core Y.

5.3 Sediment provenance variation in the central NJP

5.3.1 Quantification of source contribution using the PI model

The sedimentation in the NJP is primarily controlled by large volumes of sediment derived from the surrounding large rivers (e.g., the Yangtze and Yellow rivers) and the smaller rivers (e.g., the Huai River). The modern Changjiang and Huanghe rivers, respectively, deliver 470 Mt and 1100 Mt of suspended sediments annually to the East Asian marginal seas (Milliman and Farnsworth, 2011). The contribution of other small localized rivers to the study area (e.g., the Huai River) is likely negligible because of the relatively low suspended sediment flux in total (e.g., ~14 Mt/yr of the Huai River) from these rivers (Milliman and Farnsworth, 2011). It has been well established that source rock compositions and weathering mechanisms basically impose constraints on the distinct geochemical compositions of the Yangtze River and the Yellow River sediments (Zhao and Yan, 1992; Chen et al., 2000; Yang et al., 2002). The Yangtze River sediments are characterized by high enrichment of transition metals (e.g., Cu, Zn, Pb, Fe, Co, Ni, Mn, Sc, and Ti), whereas the Yellow River sediments have relatively high concentrations of alkali and alkaline earth elements (e.g., Na, Ca, Sr, and Ba) (Zhao and Yan, 1992; Yang et al., 2002) (Table 3). Therefore, the marked difference in elemental compositions between both rivers' sediments could provide a basis for the discrimination of sediment sources in the North Jiangsu Plain. For the discrimination of the core sediments, five elements, namely, Al, Ti, Ni, Cr, and V, were chosen because these metals show big differences in concentrations between the Yangtze River and Yellow River and moreover, are known to behave conservatively in sedimentary environments (Taylor and McLennan, 1985; Yang et al., 2002). A two-end-member mixing model was adopted by assuming that the Yangtze River and the Yellow River are two provenances to the North Jiangsu Plain sediments and that the sediments from other sources (e.g., Huaihe River-derived sediments and sediments from other local small rivers, etc.; in fact, these rivers are too confined or too small to contribute much sediment) are negligible (Yu and Oldfield, 1989). This model has been applied in the modern Yellow River Delta (Yang et al., 2001), the north Jiangsu coastal plain (Yang et al., 2002), and west of the South Yellow Sea sediments (Lu, 2013) in China. A detailed computational process can be seen in Yang et al. (2002).

$$\mathrm{PI} = \frac{A_{i1}}{A_{i1} + A_{i2}},$$

$$A_{i1} = \sum_{i=1}^{n} \frac{|C_{ix} - C_{i1}|}{\mathrm{range}\,(i_{x,1})},$$

$$A_{i2} = \sum_{i=1}^{n} \frac{|C_{ix} - C_{i2}|}{\mathrm{range}\,(i_{x,2})},$$

where PI indicates provenance index; A_{i1} and A_{i2} represent degrees of similarity for element i of the sediment sample to the end-members 1 (Yellow River-derived sediment) and 2 (Yangtze River-derived sediment), respectively; C_{ix}, C_{i1}, and C_{i2} are concentrations of element i in the sediment sample and end-member sediments 1 and 2, respectively; the range is the difference between the maximum and minimum concentrations of element i in the sample and end-member sediments altogether; and n is the number of determined elements. Since the Yellow River and Yangtze River sediments are regarded as end-members 1 and 2, respectively, their theoretical PI values are expected to be 0 and 1, respectively. The whole composition of a sediment sample approximates that of end-member 1 if the PI nears 0, otherwise approximates that of end-member 2 if the PI approaches 1. Considering the bulk sample being used to determine element concentration in this paper, the values of Al, Ti, Ni, Cr, and V are derived from Zhao and Yan (1992).

Almost all of the PI values of the MIS 2 sediments of Core M are more than 0.50 with an average of 0.59 (Figure 7), implying that the sediments have been derived predominantly from the Yangtze River, whereas most of the PI values of the MIS 1 sediments are less than 0.50 (0.13–0.62) with an average of 0.32, representing a dominant influence from the Yellow River. Almost all of the PI values exceed 0.50 for the sediments of Core Y, averaging 0.59 (Figure 7); this indicated a

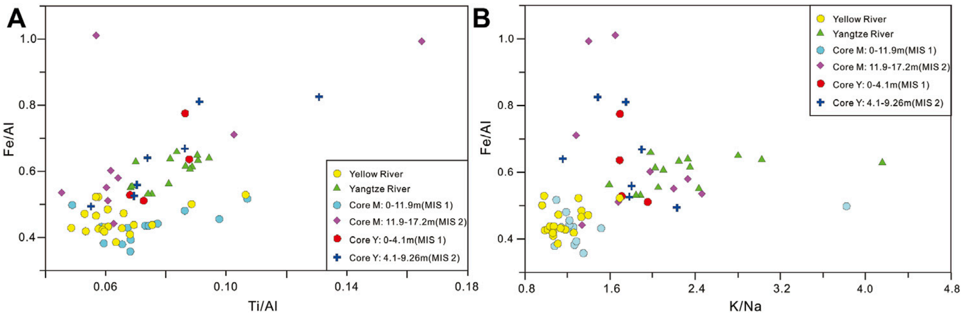

FIGURE 8
Cross plot of Fe/Al vs. Ti/Al **(A)** and Fe/Al vs. K/Na **(B)** of the M and Y core sediments from the NJP. Yellow River and Yangtze River element data are derived from Yang et al. (2002).

relatively stable sediment source from the Yangtze River for Core Y since MIS 2.

5.3.2 Sediment provenance discrimination using element ratios

The differences in elemental compositions between the Yangtze River and Yellow River sediments can be used as provenance indices to better understand the evolution and formation of the North Jiangsu Plain. Some element ratios, i.e., Fe/Al, K/Al, and Ti/Al, have especially been used to identify the sediment sources due to their relatively conservative behaviors during the sediment formation process (Han et al., 2019; Sun et al., 2019). K/Na is usually used as a proxy for the chemical maturity of sedimentary units. Chemical weathering is stronger in the Yangtze River basin than in the Yellow River basin, where physical weathering predominates (Yang et al., 2001). Therefore, the geochemical compositions of sediments derived from the Yangtze River and Yellow River can be distinguished based on the different weathering patterns and rock compositions (Yang et al., 2001). In this study, Fe/Al–Ti/Al and Fe/Al–K/Na scatter diagrams were used to identify the sources of sediments in the study area.

Figure 8 shows that the upper part (0–11.9 m) of the M core is clearly different from the lower unit (11.9–17.2 m) using plots of Fe/Al vs. Ti/Al and Fe/Al vs. K/Na, which indicates that the upper and deeper core units may have different provenances. The Fe/Al (0.36–0.52) and Ti/Al (0.05–0.11) values from 0 to 11.9 m in the M core fall within the ranges of the Yellow River field, implying that its source may be from the Yellow River. The Fe/Al (0.44–1.01) and Ti/Al (0.05–0.17) values of the lower part (11.9–17.2 m) are relatively widely distributed with some samples falling within the range of the Yellow River field and others seemingly falling within the range of the Yangtze River field (Figure 8). This implies that the source conditions of the deeper sediments are mainly composed of Yangtze and Yellow River sediments during MIS 2. Almost all samples of Core Y (0–4.10 m and 4.10–9.26 m) located in the Yangtze River field show very little variation and are unambiguously different from the Yellow River sediments (Figure 8); this trend can be interpreted to mean that the Y core sediments were primarily sourced from the Yangtze River.

Consequently, Fe/Al-Ti/Al and Fe/Al-K/Na ratios suggest that sediments settled on the study site during MIS 2 were mainly controlled by the Yangtze River, and later, Core Y in the southern part of NJP was dominated by Yangtze River sediments, whereas Core M in the northern part was supplied by the Yellow River for the last 10 ka.

5.4 Factors controlling environmental and provenance changes since MIS 2

Both PI values and Fe/Al-Ti/Al and Fe/Al-K/Na ratios indicate an alternating influence of the Yellow River and the Yangtze River on the North Jiangsu Plain since MIS 2. The Yangtze River sediments dominated the study area during MIS 2, and the MIS 1 sediments of Core Y still received the Yangtze River sediments, while Core M was controlled by the Yellow River-derived sediments.

The Yellow River-derived sediments in Core M were dark gray sandy silt and a large number of mica pieces were observed, indicating that these sediments might have been transformed and accumulated in this area by the transport of previously deposited sediments by strong tidal currents and intense waves during the transgression period. According to Chen (1989), sediments of the Yellow River usually show light yellow or yellow–brown color, which is composed of silt or silty sand, whereas once the sediments were transformed, the color would be darker because of the river–sea interaction. Waves and tides represent the dominant hydrodynamic forcing for the coast-shelf environment (Gao and Collins, 2014), especially in shallow waters, wave-generated currents can cause intense sediment transport (Dyer, 1986). The tidal current is often responsible for landward transport. Waves can cause landward transport of sand and gravel on the continental shelf (Gao and Collins, 2014), and the coarse grain size of PG sediments of Core M also indicates strong hydrodynamic conditions (Figure 2). Furthermore, the tidal current is also recognized as the primary agent of foraminifera transport, and the small size, high diversity, and stenohaline species of the foraminiferal assemblage are important marks of a strong-medium tidal estuary (Wang et al., 1986). The foraminiferal assemblage at 4.10 m–9.94 m in Core M is a mixture of benthic and planktonic species and euryhaline and stenohaline species, with high abundance and diversity, which might also be a reflection of strong tidal currents during this period.

Based on the lithologic characteristics of several cores, Chen (1989) concluded that the Yellow River sediments began to influence the North Jiangsu Plain in the Late Pleistocene. Liu et al. (1987) thought that the Yellow River might have directly flowed into the Yellow Sea in the northern Jiangsu coastal area for quite a long time during the Pleistocene. Zhang et al. (2016) proposed that the Yellow River invasion into the Huaihe River drainage basin occurred during the last deglaciation (~13.2 ka). In addition, on the basis of geochemical analysis, Yang et al. (2002) also detailed that the Yellow River supplied considerable sediments to the north part of the Jiangsu coastal plain by tidal reworking or southward shift of the Yellow River during 7000–3000 a BP and somewhat to the central and southern parts. Some differences were observed when the Yellow River began to influence the North Jiangsu Plain since the postglacial period. These studies were primarily concentrated on the northern Jiangsu coast plain region, and the deposition rate of this area is usually not only higher but also strongly eroded; compiled with the late frequent scouring and redeposition, the stratigraphic sequence is extremely complex, which might disturb the proper understanding of the stratum development history (Li and Wang, 1998). However, the study area in this paper is located at the back of the northern part of the Yangtze River Delta and west of the northern Jiangsu coastal plain, with the relatively weak influence of the strong coastal hydrodynamic condition and physical and biological disturbances since the LGM, which might be a potential area for high-resolution stratigraphic study (Li and Wang, 1998). The results in this study clearly showed that the Yellow River supplied considerable sediments to part of the central North Jiangsu Plain during the postglacial period. The Yellow River probably had shifted its course to the south and may have directly flowed into the northern Jiangsu coastal area during the postglacial period. In addition, the Yellow River sediments might have accumulated in this area by the transport of previously deposited sediments by strong tidal currents and intense waves during the transgression period.

Although Core M and Core Y are only ~15 km apart, our research results show that the sedimentary environment and sediment source recorded by the two boreholes vary greatly. The burial depth of the MIS 2 deposit in Core M and Core Y was 11.9–17.2 m and 4.0–9.3 m, respectively. Therefore, the terrain of Core Y in the south of the study area is nearly 9 m higher than that of Core M in the north at late MIS 2. This topographic relief was an important factor controlling the direction and scope of transgression in the postglacial stage. Coupled with the climate change, sea-level fluctuation, and river channel migration of the Yangtze River, Yellow River, and Huaihe River in the historical period, the paleogeography and paleoenvironment evolution were extremely complex in the NJP; sediment stratigraphic records of the adjacent borehole even vary considerably, not only in the number of transgression layers but also in the lateral variation of sedimentary facies (Li and Wang, 1998). In fact, it is a common phenomenon in the Yangtze River Delta and the NJP area. For example, 3 and 4 transgression layers were recorded in Core M and Core Y since the middle Pleistocene, respectively (Chen, 2016). However, 1 transgression layer in XH1 and XH2 and 3 in CSJA3 were recorded since the Quaternary, respectively (Figure 1), which were only 10–20 km away from Core M (Zhang, 2009; Yu et al., 2016). A thorough review was carried out by Chen et al. (2020) on the distribution of buried channels in the region of NJP and the western South Yellow Sea; the results show that paleo-river channels are particularly developed in the region left behind by the paleo-Yangtze River since the Quaternary, resulting in a more complicated sedimentary environment and sediment source.

6 Conclusion

Based on a comprehensive analysis of Core M and Core Y, the evolution of the sedimentary environment and changes in sediment supplies of the central NJP were discussed.

River floodplain deposits were developed during MIS 2 in the central NJP. Coastal marsh deposits were developed in the south central NJP during MIS 1, and coastal marsh and shallow bay deposits were developed in the north central NJP during early MIS 1 when the postglacial transgression reached the maximum (~7000 a BP); after the postglacial transgression reached the maximum, the sea level tended to be stable, the paleo-coastline advanced to the east of the study area, and coastal marsh deposits were again developed in the north central NJP.

Sediments delivered to the study site during MIS 2 were mainly derived from the Yangtze River and were later dominated by the Yangtze River in the south and the Yellow River in the north. These Yellow River sediments might be transported from previously deposited sediments by strong tidal currents and intense waves to this area or be a reflection of a southward shift of the Yellow River during this period. Changes in sediment supplies and the sedimentary environment in the central NJP were controlled primarily by sea-level fluctuations, regional geomorphic patterns, and shift of the rivers.

Data availability statement

The original contributions presented in the study are included in the article/Supplementary Material; further inquiries can be directed to the corresponding author.

Author contributions

ZZ and YC designed the study; YC wrote the manuscript; YC, FX, and ZZ analyzed the data and contributed to the discussion and interpretation of the results; QX collated and processed the data; and YC and FG drew the drawings. All authors contributed to the article and approved the submitted version.

Funding

This work was supported by the National Natural Science Foundation of China (Grant Nos 41701101, 41901107, 41371024, and 41230751), the Open Fund of the State Key Laboratory of Loess and Quaternary Geology (Grant No. SKLLQ 1902), and a Project Funded by the Priority Academic Program Development of Jiangsu Higher Education Institutions.

Acknowledgments

The authors are very grateful to Prof. Xin Hu and Senior Engineer Yijun Chen at the Center of Modern Analysis, Nanjing University, for their assistance with the chemical experiment and to Huazhang Pan and Xiu Lan at the Nanjing Institute of Geology and Palaeontology, Chinese Academy of Sciences, for their assistance with the species identification of gastropod and bivalve fossils.

Conflict of interest

The authors declare that the research was conducted in the absence of any commercial or financial relationships that could be construed as a potential conflict of interest.

Publisher's note

References

Aslan, A., and Autin, W. J. (1998). Holocene flood-plain soil formation in the southern lower Mississippi valley: Implications for interpreting alluvial paleosols. *Geol. Soc. Am. Bull.* 110 (4), 433–449. doi:10.1130/0016-7606(1998)110<0433:HFPSFI>2.3.CO;2

Blott, S. J., and Pye, K. (2001). Gradistat: A grain size distribution and statistics package for the analysis of unconsolidated sediments. *Earth Surf. Proc. Land.* 26 (11), 1237–1248. doi:10.1002/esp.261

Chen, B. Z., Li, C. X., and Ye, Z. Z. (1995). Postglacial sedimentation and environmental evolution of the northern part of the Yangtze River Delta. *Acta Oceanol. Sin.* 17 (1), 64–75. (in Chinese).

Chen, J. S., Wang, F. Y., Li, X. D., and Song, J. J. (2000). Geographical variations of trace elements in sediments of the major rivers in eastern China. *Environ. Geol.* 39 (12), 1334–1340. doi:10.1007/s002540000224

Chen, Q. Q., Li, C. X., Li, P., Liu, B. Z., and Sun, H. P. (2008). Late quaternary palaeosols in the Yangtze delta, China, and their palaeoenvironmental implications. *Geomorphology* 100 (3), 465–483. doi:10.1016/j.geomorph.2008.01.015

Chen, X. X. (1989). Holocene sedimentary characteristics of the huanghuai plain, Jiangsu. *J. Stratigr.* 13 (3), 213–218. (in Chinese with English abstract).

Chen, Y. Y. (2016). *Evolution of depositional environment and sediment sources of the northern Yangtze River Delta since the middle Pleistocene*. Nanjing China: Doctor Dissertation of Nanjing University. (in Chinese with English abstract).

Chen, Y. Y., Xia, F., Zhang, Z. K., Xu, Q. M., and Chen, S. Y. (2020). Research progress on distribution of Quaternary buried paleo-Yangtze River channels in the North Jiangsu-Western South Yellow Sea. *Mar. Geol. Quat. Geol.* 40 (4), 40–54. (in Chinese with English abstract).

Chen, Y. Z., Syvitski, J. P. M., Gao, S., Overeem, I., and Kettner, A. J. (2012). Socio-economic impacts on flooding: A 4000-year history of the Yellow River, China. *Ambio* 41 (7), 682–698. doi:10.1007/s13280-012-0290-5

Chen, Z. Y., and Stanley, D. J. (1995). Quaternary subsidence and river channel migration in the Yangtze delta plain, eastern China. *J. Coast. Res.* 11 (3), 927–945.

Dyer, K. R. (1986). *Coastal and estuarine sediment dynamics*. Chichester: John Wiley.

Editorial Board on Records of Huaihe River (1997). *Annals of the Huaihe River* (Beijing: Science Press), 1. (in Chinese).*Records of Huaihe River*.

Fairbanks, R. G. (1989). A 17, 000-year glacio-eustatic sea level record: Influence of glacial melting rates on the younger dryas event and deep-ocean circulation. *Nature* 342 (6250), 637–642. doi:10.1038/342637a0

Folk, R. L., and Ward, W. C. (1957). Brazos River bar: A study in the significance of grain size parameters. *J. Sediment. Pet.* 27 (1), 3–26. doi:10.1306/74d70646-2b21-11d7-8648000102c1865d

Gao, S., and Collins, M. B. (2014). Holocene sedimentary systems on continental shelves. *Mar. Geol.* 352, 268–294. doi:10.1016/j.margeo.2014.03.021

Gu, J. Y., Yan, Q. S., and Yu, Z. Y. (1983). The cheniers of the northern coastal plain of Jiangsu Province. *Acta Sedimentol. Sin.* 1 (2), 47–59. (in Chinese with English abstract).

Han, L., Hao, Q. Z., Qiao, Y. S., Wang, L., Peng, S. Z., Li, N., et al. (2019). Geochemical evidence for provenance diversity of loess in southern China and its implications for glacial aridification of the northern subtropical region. *Quat. Sci. Rev.* 212, 149–163. doi:10.1016/j.quascirev.2019.04.002

Hanebuth, T., Stattegger, K., and Grootes, P. M. (2000). Rapid flooding of the sunda shelf: A late-glacial sea-level record. *Science* 288, 1033–1035. doi:10.1126/science.288.5468.1033

Johnson, S. Y., Beeson, J. W., Watt, J. T., Sliter, R. W., and Papesh, A. G. (2020). Controls on sediment distribution in the coastal zone of the central California transform continental margin, USA. *Mar. Geol.* 420, 106085. doi:10.1016/j.margeo.2019.106085

Li, C. X., Wang, P. X., Sun, H. P., Zhang, J. Q., Fan, D. D., and Deng, B. (2002). Late Quaternary incised-valley fill of the Yangtze delta (China): Its stratigraphic framework and evolution. *Sediment. Geol.* 152 (1), 133–158. doi:10.1016/S0037-0738(02)00066-0

Li, C. X., Chen, Q. Q., Zhang, J. Q., Yang, S. Y., and Fan, D. D. (2000). Stratigraphy and paleoenvironmental changes in the Yangtze delta during the late Quaternary. *J. Asian Earth Sci.* 18 (4), 453–469. doi:10.1016/S1367-9120(99)00078-4

Li, C. X., and Wang, P. X. (1998). *Late quaternary stratigraphy of the Changjiang delta*. Beijing: China Science Press. (in Chinese).

Li, C. X., Zhang, J. Q., and Deng, B. (2001). Holocene regression and the tidal radial sand ridge system formation in the Jiangsu coastal zone, east China. *Mar. Geol.* 173 (1), 97–120. doi:10.1016/s0025-3227(00)00169-9

Liu, J. P., Milliman, J. D., Gao, S., and Cheng, P. (2004). Holocene development of the Yellow River's subaqueous delta, north Yellow Sea. *Mar. Geol.* 209 (1), 45–67. doi:10.1016/j.margeo.2004.06.009

Liu, J., Wang, H., Wang, F. F., Qiu, J. D., Saito, Y., Lu, J. F., et al. (2016). Sedimentary evolution during the last ~1.9Ma near the western margin of the modern Bohai Sea. *Palaeogeogr. Palaeocl.* 451, 84–96. doi:10.1016/j.palaeo.2016.03.012

Liu, J., Zhang, X. H., Mei, X., Zhao, Q. H., Guo, X. W., Zhao, W. N., et al. (2018). The sedimentary succession of the last ~3.50 Myr in the western South Yellow sea: Paleoenvironmental and tectonic implications. *Mar. Geol.* 399, 47–65. doi:10.1016/j.margeo.2017.11.005

Liu, M. H., Wu, S. Y., and Wang, Y. J. (1987). *Late quaternary deposit of South Yellow Sea*. Beijing: China Ocean Press. (in Chinese).

Loeblich, A. R., and Tappan, H. (1988). *Foraminiferal genera and their classification*. New York: Van Nostrand Reinhold.

Lu, J. (2013). *Sedimentary characteristics and significance of provenance and sedimentary environment since the late Pleistocene in the western South Yellow Sea*. PhD Thesis (Institute of Oceanology, Chinese Academy of Sciences). (in Chinese with English abstract).

Milliman, J. D., and Farnsworth, K. L. (2011). *River discharge to the coastal ocean: A global synthesis*. New York: Cambridge University Press.

Milliman, J. D., Qin, Y. S., Ren, M. E., and Saito, Y. (1987). Man's influence on the erosion and transport of sediment by Asian rivers: The Yellow River (Huanghe) example. *J. Geol.* 95 (6), 751–762. doi:10.1086/629175

Murray, J. W. (1968). Living foraminifers of lagoons and estuaries. *Micropaleontology* 14 (4), 435–455. doi:10.2307/1485088

Pan, F. Y. (1983). A sketch of the transition of the lakes between the Yangtze River and the Huaihe in the late Holocene. *Sci. Geogr. Sin.* 3 (4), 361–368. (in Chinese with English abstract).

Provincial Geomatics Center of Jiangsu Province (2004). *Atlas of the Jiangsu Province*. Beijing: China Cartographic Publishing House. (in Chinese).

Ren, M. E., and Shi, Y. L. (1986). Sediment discharge of the Yellow River (China) and its effect on the sedimentation of the Bohai and the Yellow Sea. *Cont. Shelf Res.* 6 (6), 785–810. doi:10.1016/0278-4343(86)90037-3

Shi, X. F., Yao, Z. Q., Liu, J. X., Qiao, S. Q., Liu, Y. G., Li, X. Y., et al. (2021). Dominant role of sea level on the sedimentary environmental evolution in the Bohai and Yellow seas over the last 1 million years. *Front. Earth Sci.* 9, 638221. doi:10.3389/feart.2021.638221

Sun, S., Li, Y., Liu, D. W., and Hu, K. (2022). Clay mineralogical records in the North Bohai coast of China in the last century: Sediment provenance and morphological implications. *Front. Earth Sci.* 10, 865839. doi:10.3389/feart.2022.865839

Sun, X. Q., Liu, S. F., Li, J. R., Zhang, H., Zhu, A. M., Cao, P., et al. (2019). Major and trace element compositions of surface sediments from the lower bengal fan: Implications for provenance discrimination and sedimentary environment. *J. Asian Earth Sci.* 184, 104000–104010. doi:10.1016/j.jseaes.2019.104000

Sun, Z. Y., Li, G., and Yin, Y. (2015). The Yangtze River deposition in southern Yellow Sea during marine oxygen Isotope stage 3 and its implications for sea-level changes. *Quat. Res.* 83 (1), 204–215. doi:10.1016/j.yqres.2014.08.008

Taylor, S. R., and McLennan, S. M. (1985). *The continental crust: Its composition and evolution*. Oxford: Blackwell.

Waelbroeck, C., Labeyrie, L., Michel, E., Duplessya, J. C., McManusc, J. F., Lambeckd, K., et al. (2002). Sea-level and deep water temperature changes derived from benthic foraminifera isotopic records. *Quat. Sci. Rev.* 21 (1), 295–305. doi:10.1016/S0277-3791(01)00101-9

Wang, P. X. (1988). *Foraminifera and ostracod assemblage of bottom substrate of the East China Sea*. Beijing: China Ocean Press. (in Chinese).

Wang, P. X., Min, Q. B., and Bian, Y. H. (1985). Quaternary stratigraphy of marine-continental transitional facies in east China. *Quat. Sci.* 6 (1), 35–43. (in Chinese with English abstract).

Wang, P. X., Min, Q. B., and Bian, Y. H. (1986). Transport of foraminiferal tests in estuaries and its paleoenvironmental implications. *Mar. Geol. Quat. Geol.* 6 (2), 53–66. (in Chinese with English abstract).

Wang, Y., Zhang, Z. K., Zhu, D. K., Yang, J. H., Mao, L. J., and Li, S. H. (2006). River-sea interaction and the North Jiangsu Plain formation. *Quat. Sci.* 26 (3), 301–320. (in Chinese).

Xia, F., Zhang, Y. Z., Wang, Q., Yin, Y., Wegmann, K. W., and Liu, J. P. (2013). Evolution of sedimentary environments of the middle Jiangsu coast, South Yellow Sea since late MIS 3. *J. Geogr. Sci.* 23 (5), 883–914. doi:10.1007/s11442-013-1051-5

Xia, F., Zhang, Y. Z., Wang, R. F., Liu, J. P., Zhang, Z. K., and Peng, X. Q. (2015). Review for the studies on sedimentation range of the abandoned Yellow River subaqueous delta, North Jiangsu plain coast, China. *Acta Geogr. Sin.* 70 (1), 29–48. (in Chinese with English abstract).

Yang, S. Y., Cai, J. G., Li, C. X., and Deng, B. (2001). New discussion about the run-through time of the Yellow River. *Mar. Geol. Quat. Geol.* 21 (2), 15–20. (in Chinese with English abstract).

Yang, S. Y., Li, C. X., and Cai, J. G. (2006). Geochemical compositions of core sediments in eastern China: Implication for late Cenozoic palaeoenvironmental changes. *Palaeogeogr. Palaeocl.* 229 (4), 287–302. doi:10.1016/j.palaeo.2005.06.026

Yang, S. Y., Li, C. X., Jung, H. S., and Lee, H. J. (2002). Discrimination of geochemical compositions between the Changjiang and the Huanghe sediments and its application for the identification of sediment source in the Jiangsu coastal plain, China. *Mar. Geol.* 186 (3), 229–241. doi:10.1016/S0025-3227(02)00335-3

Yoneda, M., Uno, H., Shibata, Y., Suzuki, R., Kumamoto, Y., Yoshida, K., et al. (2007). Radiocarbon marine reservoir ages in the western pacific estimated by pre-bomb Molluscan shells. *Nucl. Instrum. Meth. B* 259 (1), 432–437. doi:10.1016/j.nimb.2007.01.184

Yu, J. J., Lao, J. X., Jiang, R., Zeng, J. W., Peng, B., Ma, X., et al. (2016). Reconstruction of the late quaternary palaeoenvironment on the north wing of Yangtze River Delta, based on comparative study of the multistratigraphies. *Geol. Bull. China* 35 (10), 1692–1704. (in Chinese with English abstract).

Yu, L. Z., and Oldfield, F. (1989). A multivariate mixing model for identifying sediment source from magnetic measurements. *Quat. Res.* 32 (2), 168–181. doi:10.1016/0033-5894(89)90073-2

Zhang, L., Qin, X. G., Liu, J. Q., Sun, C. Q., Mu, Y., Gao, J. L., et al. (2016). Geochemistry of sediments from the Huaibei Plain (east China): Implications for provenance, weathering, and invasion of the Yellow River into the Huaihe River. *J. Asian Earth Sci.* 121, 72–83. doi:10.1016/j.jseaes.2016.02.008

Zhang, M. H. (2009). Sedimentary infilling and environmental changes of the northern Jiangsu basin since latest Miocene recorded in Xinghua cores. Doctor Dissertation (Nanjing, China: Nanjing Normal University). (in Chinese with English abstract).

Zhang, S. P. (2008). *Atlas of marine molluscs in China*. Beijing: China Ocean Press. (in Chinese).

Zhang, Z. K., Xie, L., Zhang, Y. F., Xu, J., Li, S. H., and Wang, Y. (2010). Sedimentary records of the MIS 3 transgression event in the North Jiangsu plain, China. *Quat. Sci.* 30, 883–891. (in Chinese with English abstract).

Zhao, J., Li, C. X., and Zhang, G. J. (1997). Discovery of the tidal-genetic sandy sedimentary area at Subei coast plain and its geological significance. *J. Tongji Univ.* 25 (1), 82–86. (in Chinese).

Zhao, Y. Y., and Yan, M. C. (1992). Abundance of chemical elements in sediments from the Huanghe River, the Changjiang River and the continental shelf of China. *Chin. Sci. Bull.* 47 (15), 1201–1204. (in Chinese).

Zheng, X. D. (2013). *Atlas of aquatic molluscs in China*. Qingdao: Qingdao Publishing Group. (in Chinese).

Zhou, L., Shi, Y., Zhao, Y., Yang, Y., Jia, J., Gao, J., et al. (2021). Extreme floods of the Changjiang River over the past two millennia: Contributions of climate change and human activity. *Mar. Geol.* 433, 106418. doi:10.1016/j.margeo.2020.106418

frontiers | Frontiers in Earth Science

TYPE Original Research
PUBLISHED 12 January 2023
DOI 10.3389/feart.2022.1107495

EDITED BY
Dario Gioia,
Institute of Cultural Heritage Sciences (CNR), Italy

REVIEWED BY
Giuseppe Corrado,
University of Basilicata, Italy
Domenico Chiarella,
University of London, United Kingdom

*CORRESPONDENCE
Lei He,
✉ hel_qimg@sina.com

SPECIALTY SECTION
This article was submitted to Quaternary Science, Geomorphology and Paleoenvironment, a section of the journal Frontiers in Earth Science

RECEIVED 25 November 2022
ACCEPTED 29 December 2022
PUBLISHED 12 January 2023

CITATION
He L, Ye S, Xue C, Zhao G, Yang S and Amorosi A (2023), Sedimentology and evolution of the Holocene radial tidal sand ridge in the south Yellow Sea, China.
Front. Earth Sci. 10:1107495.
doi: 10.3389/feart.2022.1107495

Sedimentology and evolution of the Holocene radial tidal sand ridge in the south Yellow Sea, China

Lei He[1,2]*, Siyuan Ye[1,2,3], Chunting Xue[1], Guangming Zhao[1,2], Shixiong Yang[1,2] and Alessandro Amorosi[4]

[1]Key Laboratory of Coastal Wetland Biogeosciences, Qingdao Institute of Marine Geology, China Geological Survey, Qingdao, China, [2]Laboratory for Marine Geology, Laoshan Laboratory, Qingdao, China, [3]Institute of Marine Science and Technology, Shandong University, Qingdao, China, [4]Department of Biological, Geological and Environmental Sciences, University of Bologna, Bologna, Italy

The radial tidal sand ridge (RTSR) off the Jiangsu Coast in the south Yellow Sea is one of the most fantastic and unique natural landscapes in the world. A large number of investigations on geomorphology and marine geology have been implemented during the last several decades. The formation and evolution of the RTSR, however, are still under debate. To resolve this issue, 10 ~30–60 m-long cores were retrieved from the Jiangsu coastal plain and offshore sand ridge field in 2018–2019. Stratigraphic transects chronologically constrained by abundant radiocarbon dates were built based on sedimentological and paleoecological (i.e., foraminifer) data from selected cores. Combined with well-documented core stratigraphy from earlier studies, an age–depth plot with a local sea-level change curve revealed that the RTSR initiated approximately 9,000 cal a BP in a sandy bedform shape under transgressive conditions, continued throughout the Holocene, but developed mostly after 1128 AD, when the Yellow River flowed southward into the Yellow Sea. Abundant sediment supply, thus, appears to have played a major role in the formation and evolution of the RTSR in the south Yellow Sea.

KEYWORDS

tidal sand ridge, sedimentary evolution, south Yellow Sea, Yellow River, age–depth curve

1 Introduction

Shelf sand ridges having longitudinal crests that are over tens of kilometers long with spacings of hundreds to thousands of meters are well known from ancient and modern continental margins (Emery, 1968; Johnson, 1977; Brenner, 1980; Wagle and Veerayya, 1996; Park et al., 2003; Wu et al., 2017; Chiarella et al., 2020; Longhitano et al., 2021). They generally form parallel to the dominant current flow on sediment-laden shelves, regardless of tidal or storm origin (Houbolt, 1968; Swift, 1975; Swift et al., 1978; Stride, 1982). Well-documented examples of tide-dominated shelf sand ridges have been reported from the south-eastern North Sea (Davis and Balson, 1992; Trentesaux et al., 1999), the English Channel and the Celtic Sea between Ireland and France (Berne et al., 1998; Reynaud et al., 1999), the western Yellow Sea off China (Liu et al., 1989; Li et al., 2001), the inner shelf off Korea (Park and Lee, 1994; Chough et al., 2004), the southern Yellow Sea and the East China Sea (Yang, 1989; Berne et al., 2002; Liu et al., 2007), the Bohai Strait (Liu et al., 1998), the Taiwan Strait (Liao and Yu, 2005), and the southwest Florida inner shelf (Davis et al., 1993). Storm-dominated sand ridges have been described in the U.S. Atlantic Bight (Swift and Field, 1981; Goff et al., 1999; Snedden et al., 2011), the Brazilian shelf (Figueiredo et al., 1982), the Argentinean shelf (Parker et al., 1982), the Japanese Sendai shelf (Saito, 1989), the Canadian shelf (Hoogendoorn and Dalrymple, 1986),

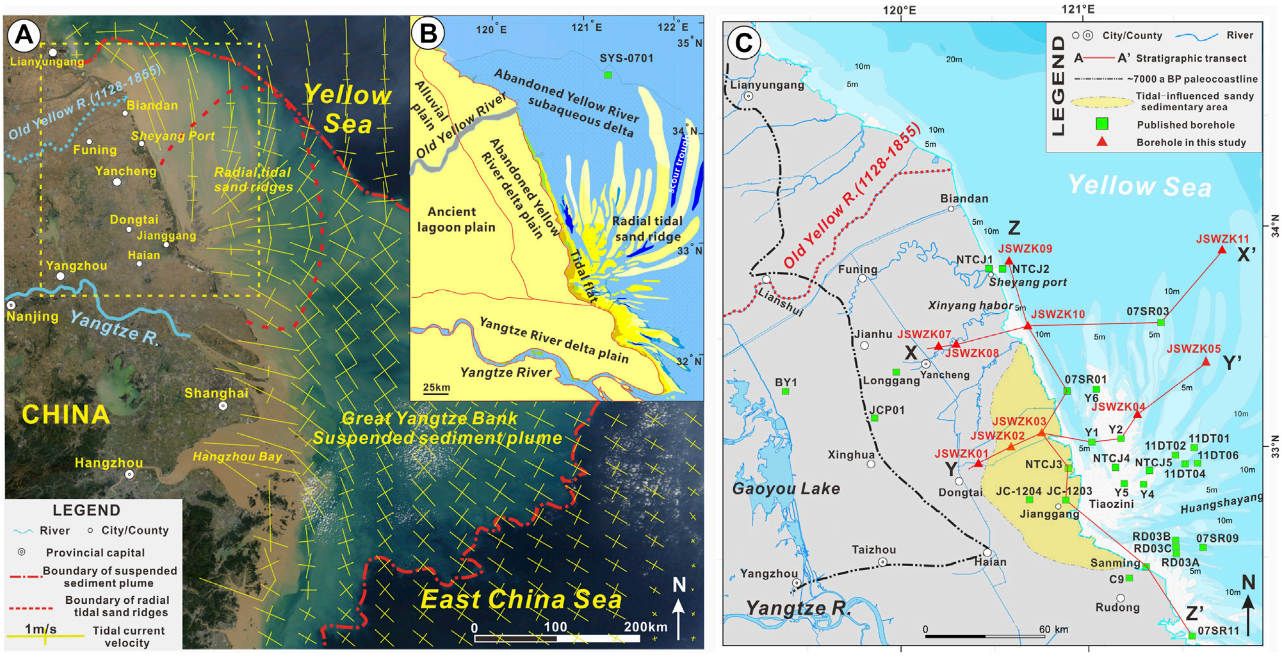

FIGURE 1
Radial tidal sand ridge and distribution of borehole data in this study. **(A)** Remote sensing satellite map of the Yellow Sea and East China Sea captured by NASA's Terra satellite at 9 November 2017. Notice that the suspended sediment plume of the great Yangtze bank and radial tidal sand ridges is outlined by the red dashed–dotted line and the dotted line, respectively. The yellow cross lines represent the distribution of M2 current ellipses (crosses) and magnitudes of semi-major axes (Uehara et al., 2002). **(B)** Schematic map of geological sedimentary units in the study area, modified from Li et al. (2001) and Xue et al. (2010). **(C)** Distribution of 10 boreholes and other previously published boreholes in the north Jiangsu coastal plain and in the radial tidal sand ridge region. The black dashed–dotted line represents the limit of the Holocene maximum transgression in the northern Jiangsu Coast (Xue et al., 2010). The red dashed line indicates the old Yellow River course between 1128 and 1855 AD.

the central Dutch coast (van de Meene and van Rijn, 2000), the German shelf (Antia, 1996), and the West Florida shelf (Twichell et al., 2003; Knobles et al., 2008).

Surface characteristics of shelf sand ridges have been extensively studied since the early 1970s by using various techniques in the hot-spot region, such as the U.S. Atlantic Bight (Swift et al., 1972; Goff et al., 1999; Pendleton et al., 2017). Early approaches to shelf sand ridges mainly focused on acoustic observations and surficial sampling (Green, 1986; Davis and Balson, 1992). Further progress in understanding the origin and evolution of shelf sand ridges was derived from the measurement of high-resolution seismic profiles and longer vibracores with a few radiocarbon dates (Park et al., 2006; Snedden et al., 2011). Recent studies of sand ridges have gradually turned to hydrodynamic model simulations, *in situ* underwater video camera observations, and remote sensing satellite monitoring (Vis-Star et al., 2007; Shi et al., 2011; Yoshikawa and Nemoto, 2014).

Previous studies have documented that shelf sand ridges predominantly occur in passive continental margins and broad continental shelf areas (Amos and King 1984; Snedden and Dalrymple 1999). Their morphological characteristics are closely related to the dominant ocean current (Galloway and Hobday, 1983) and are controlled by geologic (i.e., relative sea-level rise, shoreline transgression, and antecedent morphological relief), oceanographic (i.e., storms, tidal currents, and offshore-directed currents), and other (i.e., sediment supply and net sediment transport direction) processes (McBride and Moslow, 1991; Park et al., 2006; Nnafie et al., 2014; Ridente, 2018). However, two different hypotheses have been proposed for the origin of shelf sand ridges. The first hypothesis states that they represent relict features of the transgression, such as deltas or estuarine shoals, which became stranded, eroded, reworked, and then eventually submerged after a relative sea-level rise (McClennan and McMaster, 1971; McBride and Moslow, 1991). An alternative thought is that sand ridges were formed and stabilized by post-transgressive oceanographic processes related to the inherent dynamic interactions between the hydrodynamic force and sandy beds (Swift and Freeland, 1978; Trowbridge, 1995; Twichell et al., 2003). High-resolution seismic measurements in various sea regions supported the relict hypothesis (Berne et al., 1998; Jung et al., 1998; Park et al., 2006), whereas numerical modeling and hydrodynamic simulations were in favor of the hydrodynamic hypothesis (Calvete et al., 2001; Uehara et al., 2002; Vis-Star et al., 2007). A lack of studies on Holocene stratigraphic sequences with accurate chronological constraints in shelf sand ridge regions might explain these different views (Ridente, 2018).

The radial tidal sand ridge (RTSR) off the Jiangsu Coast in the south Yellow Sea is one of the world's unique geomorphic units. It is famous for its radial current pattern, which includes dozens of large either subaerial or subaqueous radial sand ridges and high suspended sediment concentrations (Figure 1A; Wang, 2002; Liu and Xia, 2004). To understand the origin and mechanism of this unique unit, a variety of field investigations have been carried out in this region since the 1960s, including geomorphology, geology, meteorology, hydrology, and sediment dynamics (see the summary in Wang Y. et al., 2012).

Since then, a large number of papers have been published on sand ridge morphology, sediment characteristics and provenance, sedimentary dynamic mechanisms, sand ridge migration, and genetic models (Geng et al., 1983; Wang et al., 1999; Li et al., 2001; Yin et al., 2008; Yin et al., 2016; Gao, 2009; Wang Y. et al., 2012; Zhang C. et al., 2013; Rao et al., 2015; Xu et al., 2019; Liu et al., 2021). However, the timing and mechanisms of formation of the Jiangsu radial tidal sand ridge are still largely under debate (Li and Zhao, 1995; Wang et al., 1998; Li and Yin, 2013; Yin et al., 2016). Several cores with long-time sequences, accurate dating, and seismic profiles have been documented in detail in this region (Sun et al., 2015; Yin et al., 2016). Nevertheless, these data clarified neither the origin nor the timing of formation of the RTSR, due to lack of detailed sea–land stratigraphic correlation, especially from the tidal sandy coast to the inner-shelf sand ridge (see the "tidal-genetic sandy deposition" in Li et al., 2001). Based on the analysis of sedimentary facies, stratigraphy and relatively precise chronology from 10 ~30–60 m-long cores recovered in the Jiangsu coast plain and in the radial sand ridge region in 2018–2019 (Figure 1C), and numerous previously published boreholes, this study aims to 1) reconstruct the detailed stratigraphic architecture from the coastal plain to the sand ridge region, 2) examine its late Pleistocene evolution, and 3) explore the mechanisms and timing of formation of the Jiangsu radial tidal sand ridge.

2 Geological setting

2.1 Modern radial tidal sand ridge off the Jiangsu Coast

The modern RTSR distributes at the apex of Jianggang (town) and forms a radial underwater topography with alternating ridges and troughs off the Jiangsu Coast in the south Yellow Sea (Figure 1B). Sand ridges are ~260 km long in the N–S direction and over 150 km long in the W–E direction, with a total area of ~30,000 km^2 (Liu and Xia, 2004). More than 70 sand ridges alternating with tidal current channels have been identified in this area. At least 19 large-scale submarine sand ridges were found, most of which are ~10–100 km in length and ~10–15 km in width. The depth of tidal current channels between sand ridges is ~10–30 m, and the maximum depth is ~48 m (Wang, 2002).

Sand ridges at the apex (Jianggang) are cut by grooves, and sand bodies are small, diverse, and disordered (i.e., a length of ~4.4 km around Tiaozini, Figure 1C), whereas sand ridges are well developed with an average of ~52 km in 13 major ridges outside the apex (Wang, 2002). The heads and tails of each sand ridge are narrow (mostly <2 km), whereas the middle parts are wide (~15 km wide in the major ridges (Liu and Xia, 2004)). Within each sand ridge, the head has the highest elevation. As the sand ridge extends outward, its elevation also decreases. The troughs between sand ridges become wider and deeper from the shallow to the deep sea (Ren, 1986).

Bounded by Jianggang, the north slope of the sand ridges is steeper than the south slope on the northern side of Jianggang (Figure 1C). Sand bodies are large and densely distributed, and troughs are generally shallow. As troughs in the NE direction are adjacent to the open sea, erosion is present on both sides of the sand ridges and troughs, and sand ridges gradually retreat and disappear (Wang et al., 2004). On the southern side of Jianggang, in general, the southern slopes of the sand ridges are steeper than the northern slopes. This region is characterized by low sediment accumulation and erosion with scattered deep troughs. The coastal tidal flat gradually silts into the sea, and a new sand ridge is formed at the top of the tidal channel. Even so, the overall deposition pattern is relatively stable in the southern region (Wang, 2002).

Sediment at the surface of the sand ridges generally consists of well-sorted fine sand and silty sand within 100 km of the apex (Wang, 2002). The proportion of fine sand is >80%, including the sand ridges and tidal current channels (Liu and Xia, 2004). Low-lying sectors contain small amounts of silt, whereas in tidal current channels, gravelly sand is quite abundant (~29%) with medium grain sizes between 1.2 Φ and 2.6 Φ in local major channels, and grain size becomes smaller (2.9–5.0 Φ of medium grain sizes) at both sides (Wang et al., 1999; Wang, 2002). Clayey silt is distributed in the outermost parts of the sand ridge region, where water depth is commonly 18–20 m. The radial apex is generally composed of silty sand and sandy silt and turns to a muddy tidal flat landward. On the whole, grain size gradually decreases from the core area to the periphery of the RTSR, which is consistent with the pattern of hydrodynamic strength (Liu and Xia, 2004).

2.2 Coastal hydrology of the south Yellow Sea

The study area is adjacent to the south Yellow Sea (SYS), where tidal currents, waves, and coastal currents are prevailing (Figure 1A). The Yellow Sea is a semi-enclosed sea that is generally influenced by two types of tidal waves: a progressive tidal wave from the Western Pacific region and a local reflected tidal wave formed by the obstruction of the Shandong Peninsula in the northwest (Zhang et al., 1999; Su and Yuan, 2005). These two tidal waves converge offshore the Jiangsu Coast in the south Yellow Sea, forming the rotating tidal wave systems and the radial tidal field in the north and east of Jianggang (Wang, 2002).

The Jiangsu coastal area generally rules the regular semidiurnal tide, with very short duration (an average of ~.38 h) between tidal rise and fall (Wang, 2002). In addition, the onshore shallow water area and radial sand ridge field, such as Xinyang Harbor and Jianggang, rule the irregular semidiurnal tide with a relatively long duration (4–5 h) (Liu and Xia, 2004). Tidal ranges normally average 2.5–4 m in the study area but can reach up to 9.28 m in the Huangshayang Channel, which is the maximum value recorded in the China Seas (Ye et al., 1988). In the RTSR field, tidal currents are very strong, averaging a velocity of ~1.5–2 m s^{-1} in the spring tidal current, with a maximum tidal current velocity exceeding 4.0 m s^{-1} (Wang, 2002).

The Jiangsu Coast is primarily affected by northward and northeastern main waves, with remarkable seasonal changes. Wind-induced waves commonly go toward the southeast during the summer, whereas waves from northerly and northeasterly directions prevail in the winter (Wang Y. et al., 2012). The height of wind-induced waves ranges between .5 m and 3 m in this region, occasionally exceeding 4 m during typhoons and severe storms (Liu and Xia, 2004; Liu et al., 2010).

The oceanic circulation in the SYS generally includes the Yellow Sea Warm Current (YSWC) and Shandong–Jiangsu coastal currents (Su and Yuan, 2005). The YSWC is a branch of the Kuroshio Current that carries warm and salty water northward into the Yellow Sea (Lan et al., 1986). In the China Seas, coastal currents with relatively low salinity due to the input of riverine water typically flow southward in

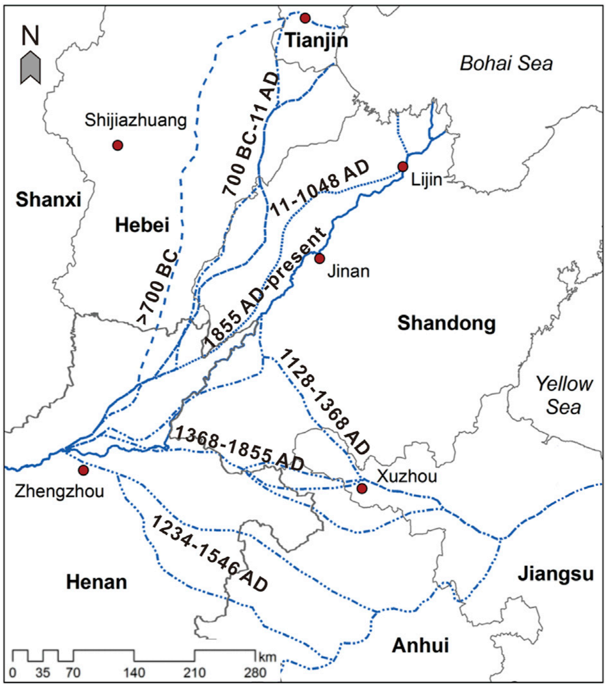

FIGURE 2
River diversion of the Lower Yellow River course in recorded history modified from Xue et al. (2003), Wang and Su (2013). Despite the Yellow River changing its course southward to Yellow Sea several times, the overall flowing time is limited between 1128 and 1855 AD.

winter and northward in summer. However, the YSWC is too weak to reach north of 35°N in summer because the southward-flowing cold water mass in the central SYS hinders the warm currents (Su and Yuan, 2005). Given the northward and northeastern main waves in the Jiangsu Coast throughout the year, the Jiangsu coastal currents flow persistently southward during both summer and winter (Beardsley, 1983). Recent studies of green tide (*Enteromorpha prolifera*) along the Jiangsu–Shandong coast revealed that coastal currents may flow northeast for a short period during the summer (Lee et al., 2011; Song et al., 2018).

2.3 River diversion of the lower Yellow River courses since 20 ka BP

The Yellow River is well known for its high sand content (Ren and Shi, 1986). The annual sediment load carried by the Yellow River has been ~1.1 × 10^9 tons over the past 2,000 years (Wang et al., 2007a). When the Yellow River flowed through the central mountain area into the flat, lower alluvial plain, it easily plugged and breached; therefore, its lower reaches migrated because of its huge sediment load (Cheng and Xue, 1997; Wang et al., 2007a). Previous studies revealed that at least seven times of major diversions occurred in the lower Yellow River course over recorded history (Xue et al., 2003; Wang and Su, 2013), with the river flowing north into the Bohai Sea and south through the Huaihe River into the south Yellow Sea (Figure 2).

It is to be noted that no direct sedimentary record suggests that the Yellow River delivered sediments into the south Yellow Sea during the Holocene, except for 1128–1855 AD. Instead, since 7,000 a BP, the Yellow River has entered the Bohai Sea and formed at least seven phases of deltas in the Bohai Coast (Xue, 1993; He et al., 2019). During the early Holocene, the Yellow River appeared to flow through the Bohai Strait into the north Yellow Sea, forming the Shandong mud–clinoform deposits during 9,600–5,000 a BP (Liu et al., 2004; Liu et al., 2010; Xue et al., 2018). Recent study of the ancient river channel in the Bohai Bay revealed that the ancient Yellow River seems to pass through the Bohai Bay and flow eastward consistently between 21.8 and ~9 ka BP (Lei et al., 2021), although some research studies on Late Pleistocene losses in the Huaihe River Basin implied that the Yellow River may partly go across the Huaihe River Basin and empty into the south Yellow Sea during the MIS 2 (marine isotope stage 2) period (~13.2 ka BP) (Zhang et al., 2016).

2.4 Abandoned Jiangsu Yellow River Delta

To hold back the invasion of the Jurchen army from North China, many dykes in the south bank of the Yellow River were artificially destroyed at 1128 AD in central Henan Province, resulting in a major southward shift of the Yellow River Channel since then (Figure 2; Liu et al., 2013). During a period of more than 700 years (1128–1855 AD), the Yellow River captured several tributaries of the Huaihe River and emptied into the Yellow Sea, where it formed a large delta lobe along the Jiangsu Coast (Xue et al., 2003; Xue et al., 2011). Furthermore, the Yellow River largely shifted its course from the Yellow Sea back to the Bohai Sea after 1855 AD, leading to the abandonment of the Jiangsu Yellow River Delta.

The terrestrial part of the abandoned Jiangsu Yellow River Delta is distributed on the east side of 1128 AD ancient shoreline in northern Jiangsu (Figure 1B). Bounded by the old Yellow River mouth, an asymmetrical, long-oval shape of deltaic bodies was formed, of which the southern part may extend to the Jianggang area under the action of the consistently southward longshore current, and the northern part expands to the Lianyungang region (Figure 1B; Xue et al., 2010; Liu et al., 2013). Additionally, the proximal subaqueous Jiangsu Yellow River Delta is mainly distributed near the abandoned Yellow River mouth, but the distal part is widely dispersed on the broad shelf of the south Yellow Sea and can even be transported to the slope of the platform edge (water depth below 20 m) under the action of late erosion (Liu et al., 2010; Zhou et al., 2014). Up until now, the boundary between the abandoned Jiangsu Yellow River Delta and the radial tidal sand ridge is not exactly defined in the study area, no matter whether it is on the shoreface or offshore (the south Yellow Sea shelf). Previous studies commonly recognized the dividing line of clayey silt/sand as the boundary, which approximately distributes eastward along the Xinyang Harbor (Li et al., 2001; Liu et al., 2010).

3 Materials and methods

A total of 10 cores, each 90 mm in diameter, were retrieved from the Jiangsu coastal plain and radial tidal sand ridges by rotary drilling in 2018–2019 (Figure 1C). Their coordinates, elevations, lengths, and coring recovery rates (always >90%) are summarized in Table 1. The lithology of each core as well as its sediment color, composition, sedimentary structures, bedding, grain size, and fossils was examined to identify the sedimentary facies.

TABLE 1 General information about the 10 cores investigated in this study.

Core	Coordinate		Elevation (m)	Length (m)	Recovery rate (%)
	Latitude (N)	Longitude (E)			
JSWZK01	32°56′31.36″	120°24′57.78″	3.15	31.8	92.8
JSWZK02	33°00′58.25″	120°35′30.02″	3.18	33.3	96.8
JSWZK03	33°04′41.73″	120°45′28.32″	3.26	61.4	98.2
JSWZK04	33°09′27.62″	121°16′25.27″	−4.2	40.9	91.6
JSWZK05	33°23′27.09″	121°38′53.21″	−20.1	40.7	90.3
JSWZK07	33°28′27.65"	120°12′02.54"	1.88	31.7	94.0
JSWZK08	33°28′58.19"	120°17′54.12"	2.11	32	96.8
JSWZK09	33°51′33.69"	120°35′12.94"	−13.7	30.1	95.0
JSWZK10	33°33′51.81"	120°41′11.10"	−9.5	30.3	94.0
JSWZK11	33°53′56.14"	121°44′40.74"	−18.6	30.2	90.5

A total of 54 samples were collected and analyzed for ^{14}C dating with an accelerator mass spectrometer (AMS) by Beta Analytic (Miami) and Pilot National Laboratory for Marine Science and Technology (Qingdao), respectively. These samples included mollusk shells, plant fragments, organic matter, and organic sediments. Age determinations were based on a Libby half-life of 5,568 years. Radiocarbon ages were corrected for the regional marine reservoir effect ($\Delta R = -100 \pm 36$ a), a regional average determined for the Yellow Sea by Southon et al. (2002), and calibrated using Calib Rev. 7.02 with one standard deviation (1σ) uncertainty (Reimer et al., 2013).

A total of 23 samples were collected for optically stimulated luminescence (OSL) dating from relatively homogeneous silty-sandy layers. Each sample was sealed into two black, opaque cartridges, 6 cm in height and 3.5 cm in diameter, in a dimly lit environment. All samples were kept in shockproof and lightproof bags and finally examined in the Inspection & Test Center of Marine Geology (Ministry of Natural Resources of China), using the method of Murray and Wintle (2000). The contents of U and Th required for dose rate calculation were obtained by a CANBERRA-E3830 high-purity germanium γ spectrometer, while the content of K was detected by an IRIS Intrepid Ⅱ XSP plasma emission spectrometer. The equivalent dose was obtained using the Lexsyg research luminescence meter, and the experimental excitation light source was a blue light diode ($\lambda = 470 \pm 30$ nm), with the instrument's irradiation source being 90Sr/90Y.

About 800 samples were collected for grain size analysis in cores JSWZK01, JSWZK03, and JSWZK07. The average sampling interval was ~.15 m. The weight of each sample was about 10 g. Grain size was determined using a Mastersizer 2000 laser particle size analyzer after pre-treating with 10% H_2O_2 and .10 N HCl to remove organic matter and carbonates. The range of particle sizes was .02–1,000 μm; standard deviations were <1% of the mean values; and reproducibility (φ50) was also <1%. Grain-size classification was based on the Krumbein phi (Φ) scale (Krumbein and Sloss, 1963). Size parameters were calculated based on the methods of Folk and Ward (1957).

A total of ~300 foraminiferal samples were collected in cores JSWZK01, JSWZK03, and JSWZK07. The average sampling interval was ~.2 m in silty and muddy layers and ~1 m in sandy beds. All samples were dried at 50°C in an oven and weighed at around 50 g per sample. About 10% H_2O_2 was added to soak the sediment for full dispersion and then washed over a 63-μm sieve. After drying, foraminifera were concentrated and separated using the CCl_4 flotation method (Wang et al., 1985). Sample subdivision was carried out when the foraminiferal abundance of a sample was very high. A representative number of more than 200 individuals was commonly obtained for each assemblage. Otherwise, all available tests were picked and identified under a Zeiss optical stereoscope. The "foraminiferal abundance" parameter in this study is the number of foraminifera per 50 g of dry sediment. The "simple diversity" is the number of foraminiferal species in each sample.

4 Results

4.1 Dating results

Tables 2, 3 list 54 radiocarbon dates and 23 OSL ages that were obtained from the 10 boreholes in the Jiangsu coastal plain and radial tidal sand ridges. For radiocarbon dating results, about three-quarters of these data are less than 10,000 years old, which are mostly reliable except for a few reversals (old layers at young ages; see the similar reversals in Stanley and Chen, 2000). The remaining quarter of dating ages are more than 35,000 years old, close to the carbon-14 dating limit. These old data, which are usually collected from deep sampling points, can only be used for reference purposes.

For OSL ages, similarly, more than two-thirds of the dates are less than 100 ka old, which is within the range of confidence. The rest is more than 100 ka old, even older than 150 ka, which exceeds the OSL dating limit and can only be used for reference.

4.2 Sedimentary facies

A total of 12 facies associations (hereinafter called "facies," Figure 3) were grouped into five depositional systems (alluvial,

TABLE 2 Radiocarbon dating results of 54 samples from the investigated boreholes.

Core	Sample	Depth (m)	Lab no.	Materials	δ^{13}C (per mil)	Conventional age (a BP)	Calendar ages (cal a BP)	
							Intercept	Range (1σ)
JSWZK01	J1S01	1.95	510290	Organic sediment	−20.1	4,620 ± 30	5,410	5,308–~5,445
	J1S02	10.88	510291	*Potamocorbula laevis*	1.0	7,630 ± 30	8,205	8,151–~8,273
	J1S03	11.7	510292	*Pelecyora trigona*	−1.7	7,440 ± 30	7,995	7,936–~8,041
	J1S05	12.54	Q200206	*Ruditapes philippinarum*	—	5,670 ± 25	6,195	6,160–~6,260
	J1S04	13.3	510293	*Potamocorbula laevis*	−.5	7,620 ± 30	8,190	8,140–~8,269
JSWZK02	J2S01	3.3	510294	Organic sediment	−23.7	3,290 ± 30	3,520	3,480–~3,560
	J2S02	12.36	510295	Plant materials	−25.9	8,570 ± 30	9,540	9,529–~9,545
	J2S05	14.82	Q200456	Organic matters	−25.5	9,156 ± 40	10,325	10,246–~10,377
	J2S03	24.76	510296	Plant materials	−28.9	7,820 ± 30	8,600	8,578–~8,628
	J2S04	31.58	510297	Plant materials	−25.9	11,080 ± 30	12,955	12,897–~13,028
JSWZK03	J3S01	7.35	510298	Shell fragments	2.8	1,480 ± 30	1,140	1,079–~1,204
	J3S02	11.88	510299	Shell fragments	0.0	1,620 ± 30	1,275	1,231–~1,318
	J3S03	24.7	510300	Plant materials	−26.7	8,880 ± 30	10,030	9,918–~10,149
	J3S04	36.93	510301	Plant materials	−27.4	>43,500		
	J3S05	57.16	510302	Oyster fragments	−3.2	>43,500		
JSWZK04	J4S01	4.85	510303	Organic sediment	−20.8	8,720 ± 30	9,665	9,597–~9,705
	J4S02	7.12	510304	Organic sediment	−21.5	10,480 ± 30	12,465	12,404–~12,527
	J4S03	12.55	510305	Organic sediment	−22.4	9,660 ± 30	11,110	10,898–~11,173
	J4S06	16.76	Q200215	*Arca subcrenata*	—	2,695 ± 20	2,515	2,475–~2,645
	J4S04	17.18	510306	Oyster fragments	.9	5,170 ± 30	5,630	5,578–~5,671
	J4S05	29.9	510307	*Corbicula fluminea*	−9.1	>43,500		
JSWZK05	J5S01	.69	510308	Shell fragments	−1.1	3,580 ± 30	3,590	3,534–~3,667
	J5S02	5.62	510309	Shell fragments	−2.5	5,420 ± 30	5,905	5,859–~5,967
	J5S03	9.15	510310	*Potamocorbula laevis*	−.6	8,440 ± 30	9,175	9,100–~9,253
	J5S04	11.7	510311	Oyster fragments	.9	8,790 ± 30	9,535	9,482–~9,582
JSWZK07	J7S01	8.88	542791	Organic matters	−29.0	50 ± 30	145	31–~256
	J7S02	14.34	542792	Plant materials	−27.9	6,390 ± 30	7,320	7,270–~7,368

(Continued on following page)

TABLE 2 (*Continued*) Radiocarbon dating results of 54 samples from the investigated boreholes.

Core	Sample	Depth (m)	Lab no.	Materials	δ^{13}C (per mil)	Conventional age	Calendar ages (cal a BP)	
						(a BP)	Intercept	Range (1σ)
	J7S06	15	Q200216	*Arca subcrenata*	–	5,350 ± 25	5,820	5,767–~5,884
	J7S03	15.07	542793	Oyster fragments	1.2	5,450 ± 30	5,940	5,885–~5,985
	J7S04	15.12	542794	Organic matters	−19.7	13,670 ± 40	16,480	16,359–~16,579
	J7S05	25.9	542795	Shell fragments	−6.4	32,270 ± 190	35,870	35,653–~36,105
JSWZK08	J8S04	16.22	Q200212	Oyster fragments	—	5,465 ± 30	5,955	5,891–~5,998
	J8S01	16.45	542796	Oyster fragments	−2.1	5,620 ± 30	6,135	6,064–~6,204
	J8S05	17.46	Q200214	Oyster fragments	—	5,225 ± 25	5,680	5,619–5,729
	J8S02	17.91	542797	Oyster fragments	−2.4	5,490 ± 30	5,980	5,906–~6,034
	J8S03	31.59	542798	*Potamocorbula ustulata*	−3.3	>43,500		
JSWZK09	J9S08	4.68	Q200766	*Potamocorbula laevis*	—	8,080 ± 40	8,675	8,578–~8,756
	J9S06	11.57	Q200210	Gastropod fragment	—	36,050 ± 420	40,365	39,893–~40,859
	J9S07	12.35	Q200207	*Nassarius variciferus*	—	32,580 ± 280	36,165	35,840–~36,455
	J9S01	16.96	542799	Oyster fragments	−8.0	>43,500		
	J9S02	18.58	542800	Gastropod fragment	−2.7	>43,500		
	J9S03	19.08	542801	Bivalve fragment	−1.1	>43,500		
	J9S04	19.23	542802	Organic matters	−18.1	34,280 ± 220	38,770	38,519–~38,981
	J9S05	24.93	542803	Bivalve fragment	−1.0	42,950 ± 620	45,900	45,300–~46,445
JSWZK10	J10S05	3.96	Q200961	Organic sediment	—	5,425 ± 45	6,235	6,206–~6,284
	J10S01	7.58	542804	*Barbatia bistrigata*	−1.3	6,170 ± 30	6,725	6,658–~6,778
	J10S02	11.2	542805	Corbicula fluminea	−10.3	>43,500		
	J10S03	24.3	542806	Gastropod fragment	−2.6	41,470 ± 500	44,645	44,205–~45,129
JSWZK11	J11S01	1.63	542790	*Pelecyora trigona*	−0.1	1,330 ± 30	980	924–~1,029
	J11S02	3.06	542791	Shell fragments	−0.4	1,290 ± 30	940	888–~993
	J11S06	11.42	Q200213	*Pelecyora trigona*	—	3,500 ± 20	3,495	3,442–~3,551
	J11S03	12.95	542792	*Oliva mustelina*	−1.0	7,050 ± 30	7,620	7,573–~7,657
	J11S04	15.92	542793	Shell fragments	−0.3	8,140 ± 30	8,770	8,659–~8,859
	J11S05	25.05	542794	Shell fragments	−13.0	>43,500		

*The lab numbers with Q as the prefix were the laboratory numbers of the Pilot National Laboratory for Marine Science and Technology (Qingdao), and the rest were from Beta Analytic (Miami).

TABLE 3 OSL dates of 23 samples from the investigated boreholes.

Sample no.	Depth (m)	Core	Lab no.	U (μg/g)	Th (μg/g)	K (%)	Mass water content (%)	Dose rate (Gy)	Age (Ka)	Deviation (Ka)
JSW01	20.35	JSWZK01	2018A123	1.07	5.91	1.91	23.94	154.9	62.2	5.9
JSW02	26.65	JSWZK01	2018A124	1.19	5.61	1.89	7.45	320.7	113.8	11.4
JSW03	13.95	JSWZK03	2018A125	1.21	6.16	1.88	20.77	19.9	7.9	.3
JSW04	18.35	JSWZK03	2018A126	1.19	6.08	1.93	25.65	30.6	12.5	3.9
JSW05	30.7	JSWZK03	2018A127	1.19	5.81	1.97	9.24	270	94.5	4.8
JSW06	45.95	JSWZK03	2018A128	1.25	6.57	2.01	12.03	>400	>137.3	
JSW07	48.9	JSWZK03	2018A129	1.24	6.59	2.08	9.62	>400	>134.2	
JSW08	53.53	JSWZK03	2018A130	1.14	6.04	1.84	11.50	>400	>150.3	
JSW09	56.75	JSWZK03	2018A131	1.18	5.98	1.83	18.39	>400	>170.0	
JSW10	21.25	JSWZK04	2018A132	1.10	6.64	2.14	10.15	247.7	82.3	7.5
JSW11	30.75	JSWZK04	2018A133	1.18	5.65	2.06	10.55	270.2	94.1	10.5
JSW12	34.3	JSWZK04	2018A134	1.26	5.46	1.86	12.78	259.3	99.2	14.3
JSW13	37.7	JSWZK04	2018A135	1.30	5.47	1.86	13.32	260	97.1	17.1
JSW14	20.67	JSWZK05	2018A136	1.25	5.47	2.16	9.02	320.1	105.9	10.1
JSW15	27.75	JSWZK05	2018A137	1.22	6.47	2.10	13.96	>400	>166	
OSL-23	14.55	JSWZK07	2020A035	2.38	6.93	1.94	12	10.37	3.3	.2
OSL-24	21.15	JSWZK07	2020A036	2.14	8.68	1.94	24	84.14	31.0	5.6
OSL-25	24.1	JSWZK07	2020A037	2.17	5.40	1.89	17	99.49	36.8	5.4
OSL-26	26.3	JSWZK07	2020A038	2.08	7.33	1.98	19	111.63	39.4	7.1
OSL-27	30.5	JSWZK07	2020A039	3.10	8.80	1.89	21	219.43	71.4	7.3
OSL-28	1.85	JSWZK10	2020A040	2.02	7.94	2.17	19.5	3.65	1.2	.3
OSL-29	14	JSWZK10	2020A041	1.91	6.71	1.63	33	55.49	28.3	7.8
OSL-30	22.1	JSWZK10	2020A042	1.82	6.83	1.62	23.5	169.21	74.7	3.0

coastal, deltaic, subtidal, and shallow sea deposits). Individual facies associations were differentiated on the basis of sedimentological and fossil features, reflecting changes in depth, salinity, and degree of confinement. Diagnostic grain size characteristics for facies identification are summarized in Table 4. Depositional systems and their component facies are described from updip to downdip locations.

4.2.1 Alluvial deposits

Three facies (river channel, floodplain, and lacustrine bog) were recognized within alluvial deposits. These facies are described in detail as follows.

4.2.1.1 Facies I: River channel

This facies, commonly 3–10 m thick, is dominated by light gray fine-medium sand and gray coarse silt, with an overall fining upward trend (Figure 3A). The facies has a mean grain size (*Mz*) of 2.72–5.93 Φ with a sand proportion of 11%–83%, locally as high as 90%. Sorting is moderate to poor with a standard deviation (*SD*) of .85–1.55 Φ. The grain size frequency curve generally shows a unimodal distribution with a narrow peak (2–4 Φ of peak value) (Table 4). The grain size accumulation curve commonly exhibits a two-tier mode (Figure 4A). The saltating component dominates the curve with a proportion of >70%. Black organic mottles and calcareous concretions were occasionally found in some layers. No obvious marine fossils were found, except for some severely abraded shell fragments occasionally presenting in this facies. This facies generally has a sharp or erosional boundary with the underlying depositional units, typically representing a floodplain.

Thick sand bodies with lower erosional boundaries, an overall fining upward trend, and a lack of marine fossils are the characteristic features of fluvial deposits (Galloway and Hobday, 1983; Miall, 1992; Hori et al., 2001). Both the frequency and accumulation curves of this facies reveal a high-energy and steady single flowing-direction water environment (Folk and Ward, 1957). Accordingly, we interpret this facies as formed in laterally accreting river channels. Two AMS ^{14}C ages and eight reliable OSL ages ranged from 12,955 cal a BP to 106 ± 10 ka BP. These ages mostly fall within marine isotope stages 2 and 4. This facies, thus, seems to have been deposited through multiple cycles of fluvial activity during the Late Pleistocene.

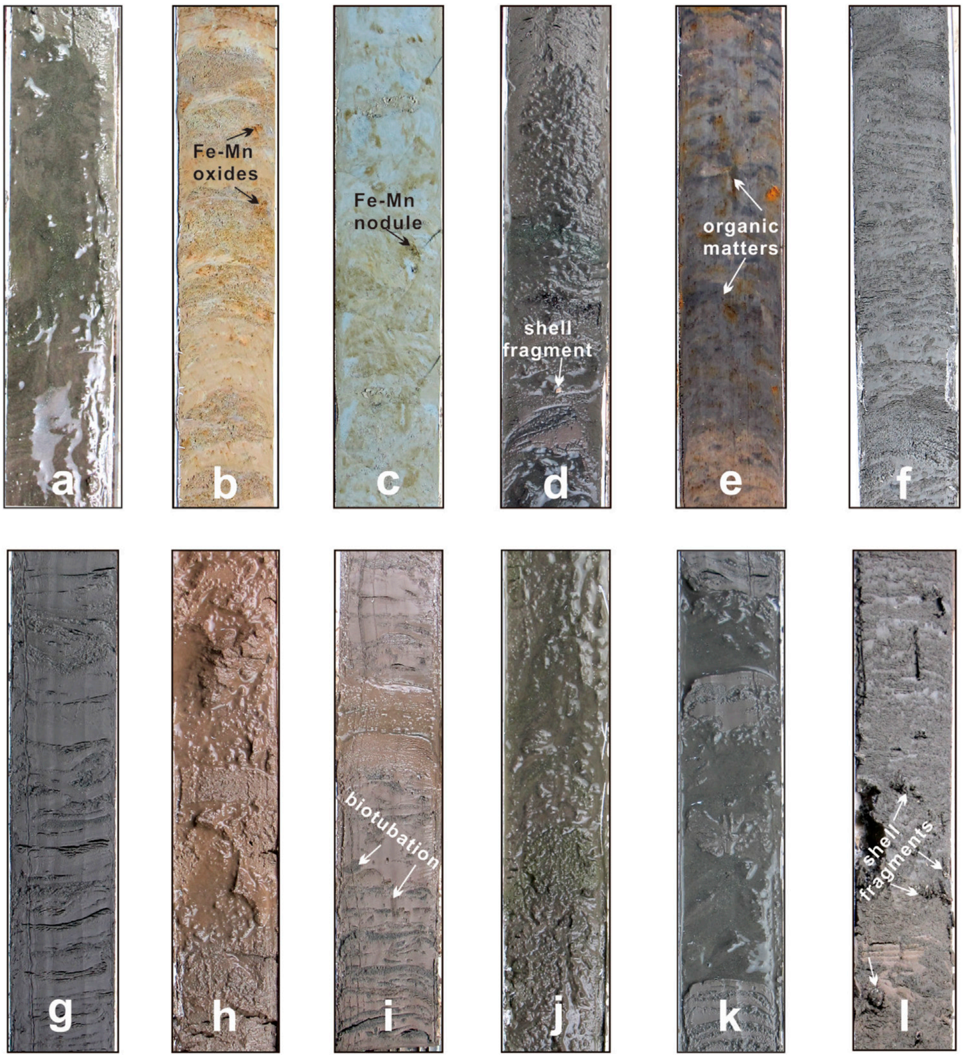

FIGURE 3
Representative photographs of facies in the Jiangsu coastal plain and radial tidal sand ridges. **(A)** River channel (depth 18.7–19.16 m) in the core JSWZK02; **(B)** floodplain (depth 13.4–13.87 m) in the core JSWZK05; **(C)** lacustrine bog (depth 59–59.4 m) in the core JSWZK03; **(D)** tidal river channel (depth 31–31.4 m) in the core JSWZK01; **(E)** supratidal flat (depth 1.8–2.2 m) in the core JSWZK01; **(F)** tidal flat (depth 9.7–10.1 m) in the core JSWZK05; **(G)** lagoon (depth 9.6–10 m) in the core JSWZK01; **(H)** delta front (depth 18.7–19.1 m) in the core JSWZK02; **(I)** prodelta (depth 11.8–12.2 m) in the core JSWZK08; **(J)** tidal sand ridge (depth 13.4–13.8 m) in the core JSWZK05; **(K)** tidal sand flank (depth 20.9–21.3 m) in the core JSWZK03; and **(L)** offshore (depth 7.4–7.8 m) in the core JSWZK10. All column lengths are 40 cm.

4.2.1.2 Facies II: Floodplain

This facies, generally 2–6 m thick, consists of gray to grayish-yellow silty clay and silt, locally interbedded with sandy silt layers (Figure 3B). The mean grain size ranges between 3.58 Φ and 7.71 Φ with poor to very poor sorting (SD: 1.07–2.65). Sand, silt, and clay contents are <10%, 24.2%–82.8%, and 2.65%–40.9%, respectively (Table 4). The grain size frequency curve principally outlines a unimodal-tailed distribution with a wide peak (4.5–6.5 Φ of peak value). The grain size accumulation curve commonly displays a two-tier mode (Figure 4B). The suspension component dominates the curve with a proportion of >80%. This facies generally contains plant material, iron manganese oxides, and calcareous concretions in some layers.

Scattered iron manganese oxides and calcareous concretions are good indicators of pedogenic processes in a subaerial terrestrial environment (Galloway and Hobday, 1983; Tanabe et al., 2006). Both the frequency and accumulation curves indicate a low-energy environment with gradually waning flows (Mycielska-Dowgiałło and Ludwikowska-Kędzia, 2011). Based on the aforementioned features, this fine-grained, poorly sorted facies is interpreted to represent a well-drained floodplain environment (Miall, 1992). No chronological data are available from this facies. However, as this unit is generally sandwiched between two river channel sediment bodies (i.e., facies I), it is likely that this facies may also be assigned to MIS 4 and 2.

4.2.1.3 Facies III: Lacustrine bog

This facies is dominated by steel gray to dark gray silty clay and clayey silt, partly interbedded with silt layers (Figure 3C). The thickness range is commonly 2–4 m. The mean grain size ranges from 5.8 to 7.1 Φ, with poor to very poor sorting (SD: 1.48–2.26). Sand, silt, and clay contents are .99%–12.14%, 68.77%–79.71%, and 14.38%–27.83%, respectively (Table 4). The grain size frequency curve

TABLE 4 Summary of grain size characteristics of facies associations.

Facies association	Mean grain size (Φ)	Sorting	Sand content (%)	Silt content (%)	Clay content (%)	Frequency curve	Accumulation curve
River channel	2.72–5.93	.85–1.55	11.09–83.01	7.24–75.7	.8–16.59	Unimodal distribution with a narrow peak (2–4 Φ of peak value)	Two-tier mode, saltating component dominating
Floodplain	3.58–7.71	1.07–2.65	1.86–68.93	24.22–82.78	2.59–40.97	Unimodal-tailed distribution with a wide peak (4.5–6.5 Φ of peak value)	Two-tier mode, suspension component dominating
Lacustrine bog	5.8–7.1	1.48–2.26	.99–12.14	68.77–79.71	14.38–27.83	Unimodal-tailed or bimodal-tailed distribution with a wide peak (4.5–7 Φ of peak value)	One-tier or two-tier mode, suspension component dominating
Tidal river channel	3.36–6.42	.77–1.76	7.5–78.49	18.7–74.2	1.42–21.33	Bimodal distribution with a coarse main peak (2.8–4.2 Φ of peak value) and a fine secondary peak (6–7.3 Φ of peak value)	Two-tier or three-tier mode, saltating component dominating
Supratidal flat	5.99–6.71	1.58–2.51	.66–5.24	76.47–81.19	13.82–21.3	Unimodal-tailed distribution with a wide peak (5–6 Φ of peak value)	Two-tier or three-tier mode, suspension component dominating
Tidal flat	4.56–6.88	.88–2.06	2.27–45.66	45.78–86.13	3.81–25.23	Bimodal distribution with a coarse main peak (4.3–5.1 Φ of peak value) and a fine secondary peak (7–8.2 Φ of peak value)	Two-tier or three-tier mode, saltating component dominating
Lagoon	4.39–6.82	1.17–2.25	.9–36.11	57.24–82.93	3.91–22.83	Bimodal or multimodal distribution with a wide peak (4.2–6.2 Φ of peak value)	Three-tier or multiple-tier mode, saltating component dominating
Delta front	4.28–6.17	.95–2.01	6.84–36.1	61.25–77.38	2.66–20.32	Bimodal distribution with a coarse main peak (3.8–5.2 Φ of peak value) and a fine secondary peak (6–7.5 Φ of peak value)	Two-tier or three-tier mode, saltating component dominating
Prodelta	4.79–7.25	1.18–2.06	.58–28.13	58.84–87.73	6.13–31.78	Unimodal-tailed distribution with a wide peak (4.2–7 Φ of peak value)	Two-tier or three-tier mode, suspension component dominating
Tidal sand ridge	2.23–5.27	.73–1.76	11.35–93.06	6.08–73.93	.71–20.34	Bimodal distribution with a coarse narrow peak (2–4.2 Φ of peak value) and a fine peak (6–7.5 Φ of peak value)	Three-tier mode, saltating component dominating
Tidal sand flank	3.6–7.02	.71–2.56	1.05–73.41	23.39–79.02	1.28–29.11	Unimodal-tailed distribution with a wide peak (4.2–6.5 Φ of peak value)	Two-tier or three-tier mode, saltating component dominating
Offshore	4.52–7.23	.99–2.27	1.14–65.12	25.8–78.61	2.66–29.74	Unimodal or bimodal distribution with a coarse main peak (4.3–5.1 Φ of peak value) and a fine secondary peak (7–8.2 Φ of peak value)	Two-tier or three-tier mode, suspension component dominating

mainly presents a unimodal-tailed or bimodal-tailed distribution with a very wide peak (4.5–7 Φ of peak value). The grain size accumulation curve commonly displays a one- or two-tier mode (Figure 4C). The suspension component dominates the curve with a proportion of >90%. Horizontal bedding and bioturbation are well displayed locally. Fe-Mn nodules and calcareous concretions were commonly found in the clay (Figure 3C). Some small freshwater gastropods, including *Radix* sp. and *Biomphalaria* sp., can be found in some beds.

Sediments in this facies invariably overlie with a sharp contact river–channel deposit, reflecting an abrupt channel abandonment (Amorosi et al., 2008). Horizontal bedding and bioturbation with very fine grain size reflect a low-energy sedimentary environment, consistent with grain size accumulation curves. Fe-Mn nodules and calcareous concretions commonly indicate the pedogenic processes in a terrestrial environment (Galloway and Hobday, 1983). Given the presence of a typical freshwater fauna, this facies is considered to have formed in a bog after channel abandonment (Hori et al., 2004). Like for floodplain deposits, neither AMS ^{14}C data nor OSL data are available from this facies.

4.2.2 Coastal deposits

Coastal deposits have been recognized in all study cores and can be subdivided into five facies referable to the tidal river channel, supratidal zone, tidal flat, and lagoon.

4.2.2.1 Facies IV: Tidal river channel

This facies, with a thickness of ~3–8 m, is mainly composed of gray fine sand and silt containing some marine and brackish water mollusk shells (Figure 3D), such as *Talonostrea* and *Corbicula fluminea*. The mean grain size ranges from 3.36 Φ to 6.42 Φ; the standard deviation (.77–1.76 Φ) indicates moderate to poor sorting. Sand, silt, and clay contents are 7.5%–78.49%, 18.7%–74.2%, and 1.42%–16.32%, respectively (Table 4). The grain size frequency curve mainly shows a bimodal distribution with a coarse main peak (2.8–4.2 Φ of peak value) and a fine secondary peak (6–7.3 Φ of peak value). The grain size accumulation curve commonly displays two- or three-tier modes (Figure 4D). Two saltation components dominate the curve with a total proportion of >90%. The fine saltation component generally has worse sorting but a higher content than the coarse

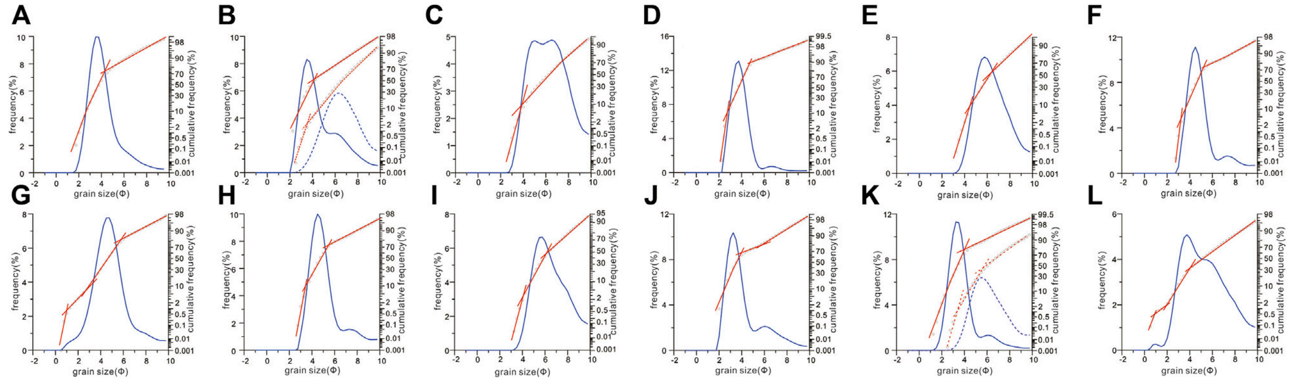

FIGURE 4
Grain size frequency (blue curve) and accumulation curves (red polyline) of typical sedimentary facies in the Jiangsu coastal plain and radial tidal sand ridges. **(A)** River channel at a depth of 25.55 m in the core JSWZK11; **(B)** floodplain at depths of 36.65 m (solid) and 40.75 m (dotted) in the core JSWZK04; **(C)** lacustrine bog at a depth of 15.35 m in the core JSWZK01; **(D)** tidal river channel at a depth of 26.45 m in the core JSWZK01; **(E)** supratidal flat at a depth of 1.75 m in the core JSWZK01; **(F)** tidal flat at a depth of 4.45 m in the core JSWZK02; **(G)** lagoon at a depth of 5.65 m in the core JSWZK01; **(H)** delta front at a depth of 1.25 m in the core JSWZK10; **(I)** prodelta at a depth of 4.25 m in the core JSWZK08; **(J)** tidal sand ridge at a depth of 16.35 m in the core JSWZK02; **(K)** tidal sand flank at depths of 20.55 m (solid) and 20.65 m (dotted) in the core JSWZK03; and **(L)** offshore at a depth of 7.45 m in the core JSWZK10.

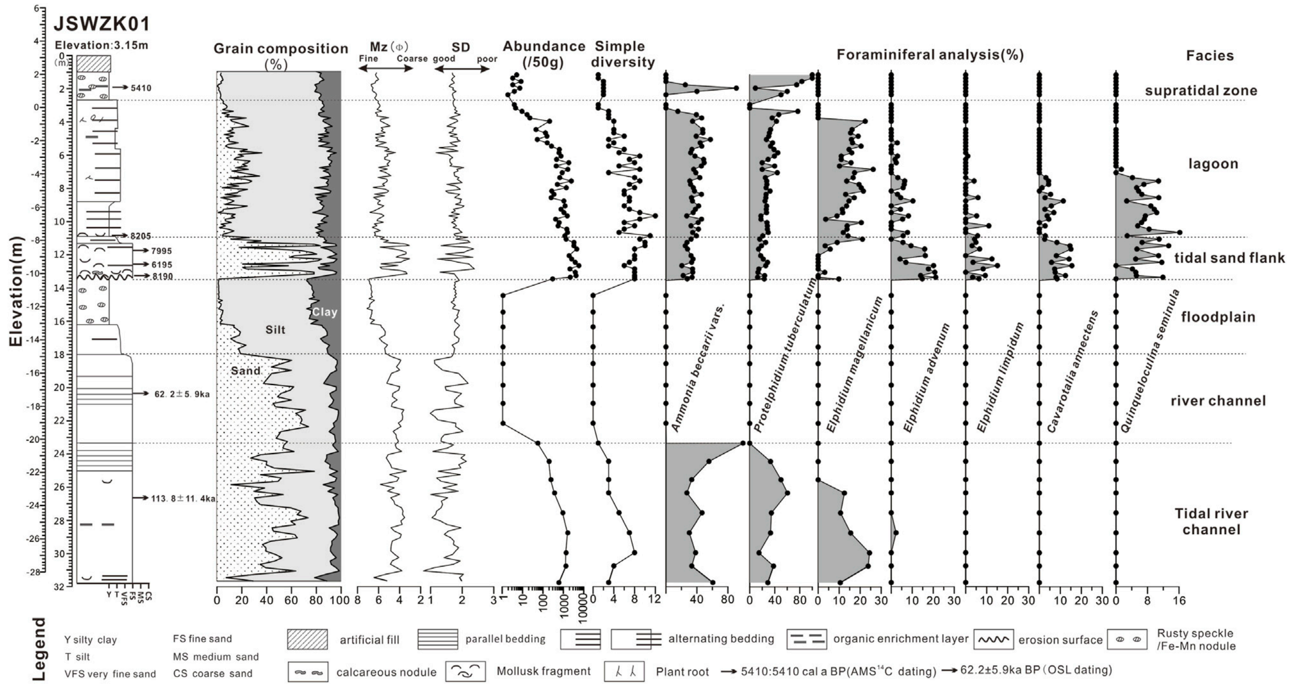

FIGURE 5
Comprehensive stratigraphic log of the core JSWZK01, showing lithology, grain size, and foraminiferal content. The borehole is divided into six sedimentary facies from the late Pleistocene tidal river channel and floodplain to the Holocene tidal sand flank, lagoon, and supratidal zone. It is to be note that the foramiferal data (i.e., abundance) changed abruptly at depths of 23.3 m and 13.4 m, indicating the end of Late Pleistocene marine transgression and the initiation of Holocene aggression in the core JSWZK01, relatively. For more detailed foraminiferal data, see Supplementary Table S1 in the attachment.

saltation component (Figure 4D). Average foraminiferal abundance and simple diversity in this facies (core JSWZK01) are 419 and 4, respectively. Benthic foraminifers are dominated by euryhaline taxa, such as *Ammonia beccarii* varsus (average percentage: 46.6%), *Protelphidium tuberculatum* (32.7%), and *Elphidium magellanicum* (11.18%) (Figure 5).

This facies has similar lithologic characteristics as the river channel facies, being characterized by well-sorted sandy deposits. However, the presence of mollusk shells and of a few euryhaline foraminifers indicates that these deposits accumulated in a brackish environment (Hori et al., 2001; Hori et al., 2004; Tanabe et al., 2006). The grain size frequency curve and accumulation curve are

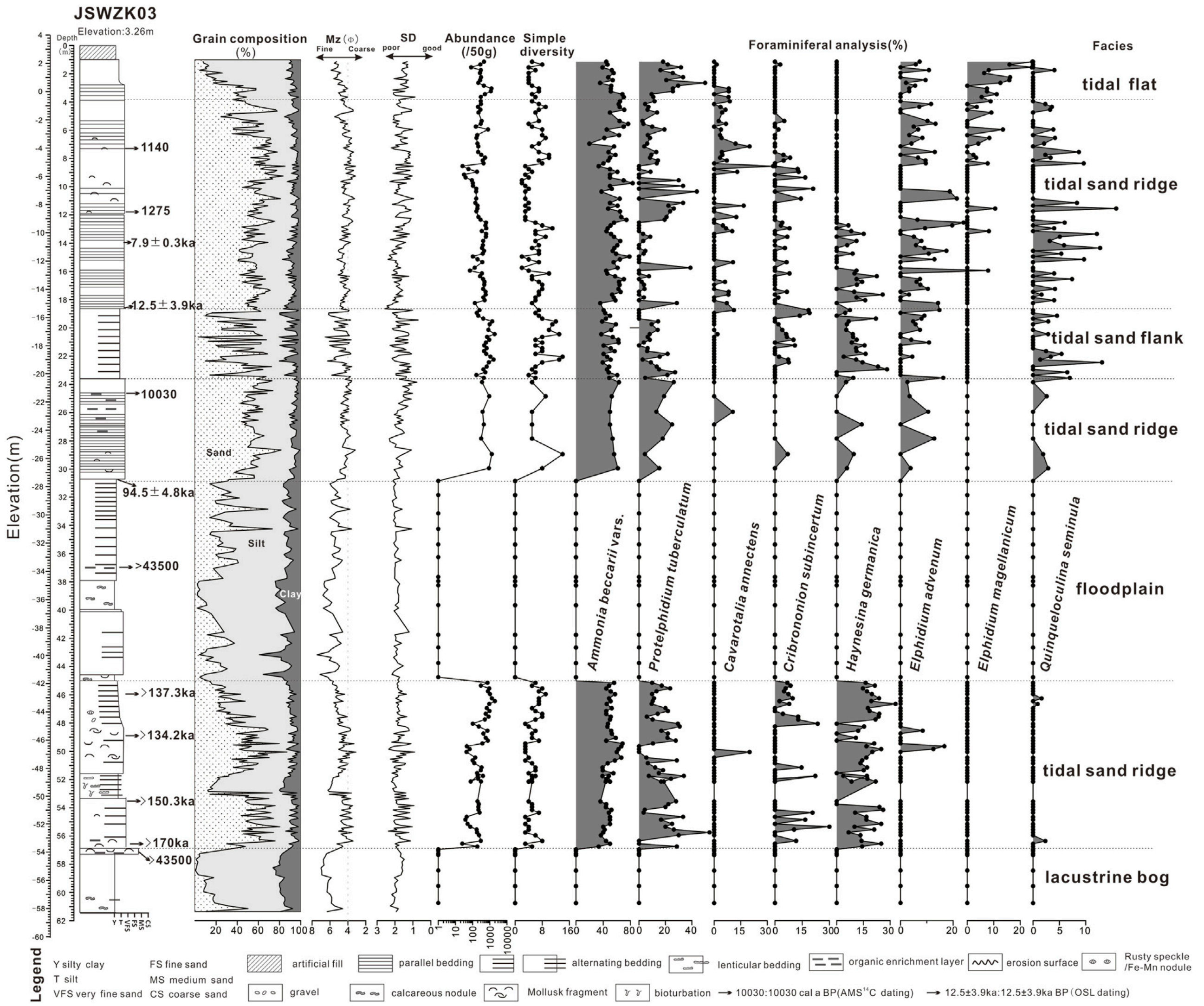

FIGURE 6
Comprehensive stratigraphic log of the core JSWZK03, showing lithology, grain size, and foraminiferal content. The borehole is divided into five sedimentary facies from the Late Pleistocene lacustrine bog, tidal sand ridge, and floodplain to the Holocene tidal sand ridge, tidal sand flank, and tidal flat. It is to be noted that the OSL ages are older than 130 ka BP below the depth of 45 m, indicating an age-unconstrained strata in this borehole. For more detailed foraminiferal data, see Supplementary Table S2 in the attachment.

also different from those of the river channel facies, which commonly miss the fine secondary peak and the fine saltation component (Figures 4A, D). Thus, this facies association is interpreted to reflect a tidal river channel that was intermittently influenced by tidal currents. A few AMS ^{14}C and OSL data in cores JSWZK01 and JSWZK07 reveal two stages of development for this facies, namely, ~30–40 ka BP and ~100 ka BP, which approximately correspond to stages MIS 3 and 5, respectively.

4.2.2.2 Facies V: Supratidal flat

This facies association consists of brown to yellowish-gray silt, partly interbedded with gray clayey silt or silty clay, containing abundant plant roots and ferruginous nodules (Figure 3E). Organic material and peat are locally present. Freshwater and brackish shells are common, including *Radix swinhoei* and *Gyraulus albus*. The range of *Mz* is 5.99–6.71 Φ, and the standard deviation of 1.58–2.51 Φ indicates poor to very poor sorting. Sand, silt, and clay contents are .66%–5.24%, 76.47%–81.19%, and 13.82%–21.3%, respectively (Table 4). The grain size frequency curve mainly shows a unimodal-tailed distribution with a wide peak (5–6 Φ of peak value). The grain size accumulation curve commonly displays two- or three-tier modes (Figure 4E). The suspension component dominates the curve with a total proportion of >50%.

Ferruginous nodules suggest subaerial exposure and pedogenic modification (Liu et al., 2016). Abundant plant roots, organic materials, and brackish/freshwater mollusk shells are commonly found in coastal marsh environments, which are typically located in the upper tidal flat to the supratidal zone (Hori et al., 2004). The dominant suspension component with a unimodal-tailed distribution also reveals a low-energy environment with gradually waning flows, which is possible during the ebb and flood. Based on distinct grain sizes and fossil characteristics, this facies is considered to have formed in a supratidal flat environment.

4.2.2.3 Facies VI: Tidal flat

This facies consists of alternating gray to yellowish-gray silt with gray clayey silt or silty clay (Figure 3F). Wavy bedding and lenticular bedding are clearly recognized, whereas bioturbation and iron oxides are occasionally found. The mean grain size of this facies ranges from 4.56 Φ to 6.88 Φ with .88–2.06 Φ of standard deviation, indicating moderate to poor sorting. Sand, silt, and clay contents are 2.27%–45.66%, 45.78%–86.13%, and 3.81%–25.23%, respectively (Table 4). The grain size frequency curve and accumulation curves are similar to those of the tidal river facies association, with a bimodal distribution with a coarse main peak (4.3–5.1 Φ of peak value) and a fine secondary peak (7–8.2 Φ of peak value) in the frequency curve (Figure 3F). The grain size accumulation curve also displays two- or three-tier modes. The two saltation components dominate the curve with a total proportion of >80%. The fine saltation component has poorer sorting but a higher content than the coarse saltation component. The average foraminiferal abundance and simple diversity of this facies are 273 and 6 in the core JSWZK03, respectively. Similar to tidal river deposits, this facies is dominated by euryhaline foraminifera, such as *A. beccarii* vars (46.9%), *P. tuberculatum* (26.7%), and *E. magellanicum* (16.2%) (Figure 6).

Wavy bedding and lenticular bedding are reliable indicators of tidal processes (Galloway and Hobday, 1983). The grain size frequency and accumulation curves reveal a low-energy, multi-sourced, or bimodal current environment (Wang and Ke, 1997). The foraminiferal assemblage indicates the transition from a marine to a brackish/freshwater environment. As a whole, this facies is interpreted as a tidal flat. According to several AMS ^{14}C and OSL dates from the study cores, the development of the tidal flat took place at least in three distinct stages, including MIS 3, the early Holocene, and modern times.

4.2.2.4 Facies VII:Lagoon

This facies is composed mainly of gray to dark gray coarse silt alternating with gray silty clay (Figure 3G). The range of *Mz* is 4.39–6.82 Φ, and the standard deviation is 1.17–2.25 Φ, thus indicating poor to very poor sorting. The sand, silt, and clay contents are .9%–36.11%, 57.24%–82.93%, and 3.91%–22.83%, respectively (Table 4). The grain size frequency curve mainly shows bimodal or multimodal distributions with a wide peak (4.2–6.2 Φ of peak value). The grain size accumulation curve commonly displays three-tier or multiple-tier modes (Figure 4G). The two saltation components dominate the curve with a total proportion of >70%. Tiny marine shells or fragments are commonly found, including *Potamocorbula laevis, Umbonium thomasi,* and *Mactra veneriformis*. The average abundance and simple diversity in core JSWZK01 are 319 and 6, respectively. The dominant foraminiferal species are *A. beccarii* vars (37.1%), *P. tuberculatum* (30.2%), and *E. magellanicum* (13.18%) (Figure 5).

The rhythmical alternation of silt clay layers and the foraminiferal assemblage in this facies association are characteristic features of tidal flat deposits. However, frequency and accumulative curves are clearly distinct between lagoon and tidal flat facies (Figure 4; Wang Y. Z. et al., 2012). In addition, the brackish-dominated macrofaunal assemblage, some plant roots, and the small size of marine fossils indicate a high-salinity, barred marine environment, such as a lagoon (Como and Magni, 2009). Consistent with stratigraphic relations with underlying tidal sandy deposits, this facies is interpreted as having formed in a lagoon environment under conspicuous tidal influence. The lagoon likely evolved to a more restricted environment, as documented by the gradual decrease in abundance and simple diversity of foraminiferal assemblages from the bottom up in the core JSWZK01 (Figure 5). The AMS ^{14}C dates fall between 6,200 cal a BP and 5,410 cal a BP in the core JSWZK01, indicating that this facies association developed in a back-barrier environment at the onset of progradation of coastal barriers or delta systems during the middle Holocene (Li and Wang, 1991).

4.2.3 Deltaic deposits

Deltaic deposits were mostly recognized in cores from the NW part of our study area. Two distinct facies, namely, delta front and prodelta, were identified.

4.2.3.1 Facies VIII: Delta front

This facies is composed of gray coarse silt that in its lower part is interbedded with light gray fine sand and clayey silt (Figure 3H). It contains *Potamocorbula laevis*, *Talonostrea*, and *Mitrella bella*. No bioturbation was observed in the upper part of this facies. The range of *Mz* is 4.28–6.17 Φ, with a standard deviation of .95–2.01 Φ, indicating moderate to poor sorting. Sand, silt, and clay contents are 6.84%–36.1%, 61.25%–77.38%, and 2.66%–20.32%, respectively (Table 4). The grain size frequency curve mainly shows a bimodal distribution with a coarse main peak (3.8–5.2 Φ of peak value) and a fine secondary peak (6–7.5 Φ of peak value). The grain size accumulation curve commonly displays two- or three-tier modes (Figure 4H). The two saltation components dominate the curve with a total proportion of >80%. The fine saltation component has poorer sorting but a higher content than the coarse saltation component. The average benthic foraminiferal abundance is ~647, whereas simple diversity reaches ~18 in the core JSWZK07 (Figure 7). The dominant foraminiferal species are *A. beccarii* vars (36.7%), *A. pauciloculata* (14.8%), and *Nonionella decora* (10.2%) (Figure 7).

Relatively well-sorted coarse silt and the nearly absence of bioturbation in the upper part of this facies may reflect high-energy conditions and high sediment accumulation rates (Abrahim et al., 2008; Liu et al., 2009). Silt-sand alternations in the lower part of this facies and the bimodal distribution are inferred to reflect a combined hydrodynamic environment. Considering the euryhaline foraminiferal assemblage and stratigraphic relations with adjacent facies, this facies likely represents a delta front deposit (Galloway and Hobday, 1983), whereas its lower and upper parts represent distal to proximal sandy bars, respectively. The overall yellowish color in this facies suggests that the sediment source may have derived from the Yellow River (Cheng and Xue, 1997; Figure 3H). A few AMS ^{14}C and OSL dates from this facies fall between 3.3 ka BP and 145 cal a BP in the core JSWZK07.

4.2.3.2 Facies IX: Prodelta

This facies consists of gray to dark gray silty clay, alternating with light gray silt and fine sand layers or lenses. Lenticular bedding is common, and bioturbation is moderate (Figure 3I). This facies contains a few fragments of mollusk shells, such as *Arca subcrenata*, *Anomia chinensis*, *Dosinia biscocta, P. laevis,* and *Pelecyora trigona.* The mean grain size of this facies ranges from 4.79 Φ to 7.25 Φ, with a standard deviation of 1.18–2.06 Φ, indicating

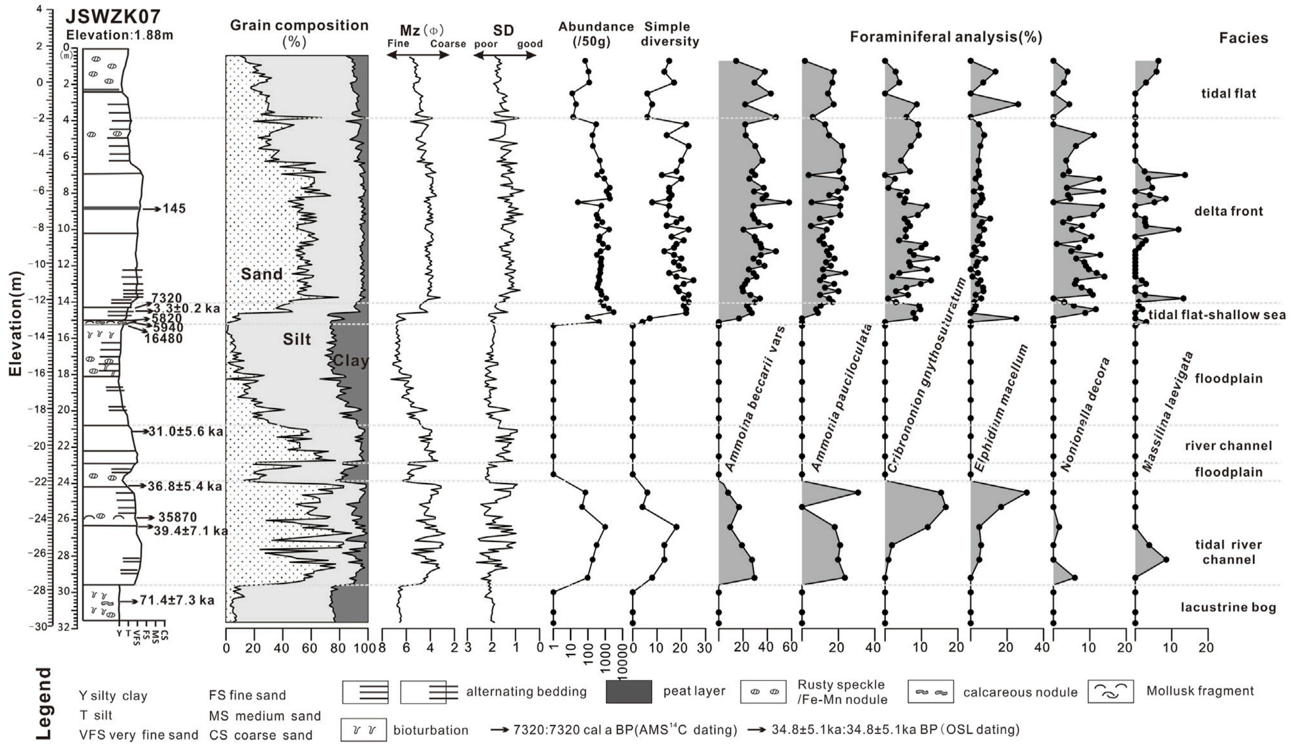

FIGURE 7
Comprehensive stratigraphic log of the core JSWZK07, showing lithology, grain size, and foraminiferal content. The borehole can be divided into six sedimentary facies from the Late Pleistocene lacustrine bog, tidal river channel, river channel, and floodplain to the Holocene tidal flat–shallow sea, delta front, and tidal flat. It is to be noted that the foramiferal data (i.e., abundance) changed abruptly at the depths of 24 m and 15.2 m, indicating the end of MIS 3 marine transgression and the initiation of Holocene aggression in the core JSWZK07, relatively. For more detailed foraminiferal data, see Supplementary Table S3 in the attachment.

poor to very poor sorting. Sand, silt, and clay contents are .58%–28.13%, 58.84%–87.73%, and 6.13%–31.78%, respectively (Table 4). The grain size frequency curve principally shows a unimodal-tailed distribution with a wide peak (4.2–7 Φ of peak value). The grain size accumulation curve commonly displays two- or three-tier modes (Figure 4I). The suspension component dominates the curve with a proportion of >50%.

The high proportion of suspended load, concurrently with a moderately abundant marine fossil assemblage and a moderate degree of bioturbation, is a reliable indicator of a low-energy, stressed marine depositional environment. This sedimentary environment was likely close to a fluvial mouth, such as a prodelta (Coleman and Wright, 1975). The overall brownish-yellow color (Figure 3I) may indicate direct sediment supply from the Yellow River (Cheng and Xue, 1997). This facies association developed during two distinct periods on the basis of a few chronological data, including MIS 3 and the late Holocene.

4.2.4 Subtidal deposits

Subtidal deposits are well exposed in seaward cores. They can be subdivided into two facies, namely, the tidal sand ridge and tidal sand flank.

4.2.4.1 Facies X: Tidal sand ridge

This facies is dominated by yellowish-gray to gray fine-medium sand and coarse silt (Figure 3J). *Mz* ranges from 2.23 to 5.27 Φ, and the contents of sand, silt, and clay are 11.35%–93.06%, 6.08%–73.93%, and .71%–20.34%, respectively. Sorting is moderate to poor. Like the tidal river facies, the grain size frequency curve mainly shows a bimodal distribution with a coarse, narrow peak (2–4.2 Φ of peak value) and a fine peak (6–7.5 Φ of peak value) (Figure 4J). The grain size accumulation curve commonly displays a three-tier mode. The two saltation components dominate the curve with a total proportion of >80% (Table 4). The fine saltation component generally has poorer sorting and a lower concentration than the coarse saltation component. Marine mollusk shells are scarce and mostly fragmented. In the core JSWZK03, the average foraminiferal abundance and simple diversity are ~333 and 6, respectively. Euryhaline *A. beccarii* vars (57.3%) and *P. tuberculatum* (10.1%) are the dominant foraminiferal species (Figure 6).

Relatively well-sorted coarse sediments and a few marine shell fragments are characteristic of a high-energy, marine-influenced environment. The bimodal distribution and three-tier mode with two saltation components of grain size curves are consistent with a to-and-fro movement in a tidally influenced environment. Although it is difficult to distinguish this facies from tidal river channel deposits on the basis of grain size analysis alone (Figures 4D, J), the fossil assemblages showed some marked differences. For example, the tidal channel river facies had some brackish shell fragments, such as *Corbicula fluminea*, which were only rarely found in this facies. This facies also had a higher diversity of foraminifers (4–10) than those of the tidal river channel (2–5) (see Figures 5, 6), indicating a subtidal environment. Additionally, the grain size frequency curve of this facies commonly displays a bimodal distribution with a coarse narrow peak and a fine peak, which is similar to grain size characteristics of tidal sand ridges detailed by previous studies in the south Yellow Sea (Wang et al., 2019a). This facies, thus, is interpreted as having formed in a tidal sand ridge. Based on numerous AMS ^{14}C and OSL dates in cores JSWZK03, JSWZK04, and JSWZK05, tidal sand ridges developed at least during two distinct phases, namely, the early–middle Holocene and an age possibly older than MIS 5, although OSL data are not conclusive.

4.2.4.2 Facies XI: Tidal sand flank

This facies consists of light gray fine sand, alternating with gray to dark gray clayey silt and silt (Figure 3K). It contains a few fragments of mollusk shells, such as *Arca subcrenata* and *P. laevis.* The mean grain size of this facies ranges from 3.6 Φ to 7.02 Φ with a standard deviation of .71–2.56 Φ, indicating moderate to very poor sorting. The sand, silt, and clay contents are 1.05%–73.41%, 23.39%–79.02%, and 1.28%–29.11%, respectively (Table 4). The grain size frequency curve of sandy layers is similar to that of tidal sand ridges, whereas the curve of clayey silt principally shows a unimodal-tailed distribution with a wide peak (4.2–6.5 Φ of peak value). The grain size accumulation curve commonly displays two- or three-tier modes (Figure 4K). The suspension component dominates the curve with a proportion of >60% in the silty layer. The average foraminiferal abundance and simple diversity are ~716 and 8 in the core JSWZK03, respectively (Figure 6). Euryhaline *A. beccarii* vars (48.8%) and *Haynesina germanica* (10.1%) are the dominant foraminiferal species.

The lithological characteristics are quite similar to the “tidal inlet” facies of published boreholes 11DT03 and 11DT04 described by Ji et al. (2015) or the sand ridge bottom facies described by Yin et al. (2016). This facies shows characteristic sand–mud couplets, with obviously contrasting grain size characteristics (see Figure 4K). This facies exhibits a lateral transition to tidal sand ridge deposits and shows intermediate characteristics between the tidal sand ridge and offshore facies in terms of grain size and foraminiferal abundance. Thus, it is inferred to represent a slightly deeper and lower-energy (subtidal) environment than tidal sand ridges, which we interpret as a tidal sand flank.

4.2.5 Shallow sea deposits

4.2.5.1 Facies XII: Offshore

This facies is dominated by dark gray clayey silt and silty clay, locally interbedded with lenses of gray coarse silt and fine sand (Figure 3L). It has an *Mz* range of 4.52–7.23 Φ, with contents of sand, silt, and clay of 25.8%–78.61%, 2.66%–29.74%, and 1.14%–65.12%, respectively (Table 4). Sorting is poor to very poor. The grain size frequency curve mainly shows a unimodal or bimodal distribution with a coarse main peak (4.3–5.1 Φ of peak value) and a fine secondary peak (7–8.2 Φ of peak value). The grain size accumulation curve commonly displays two- or three-tier modes (Figure 4L). The suspension components dominate the curve, with a proportion of >50%.

Bioturbation is very common. Marine mollusk shells are abundant and include *Arca subcrenata*, *Mactra veneriformis*, *Potamocorbula laevis*, *Talonostrea,* and *Anomia* sp. The average foraminiferal abundance of this facies has the highest value (~1,645 per 50 g of dry sediment) of the whole succession. The average simple diversity is also the highest, up to 25. The dominant foraminiferal species are *A. beccarii* vars (24.8%), *Cribrononion gnythosuturatum* (10.3%), *Nonionella decora* (8.2%), and *A. pauciloculata* (6.8%) (Figure 7).

The abundance of marine shells and bioturbation, the high diversity, and abundance of foraminifers with high concentrations of relatively stenohaline species coupled with a predominant fine-grained sediment and a dominant suspension component indicate a low-energy offshore environment (He et al., 2018; 2019). The development of this facies association took place at least during two distinct periods, including MIS 3 and the mid-late Holocene, respectively.

4.3 Late Pleistocene to Holocene stratigraphic architecture of the Jiangsu coastal plain and tidal sand ridge area

To reconstruct the Late Pleistocene to Holocene facies architecture in the Jiangsu coastal plain and tidal sand ridge area, we performed stratigraphic correlation among the 10 cores investigated in this study and eight cores from previously published studies (see Figure 1C). The stratigraphy of the study area was depicted through two SW–NE (along-dip)-oriented stratigraphic transects (Figures 8, 9), transversal to the modern coastline, and a NW–SE (along-strike)-oriented transect (Figure 10), parallel to the modern coastline.

4.3.1 Along-dip transects

4.3.1.1 Transect X-X′

This transect (Figure 1C) is located in the northern part of the Jiangsu coastal area. From proximal to distal locations, it includes cores JSWZK07, JSWZK08, JSWZK10, 07SR03, and JSWZK11 (Figure 8, core 07SR03 modified from Zhang et al., 2014).

Two major intervals with marine or mixed marine-coastal deposits represent a prominent feature across the whole transect. Marine and coastal deposits are invariably separated from underlying laterally continuous alluvial units by distinctive transgressive surfaces (Figure 8). The marine influence is highest at or a few meters above the transgressive surfaces, where shallow marine deposits are dominant. Offshore clays are generally overlain by prograding deltaic or subtidal sandy complexes. There is also clear distal to proximal transition from thick tidal sand ridge and shallow sea sediments in the NE to deltaic and tidal river channel facies in a more SW position. A large number of AMS ^{14}C and OSL dates assign the uppermost marine interval (tidal flat and shallow marine sediments) to the early Holocene, suggesting that marine ingression in the current tidal sand ridge area occurred before 8,800 cal a BP. According to the available radiocarbon dates and based on the morphological evolution of the study area, the overlying, prograding delta complex is thought to be the old Yellow River Delta of northern Jiangsu during the period in which the Yellow River captured the Huaihe River in 1128–1855 AD (Xue et al., 2010; Liu et al., 2013).

Unlike the Holocene marine interval, the older one is made up predominantly of tidal river channels and deltaic deposits, testifying to a more complex fluvial–marine interaction. The age of this older marine deposit is centered around 35–38 ka BP, with a few data ranging between 28 and 39 ka BP (Figure 8). This suggests an age attribution to the MIS 3 period. Clearly, deltaic progradation during MIS 3 occurred more seaward than Holocene progradation, which is consistent with the significantly lower eustatic rise during MIS 3.

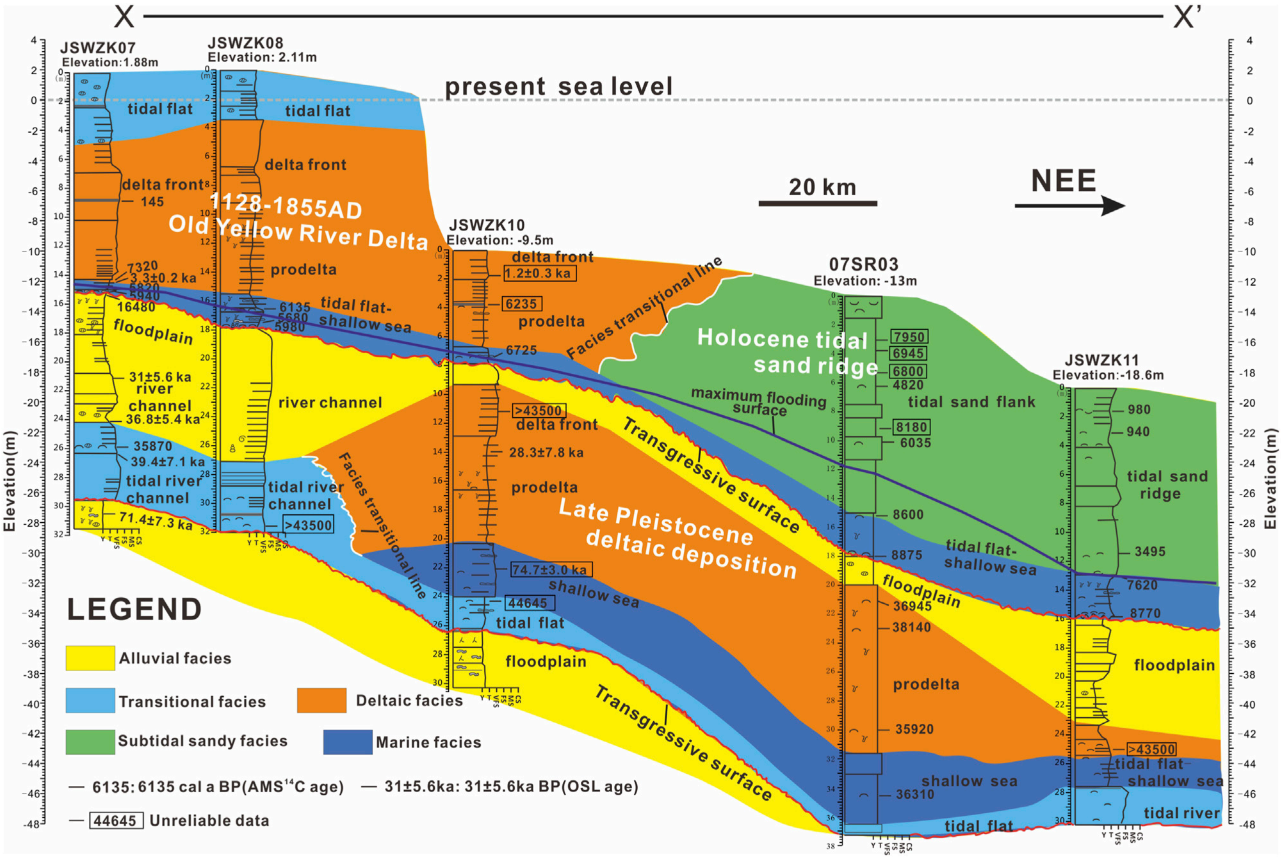

FIGURE 8
Facies architecture along coastal transect X-X′. The core 07SR03 is modified from Zhang et al. (2014).

4.3.1.2 Transect Y-Y′

This transect is located in the south of the Jiangsu coastal plain and partly across the shelf tidal sand ridge area, about 60 km south of transect X-X′. From proximal to distal locations, this transect includes cores JSWZK01, JSWZK02, JSWZK03, Y1, Y2, JSWZK04, and JSWZK05 (Figure 9, cores Y1 and Y2 are modified from Wang et al. (2015) and Yin et al. (2016), respectively).

The stratigraphy reconstructed from seven boreholes displays striking similarities with the facies architecture illustrated along transect X-X′; two major intervals of marine sedimentation, bounded by prominent transgressive surfaces, are separated by a thicker alluvial unit (Figure 9). Along transect Y-Y′, marine sediments consist entirely of tidal sand ridge facies at seaward locations, whereas the landward areas are dominated by coastal facies, including lagoon and tidal river channel deposits (Figure 9).

A large number of radiocarbon dates from transect Y-Y′ reveal that the uppermost marine interval, about 10–30 m thick, is of Holocene age. Sedimentary facies in the westernmost core JSWZK01 are composed of tidal sand bar and lagoon facies that gradually transition seaward to tidal sand ridge and tidal sand flank facies (Figure 9). Multiple dating along this transect suggests that the sea may have reached the current sand ridge region around 9,000 cal a BP (see core JSWZK05 in Figure 9).

The older marine deposits are mainly tidal sand ridge and tidal sand flank facies in landward transition to tidal river channel deposits. Several AMS ^{14}C dates from this marine interval yielded ages older than 40,000 a BP, which may not be reliable due to the limit of carbon-14 dating. In contrast, a few OSL dates cluster around 110–170 ka BP (though they may exceed 130 ka BP locally—Figure 9), suggesting that the older marine interval may have formed during MIS 5.

Alluvial deposits between these two marine intervals are mostly river channel and floodplain facies and yielded ages ranging between 20,000 and 90,000 a BP, suggesting deposition between MIS 2 and MIS 4. Unlike section X-X′, MIS 3 deposits were not encountered in transect Y-Y′, which may imply that they originally were relatively thin or that they were eroded by subsequent fluvial activity.

4.3.2 Along-strike transect

4.3.2.1 Transect Z-Z′

This transect runs along strike, parallel to the present coastline of the northern Jiangsu coastal plain, including cores JSWZK09, JSWZK10, 07SR01, JSWZK03, NTCJ3, JC-1203, Sanming, and 07SR11 from north to south, respectively (Figure 10, cores 07SR01, NTCJ3, JC-1203, Sanming, and 07SR11 modified from Yin and Zhang (2010), Wang Y. et al. (2012), Zhang X. et al. (2013), Sun et al. (2015), and Xiao (2015), respectively).

Similar to the along-dip transects, two intervals of marine or coastal-marine sedimentation and two intervals of alluvial deposits can be found in most cores along this transect. The uppermost marine interval in this transect mainly consists of Holocene tidal sand ridges that gradually turn into deltaic sediments from south to north. A few radiocarbon dates reveal that deltaic deposits were the subaqueous

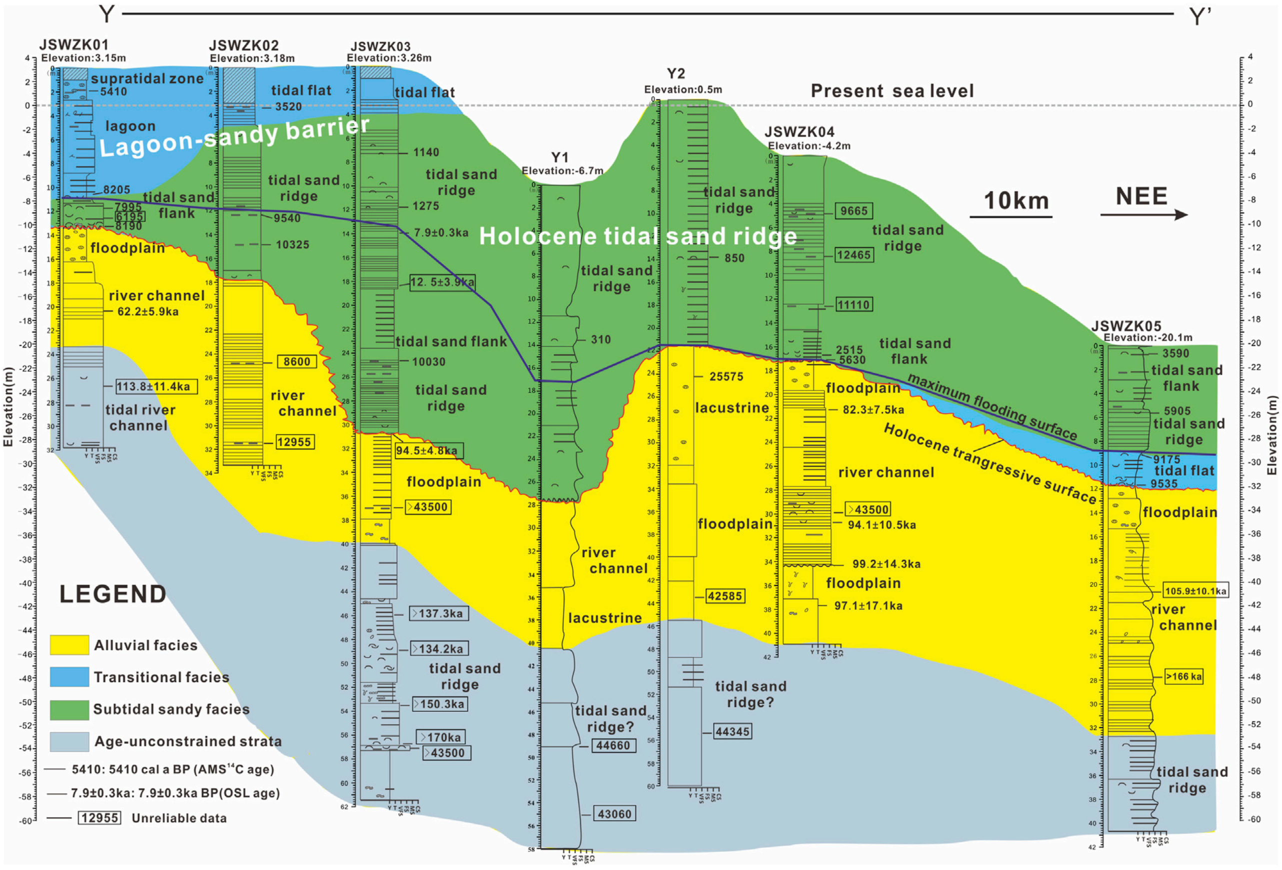

FIGURE 9
Facies architecture along coastal transect Y-Y′. Cores Y1 and Y2 are modified from Wang et al. (2015) and Yin et al. (2016), respectively.

delta part of the old Yellow River Delta between 1128 and 1855 AD in Jiangsu Province. The tidal sand ridge seems to have formed earlier than 4,800 cal a BP near the present coastline (see Figure 10).

Older (Late Pleistocene) marine or coastal-marine deposits in transect Z-Z′ are (i) suspected tidal sand ridge and tidal sand flank facies in the southern part of the study area, likely assigned to MIS 5, and (ii) deltaic deposits in the north, attributed to MIS 3. The ~30-m-long boreholes in the northern side may be too short to unravel MIS 5 deposits. On the other hand, transgressive MIS 3 deposits in the south are missing. The southernmost core (07SR11) lacks Holocene tidal sand ridge/sand flat facies, which are replaced by thicker tidal flat to shallow marine deposits, indicating the limit of tidal sandy influence.

5 Discussion

5.1 Changes in sedimentation rates and Holocene radial tidal sand ridge development

The formation of the RTSR in this area has been widely discussed by several studies (Li and Zhao, 1995; Li et al., 2001; Wang Y. et al., 2012; Yin et al., 2016). A consensus has been reached that a convergent–divergent tidal current field and large amounts of sediment are prerequisites for the formation of the RTSR (Zhu, 1998). Thus, the initiation of the convergent–divergent tidal current field and periods of high sediment flux appear to be critical to understanding the evolution of the RTSR.

According to simulations of regional paleotidal currents since the Holocene (Wang et al., 1998), the convergent and divergent tidal current fields in the study area were established between 10 and 8.5 ka BP, which implies that the RTSR could develop in the coastal area of Jiangsu Province after 10 ka BP. Zhu and Chang (2001) generally agreed with this opinion; however, they considered the early Holocene RTSR smaller than the present one due to reduced sediment supply during the early Holocene. Based on the evolution history of large rivers flowing to the SYS and a few ancient charts in the study area (Zhang, 1988), Liu and Xia (2004) proposed that the present RTSR could have formed since 2 ka BP and that it developed rapidly in response to the southward migration and supply of a large amount of sediment by the Yellow River after 1128 AD. Strong tidal currents could have shaped the radial morphology of the RTSR after the Yellow River flowed northward to the Bohai Sea since 1855 AD. Yin et al. (2016) concluded likewise that the formation of tidal sand ridges was highly related to remarkable sand input from the old Yellow River Delta after 1128 AD, as some radiocarbon ages from their cores indicated the initiation of tidal ridges since 600 years ago.

On the basis of seismic profiles and core data from the subaqueous sand ridge field, Wang et al. (1998) hypothesized that the RTSR could have formed after the early Holocene transgression, like other

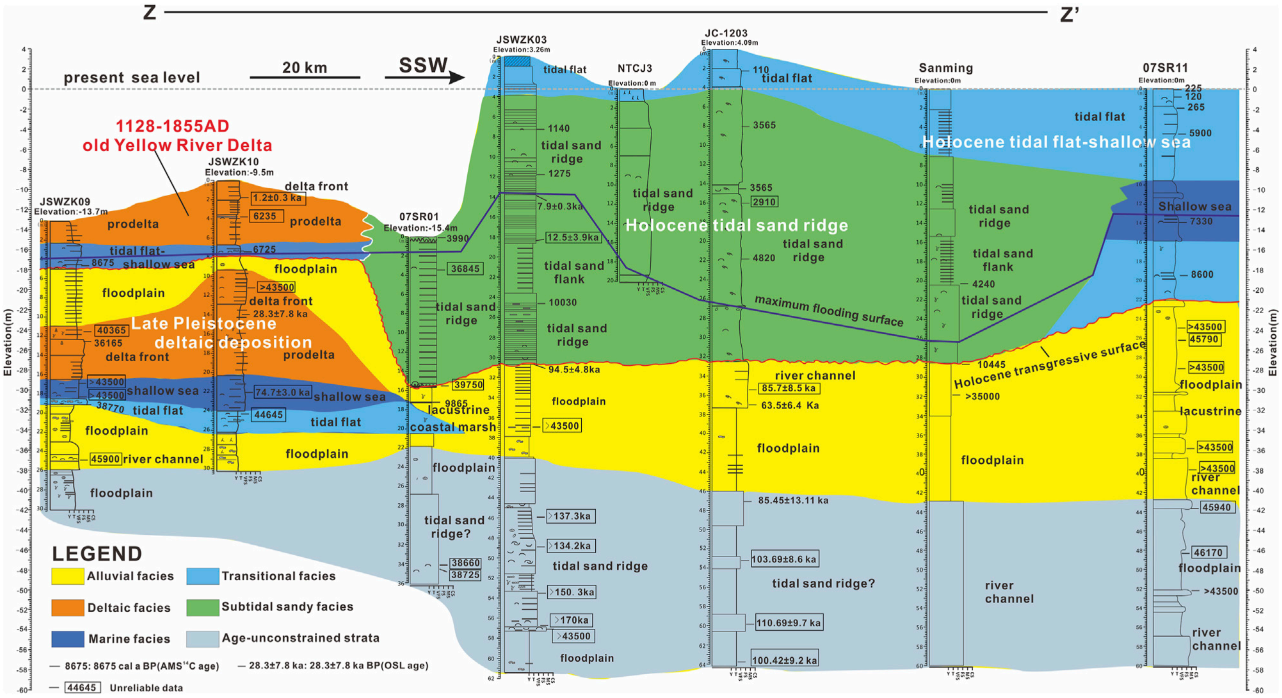

FIGURE 10
Facies architecture along coastal transect Z-Z′. Cores 07SR01, NTCJ3, JC-1203, Sanming, and 07SR11 are modified from Yin and Zhang (2010), Zhang X. et al. (2013), Xiao (2015), Wang Y. et al. (2012), and Sun et al. (2015), respectively.

Holocene sand ridges around the world (McBride and Moslow, 1991; Park et al., 2006). This hypothesis also agrees with simulations of regional paleotidal currents since the Holocene (Wang et al., 1998; Wang, 2002). Moreover, based on detailed sequence stratigraphic analysis of the SYS area since the MIS 5 period, Xia et al. (2012) delineated the relationship between relative sea-level change and the evolution of the RTSR, suggesting that the RTSR could start to develop after the submergence of the study area, following the early Holocene sea level jump around 9 cal ka BP.

However, contrary to the investigations of subaqueous sand ridges, studies from terrestrial tidally influenced sandy sediment attached to the present RTSR presented a different interpretion on the formation history of the Jiangsu coastal area (Figure 1C). Chen et al. (1995) recognized the terrestrial tidally influenced sandy sediment as the earliest sand ridges after detailed analysis of sedimentary facies, which were related to large sediment input from the Yangtze River around 7–6.5 ka BP, during the Holocene maximum transgression. Li et al. (2001) argued that the RTSR developed after 7.5 ka BP, prograding seaward under the Holocene normal regression. Chough et al. (2004) also considered that the RTSR off the Jiangsu Coast may represent “regressive,” highstand deposits that formed when sea level reached the present position at about 6 ka BP.

In summary, contrasting opinions about the formation and evolution of the RTSR mainly focused on when and where the original sand ridges developed, and distinct views led to highly different reconstructions. In order to contribute new data to this debate, in this study, we applied to the Holocene RTSR a technique based on age–depth plots from previous work (Figure 11A), which has proved to be an effective method to figure out the complex sedimentary evolution of depositional systems under high sediment supply conditions (He et al., 2019). The initiation of the RTSR in the study area is defined by the oldest depositional age obtained from tidal flat deposits, namely, ~9,000 cal a BP (Figure 11A; Liu et al., 2013; Xue, 2014).

Using published chronological data from cores, we found that sedimentation rates are clearly distinct before and after ~800 cal a BP. In particular, sedimentation rates range between .37 mm/a and 3.3 mm/a during ~9,000–800 cal a BP, but they dramatically increase to 18.9–108.7 mm/a after ~800 cal a BP (Figure 11B). This abrupt increase in the sedimentation rate of tidal sand ridges strikingly coincides with the moment (1128–1855 AD) in which the Yellow River delivered sediments to the Yellow Sea, following the capture of the Huaihe River (Xue et al., 2010; Liu et al., 2013). Thus, the growth of the RTSR can be subdivided into two stages. The first stage of bedform migration, from ~9,000 cal a BP to 1128 AD, is characterized by generally slow deposition, with locally increasing sedimentation rates under highstand conditions (since 5,000–3,000 a BP). The second stage, after 1128 AD, is a period of rapid development, when the sand ridge field received a large amount of sediment from the Yellow River and rapidly built its modern shape. A significant development of the RTSR following maximum marine ingression, particularly during the latest Holocene, can be clearly observed in the stratigraphic cross sections of Figures 9, 10. According to the available data, no direct evidence was found for the renewed growth of the sand ridges after the Yellow River re-entered the Bohai Sea northward in 1855 AD.

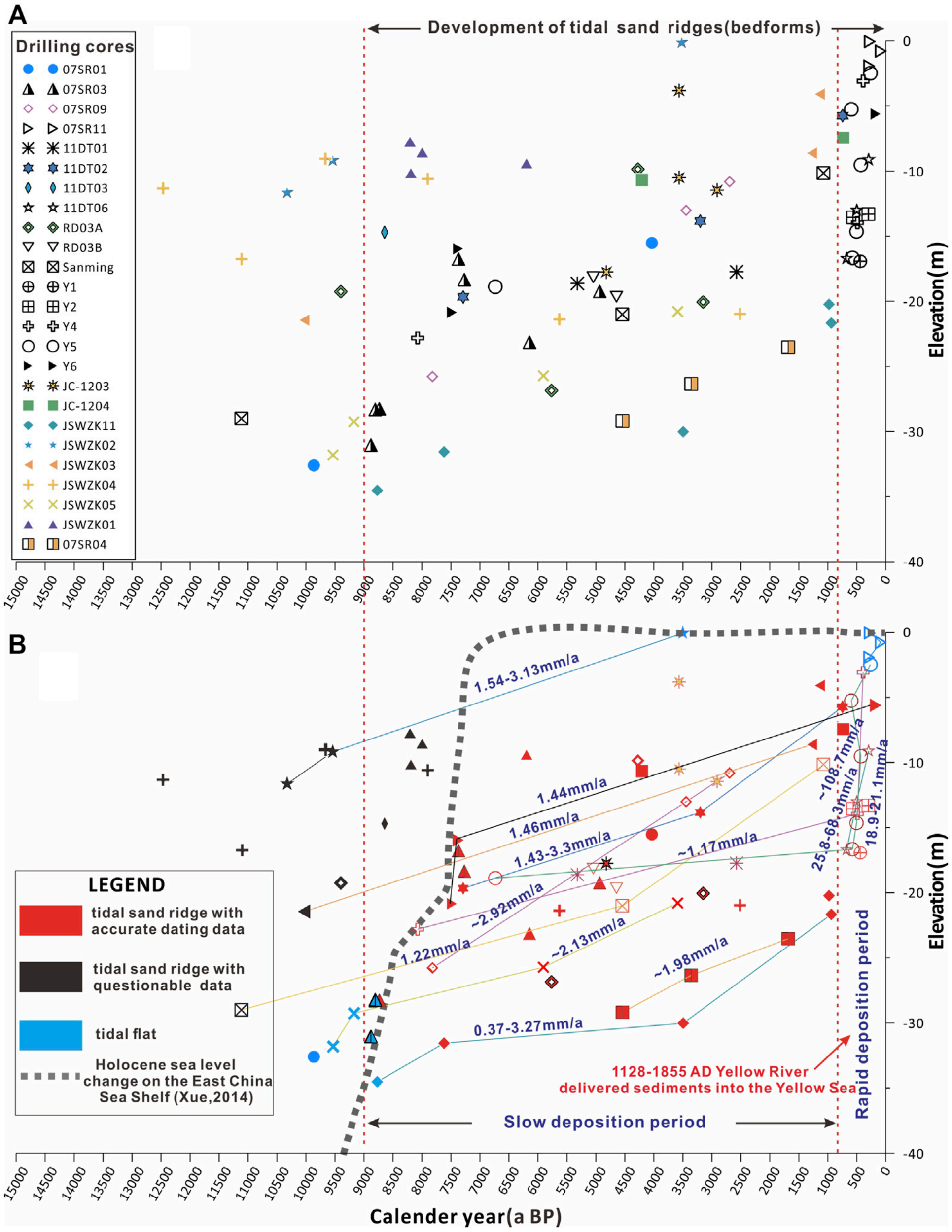

FIGURE 11
(A) Age–depth plot of collected drilling cores in the RTSR; **(B)** different sedimentary rates of the tidal sand ridge during 9,000 a BP–1128 AD and 1128–1855 AD.

5.2 Sedimentary evolution of the radial tidal sand ridge region since the Late Pleistocene

According to the stratigraphic analysis of 10 continuous cores and previous data (Figures 8–10), the study area documents a cyclic sedimentation pattern of alluvial and coastal/shallow marine deposits that define transgressive–regressive successions deposited over the last two interglacial–glacial cycles. Along-dip facies changes include a transition from fluvio-deltaic deposits in the northern part of the study area to tidally influenced sand deposits to the south.

5.2.1 MIS 5 and older periods (>100 ka BP)

Although results from OSL dating are not conclusive about its age, the sand tidal ridge facies assigned to the early MIS 5 (and possibly to older periods) is well preserved in the southern part of the study area (e.g., core JSWZK03) (Figures 9, 10). Previous numerical simulations have revealed that the formation and evolution of the tidal current system in the south Yellow Sea were mainly controlled by the interaction between the East China advancing tide wave and the position of the Jiangsu–Shandong paleocoastline, especially the Jiangsu paleocoastline (Wang et al., 1998; Uehara et al., 2002), as the bedrock coast of the Shandong Peninsula has basically kept steady since the Early Cretaceous (Wang S. J. et al., 2009). The reconstruction of Pacific sea-level changes since the Late Pleistocene implies that the early MIS 5 sea-level position was comparable to the present position (Chappell et al., 1996). The sediment source for the MIS 5 RTSR likely was the paleo Yangtze River (Wang et al., 2007b; Wang Y. et al., 2012; Wang et al., 2019b).

No early MIS 5 deposits were encountered in the north because of insufficient borehole depth (Figures 8, 10). However, two ~70-m-long cores (SYS-0701 and SYS-0702) from the south Yellow Sea, adjacent to the northernmost part of the study area, at a water depth of ~33 m, revealed the presence of a MIS 5 nearshore to shallow marine facies (Liu et al., 2010). Neither prominent deltaic deposits nor tidal sand ridge facies were encountered in the northern area. Tidal river deposits assigned to the early MIS 5 were observed on the basis of individual (JSWZK01) core data.

5.2.2 Late MIS 5 and MIS 4 periods (~60–100 ka BP)

Terrestrial deposition, including riverine and floodplain environments, dominated the study area during the late MIS 5 and MIS 4. River channel facies made up of thick, homogeneous coarse sand bodies was recognized in most cores (e.g., JSWZK04, Figure 9). Severely abraded marine shell fragments locally floor erosion surfaces, indicating the widespread occurrence of condensed stratigraphic intervals and hiatal surfaces during this period (see core JSWZK04 in Figure 9). The sedimentary evolution of the study area was highly related to sea-level fluctuations during the Late Pleistocene in the Yellow Sea (Liu et al., 2010).

5.2.3 MIS 3 period (~24–60 ka BP)

Tidal flat and shallow marine deposits assigned to MIS 3 mark the onset of renewed (minor) transgression in the study area. These deposits are overlain by a characteristic prograding succession of deltaic deposits in northern cores (e.g., JSWZK09 and JSWZK10) (Figures 8, 10), whereas tidal river deposits can be found in landward cores (e.g., JSWZK07 and JSWZK08).

The existence of marine deposits assigned to MIS 3 on the Jiangsu Coast has been debated in previous studies. Sedimentological analysis of cores BY1, 07SR01, and Longgang indicates that marine-influenced environments likely existed during MIS 3 (e.g., Zhang et al., 2010; Xia et al., 2013; Xia and Zhang, 2018); this hypothesis is also supported by numerical modeling of the MIS 3 transgression along the Jiangsu and Fujian coasts (Ye et al., 2016; Yu et al., 2016). Conversely, nearby boreholes, such as cores 07SR09 and 07SR11 (Sun et al., 2014; 2015), showed that MIS 3 deposits are entirely of continental origin. Unfortunately, most chronologic attributions to MIS 3 lack supporting OSL dates or are mostly constrained by AMS ^{14}C ages ranging between 35,000 and 40,000 a BP, which is close to the dating limits and could be questionable (Yin and Zhang, 2010; Zhang et al., 2010; Xia et al., 2013; Sun et al., 2014; Sun et al., 2015; Xia and Zhang, 2018).

Marine deposits have been reported at −20–−50 m elevation around the present coastline on the basis of macro- and micro-fossil (foraminifers) analyses from cores JC-1204 and 07SR01 (Xia et al., 2013; Xiao, 2015). Liu et al. (2013) confirmed the presence of MIS 3 deltaic deposits from core SYS-0701 through OSL dating in the southern Yellow Sea. Gao et al. (2021) detailed a mass of post-infrared (IR) IR-stimulated luminescence (pIRIR) ages and found no MIS 3 marine deposits in the core JCP01 beyond the limit of Holocene marine ingression. Therefore, it thus appears to exist a marked correlation between the formation of MIS 3 marine deposits and the distance from the coastline.

Although dating of JSWZK10 deltaic deposits yielded two AMS ^{14}C ages >40 ka BP and two OSL results ranging between 28 ka and 75 ka BP, the adjacent core JSWZK07 provided consistent OSL results in tidally influenced strata (36.8 ± 5.4 ka BP and 39.4 ± 7.1 ka BP, respectively) (see Figures 7, 8). We considered these adjacent tidal and deltaic deposits as indicators of coeval MIS 3 sedimentation because of the same elevation (−20–−30 m) and short distance between them. Our findings support the presence of a large active delta during MIS 3, which had been recognized from a series of seismic profiles and core data in the south Yellow Sea (Liu et al., 2010). The delta likely formed between 40 ka BP and 28 ka BP in the late MIS 3. Progradation of the MIS 3 delta took place in a more seaward position relative to its Holocene counterpart (Figure 8), which is consistent with a lower relative sea-level position during this period (Chappell et al., 1996).

It is remarkable that almost no MIS 3 deltaic or marine sediments were found in the southern part of our study area (Figures 9, 10), though thin marine layers have been reported from cores 07SR09 and 07SR04 in adjacent areas (Sun et al., 2014; Sun et al., 2015). This could be related to a relatively weak MIS 3 marine transgression and/or later (MIS 2) intense fluvial erosion in the region.

5.2.4 MIS 2 and the early Holocene period (~9–24 cal ka BP)

The whole south Yellow sea shelf was mostly subaerially exposed when sea-level position retreated to the Okinawa trough during the Last Glacial Maximum and early Holocene (Li et al., 2014). At that time, terrestrial, riverine, and lacustrine environments dominated the study area. A ~2–4-m-thick stiff clay layer was found in several cores, such as JSWZK01 (13.4–16.2 m), JSWZK04 (17.18–19.68 m), JSWZK06 (10.4–12.3 m), and JSWZK07 (15.08–18.1 m) (Figures 9, 10), thus representing a laterally continuous marker bed for stratigraphic correlation in the southern Jiangsu Plain and in the Yangtze deltaic area (Li et al., 2001; Sun et al., 2015). This overconsolidated horizon represents a stratigraphic unconformity of worldwide significance; it corresponds to a weakly developed paleosol that formed at the MIS 3/2 transition in response to the last phase of sea-level fall (Amorosi et al., 2017), and it is likely correlative with the development of the adjacent Yangtze River incised-valley systems (Saito et al., 2001; Li et al., 2002).

5.2.5 9,000–7,000 cal a BP

Marine ingression occurred in the present RTSR field area during the early Holocene sea-level jump, around 9,000–8,500 cal a BP (Hori and Saito, 2007). This transgressive trend is documented by the presence of typical tidal flat facies in the seaward-most cores (i.e., core JSWZK05) (Figures 8, 9, 12A). Radial tidal sand ridges are supposed to have been formed during this period by numerous hydrodynamic model simulations (Wang et al., 1998; Zhu and Chang, 2001). Our detailed sedimentary facies analysis, corroborated by several radiometric dates, supports this hypothesis, indicating that tidal sand ridges were active since about 9,000 cal a BP.

With rapid relative sea-level rise, the shoreline reached its present position around 8,200–8,500 cal a BP (see the cores JSWZK01 and JSWZK09 in Figures 8, 10). In the northern region, tidal flat and shallow marine environments developed with no apparent influence of radial tidal currents. In contrast, tidal sand ridges (bedforms) migrated in the southern area. A coastal barrier–lagoon system was

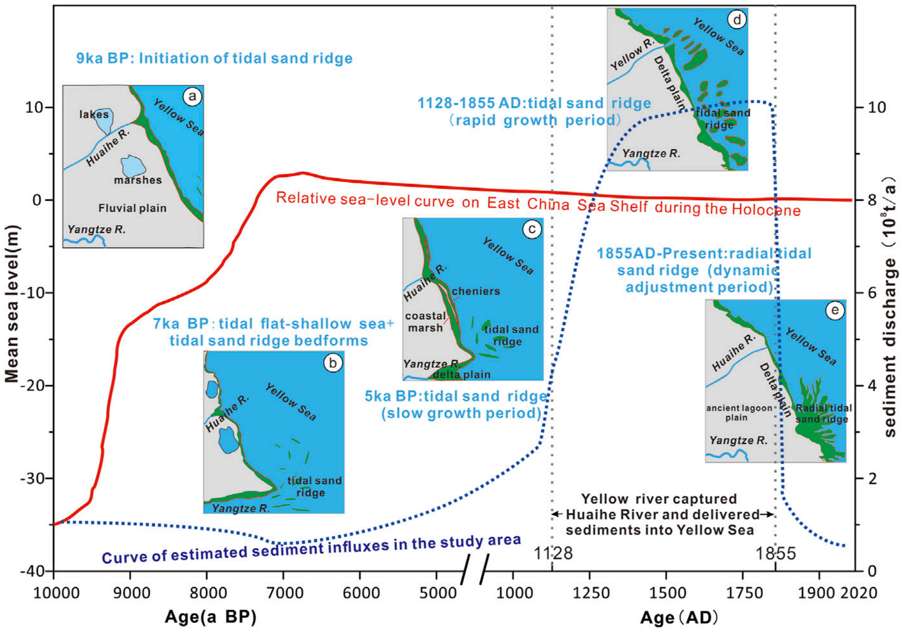

FIGURE 12
Synoptic geomorphological diagram revealing the relationships between Holocene evolution of the tidal sand ridge and relative sea-level change and sediment supply in the south Yellow Sea. The relative sea-level curve on the East China Sea shelf is modified from Xue (2014). The curve of estimated sediment influxes in the study area is referred to as the estimated sediment discharge of the Yellow River by Wang et al. (2007a). **(A)** 9 ka BP: initiation of tidal sand ridge bedforms during the rapid sea-level rise at the early Holocene; **(B)** 7 ka BP: the tidal flat and shallow sea environments well developed in the study area during the Holocene maximum transgressive period. The tidal sand ridge may mostly occur outside the Yangtze River mouth according to Li et al. (2001); **(C)** 5 ka BP: the tidal sand ridge developed slowly in the south Yellow Sea, while the cheniers and coastal marshes are well developed in the coastal area (Wang and Ke, 1989); **(D)** 1128–1855 AD: rapid growth of the tidal sand ridge after the Yellow River capturing the Huaihe River and subsequently delivering a large amount of sediment into the study area; and **(E)** 1855 AD–present: dynamic adjustment of the radial tidal sand ridge after the Yellow River emptying back into the Bohai Sea.

reconstructed from the core JSWZK01 (Figure 9), confirming that tidal sand deposition occurred during the Holocene transgression.

5.2.6 7,000–1,128 cal a BP

The Holocene maximum marine ingression took place around 7,000 cal a BP in the SYS region (Liu et al., 2004; Xue, 2014—Figures 8–10, 12B). Previous model simulations revealed that the apex of the radial tidal current was located at the paleo Yangtze River Channel mouth (Uehara et al., 2002; Figure 12B). In the southern region, tidal sand ridges gradually received more abundant supplies of sediment, while in the northern part, sedimentation occurred in a shallow marine environment and a chenier–coastal marsh sedimentary system on the landward side (Figure 12C; Wang and Ke, 1989). As the coastline prograded seaward after 7,000 cal a BP, the study area was gradually subdivided into a northern (deltaic) area and a southern (tidal sand ridge) area.

5.2.7 1128–1855 AD

The Yellow River captured the Huaihe River from the north of Jiangsu to the sea after 1128 AD (Liu et al., 2013). With 1 billion tons of sediment discharge into the south Yellow Sea per year, a new Yellow River Delta lobe formed in the north of Jiangsu, and the shoreline migrated southward at an average rate of 250–300 m/a (Zhang, 1984). Moreover, a large subaqueous delta also emerged in the northern part of the study area (Zhou et al., 2014; Figure 1B; Figures 8, 10). During this period, the tidal sand ridge system was fed by a huge amount of sediment, which is reflected in very high sediment accumulation rates (Figure 11), and the size of the RTSR dramatically increased in height and width (Liu and Xia, 2004). The submerged sand ridges gradually emerged, especially their nearshore portion (Figure 12D; see several ancient charts collected by Su et al., 2017a).

5.2.8 After 1855 AD

The Yellow River went back to the Bohai Sea after 1855 AD, and the Jiangsu Yellow River Delta was abandoned. The Jiangsu coastline and underwater bedforms were continuously and dynamically adjusted with the abrupt decrease in sediment influx (Zhou et al., 2014). The abandoned subaqueous delta suffered severe erosion under the combined effect of tidal currents and alongshore waves (Liu et al., 2013). Meanwhile, the huge deposit left by the Yellow River was gradually shaped by tidal currents into a new submarine linear bedform (Liu and Xia, 2004). This bedform combined with the southern sand ridges to form the present Jiangsu offshore sand ridge system (Figure 12E; Su et al., 2017b).

5.3 Controlling factors on the formation and evolution of the RTSR

Previous studies highlighted that sand ridge formation, growth, migration, and eventual drowning on storm-dominated shelves are the results of geologic processes (i.e., relative sea-level rise and shoreline transgression), oceanographic processes (i.e., storms and offshore-directed currents), and other factors (sediment supply and antecedent geology) (Figueiredo et al., 1981; McBride and Moslow, 1991; Nnafie et al., 2014). These factors can also be essential to explain the distribution, evolution, and morphology of the RTSR on the tide-dominated Yellow Sea shelf.

5.3.1 Relative sea-level rise and marine transgression

Holocene coastal and shelf sedimentary systems, including the sand ridge facies, were sensitive to sea-level changes in the East China Sea (Gao and Collins, 2014; Li et al., 2014). The same holds for Late Pleistocene sea-level changes, which clearly affected the sedimentary evolution of the shelf in our study area.

The magnitude of eustatic rise since the Late Pleistocene primarily controlled the formation of sand ridge facies in the SYS. Previous research on paleo sea-level reconstructions indicated that the extent of the MIS 3 transgression was smaller than that of the Holocene and MIS 5 ages (Chappell et al., 1996). This implies that no sufficient accommodation was created in the Yellow Sea to host a thick tidal system during this period. Indeed, an alternation of terrestrial and marine facies prevailed in the northern region, and barely no marine facies developed in the south during MIS 3 (Figure 10). In contrast, at least 15-m-thick tidal sand ridge facies accumulated in the study boreholes during the Holocene and MIS 5 (See Figure 9, 10).

In addition, changes in the rates of relative sea-level rise likely affected sand ridge growth and migration in the SYS shelf. Liu et al. (2004) outlined a classical stepwise post-glacial sea-level rise in the western Pacific and postulated a close tie between phases of rapid relative sea-level rise and distinct meltwater pulse events. Rapid relative sea-level rise, especially in the early Holocene around 9,000 cal a BP, largely favored the development of transgressive depositional systems, including the sand ridge facies (Hori and Saito, 2007; Xia et al., 2012). Sand ridges developed as bedforms or sandy shoals during this phase of rapid relative sea-level rise and migrated landward under continuing transgression. When the relative sea-level rise decelerated and kept steady after 7,000 cal a BP, the tide-wave system had enough time to shape the sandy bedforms or shoals into the final form of the RTSR.

5.3.2 Sediment supply

Sediment provenance is another aspect of debate about the evolution of the RTSR. Based on the interpretation of shallow seismic profiles and stratigraphic correlation between the northern Jiangsu plain and Yangtze River Delta, early studies indicated that the tidal sand ridge area represented an independent “desert accumulation” during the LGM (Zhao, 1991). However, based on grain size analysis and the clastic mineral composition of sediments in the tidal sand ridge area, Wang et al. (1999) proposed that the sediments of the RTSR were mainly derived from the ancient Yangtze River. This hypothesis has been recently supported by detrital zircon geochronology in the SYS (Su et al., 2018). However, based upon heavy minerals and geochemical analysis from cores in the northern Jiangsu land area and in the tidal sand ridge area, most researchers believe that the ancient Yellow River and Yangtze River catchments were the major sediment sources for the RTSR, with the relative influence of each river depending on the distance from the ancient river mouth (Li et al., 2001; Yang et al., 2002; Wang Y. et al., 2009; Wang et al., 2013; Wang Z. B. et al., 2019). Moreover, Liu and Xia (2004) postulated multiple sources for the sand ridge systems: 1) Yellow River provenance for its southern part, mainly supplied in the historical period; 2) Yangtze River provenance for the southern sand ridge; and 3) glacial terrestrial sediments for the SYS shelf.

Although the debate is still open, most authors agree that a huge amount of sediment was necessary for the development of the enormous RTSR in the SYS (Li and Zhao, 1995; Zhu, 1998). Our age–depth plot of core data may provide new insights into this subject. The rates of tidal sand ridges were consistently 1.1–3.3 mm/a before 1128 AD, slightly 2–3 times than the average sedimentary rate on the SYS shelf, and dramatically increased to 18.9–108.7 mm/a after 1128 AD. We, thus, believe that the Yellow River played a key role in the rapid accretion (growth) of the RTSR through enormous sediment input into the Yellow Sea during 1128–1855 AD.

5.3.3 Oceanographic processes

The morphology of sand ridges on terrigenous shelves is generally parallel to the dominant current flow. This is particularly clear for the tidal sand ridges on the SYS shelf (Figure 1A). In this area, the radial morphology of the RTSR coincides with the directions of the current flow in the present radial tidal field (Wang, 2002).

There is some uncertainty about the relationship between ancient ocean dynamics and sand ridge growth in the study area. Although several hydrodynamic model simulations revealed that the radial tidal field could have formed off the Jiangsu Coast around 10,000–8,500 a BP, the radial center of tidal currents migrated north and south repeatedly, following the movement of the Jiangsu paleocoastline (Li et al., 2001; Uehara et al., 2002). This means that the formation and migration of the sand ridges could have been very complex due to unpredictable hydrodynamic conditions since the early Holocene in the SYS area.

As a matter of fact, the typical morphology of the RTSR became radial in shape only after 1900 AD, which is consistent with previous ancient charts (Zhang, 1988). In addition, wave currents appear to have dominated the Jiangsu Coast, leading to the formation of coastal barrier–lagoon systems in the northern Jiangsu coastal plain between ~8,500 a BP and 1128 AD (see studies of shelly sand bars by Wang and Ke, 1989; Ling, 2002; Xue et al., 2010). A large amount of Yellow River sediments emptied into the Yellow Sea and filled the Jiangsu Coast during 1128–1855 AD, resulting in the formation of the northern Jiangsu Yellow River Delta (Xue et al., 2010). In the meanwhile, the SYS shelf became wide and had a low gradient, which likely weakened wave activity and strengthened the influence of local tidal currents. After the Yellow River re-entered the Bohai Sea, tidal currents played a prominent role in redistributing the abandoned subaqueous deltaic sediments, shaping the irregular morphologies of the sand ridges into their present radial form (Liu and Xia, 2004).

6 Conclusion

A total of 10 ~30–60 m-long cores were retrieved from the Jiangsu coastal plain and offshore a sand ridge field in the south Yellow Sea (SYS) during 2018–2019. Based on a comprehensive analysis of sedimentary facies, grain size, foraminifers, radiocarbon dates (AMS ^{14}C), and optically stimulated luminescence (OSL) ages, we reconstructed the detailed Late Pleistocene sedimentary evolution of the radial tidal sand ridge (RTSR) region. This area evolved from a tidal sand ridge system during the late MIS 5 to an alluvial plain, with river channels and floodplains during MIS 4. A deltaic sedimentary system, reconstructed in the northern part of the RTSR region, developed approximately in the early MIS 3. After a period of fluvial incision, channel belt sedimentation, and paleosol formation during the Last Glacial Maximum, the RTSR began to form during the early Holocene. Our stratigraphic correlation of along-dip and along-strike transects indicates that deltas and tidal sand ridges are important sedimentary components in this region, representing the relative sea-level change history since the Late Pleistocene. Age–depth plots reveal that the RTSR likely initiated in a sandy bedform shape at approximately 9,000 cal a BP, with sedimentation rates of 1.1–3.3 mm/a and continued throughout the Holocene. Sedimentation rates increased rapidly to 18.9–108.7 mm/a after 1128 AD, when the Yellow River captured the Huaihe River, flowing southward into the Yellow Sea. This study suggests that increased sediment supply played a major role in the formation and evolution of the Holocene RTSR in the south Yellow Sea. Relative sea-level change created sufficient accommodation to host a thick tidal system during this period in the SYS and also likely affected sand ridge growth and migration by changing the rates of relative sea-level rise in the SYS shelf. Oceanographic processes, namely, the radial current flow in the SYS, dominated the formation of radial morphology in the RTSR. Thus, our studies also highlight that relative sea-level change and oceanographic processes were important controlling factors of the distribution, evolution, and morphology of the RTSR on the tide-dominated Yellow Sea shelf.

Data availability statement

The original contributions presented in the study are included in the article/Supplementary Material; further inquiries can be directed to the corresponding author.

Author contributions

LH: writing and editing—original draft. SY: project administration. CX: conceptualization and methodology. GZ: investigation. SY: visualization. AA: writing—review and editing and supervision.

Funding

This research was jointly supported by Laoshan Laboratory (LSKJ202204003), China Geological Survey projects (Grant Nos. DD20189503, DD20221775), Asian Cooperation Fund (Comparative Study of geoenvironment and Geohazards in the Yangtze River Delta and the Red River Delta) and the National Natural Science Foundation of China (Grant Nos. U22A20558, 42076070).

Acknowledgments

The authors thank Hongming Yuan, Xigui Ding, Guohua Hou, Shaofeng Pei, Liujuan Xie, Dapeng Su, Liangyong Zhou, Xiaoyong Duan, and Jian Liu for their help in the geological survey or in manuscript preparation. They also thank Dr. Dario Gioia (editor), Dr. Domenico Chiarella, and another reviewer for their helpful comments on an earlier draft of this paper.

Conflict of interest

The authors declare that the research was conducted in the absence of any commercial or financial relationships that could be construed as a potential conflict of interest.

Publisher's note

Supplementary material

The Supplementary Material for this article can be found online at: https://www.frontiersin.org/articles/10.3389/feart.2022.1107495/full#supplementary-material

References

Abrahim, B. M. S., Nichol, S. L., Parker, R. J., and Gregory, M. R. (2008). Facies depositional setting, mineral maturity and sequence stratigraphy of a Holocene drowned valley, Tamaki Estuary, New Zealand. *Estuar. Coast. Shelf S.* 79, 133–142. doi:10.1016/j.ecss.2008.03.007

Amorosi, A., Pavesi, M., Lucchi, M. R., Sarti, G., and Piccin, A. (2008). Climatic signature of cyclic fluvial architecture from the Quaternary of the central Po Plain. *Italy. Sediment. Geol.* 209, 58–68. doi:10.1016/j.sedgeo.2008.06.010

Amorosi, A., Bruno, L., Cleveland, D. M., Morelli, A., and Hong, W. (2017). Paleosols and associated channel-belt sand bodies from a continuously subsiding late Quaternary system (Po Basin, Italy): New insights into continental sequence stratigraphy. *Geol. Soc. Am. Bull.* 129, 449–463. doi:10.1130/b31575.1

Amos, C., and King, E. (1984). Bedforms of the Canadian eastern seaboard: a comparison with global occurrences. *Mar. Geol.* 57, 167–208. doi:10.1016/0025-3227(84)90199-3

Antia, E. (1996). Shoreface-connected ridges in German and US mid-atlantic bights: similarities and contrasts. *J. Coast. Res.* 12, 141–146.

Beardsley, R. (1983). "Structure of the changjiang river plume in the East China Sea during june 1980," in Proceedings of International Symposium on Sedimentation on the Continental Shelf, with Special Reference to the East China Sea (China Ocean Press), 265–284.

Berne, S., Lericolais, G., Marsset, T., Bourillet, J. F., and De Batist, M. (1998). Erosional offshore sand ridges and lowstand shorefaces; examples from tide-and wave-dominated environments of France. *J. Sediment. Res.* 68, 540–555. doi:10.2110/jsr.68.540

Berne, S., Vagner, P., Guichard, F., Lericolais, G., Liu, Z., Trentesaux, A., et al. (2002). Pleistocene forced regressions and tidal sand ridges in the East China Sea. *Mar. Geol.* 188, 293–315. doi:10.1016/s0025-3227(02)00446-2

Brenner, R. L. (1980). Construction of process-response models for ancient epicontinental seaway depositional systems using partial analogs. *AAPG Bull.* 64, 1223–1244.

Calvete, D., Walgreen, M., De Swart, H., and Falqués, A. (2001). A model for sand ridges on the shelf: Effect of tidal and steady currents. *J. Geophys. Res-Oceans* 106, 9311–9325. doi:10.1029/2001jc900001

Chappell, J., Omura, A., Esat, T., McCulloch, M., Pandolfi, J., Ota, Y., et al. (1996). Reconciliaion of late Quaternary sea levels derived from coral terraces at Huon Peninsula with deep sea oxygen isotope records. *Earth Planet. Sci. Lett.* 141, 227–236. doi:10.1016/0012-821x(96)00062-3

Chen, B., Li, C., and Ye, Z. (1995). A study on the Holocene buried tidal sand bodies in the south Yellow Sea coastal land (in Chinese with English abstract). *Acta Geol. Sin.* 50, 447–458.

Cheng, G., and Xue, C. (1997). *Sedimentary geology of Yellow River Delta*. Beijing: Geological publishing House, 1–47. (in Chinese).

Chiarella, D., Longhitano, S. G., Mosdell, W., and Telesca, D. (2020). Sedimentology and facies analysis of ancient sand ridges: Jurassic Rogn Formation, Trøndelag Platform, offshore Norway. *Mar. Pet. Geol.* 112, 104082. doi:10.1016/j.marpetgeo.2019.104082

Chough, S. K., Lee, H. J., Chun, S. S., and Shinn, Y. J. (2004). Depositional processes of late quaternary sediments in the Yellow Sea: a review. *Geosci. J.* 8, 211–264. doi:10.1007/bf02910197

Coleman, J. M., and Wright, L. D. (1975). *Modern River deltas: Variability of processes and sand bodies*. Houston: Houston Geological Society.

Como, S., and Magni, P. (2009). Temporal changes of a macrobenthic assemblage in harsh lagoon sediments. *Estuar. Coast. Shelf S.* 83, 638–646. doi:10.1016/j.ecss.2009.05.024

Davis, R. A., and Balson, P. S. (1992). Stratigraphy of a North Sea tidal sand ridge. *J. Sediment. Res.* 62, 116–121.

Davis, R. A., Klay, J., and Jewell, P. (1993). Sedimentology and stratigraphy of tidal sand ridges southwest Florida inner shelf. *J. Sediment. Res.* 63, 91–104.

Emery, K. (1968). Relict sediments on continental shelves of world. *AAPG Bull.* 52, 445–464.

Figueiredo, A. G., Swift, D. J. P., and Clarke, T. L. (1981). Sand ridges on the inner Atlantic shelf of North America: Morphometric comparisons with Huthnance stability model. *Geo.-Mar. Lett.* 1 (3), 187–191. doi:10.1007/BF02462432

Figueiredo, A. G., Sanders, J. E., and Swift, D. J. (1982). Storm-graded layers on inner continental shelves: Examples from southern Brazil and the Atlantic coast of the central United States. *Sediment. Geol.* 31, 171–190. doi:10.1016/0037-0738(82)90057-4

Folk, R. L., and Ward, W. C. (1957). Brazos River bar: a study in the significance of grain size parameters. *J. Sediment. Petrol.* 31, 514–519.

Galloway, W. E., and Hobday, D. K. (1983). *Terrigenous clastic depositional systems: applications to petroleum, coal, and uranium exploration*. New York: Springer.

Gao, S., and Collins, M. (2014). Holocene sedimentary systems on continental shelves. *Mar. Geol.* 352, 268–294. doi:10.1016/j.margeo.2014.03.021

Gao, L., Long, H., Tamura, T., Hou, Y., and Shen, J. (2021). A ~130 ka terrestrial-marine interaction sedimentary history of the northern Jiangsu coastal plain in China. *Mar. Geol.* 435, 106455. doi:10.1016/j.margeo.2021.106455

Gao, S. (2009). Modeling the preservation potential of tidal flat sedimentary records, Jiangsu coast, eastern China. *Cont. Shelf Res.* 29, 1927–1936. doi:10.1016/j.csr.2008.12.010

Geng, X., Wan, Y., Li, S., Zhang, Q., and Xu, X. (1983). Evolutionary process of Northern Jiangsu coastal zone and a dynamic equilibrium model of Northern Jiangsu shoal (in Chinese with English abstract). *Acta Oceanol. Sin.* 2, 284–298.

Goff, J. A., Swift, D. J., Duncan, C. S., Mayer, L. A., and Hughes-Clarke, J. (1999). High-resolution swath sonar investigation of sand ridge, dune and ribbon morphology in the offshore environment of the New Jersey margin. *Mar. Geol.* 161, 307–337. doi:10.1016/s0025-3227(99)00073-0

Green, M. O. (1986). Side-scan sonar mosaic of a sand ridge field: Southern Mid-Atlantic Bight. *Geo-mar. Lett.* 6, 35–40. doi:10.1007/bf02311694

He, L., Xue, C., Ye, S., Laws, E. A., Yuan, H., Yang, S., et al. (2018). Holocene evolution of the Liaohe Delta, a tide-dominated delta formed by multiple rivers in Northeast China. *J. Asian Earth Sci.* 152, 52–68. doi:10.1016/j.jseaes.2017.11.035

He, L., Xue, C., Ye, S., Amorosi, A., Yuan, H., Yang, S., et al. (2019). New evidence on the spatial-temporal distribution of superlobes in the Yellow River Delta complex. *Quat. Sci. Rev.* 214, 117–138. doi:10.1016/j.quascirev.2019.05.003

Hoogendoorn, E. L., and Dalrymple, R. W. (1986). Morphology, lateral migration, and internal structures of shoreface-connected ridges, Sable Island Bank, Nova Scotia, Canada. *Geology* 14, 400–403. doi:10.1130/0091-7613(1986)14<400:mlmais>2.0.co;2

Hori, K., and Saito, Y. (2007). An early Holocene sea-level jump and delta initiation. *Geophy. Res. Lett.* 34, L18401. doi:10.1029/2007gl031029

Hori, K., Saito, Y., Zhao, Q., Cheng, X., Wang, P., Sato, Y., et al. (2001). Sedimentary facies of the tide-dominated paleo-Changjiang (Yangtze) estuary during the last transgression. *Mar. Geol.* 177, 331–351. doi:10.1016/s0025-3227(01)00165-7

Hori, K., Tanabe, S., Saito, Y., Haruyama, S., Nguyen, V., and Kitamura, A. (2004). Delta initiation and Holocene seasea-level change: example from the Song hong (Red River) delta, vietnam. *Vietnam. Sediment. Geol.* 164, 237–249. doi:10.1016/j.sedgeo.2003.10.008

Houbolt, J. J. H. C. (1968). Recent sediments in the southern bight of the North Sea. *Geol. Mijnb.* 47, 245–273.

Ji, Y., Yin, Y., Li, Q., and Wang, A. (2015). The core-recorded strata and environmental changes since the Late Pleistocene in Kushuiyang area of the radial tidal sandy ridge system, Jiangsu offshore, southern Yellow Sea. *J. Nanjing Univ. (Nat. Sci.)* 51 (3), 641–657. doi:10.13232/j.cnki.jnju.2015.03.020

Johnson, H. D. (1977). Shallow marine sand bar sequences: an example from the late precambrian of North Norway. *Sedimentology* 24, 245–270. doi:10.1111/j.1365-3091.1977.tb00256.x

Jung, W., Suk, B., Min, G., and Lee, a. K. (1998). Sedimentary structure and origin of a mud-cored pseudo-tidal sand ridge, eastern Yellow Sea, Korea. *Mar. Geol.* 151, 73–88. doi:10.1016/s0025-3227(98)00058-9

Knobles, D., Wilson, P., Goff, J., and Cho, S. (2008). Seabed acoustics of a sand ridge on the New Jersey continental shelf. *J. Acoust. Soc. Am.* 124, 151–156. doi:10.1121/1.2960977

Krumbein, W. C., and Sloss, L. L. (1963). *Stratigraphy and sedimentation*. San Francisco: Free Man.

Lan, S., Gu, C., and Fu, B. (1986). Characteristics of temperature and salinity of the southern Yellow sea warm current water (in Chinese with English abstract). *Stud. Mar. Sin.* 27, 45–53.

Lee, J. H., Pang, I. C., Moon, I. J., and Ryu, J. H. (2011). On physical factors that controlled the massive green tide occurrence along the southern coast of the Shandong Peninsula in 2008: A numerical study using a particle-tracking experiment. *J. Geophys. Res-Oceans* 116, C12036. doi:10.1029/2011jc007512

Lei, Y., He, L., Ye, S., Zhao, L., Yuan, H., Yang, S., et al. (2021). Paleochannel distribution, delta development and paleoenvironment evolution in Bohai Bay since the Late Pleistocene. *Geol. China* 48 (6), 1947–1964. (in Chinese with English abstract). doi:10.12029/gc20210621

Li, C., and Wang, P. (1991). Stratigraphy of the Late Quaternary barrier-lagoon depositional systems along the coast of China. *Sediment. Geol.* 72, 189–200. doi:10.1016/0037-0738(91)90011-2

Li, Q., and Yin, Y. (2013). Sedimentary facies and evolution of the Likejiao sandy ridge, in the South Yellow Sea offshore area, eastern China. *Geogr. Res.* 32, 1843–1855. in Chinese with English abstract. doi:10.11821/dlyj201310008

Li, C., and Zhao, J. (1995). Recent research and controversy of the Jianggang radial sand ridge in Northern Jiangsu Province (in Chinese). *Mar. Sci.* 4, 58–60. doi:10.11759/HYKX.0.1995-04-016

Li, C., Zhang, J., and Deng, B. (2001). Holocene regression and the tidal radial sand ridge system formation in the Jiangsu coastal zone, east China. *Mar. Geol.* 173, 97–120. doi:10.1016/s0025-3227(00)00169-9

Li, C., Wang, P., Sun, H., Zhang, J., Fan, D., and Deng, B. (2002). Late quaternary incised-valley fill of the Yangtze delta (China): its stratigraphic framework and evolution. *Sediment. Geol.* 152, 133–158. doi:10.1016/s0037-0738(02)00066-0

Li, G., Li, P., Liu, Y., Qiao, L., Ma, Y., Xu, J., et al. (2014). Sedimentary system response to the global sea level change in the East China Seas since the last glacial maximum. *Earth Sci. Rev.* 139, 390–405. doi:10.1016/j.earscirev.2014.09.007

Liao, H., and Yu, H. (2005). Morphology, hydrodynamics and sediment characteristics of the Changyun sand ridge offshore Western Taiwan. *Terr. Atmos. Ocean. Sci.* 16, 621–640. doi:10.3319/tao.2005.16.3.621(t)

Ling, S. (2002). Study on the dynamic changes of coastline in north Jiangsu since the Holocene. *J. Oceanogr. Huanghai Bohai Seas.* 20, 37–46. in Chinese with English abstract.

Liu, Z., and Xia, D. (2004). *Tidal sands in the China seas*. Beijing: China Ocean Press. in Chinese with English abstract.

Liu, Z., Huang, Y., and Zhang, Q. (1989). Tidal current ridges in the southwestern Yellow Sea. *J. Sediment. Res.* 59, 432–437. doi:10.1111/j.1538-7836.2004.00794.x

Liu, Z., Xia, D., Berne, S., Wang, K., Tang, M., Tang, Y., et al. (1998). Tidal deposition systems of China's continental shelf, with special reference to the eastern Bohai Sea. *Mar. Geol.* 145, 225–253. doi:10.1016/s0025-3227(97)00116-3

Liu, J. P., Milliman, J. D., Gao, S., and Cheng, P. (2004). Holocene development of the Yellow River's subaqueous delta, North Yellow sea. *Mar. Geol.* 209, 45–67. doi:10.1016/j.margeo.2004.06.009

Liu, Z., Berné, S., Saito, Y., Yu, H., Trentesaux, A., Uehara, K., et al. (2007). Internal architecture and mobility of tidal sand ridges in the East China Sea. *Cont. Shelf Res.* 27, 1820–1834. doi:10.1016/j.csr.2007.03.002

Liu, J., Saito, Y., Wang, H., Zhou, L., and Yang, Z. (2009). Stratigraphic development during the late pleistocene and Holocene offshore of the Yellow River delta, Bohai Sea. *J. Asian Earth Sci.* 36, 318–331. doi:10.1016/j.jseaes.2009.06.007

Liu, J., Saito, Y., Kong, X., Wang, H., Wen, C., Yang, Z., et al. (2010). Delta development and channel incision during marine isotope stages 3 and 2 in the Western South Yellow Sea. *Mar. Geol.* 278, 54–76. doi:10.1016/j.margeo.2010.09.003

Liu, J., Kong, X., Saito, Y., Liu, J. P., Yang, Z., and Wen, C. (2013). Subaqueous deltaic formation of the old Yellow River (AD 1128-1855) on the Western South Yellow sea. *Mar. Geol.* 344, 19–33. doi:10.1016/j.margeo.2013.07.003

Liu, J., Wang, H., Wang, F., Qiu, J., Saito, Y., Lu, J., et al. (2016). Sedimentary evolution during the last ~1.9 Ma near the Western margin of the modern Bohai Sea. *Palaeogeogr. Palaeocl.* 451, 84–96. doi:10.1016/j.palaeo.2016.03.012

Liu, B., Wu, H., Zhang, Z., Wei, G., Wang, Y., Zheng, J., et al. (2021). Recent evolution of the intertidal sand ridge lines of the dongsha shoal in the modern radial Sand Ridges, east China. *Int. J. Env. Res. Pub. He.* 18, 1573. doi:10.3390/ijerph18041573

Longhitano, S. G., Rossi, V. M., Chiarella, D., Mellere, D., Tropeano, M., Dalrymple, R. W., et al. (2021). Anatomy of a mixed bioclastic–siliciclastic regressive tidal sand ridge: Facies-based case study from the lower Pleistocene Siderno Strait, southern Italy. *Sedimentology* 68 (6), 2293–2333. doi:10.1111/sed.12853

McBride, R. A., and Moslow, T. F. (1991). Origin, evolution, and distribution of shoreface sand ridges, Atlantic inner shelf, USA. *Mar. Geol.* 97, 57–85. doi:10.1016/0025-3227(91)90019-z

McClennan, C., and McMaster, R. (1971). Probable Holocene transgressive effects on the geomorphic features of the continental shelf off New Jersey, United States. *Atl. Geol.* 7, 69–72. doi:10.4138/1944

Miall, A. D. (1992). "Alluvial deposits," in *Facies models: Response to sea level change.* Editors R. G. Walker and N. P. James (Waterloo: Geological Association of Canada), 119–139.

Murray, A. S., and Wintle, A. G. (2000). Luminescence dating of quartz using an improved single-aliquot regenerative-dose protocol. *Radiat. Meas.* 32, 57–73. doi:10.1016/s1350-4487(99)00253-x

Mycielska-Dowgiałło, E., and Ludwikowska-Kędzia, M. (2011). Alternative interpretations of grain-size data from Quaternary deposits. *Geologos* 17, 189–203. doi:10.2478/v10118-011-0010-9

Nnafie, A., De Swart, H., Calvete, D., and Garnier, R. (2014). Effects of sea level rise on the formation and drowning of shoreface-connected sand ridges, a model study. *Cont. Shelf Res.* 80, 32–48. doi:10.1016/j.csr.2014.02.017

Park, S., and Lee, S. (1994). Depositional patterns of sand ridges in tide-dominated shallow water environments: Yellow Sea coast and South Sea of Korea. *Mar. Geol.* 120, 89–103. doi:10.1016/0025-3227(94)90079-5

Park, S., Han, H., and Yoo, D. (2003). Transgressive sand ridges on the mid-shelf of the southern sea of Korea (Korea strait): formation and development in high-energy environments. *Mar. Geol.* 193, 1–18. doi:10.1016/s0025-3227(02)00611-4

Park, S., Lee, B., Han, H., Yoo, D., and Lee, C. (2006). Late Quaternary stratigraphy and development of tidal sand ridges in the eastern Yellow Sea. *J. Sediment. Res.* 76, 1093–1105. doi:10.2110/jsr.2006.092

Parker, G., Lanfredi, N. W., and Swift, D. J. (1982). Seafloor response to flow in a southern hemisphere sand-ridge field: Argentine inner shelf. *Sediment. Geol.* 33, 195–216. doi:10.1016/0037-0738(82)90055-0

Pendleton, E. A., Brothers, L. L., Thieler, E. R., and Sweeney, E. M. (2017). Sand ridge morphology and bedform migration patterns derived from bathymetry and backscatter on the inner-continental shelf offshore of Assateague Island, USA. *Cont. Shelf Res.* 144, 80–97. doi:10.1016/j.csr.2017.06.021

Rao, W., Mao, C., Wang, Y., Su, J., Balsam, W., and Ji, J. (2015). Geochemical constraints on the provenance of surface sediments of radial sand ridges off the Jiangsu coastal zone, East China. *Mar. Geol.* 359, 35–49. doi:10.1016/j.margeo.2014.11.007

Reimer, P. J., Bard, E., Bayliss, A., Beck, J. W., Blackwell, P. G., Ramsey, C. B., et al. (2013). Intcal 13 and Marine13 radiocarbon age calibration curves 0-50, 000 years cal BP. *Radiocarbon* 55, 1869–1887. doi:10.2458/azu_js_rc.55.16947

Ren, M., and Shi, Y. (1986). Sediment discharge of the Yellow River (China) and its effect on the sedimentation of the Bohai and the Yellow Sea. *Cont. Shelf Res.* 6 (6), 785–810. doi:10.1016/0278-4343(86)90037-3

Ren, M. (1986). *Comprehensive investigation of coastal zone and tidal flat Resources.* Beijing: China Ocean Press. Jiangsu Province.

Reynaud, J. Y., Tessier, B., Proust, J. N., Dalrymple, R., Marsset, T., De Batist, M., et al. (1999). Eustatic and hydrodynamic controls on the architecture of a deep shelf sand bank (Celtic Sea). *Sedimentology* 46, 703–721. doi:10.1046/j.1365-3091.1999.00244.x

Ridente, D. (2018). Late pleistocene post-glacial sea level rise and differential preservation of transgressive "sand ridge" deposits in the Adriatic sea. *Geosciences* 8, 61. doi:10.3390/geosciences8020061

Saito, Y., Yang, Z., and Hori, K. (2001). The huanghe (Yellow River) and changjiang (Yangtze River) deltas: a review on their characteristics, evolution and sediment discharge during the Holocene. *Geomorphology* 41, 219–231. doi:10.1016/s0169-555x(01)00118-0

Saito, Y. (1989). Late Pleistocene coastal sediments, drainage patterns and sand ridge systems on the shelf off Sendai, northeast Japan. *Mar. Geol.* 89, 229–244. doi:10.1016/0025-3227(89)90077-7

Shi, W., Wang, M., Li, X., and Pichel, W. G. (2011). Ocean sand ridge signatures in the Bohai Sea observed by satellite ocean color and synthetic aperture radar measurements. *Remote Sens. Environ.* 115, 1926–1934. doi:10.1016/j.rse.2011.03.015

Snedden, J. W., and Dalrymple, R. W. (1999). "Modern shelf sand ridges: from historical perspective to a unified hydrodynamic and evolutionary model," in *Isolated shallow marine sand bodies: Sequence stratigraphic analysis and sedimentologic interpretation.* Editors K. M. Bergman and J. W. Snedden (SEPM), 13–28.

Snedden, J. W., Tillman, R. W., and Culver, S. J. (2011). Genesis and evolution of a mid-shelf, storm-built sand ridge, New Jersey continental shelf, USA. *J. Sediment. Res.* 81, 534–552. doi:10.2110/jsr.2011.26

Song, D., Gao, Z., Xu, F., Ai, J., Ning, J., Shang, W., et al. (2018). Spatial and temporal variability of the green tide in the South Yellow Sea in 2017 deciphered from the GOCI image. *Oceanol. Limnol. Sinic* 49 (5), 1068–1074. in Chinese with English abstract.

Southon, J., Kashgarian, M., Fontugne, M., Metivier, B., and Yim, W. W. (2002). Marine reservoir corrections for the Indian ocean and southeast asia. *Radiocarbon* 44, 167–180. doi:10.1017/s0033822200064778

Stanley, D. J., and Chen, Z. (2000). Radiocarbon dates in China's Holocene Yangtze delta: record of sediment storage and reworking, not timing of deposition. *J. Coast. Res.* 16 (4), 1126–1132. doi:10.2307/4300129

Stride, A. H. (1982). "Ancient offshore tidal deposits," in *Offshore tidal sands: Processes and deposits.* Editor A. H. Stride (Dordrecht: Springer), 172–192.

Su, J., and Yuan, L. (2005). *China offshore hydrology*. Beijing: China Ocean Press. in Chinese.

Su, M., Yao, P., Wang, Z. B., Zhang, C. K., and Stive, M. J. (2017a). Exploratory morphodynamic hindcast of the evolution of the abandoned Yellow River delta, 1578–1855 CE. *Mar. Geol.* 383, 99–119. doi:10.1016/j.margeo.2016.11.007

Su, M., Yao, P., Wang, Z. B., Zhang, C. K., and Stive, M. J. (2017b). Exploratory morphodynamic modeling of the evolution of the Jiangsu coast, China, since 1855: Contributions of old Yellow River-derived sediment. *Mar. Geol.* 390, 306–320. doi:10.1016/j.margeo.2016.10.013

Su, J., Rao, W., Wang, Y., and Mao, C. (2018). Detrital zircon geochronology of the radial sand ridge system of jiangsu coast, east China: implication for sediment provenance. *J. Earth Sci.* 29, 144–154. doi:10.1007/s12583-017-0769-x

Sun, Z., Fang, W., Yong, Y., Gang, L., Song, G., and Xu, Q. (2014). Sedimentary environment evolution of Lanshayang tidal channel within the radial sand ridges, southern Yellow Sea. *J. Nanjing Univ. (Nat. Sci.)* 50, 553–563. in Chinese with English abstract. doi:10.13232/j.cnki.jnju.2014.05.003

Sun, Z., Li, G., and Yin, Y. (2015). The Yangtze River deposition in southern Yellow Sea during marine oxygen isotope stage 3 and its implications for sea-level changes. *Quat. Res.* 83, 204–215. doi:10.1016/j.yqres.2014.08.008

Swift, D. J., and Field, M. E. (1981). Evolution of a classic sand ridge field: Maryland sector, North American inner shelf. *Sedimentology* 28, 461–482. doi:10.1111/j.1365-3091.1981.tb01695.x

Swift, D. J., and Freeland, G. L. (1978). Current lineations and sand waves on the inner shelf, Middle Atlantic Bight of North America. *J. Sediment. Res.* 48, 1257–1266.

Swift, D. J., Holliday, B., Avignone, N., and Shideler, G. (1972). Anatomy of a shore face ridge system, False Cape, Virginia. *Mar. Geol.* 12, 59–84. doi:10.1016/0025-3227(72)90029-1

Swift, D. J., Parker, G., Lanfredi, N. W., Perillo, G., and Figge, K. (1978). Shoreface-connected sand ridges on American and European shelves: a comparison. *Estuar. Coast. Mar. Sci.* 7, 257–273. doi:10.1016/0302-3524(78)90109-3

Swift, D. J. (1975). Tidal sand ridges and shoal-retreat massifs. *Mar. Geol.* 18, 105–133. doi:10.1016/0025-3227(75)90007-9

Tanabe, S., Saito, Y., Vu, Q. L., Hanebuth, T. J. J., Ngo, Q. L., and Kitamura, A. (2006). Holocene evolution of the Song hong (Red River) delta system, northern vietnam. *Sediment. Geol.* 187, 29–61. doi:10.1016/j.sedgeo.2005.12.004

Trentesaux, A., Stolk, A., and Berne, S. (1999). Sedimentology and stratigraphy of a tidal sand bank in the southern North Sea. *Mar. Geol.* 159, 253–272. doi:10.1016/s0025-3227(99)00007-9

Trowbridge, J. (1995). A mechanism for the formation and maintenance of shore-oblique sand ridges on storm-dominated shelves. *J. Geophys. Res-Oceans* 100, 16071–16086. doi:10.1029/95jc01589

Twichell, D., Brooks, G., Gelfenbaum, G., Paskevich, V., and Donahue, B. (2003). Sand ridges off sarasota, Florida: A complex facies boundary on a low-energy inner shelf environment. *Mar. Geol.* 200, 243–262. doi:10.1016/s0025-3227(03)00185-3

Uehara, K., Saito, Y., and Hori, K. (2002). Paleotidal regime in the changjiang (Yangtze) estuary, the East China sea, and the Yellow Sea at 6 ka and 10 ka estimated from a numerical model. *Mar. Geol.* 183, 179–192. doi:10.1016/s0025-3227(01)00255-9

van de Meene, J. W., and van Rijn, L. C. (2000). The shoreface-connected ridges along the central Dutch coast—part 1: field observations. *Cont. Shelf Res.* 20, 2295–2323. doi:10.1016/S0278-4343(00)00048-0

Vis-Star, N. C., De Swart, H., and Calvete, D. (2007). Effect of wave-topography interactions on the formation of sand ridges on the shelf. *J. Geophys. Res-Oceans* 112, C06012. doi:10.1029/2006JC003844

Wagle, B., and Veerayya, M. (1996). Submerged sand ridges on the Western continental shelf off Bombay, India: evidence for late pleistocene-holocene sea-level changes. *Mar. Geol.* 136, 79–95. doi:10.1016/s0025-3227(96)00053-9

Wang, Y., and Ke, X. (1989). Cheniers on the east coastal plain of China. *Mar. Geol.* 90, 321–335. doi:10.1016/0025-3227(89)90134-5

Wang, X., and Ke, X. (1997). Grain-size characteristics of the extant tidal flat sediments along the Jiangsu coast, China. *Sediment. Geol.* 112, 105–122. doi:10.1016/s0037-0738(97)00026-2

Wang, Y., and Su, Y. (2013). Influence of solar activity on breaching, overflowing and course-shifting events of the Lower Yellow River in the late Holocene. *Holocene* 23 (5), 656–666. doi:10.1177/0959683612467481

Wang, P., Min, Q. B., and Bian, Y. H. (1985). "Distributions of foraminifera and ostracoda in bottom sediments of the northwestern part of the South Huanghai (Yellow) Sea and its geological significance," in *Marine micropaleontology of China*. Editor P. Wang (Beijing: China Ocean Press), 93–114. in Chinese.

Wang, J., Lu, G., Lin, H., Song, Z., and Jia, J. (1998). Developing process and mechanism of tidal sand ridges off the coast of jiangsu province. *J. Nanjing Norm. Univ. (Nat. Sci. ed.)* 21, 95–108. in Chinese with English abstract. doi:10.13232/j.NJSF.0.1998-03-022

Wang, Y., Zhu, D., You, K., Pan, S., Zhu, X., Zou, X., et al. (1999). Evolution of radiative sand ridge field of the South Yellow Sea and its sedimentary characteristics. *Sci. China Ser. D.* 42, 97–112. doi:10.1007/bf02878503

Wang, Y. H., Zhang, R. S., Xie, Z. R., and Wang, J. (2004). Relative Sea level changes and variational trends of the jiangsu radial sandbanks. *Adv. Mar. Sci.* 2, 198–203. in Chinese with English abstract. doi:10.3969/j.issn.1671-6647.2004.02.011

Wang, H., Yang, Z., Saito, Y., Liu, J. P., Sun, X., and Wang, Y. (2007a). Stepwise decreases of the Huanghe (Yellow River) sediment load (1950-2005): Impacts of climate change and human activities. *Glob. Planet. Change* 57, 331–354. doi:10.1016/j.gloplacha.2007.01.003

Wang, H., Zhang, X., Lan, X., Zhang, Z., Lin, Z., and Zhao, G. (2007b). Geochemistry characteristics of sediment and provenance relations of sediments in core NT1 of the south Yellow sea. *J. China Univ. Geosci.* 18, 287–298. doi:10.1016/s1002-0705(08)60009-6

Wang, S. J., Wang, L. M., Wan, Y. S., Zhang, C. J., and Wang, J. G. (2009). Study on intrusive rocks forming period and stages division in ludong area (in Chinese with English abstract). *Shandong Land Resour.* 25, 8–21.

Wang, Y., Wang, X., Gao, Y., Lv, H., and Zhang, X. (2009). A review on the reference material series for China Sea and continental shelf sediments. *Geol. China* 36, 1145–1153. in Chinese with English abstract.

Wang, Y., Zhang, Y., Zou, X., Zhu, D., and Piper, D. (2012). The sand ridge field of the South Yellow sea: Origin by river-sea interaction. *Mar. Geol.* 291, 132–146. doi:10.1016/j.margeo.2011.01.001

Wang, Y. Z., Gu, D. Q., Wang, W. H., and Qiao, L. L. (2012). The surface sediments size fraction and the distribution on lagoon and sand barriers in tangshan Bay. *Period. Ocean. Univ. China* 42, 131–136. in Chinese with English abstract. doi:10.16441/j.cnki.hdxb.2012.s1.019

Wang, K., Jiang, X., Ye, Q., Shi, X., and Liu, Y. (2013). Distribution and source of heavy minerals in the surface sediment of the tidal sand ridges area in south Yellow Sea (in Chinese with English abstract). *Mar. Geol. Quat. Geol.* 33, 1–11. doi:10.3724/sp.j.1140.2013.05001

Wang, L., Hu, S., Yu, G., Ma, M., and Liao, M. (2015). Paleoenvironmental reconstruction of the radial sand ridge field in the South Yellow Sea (east China) since 45 ka using the sediment magnetic properties and granulometry. *J. Appl. Geophys.* 122, 1–10. doi:10.1016/j.jappgeo.2015.08.002

Wang, L., Hu, S., Yu, G., Wang, X., Ma, M., Liao, M., et al. (2019a). Evolution of the radial sand ridge field in the southwestern Yellow Sea, China since the late MIS 3. *Z. für Geomorphol.* 62 (3), 217–229. doi:10.1127/zfg/2019/0640

Wang, L., Li, G., Xu, J., Liu, Y., Qiao, L., Ding, D., et al. (2019b). Strata sequence and paleochannel response to tectonic, sea-level, and Asian monsoon variability since the late Pleistocene in the South Yellow Sea. *Quat. Res.* 92, 450–468. doi:10.1017/qua.2019.29

Wang, Z. B., Li, R. H., Yang, S. Y., Bai, F. L., and Lu, K. (2019). Comparison of detrital mineral compositions between stream sediments of the Yangtze River (Changjiang) and the Yellow River (Huanghe) and their provenance implication. *China Geol.* 2, 169–178. doi:10.31035/cg2018065

Wang, Y. (2002). *Radiative sandy ridge field on continental shelf of the Yellow Sea.* Beijing: China Environmental Science Press. in Chinese.

Wu, Z., Jin, X., Zhou, J., Zhao, D., Shang, J., Li, S., et al. (2017). Comparison of buried sand ridges and regressive sand ridges on the outer shelf of the East China Sea. *Mar. Geophys. Res.* 38, 187–198. doi:10.1007/s11001-016-9278-z

Xia, F., and Zhang, Y. (2018). Late Quaternary strata and environmental evolution record of core LG in Longgang, north Jiangsu plain, China. *Geogr. Res.* 37, 433–446. in Chinese with English abstract. doi:10.11821/dlyj201802015

Xia, F., Yin, Y., Wang, Q., Zhang, Y., and Liu, J. P. (2012). Sequence stratigraphy of the central part of North Jiangsu coasts since late MIS 3, eastern China. *Acta Geol. Sin.* 86, 1696–1712. in Chinese with English abstract. doi:10.3969/j.issn.0001-5717.2012.10.009

Xia, F., Zhang, Y., Wang, Q., Yin, Y., Wegmann, K. W., and Liu, J. P. (2013). Evolution of sedimentary environments of the middle Jiangsu coast, South Yellow Sea since late MIS 3. *J. Geogr. Sci.* 23 (5), 883–914. doi:10.1007/s11442-013-1051-5

Xiao, N. (2015). “The sedimentary evolution research of coastal areas in Jianggang of Jiangsu province since Last Glacial Epoch,” in *School of marine geosciences* (Qingdao: Ocean University of China), 75. in Chinese with English abstract.

Xu, M., Meng, K., Zhao, Y., and Zhao, L. (2019). Sedimentary environment evolution in east China’s coastal tidal flats: The North Jiangsu radial sand ridges. *J. Coast. Res.* 35, 524–533. doi:10.2112/jcoastres-d-18-00006.1

Xue, C. (1993). Historical changes in the Yellow River delta, China. *Mar. Geol.* 113 (3–4), 321–330. doi:10.1016/0025-3227(93)90025-Q

Xue, C., Zhou, Y., and Wang, G. (2003). Reviews of the Yellow River Delta superlobes since 700 BC. *Mar. Geol. Quat. Geol.* 23, 23–29. in Chinese with English abstract. doi:10.16562/j.cnki.0256-1492.2003.03.005

Xue, C., Liu, J., and Kong, X. H. (2010). Preliminary study of Holocene Huaihe River Delta on west coastal plain of Yellow Sea, China. *Quat. Sci.* 30, 892–901. in Chinese with English abstract. doi:10.3969/j.issn.1001-7410.2010.05.06

Xue, C., Liu, J., and Kong, X. (2011). Channel shifting of lower Yellow River in 1128-1855AD and its influence to the sedimentation in Bohai, yellow and East China seas (in Chinese with English abstract). *Mar. Geol. Quat. Geol.* 31 (5), 25–36. doi:10.3724/sp.j.1140.2011.05025

Xue, C., Qin, Y., Ye, S., Laws, E. A., and Wang, Z. (2018). Evolution of Holocene ebb-tidal clinoform off the Shandong Peninsula on East China Sea shelf. *Earth-Sci. Rev.* 177, 478–496. doi:10.1016/j.earscirev.2017.12.012

Xue, C. (2014). Missing evidence for stepwise postglacial sea level rise and an approach to more precise determination of former sea levels on East China Sea Shelf. *Mar. Geol.* 348, 52–62. doi:10.1016/j.margeo.2013.12.004

Yang, S., Li, C., Jung, H., and Lee, H. (2002). Discrimination of geochemical compositions between the Changjiang and the Huanghe sediments and its application for the identification of sediment source in the Jiangsu coastal plain, China. *Mar. Geol.* 186, 229–241. doi:10.1016/s0025-3227(02)00335-3

Yang, C. (1989). Active, moribund and buried tidal sand ridges in the East China Sea and the southern Yellow Sea. *Mar. Geol.* 88, 97–116. doi:10.1016/0025-3227(89)90007-8

Ye, H., Fang, X., and Wang, W. (1988). *Atlas of natural Resources of Jiangsu coastal zone.* Beijing: Science Press.

Ye, L., Yu, G., Liao, M., and Li, Y. (2016). Dynamic simulations of the late MIS 3 transgressions in the East China Sea and southern Yellow Sea, China. *Acta Oceanol. Sin.* 35, 48–55. doi:10.1007/s13131-016-0919-5

Yin, Y., and Zhang, N. (2010). Sedimentary environments of Xiyang tidal channel of radial tidal sand ridge system since the late period of Late Pleistocene in South Yellow Sea. *J. Palaeogeogr.* 12, 618–628. in Chinese with English abstract.

Yin, Y., Zou, X., Zhu, D., and Huang, J. (2008). Sedimentary facies of the central part of radial tidal sand ridge system of the eastern China coast. *Front. Earth Sci. China* 2, 408–417. doi:10.1007/s11707-008-0053-6

Yin, Y., Jia, P., and Li, Q. (2016). “Sedimentary facies and Late Pleistocene-Holocene evolution of the northern Jiangsu coast and radial tidal ridge field, South Yellow Sea, China,” in *Contributions to modern and ancient tidal sedimentology: Proceedings of the tidalites 2012 conference* (John Wiley & Sons), 293–312.

Yoshikawa, S., and Nemoto, K. (2014). The role of summer monsoon-typhoons in the formation of nearshore coarse-grained ripples, depression, and sand-ridge systems along the Shimizu coast, Suruga Bay facing the Pacific Ocean, Japan. *Jpn. Mar. Geol.* 353, 84–98. doi:10.1016/j.margeo.2014.03.018

Yu, Ge, Liangtao, Ye, and Liao, Mengna (2016). Simulations of coastal sediment patterns during the late Pleistocene in Jiangsu coasts(in Chinese with English abstract). *Acta Sedimentol. Sin.* 34, 670–678.

Zhang, C., Zhang, D., Zhang, J., and Wang, Z. (1999). Tidal current-induced formation-storm-induced change-tidal current-induced recovery-Interpretation of depositional dynamics of formation and evolution of radial sand ridges on the Yellow Sea seafloor. *Sci. China Ser. D.* 1, 3–14. doi:10.1007/bf02878492

Zhang, Z., Xie, L., Zhang, Y., Xu, J., Li, S., and Wang, Y. (2010). Sedimentary records of the MIS 3 transgression event in the North Jiangsu Plain, China. *Quat. Sci.* 30 (5), 883–891. in Chinese with English abstract. doi:10.3969/j.issn.1001-7410.2010.05.05

Zhang, C., Yang, Y., Tao, J., Chen, Y., Yao, P., and Su, M. (2013). Suspended sediment fluxes in the radial sand ridge field of South Yellow Sea. *J. Coast. Res.* 65, 624–629. doi:10.2112/si65-106.1

Zhang, X., Zhang, Z., Lan, X., and Li, R. (2013). *Regional geology of south Yellow sea.* Beijing: China Ocean Press. in Chinese.

Zhang, X., Ge, C. D., Yin, Y., Lu, Y. M., and Li, H. Q. (2014). The geochemical characteristic and sedimentary environment evolution of the Dabeicao channel and Dongsha shoal area among the radial tidal sand ridge system, southern Yellow Sea. *J. Nanjing Univ. (Nat. Sci.)* 50, 538–552. in Chinese with English abstract.

Zhang, L., Qin, X., Liu, J., Sun, C., Mu, Y., Gao, J., et al. (2016). Geochemistry of sediments from the huaibei plain (east China): Implications for provenance, weathering, and invasion of the Yellow River into the Huaihe River. *J. Asian Earth Sci.* 121, 72–83. doi:10.1016/j.jseaes.2016.02.008

Zhang, R. (1984). Land-forming history of the Huanghe River delta and coastal plain of north Jiangsu (in Chinese with English abstract). *Acta Geogr. Sin.* 39, 173–184.

Zhang, R. (1988). Evolution of coastal zone in jiangsu province after the Huanghe river changed its lower course. *J. Nanjing Univ. (Geogr.)* 9, 22–31. in Chinese with English abstract.

Zhao, S. (1991). Melt origin of fault-generated pseudotachylytes demonstrated by textures. *Mar. Geol. Quat. Geol.* 11, 105–112. doi:10.1130/0091-7613(1983)11<105:moofpd>2.0.co;2

Zhou, L., Liu, J., Saito, Y., Zhang, Z., Chu, H., and Hu, G. (2014). Coastal erosion as a major sediment supplier to continental shelves: example from the abandoned old huanghe (Yellow River) delta. *Cont. Shelf Res.* 82, 43–59. doi:10.1016/j.csr.2014.03.015

Zhu, Y., and Chang, R. (2001). Sediment dynamics study on the origin of the radial sand ridges in the southern Yellow Sea. *Stud. Mar. Sin.* 43, 38–50. in Chinese with English abstract.

Zhu, Y. (1998). New development of studies on origin of radiating sand ridges in the south Yellow Sea. *Mar. Geol. Quat. Geol.* 18, 113–118. in Chinese with English abstract.

frontiers | Frontiers in Earth Science

TYPE Data Report
PUBLISHED 17 March 2023
DOI 10.3389/feart.2023.1099730

OPEN ACCESS

EDITED BY
Alessandro Amorosi,
University of Bologna, Italy

REVIEWED BY
Veronica Rossi,
University of Bologna, Italy
Duccio Bertoni,
University of Pisa, Italy

*CORRESPONDENCE
Mai Duc Dong,
✉ ducdong.geo@gmail.com

SPECIALTY SECTION
This article was submitted to Quaternary Science, Geomorphology and Paleoenvironment,
a section of the journal
Frontiers in Earth Science

RECEIVED 16 November 2022
ACCEPTED 27 February 2023
PUBLISHED 17 March 2023

CITATION
Dong MD, Poizot E, Cuong DH, Anh LD, Hung DQ, Thuy Huong TT, Diep NV and Huong NB (2023), Transport trend of recent sediment within the nearshore seabed of Hai Hau, Nam Dinh province, southwest Red River Delta.
Front. Earth Sci. 11:1099730.
doi: 10.3389/feart.2023.1099730

Transport trend of recent sediment within the nearshore seabed of Hai Hau, Nam Dinh province, southwest Red River Delta

Mai Duc Dong[1]*, Emmanuel Poizot[2], Do Huy Cuong[1], Le Duc Anh[1], Duong Quoc Hung[1], Tran Thi Thuy Huong[1], Nguyen Van Diep[1] and Ngo Bich Huong[1]

[1]Institute of Marine Geology and Geophysics, Vietnam Academy of Science and Technology, Hanoi, Vietnam, [2]Cnam/Intechmer BP 324 F50103 Cherbourg Cedex, Paris, France

KEYWORDS

sediment trend, Red River Delta, end member modeling analysis, grain size trend analysis, Hai Hau coast

Introduction

Coastal sediment movements are often determined using numerical models, which draw on two different physics: hydrodynamic flow and particle motion. The former is resolved in the frame of the computational fluid dynamic (CFD). It is based mainly on Navier–Stokes equations, with the development of Reynolds-averaged Navier–Stokes approaches (RANS, URANS, etc.). Once known, fluid characteristics (speed and direction) are put into a second set of equations to compute the particle behavior. Once built, numerical models must be validated, that is, proof must be made of their accuracy to reproduce true and natural simulated processes. To do so, field measurements of processes are needed. For the speed, direction, and variation of the free surface elevation (in the case of tide), current meters—for example, acoustic Doppler current profilers (ADCPs)—are deployed at some points in the studied area, giving accurate measurements considered as a reference for the numerical model. The CFD part of the hydro-sedimentary model is validated when it gives the same results as ADCP measurements. The sedimentary part of numerical models is more tedious to validate. The choice of which particle motion equations to apply is the first main difficulty, but this aspect is not within the scope of the present paper. The second difficulty is the measurement and determination of the true sediment transport in the studied coastal area, which is still challenging. Approaches such as radionuclide tracers can give highly accurate information on sediment transport, but as such methods are cumbersome in their implementation and required equipment, they cannot be used everywhere. Therefore, methods to provide more easily and widely available information must still be developed or enhanced.

Grain size distributions, textural parameters, and curve shapes are related to the transport behavior and size-sorting processes of sediments in specific depositional environments (Flemming, 2007). In general, sediments are composed of mixtures of particle populations derived from different sources and transport processes (Flemming, 1988). The descriptive mean grain size, standard deviation, and sorting are not always sufficient to decipher related sediment processes (Weltje, 1997). From a statistical point of view, Weltje (1997) and Weltje and Prins (2003) proposed an end member modeling approach for analyzing grain size distributions to provide information about sediment provenance, transport processes, and depositional environments. After 25 years of development, EMMA is now available in various numerical contexts, such as FORTRAN code (Weltje, 1997), Matlab script (Dietze et al., 2012; Paterson and Helslop, 2015), and the R package EMMAgeo (Dietze and Dietze, 2019). This method has been successfully and widely applied in many studies, including Prins et al. (2002), Dietze et al. (2012), Collins et al. (2016) and López-González et al. (2019). The method, when combined with other available information such as wind conditions, tides, bottom flow has been used to determine sediment transport processes, provenance, and paleo-climate changes, including in Greenland, Lake Donggi Cona in China, the Harney Basin in eastern Oregon (United States), and the Alboran Sea. For example, Prins et al. (2002) established that during ice-rafted detritus events, continental material of likely Greenlandic origin increased up to 87%, and that bottom-current-derived material contains up to 40% mid-oceanic ridge fines, probably of Icelandic origin. Dietzel et al. (2012) showed that an end member with a major mode in the clay domain accounts for 34% of variance within the grain size data set. It may represent the sedimentation of suspension load from linear and laminar runoff during heavy precipitation events in summer. The clay and medium-silt end members are robust features of detrital sedimentation within Lake Donggi Cona in Qinghai Province, China.

Sediment trend analysis (STA©), first introduced by McLaren (1981), is a one-dimensional line-by-line method that establishes patterns of net sediment transport based on the spatial changes of three grain size parameters: mean, sorting, and skewness (McLaren, 1981; McLaren et al., 2007). Based on the McLaren (1981) theoretical principles, two-dimensional methods have been developed (Gao and Collins., 1992; Le Roux., 1994; Asselman., 1999) and identified as grain size trend analysis approaches (GSTAs). These methods define trend vectors (directions and patterns) based on the analysis of particular spatial relationships (trends) between the mean size, sorting, and skewness of seabed sediment (Mc Laren and Bowles, 1985; Gao and Collins, 1992). They have been discussed by Le Roux and Rojas (2007), McLaren et al. (2007), and Poizot et al. (2008). Generally, the line-by-line method is subjective because the directions of the trends must be parallel to the survey lines (Asselman, 1999), while choosing between the methods by Gao and Collins (1992) and Le Roux (1994) still remains a challenge (Poizot et al., 2008). GSTA was accepted as an investigational tool in the coastal projects of US Army Corps of Engineers (Hughes, 2005) and was successfully used in various marine and coastal environments (Gao et al., 1994; Pedreros et al., 1996; Jia et al., 2003; Mclaren and Beveridge, 2006; Duc et al., 2007; Duc et al., 2016; Van Lancker et al., 2004; Poizot and Mear, 2010; O'Shea and Murphy, 2016). A key element of the GSTA approach is the determination of a distance defining the neighboring points to be considered during computation. Gao and Collins (1992) defined the characteristic distance, denoted as Dcr, as the mean spacing between samples. The trend vectors identified for each station are then summed to produce a single vector. In this approach, neighboring stations are within Dcr and correspond to the nearest points surrounding a central station. Geostatistics is used to improve the determination of this parameter. A new distance (Dg) is proposed though the analysis of the semi-variogram (Poizot et al., 2006). The choice of the trend type to be adopted is based on the vector modulus and the number of neighbors satisfying the same trend type condition.

Despite the aim of universality asserted by the initiators of both STA® and GSTA, some works have reported the failure of the model to recover true sediment transports (Masselink, 1992; Carriquiry et al., 2001; Ríos et al., 2002). McLaren et al. (2007) and Poizot et al. (2008) reviewed the various sources of uncertainties in STA®/GSTA methods. In developing the software called GiSedTrend, Poizot and Méar (2010) applied STA®/GSTA analysis, giving the highest possible degree of freedom to scientists in their choice. The aim was to allow a better fit between the application of the method and the studied environment. In particular, the study of every kind of trend case, mixing the statistical parameters alone or combined, was possible for the first time.

In Duc et al. (2007), the nearshore zone of the Red River Delta area, which is also the study area of this article, was the subject of a GSTA analysis, following Gao and Collins's methodologies and settings. Because developments have arisen in the application of the method, and new tools are now available for conducting a GSTA-like analysis, this study presents the results of combining the EMMAgeo and GiSedTrend approaches in order to clarify the history of seabed sedimentation development in the coastal area of Hai Hau–Nam Dinh, as well as the relationships between sediment provenance and sediment transport, which has been recently affected by human activities such as river damp construction in 1965 and marine harbor construction in 2015.

The combination of EMMA and GSTA methods was addressed in some recent studies (Li and Li, 2018; Paladino et al., 2022). The direction of sediment transport at one point reflects the average of all transport processes affecting the sampling site (McLaren et al., 2007). Since the transport of different grain size fractions (or end members; EMs) is usually closely related to hydrodynamic conditions (Fleming, 2007), the spatial model of the end members should be coordinated with the direction of sediment transport. In turn, an understanding of the processes of sediment transport will have implications for the interpretation of the end members. In addition, combining the EMMAgeo and GSTA methods with information—such as the influence of wave directions and seasonal flows, and calculations of the amount of sediment moving at the estuary mouths—will help answer questions about the provenance, processes, and trends of sediment transport in the study area.

Overview of the study area

The coastal area of Hai Hau–Nam Dinh, which has a length of about 30 km, is currently heavily eroded. The sediment budget calculated by the modeling of shoreline changes shows that the net sediment transport is in the southward direction and that a large amount of fine-grained sediment is lost in deep waters. These two sediment sinks are believed to be the main causes of the serious erosion observed (Hoan et al., 2009). On the other hand, regarding human activity, spatial and temporal analyses of sedimentary facies in relation to late Holocene retrogradation show that the coastal area of Hai Hau has been eroded at a rate of ~19.5 m/yr since a hydraulic dam was built in the So River. This means that the rapid erosion off the Hai Hau coast was likely caused by the historical flood of

1787 and the construction of the hydraulic dam in 1960 (Nghi et al., 2018). Duc et al. (2003) conclude that the coastal area of Hai Hau lacks sediment because it is not supplied by the Red River and local sediments are transported to the southeast, creating erosion banks.

The coastline of Nam Dinh Province is oriented SW–NE, with the presence of estuaries such as the Day River mouth, the Ninh Co River mouth, the So River mouth, and the Ba Lat River mouth. In the study area, the sea floor topography is characterized by a slight tilt angle and a smooth surface from the shoreline to water depths of about 30 m. The surface sediment consists of sand, sandy silt, and silt, in which the recent sandy surface sediment is deposited along the shoreline at a depth between 0 and 5 m, except near the Ba Lat mouth, where sand reaches a water depth of 15 m. Further offshore, down to a depth of about 25–30 m, the sediment becomes silty with lenses of mud. Further offshore, the old surface sediments consist mostly of sandy silt and sand.

The tide regime is mixed, with a diurnal dominance. The average tidal amplitude is 2–3 m. Waves usually have a dominant direction from the east–northeast during the dry season and from east–southeast during the wet season. The average and maximum wave heights are 0.7–1.3 m and 3.5–4.5 m, respectively, but wave heights can reach over 5 m in severe storms (Duc et al., 2007).

In the Nam Dinh offshore area, there are two clear wind seasons. The winter monsoon (from November to March) is characterized by strong winds blowing from the north, lower temperature, and lower precipitation, whereas the summer monsoon (from May to September) is characterized by moderate winds blowing from the south, higher temperature, and higher precipitation. Wind field data at stations around the Hai Hau area in the transitional months between the two seasons are affected by the continental coastal morphology (Huu et al., 2012). From a geomorphological point of view, the Hai Hau coastal area, along with the development of the Red River Delta, is mainly affected by wave processes (Mather et al., 1996; Mathers and Zalasiewicz, 1999). According to Hoan et al. (2009), the maximum wave heights with 10% frequency in winter and summer are 1 m and 0.6 m, respectively.

The Ninh Co estuary area has a complicated (deep and unstable) flow and a particular cycle mainly influenced by fluvial and marine processes. The estuary is strongly influenced by the alongshore sediment transport from Hai Hau. Based on the calculation of alongshore sediment movements using formulas from energy methods such as CERC (Shore Protection Manual, 1984), Queens, and stress methods (improved Piter–Mayer formula), Huang (2010) showed that: i) from the So River mouth to the Ninh Co River mouth, the amount of sediment carried away is about 600–800 m^3/year, higher than that transported to the area, causing the phenomenon of sediment imbalance; and ii) from the southern Ninh Co River mouth to the Nga Son shore, the amount of sediment transported to the area is about 700 m^3/year higher than that carried away (Khac Nghia et al., 2003). Each year, the amount of Red River sediment through the Ba Lat River mouth is about 23 million tons, through the Day River mouth about 12 million tons, and through the Ninh Co River mouth about 18 million tons (Pruszak et al., 2002). In the Nam Dinh coastal area, the amount of sediment transported along the shore is about 150,000 m^3, with about 70% transported to the south and the remaining 30% transported to the north (Ostrowski et al., 2009).

Materials and methods

Materials

In September 2020, a total of 54 cores were collected from appr. 5–30 m water depth by a gravity core device (Figure 1). The core samples (max. 60 cm in length) covered the entire study area. Surface sediments from 0–5 cm depth were sampled from the tops of gravity cores. In each case, approximately 0.2 g of surface sediments were treated with HCl and H_2O_2 to remove carbonate and organic matter, respectively. Grain size analyses were performed using the HORIBA Laser Diffraction Particle Size Analyzer LA960. The measurement range was from 0.01 μm to 5,000 μm (20 to −0.5 ϕ). The GRADISTAT v9.1 program from Blott and Pye (2001) was used to calculate textural parameters based on the Folk and Ward (1957) percentile statistics. The results of sediment parameters from GRADISTAT include mean grain size (Md), sort (So), and skewness (Sk), shown in Table 1.

Methods

End member modeling analysis (EMMA)

EMMA, which estimates end member scores based on co-variability within grain size distributions, is a powerful tool yielding information on sediment provenance, transport, and depositional environment. EMMA is based on the study of the grain size distribution of sediment samples. It provides a direct link between particle size changes and the physical laws governing sediment production and transport (Weltje and Prins, 2003; Weltje and Prins, 2007). Particle-sized component results from the Horiba LA 960 were used as input values for the EMMAgeo library for processing and performing the grain size distribution (Dietzel E and Dietzel M, 2012, 2019). The calculation steps are provided by Dietzel et al. (2012); Dietzel and Dietzel (2019), including:

Step 1. Transform raw grain size distributions to a constant sum (e.g., 1 or 100%).

Step 2, rescaling and standardization: Minimize the effects of scale by applying a column-wise weight transformation. A weighted matrix W is derived from the columns of the original matrix X by scaling the columns based on percentiles, P, with lower (l) and upper (100−l) boundaries as weights:

$$\mathbf{W} = (\mathbf{X} - \mathbf{h}) / (\mathbf{g} - \mathbf{h}) \tag{1}$$

where vectors **h** and **g** are defined by $\mathbf{h}j$=Pl($\mathbf{x}j$) and $\mathbf{g}j$=P100−l($\mathbf{x}j$) for columns j = 1,2,. . .,p. A value of l = 0 reflects the minimum and maximum of each column; for example, a value of l = 2.5 gives percentiles between P2.5 and P97.5. For the sake of simplicity, we set lw to 0.05; however, note that the optimal value lopt is found by iteration.

Step 3. Calculate eigenvector and eigenvalue matrices. Extract the eigenvector matrix **V** and eigenvalue matrix **Λ** from the minor product matrix Γ given by

$$\Gamma = \mathbf{W}T\mathbf{W} \tag{2}$$

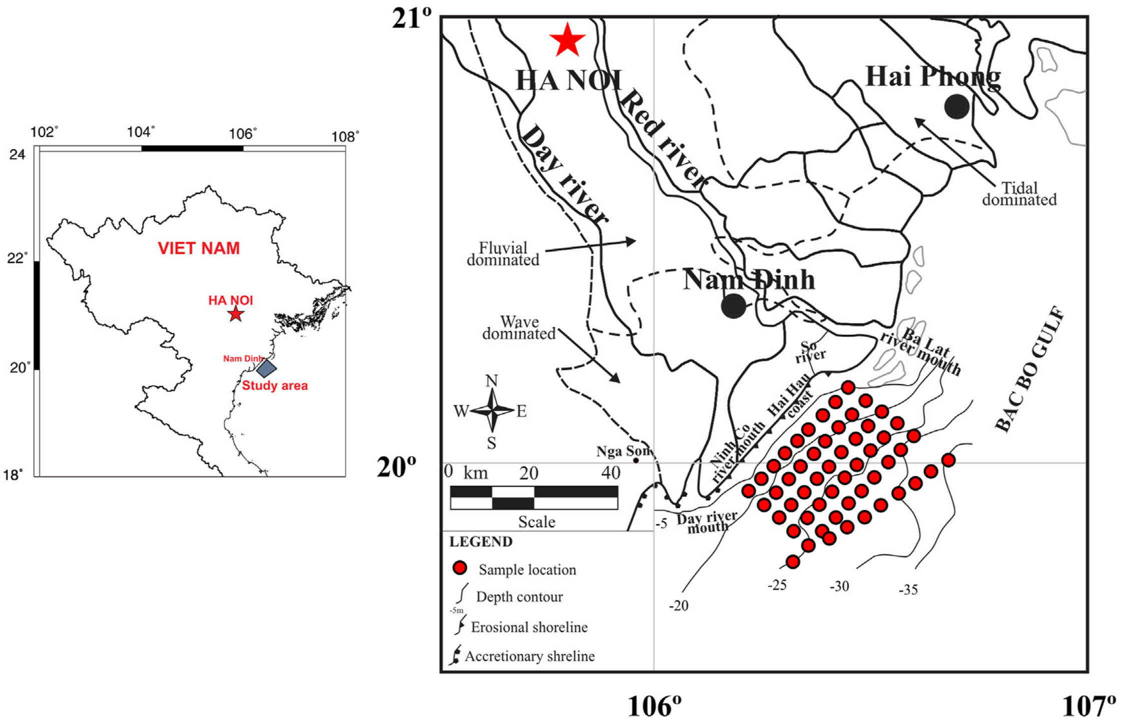

FIGURE 1
Map of the study area and location of surface sediment samples. Area of shoreline erosion and accretion is after Duc et al. (2007). Thin dashed line divides the delta region mostly affected by rivers, tides, and waves, based on the geomorphology (Mather et al., 1996; Mathers and Zalasiewicz, 1999).

TABLE 1 Input parameter values of the sediment in the study area.

Parameters	Max value	Min value	Mean value	Standard deviation
Mean	6.627	2.810	6.047	0.607698274
Sort	2.003	1.030	1.369	0.218394618
Skewness	1.005	−1.608	−0.960	0.455571384

Step 4, factor rotation: Apply factor rotation (e.g., VARIMAX) on the eigenspace of q end members to simplify the structure of the end members, thus facilitating factor interpretation. The number of end members (q) needs to be determined by iteration.

Step 5. Normalize the preliminary eigenvector loadings (**V**) to ensure the non-negativity of the rotated eigenvectors and estimate the eigenvector scores (**M**) using linear non-negative least squares as the objective function. This matrix contains the relative contributions of each end member to each sample. Usually, scores can be interpreted as time series, depth series, or spatial distribution patterns of end member abundance.

Step 6. Rescale matrices and compute variance explained. Reverse the initial weight transformation to rescale **V** and **M** to the original units of the initial data set. Normalize the rescaled matrices to fulfill the constant sum constraint. The rescaled and standardized matrices are denoted as end member loadings (**V**∗) and end member scores (**M**∗), respectively. Calculate the variance explained by each end member as the proportion of total scores variance. Scores are the relative contributions of the loadings to a sample and are thus related to the predominance of a process during the formation of the sedimentary deposit.

Step 7. Evaluate goodness of model fit. Calculate the modeled data set and the respective error matrix. Evaluate the goodness of fit, calculating mean row- and column-wise linear coefficients of determinations (R2) between **X** and **X**∗. The resulting matrix gives the explained proportion of variance of each sample and each variable, respectively (Dietzel et al., 2012).

$$\mathbf{X}^* = \mathbf{M}^*\mathbf{V}^*T \tag{3}$$

$$\mathbf{E} = \mathbf{X}^* - \mathbf{X} \tag{4}$$

Grain size trend analysis (GSTA)

According to McLaren and Bowles (1985), the direction of net sediment transport from a sediment sample point T1 to another point T2, measured in ϕ, can be either better sorted, finer, and more negatively skewed or better sorted, coarser, and more positively skewed. The vector that indicates the sediment trend is defined by

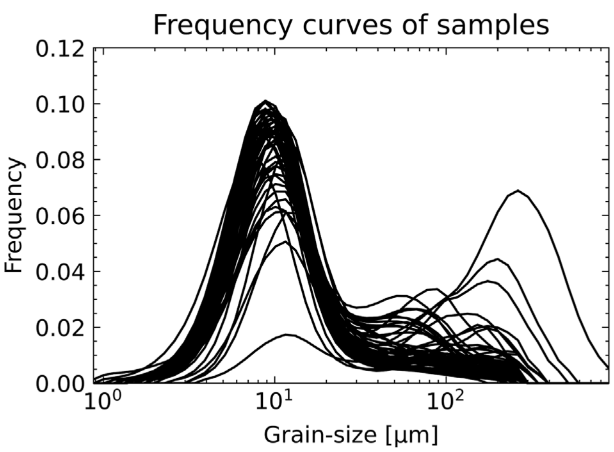

FIGURE 2
Grain size distribution curve of sediment samples in the study area.

the parameters (Md, So, and Sk) and compared with neighboring samples (stations) through sampling radius (characteristic distance; Dcr). Poizot and Méar, (2010), proposed to define the Dcr parameter (then renamed Dg) after a variogram study process. At a station there may be no or more than one unit trend vectors. In the case of multiple unit trend vectors, a single vector is computed according to Formula 5:

$$\vec{R}(x, y) = \sum_{i=1}^{n} \vec{r}(x, y)_i \tag{5}$$

where n is the number of trend vectors identified for the site, $\vec{r}(x, y)_i$ is a single trend vector (unit vector), and $\vec{R}(x, y)$ is the sum of trend vectors. Each post-calculated trend is determined by an angle and length value.

From the geostatistical analysis initially performed to define the characteristic distance Dg, a model of spatial variation is inferred, allowing for interpolations of the three statistical parameters. This operation aims to build regular grids with points equally spaced to allow the same weight for each surrounding neighborhood during vector field computation (Poizot et al., 2006).

Statistically, there are eight total combinations between the parameters Md, So, and Sk. However, Gao and Collins (1992) suggest that the combination of two of them—1) finer, better sorted, and more negative skewness (FB-) and 2) coarser, better sorted, and more positive skewness (CB+)—can be adopted to define the net transport direction. Field observations validate these combinations, as they present the highest probability of occurrence in the net transport direction.

Results

End member modeling analysis

The grain size distribution of surface (0–5 cm) samples (Figure 2) in the study area is wide-ranging, from 0 to 890 μm, and has frequency peaks between 7 and 300 μm. Samples from most locations are mainly composed of fine particle sediments.

Using EMMAgeo, the R_t^2 has been calculated from the data set (Figure 3A) using 2 to 10 EM. The results show that with 2 EM, the coefficient reaches 0.77 and that this value increases gradually (0.855, 0.86, 0.89) as the number of end members increases to 3, 4, and 5. Using 4 and 5 EM, most of the grain sizes from the model results are consistent with the dataset. By increasing the number of end members, the average coefficient does not increase and tends to decrease, showing the optimal model results at 5 EM.

Figure 3 shows the default graphical output, provided by EMMAgeo, for five end members. Panels b and c depict R^2 values (squared Pearson correlation coefficients) organized by grain size class and sample of 0.7 and 0.9, respectively. Overall, the data set was reproduced with a mean R^2_t of 0.89 (Figure 3A). The mode position and explained variance for EM1–EM5 were 56%, 26%, 6.1%, 9.9%, and 2.1%, respectively.

Each end member clearly has a dominant peak and shows a normal distribution in the grain size distribution curves of the five end members (Figure 3D). The grain size of the dominant peak increases, and the sorting improves toward finer grain size at different degrees from EM1 to EM5. EM1 has a mode position of 7.7 μm, with a majority in the fine silt range. EM2 has a mode of 15 μm, with a majority in the medium silt range. EM3 has a mode of 59 μm, with a majority in the very coarse silt range. EM4 has a mode of 200 μm, with a majority in the fine sand range, and EM5 has a mode of 340 μm, with a majority in the medium sand range. EM1 to EM5 have secondary peaks with lower peak values in the fine silt to medium sand range.

Spatial distribution of end members

Figure 4 shows the spatial distributions of the relative contents of the five end members, which range from 0% to 100%. The content of EM1 was generally higher in the study area (Figure 4A), where the highest values, largely over 70%, are concentrated in the central area (yellow-orange to red zone). The statistics show that samples with content of EM1 > 70% account for 59.2% (32/54 positions), that 12/54 (~22.2%) positions have a maximum value of 100%, and that only three samples have 0% EM1 content. In general, the large EM1 content (over 70%) has a banded shape, large width, and is oriented parallel to the shore at a water depth of about 15–30 m.

In contrast, the EM2 content is relatively low in the central part of the study area (0%–15%), where the majority of EM1 content is concentrated. The EM2 content exceeded 40% in three areas: 1) the southeast of Ninh Co River mouth, 2) the So River mouth with a banded shape oriented parallel to the shore, and 3) the southeast of study area with a higher content and a thicker contour line, where the highest values were recorded. According to statistics, in the study area, EM2 values were not recorded at 14/54 sites (EM2 values equal to 0%); all these are sites with 100% EM1 content, except at positions D29 and D30.

The content of EM3 is relatively low (Figure 4C), with an average value of 22% throughout the study area, locally higher in the coastal area and highest in the So River mouth offshore area, with the highest content values at D35 (48.5%) and D36 (40.7%), with the rest less than 25%.

The EM4 content is similar to EM3 in terms of locality, but it is mainly distributed in the offshore area, stretching from the east to the southeast (Figure 4D). The higher content is concentrated in locations with a higher depth of seabed; the highest value reaches ~67% at D52,

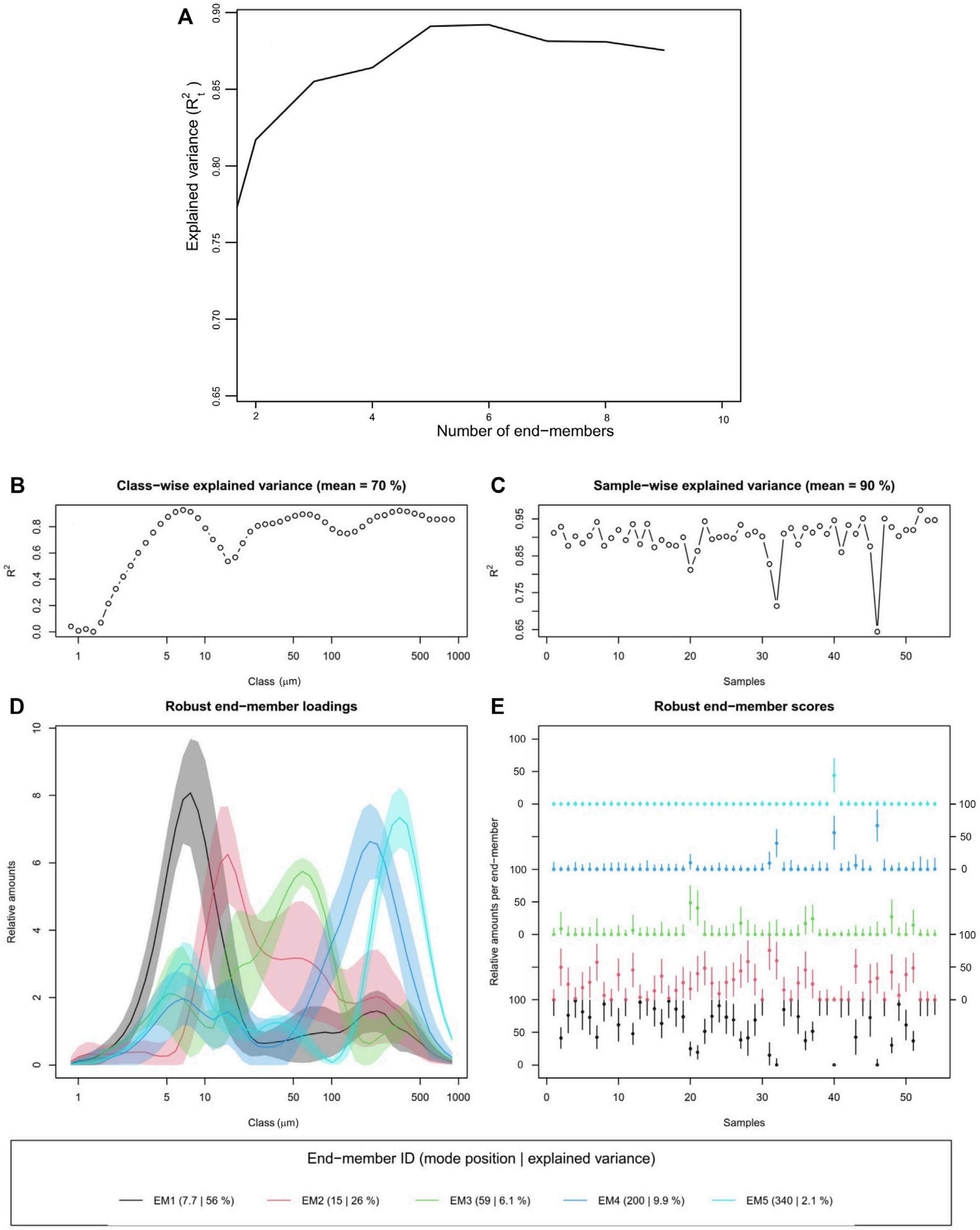

FIGURE 3
End member analysis of surface sediment grain size data from the study area. **(A)** Coefficient of determination versus the number of end-members; **(B,C)** explained variance chart for class and sample; **(D)** location of mode position with explained variance of each EM; **(E)** end-member score for each EM.

56% at D30%, and 40% at D18, while the remaining sites have a content of <10%. The EM5 content is concentrated mainly in the D30 sample area with a maximum value of ~44% (Figure 4E).

Figure 5 and Figure 6 show the relative content of EM1+2+3 and EM4+5, based on the type of sediment (silt sediment and sand sediment, respectively). It can be seen that EM1+2+3 covers almost

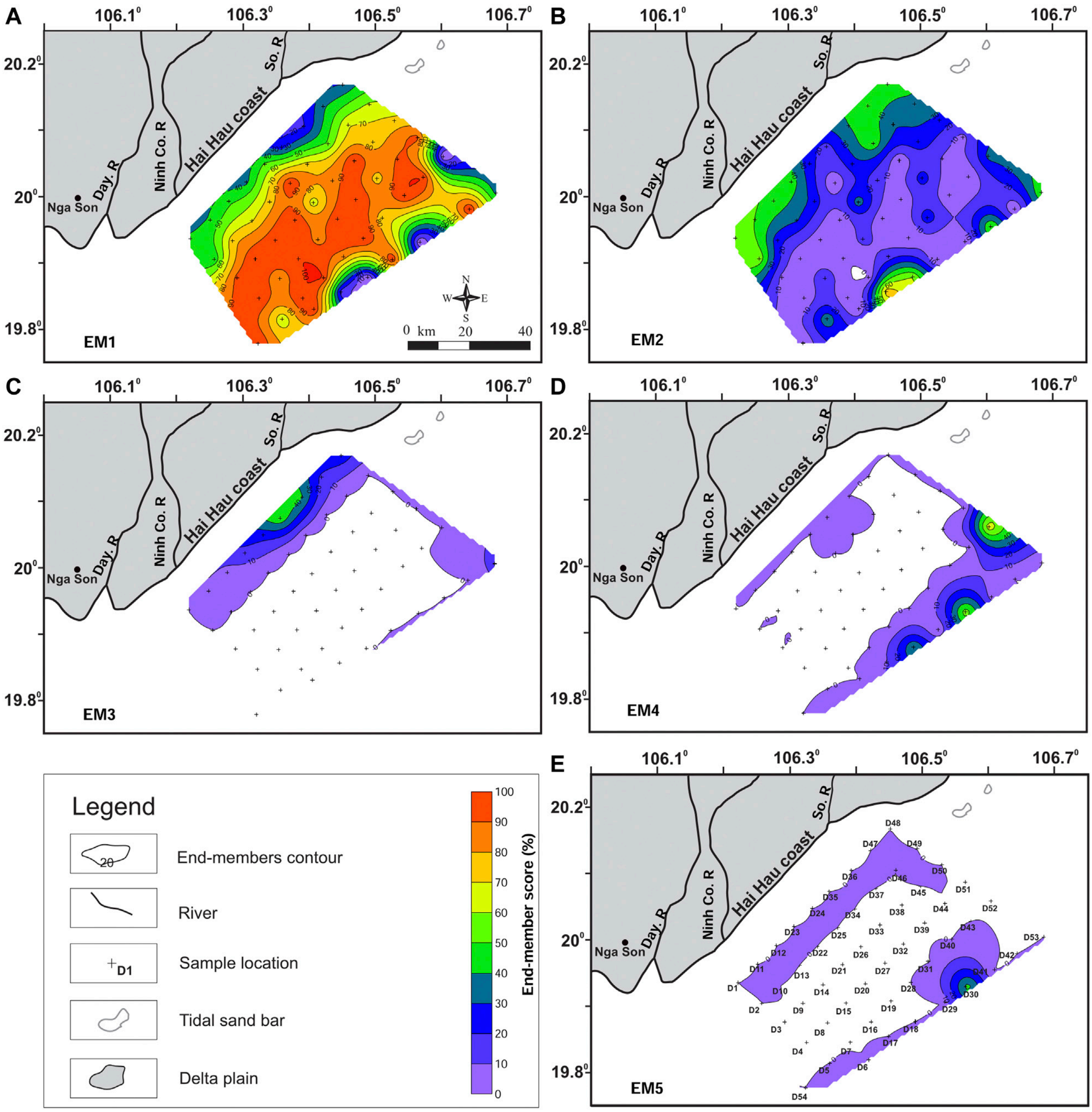

FIGURE 4
Spatial distribution and relative contents of the five end members in the studied area.

the entire study area, while EM4+5 is only locally deposited at the outer border of the study area.

Grain size trend analysis

EM1 and EM2 are quasi-complementary. The highest values of the former are the lowest of the latter, and vice versa. Both EMs gather more than 80% of the EMMA analysis information.

The FB- trend case is clearly correlated with the growing gradient values of EM1. This trend case shows transport from the lower values toward the highest values of EM1. These gradients have the highest values in two areas. The first is inside a strip parallel to the coast and covering 1/3 of the studied area Figure 7, zone A. The second is in the NE-most offshore sector Figure 7, zone B. In the central part of the studied area, corresponding to the highest percentage of EM1 and lowest gradients, FB- trends are rare or even absent. As EM1 corresponds to the finest sediment particle of the study, it can be inferred that the FB- trend case shows the transport of the finest fraction of the sediment. The FB- trend vector field then describes transport directions over the studied area.

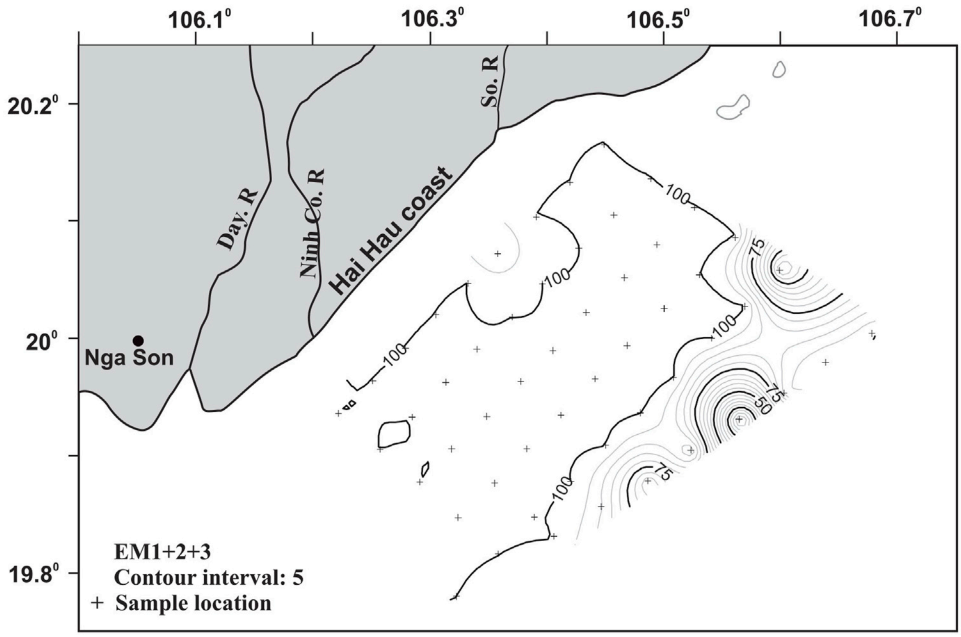

FIGURE 5
Spatial distribution and relative content (contour line) of EM1+2+3 in the study area.

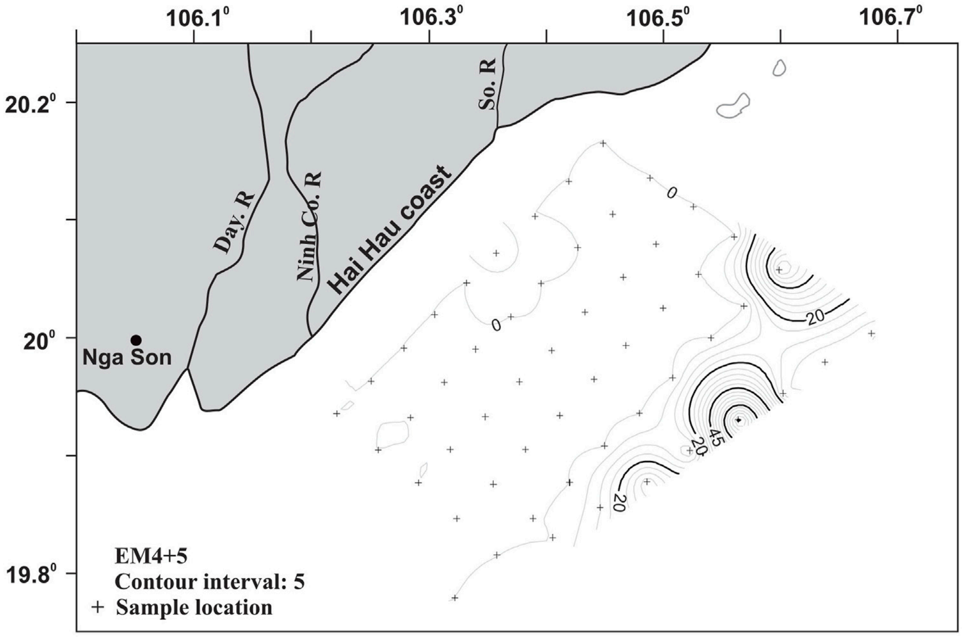

FIGURE 6
Spatial distribution and relative content (contour line) of EM4+5 in the study area.

The CB+ trend case shows vectors mainly located over the highest percentage of EM1 (Figure 8). Globally, CB+ vectors are computed over areas where the FB- trend case shows few or even no vectors. Comparisons of the CB+ trend case with the other end members (2–5) do not highlight any particular correlation to the spatial organization. In the context of the current study, the CB+ trend case seems not to represent any kind of transport but more a sediment lag deposit behavior (McLaren, 1981).

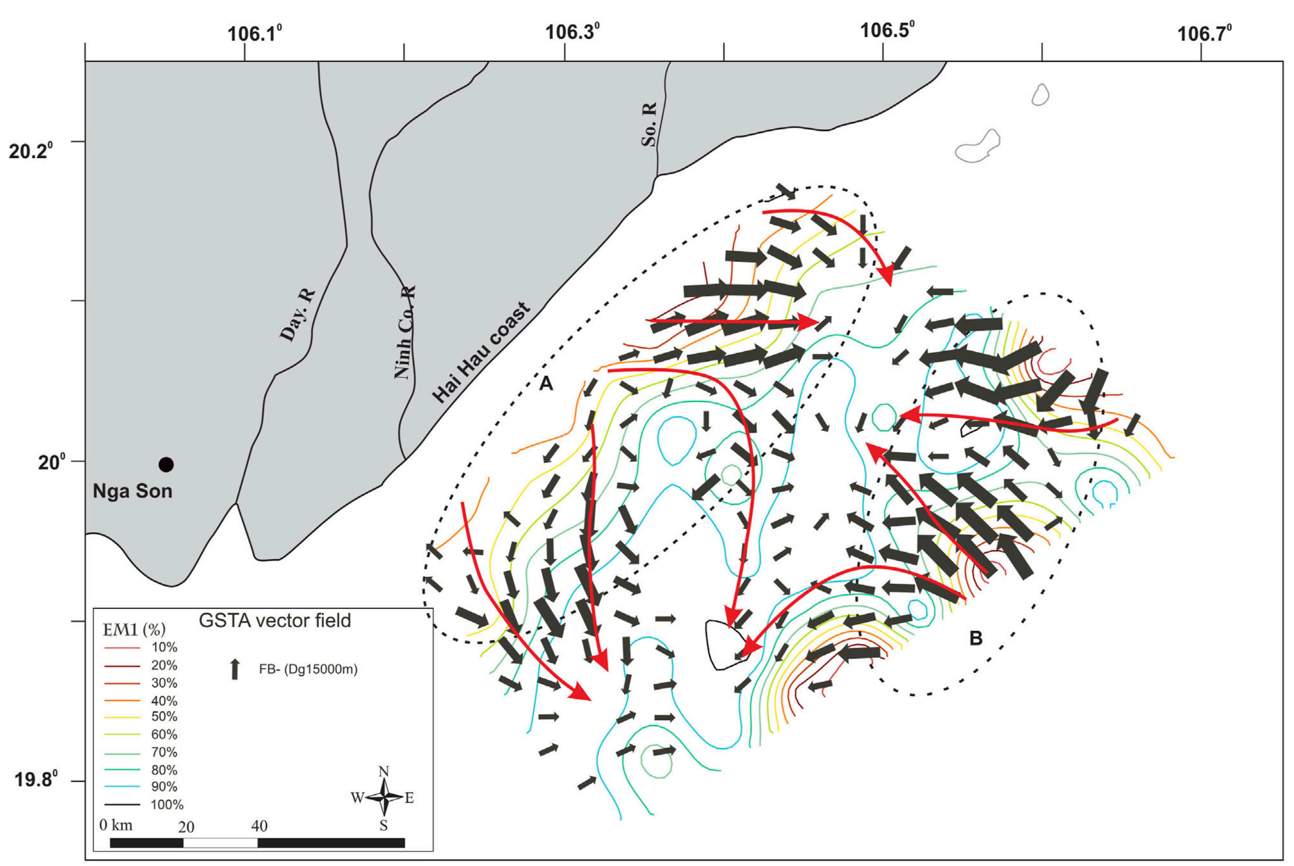

FIGURE 7
Contour lines of EM1 percentage under FB- trend vector field (black arrows) and interpretation (red arrows).

The combination of FB- and CB+ trends allows the identification of sediment transport vector trends (Figure 9). The patterns show distinct trends in three different zones. In zone 1, with a water depth of 0–15 m, the characteristic sediment transport trend is from the shore to the central area; the part around the So River mouth transports locally towards the northeast, the lower part transports along the coast to the southwest but in small quantity (the length of vector is smaller). Zone 2, at a depth of 25 m upwards, is characteristic of the transport vector from the northeast down and offshore. Transport vectors represented by Gebco bathymetry and the isometric line EM1+2+3 (mud sediment) show that in the region with high content of coarse grain size (specifically sand, where EM4+5 exists), the vectors have a greater module than those in the mud sediment area. In zone 3, the transition between zone 1 and zone 2, at a water depth of about 15–25 m and where mud sediments are dominant, sediment transport trends are unclear.

Discussion

Morphological and depositional characteristics are directly controlled by the complex hydrodynamic regime, which incorporates the regional monsoon, tides, ocean circulation, and coastal currents (Alexander et al., 1991).

The EMMAgeo model results (Figure 4) show that fine and coarse silt sediments (EM1+EM2) mostly occupy the central part of the study area (about <25 m water depth, for 56% and 26%, respectively). The fine-grained fraction (EM1) is mainly in the central part. The coarser-grained part exists on the two offshore sides of the So River mouth. A small amount of very coarse silt (EM3–6.1%) is found in the So River mouth area, while fine to medium sand (EM4, EM5) is mainly concentrated offshore, at water depths of >25 m.

Based on the distribution and orientation of EMs, combined with geomorphological features (Mather et al., 1996; Mathers and Zalasiewicz, 1999), northeast monsoon conditions (Figure 1), and the dominant wave direction from NE–SW (Duong Ngoc Tien, 2012; Huu et al., 2012), it can be hypothesized that EM1 and EM2 are affected by currents and waves along the coast. The source of EM1 (fine silt) may be erosion from the Hai Hau shore or from the north (Ba Lat River mouth area) and transport by irregular dynamic processes (sometimes strong, sometimes static) down to 28 m water depth. Coarser sediment (medium silt corresponding to EM2) is less affected by the river flow into the sea, and it is probably retained on the two banks of the riverbed. Medium silt observed on the offshore side is likely sourced from the coast of Hai Hau (for the nearshore-distributed part) and from the offshore area (for the locally distributed part). The

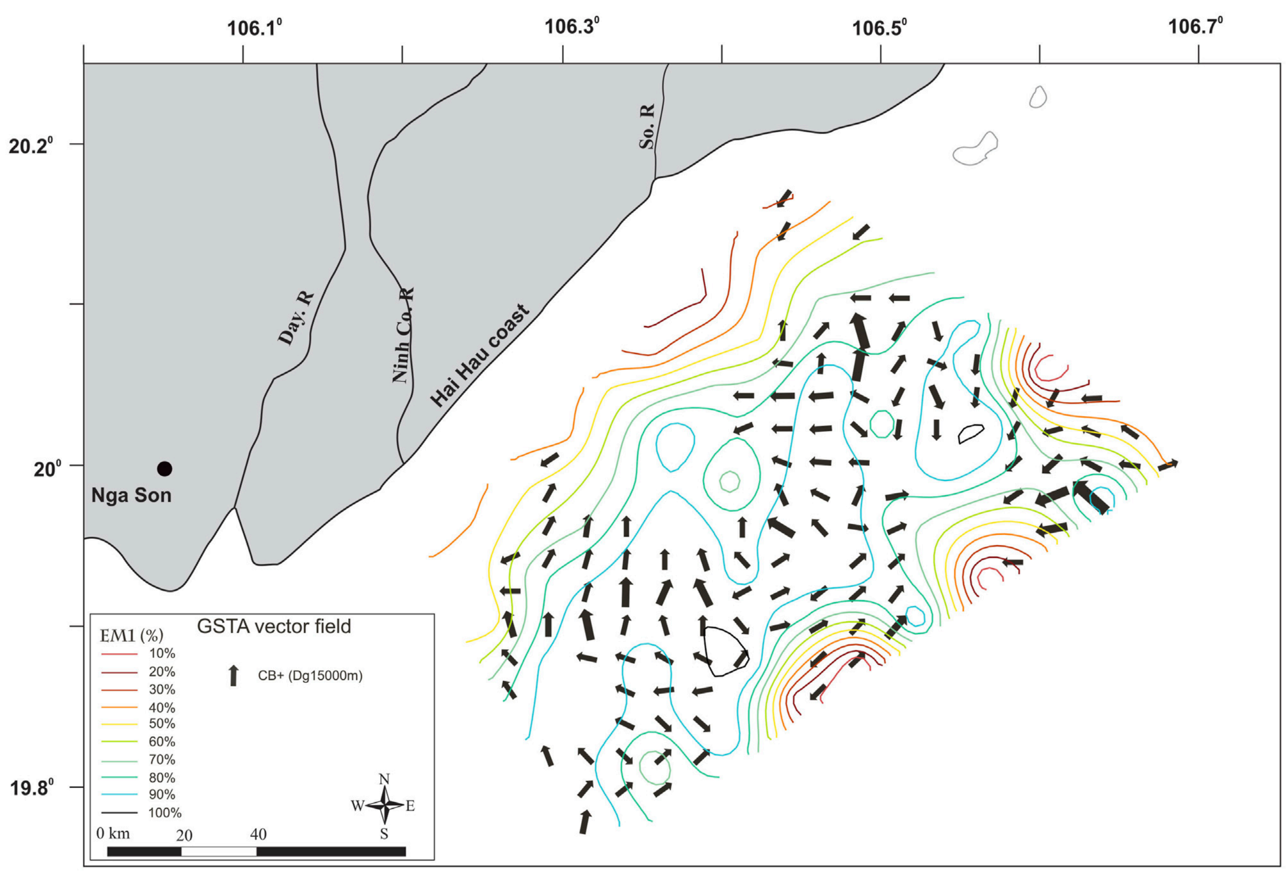

FIGURE 8
Contour lines of EM1 percentage with interpretation of the CB+ vector field.

EM3 fraction (very coarse silt) occurs in the outer area of the So River mouth, being transported from the So River. Sediment represented by EM4+5, due to its size and location (below 28 m), is likely deposited under the influence of the most energetic events of annual recurrence. Its source is tentatively assigned to the Ba Lat mouth, and it accumulates in deeper water environments or is transported from neighboring offshore areas under the influence of bottom currents.

Results of predictions of the general sediment trend from GSTA (Figure 9) in relation to the depth background have documented three distinct zones: in zone 1 (0–15 m water depth), sediment is transported from the shore to the offshore area; in zone 2 (>25 m water depth), sediment is transported from the northeast and from the offshore area; and zone 3 (15–25 m water depth) is a mixed zone in which sediment is transported from the north to the southeast and from the two previous zones. Sediments in this latter zone have no apparent clear trend. It is possible that they are subject to the mixed influence of river–sea interactions, where the impact of the sea is greater (Khac Nghia et al., 2013), causing constant disturbance, which gives the sediments collected in the area poor selectivity of 88.9%.

Representation of prediction results of sediment transport trends from GSTA in relation to mud sediments (EM1+2+3) shows that the higher the mud content, the more complex the direction of sediment transport (Figure 9).

The combination of EMMA and GSTA methods leads to the following three observations. First, sediment transport is closely related to fine-grained end members (EM1+2+3). Second, sediments in the Hai Hau–Nam Dinh offshore region are provided by three main sources, including erosion along the Hai Hau coast, sediment from the Ba Lat River mouth, and deep water environments outside the study area. Sediment transport is dominated by the river–sea interaction, which is evident in the center of the study area. Sediment destruction along the Hai Hau coast is due to the erosion mentioned in recent studies and a lack of natural sediment supply due to damming of the So River (Tranet al., 2018). Third, sediments along the Hai Hau coast are eroded and carried to the sea; most of the fine-grained fraction (EM1+2+3) is transported away from the coast and deposited in the center of the study area under the influence of various dynamic processes. The fine-grained component in the center of the study area may also derive from the Ba Lat River mouth; a part of the sand sediment (EM4+5) from the Ba Lat River mouth is also transported down but accumulates in deeper water environments (over 28 m).

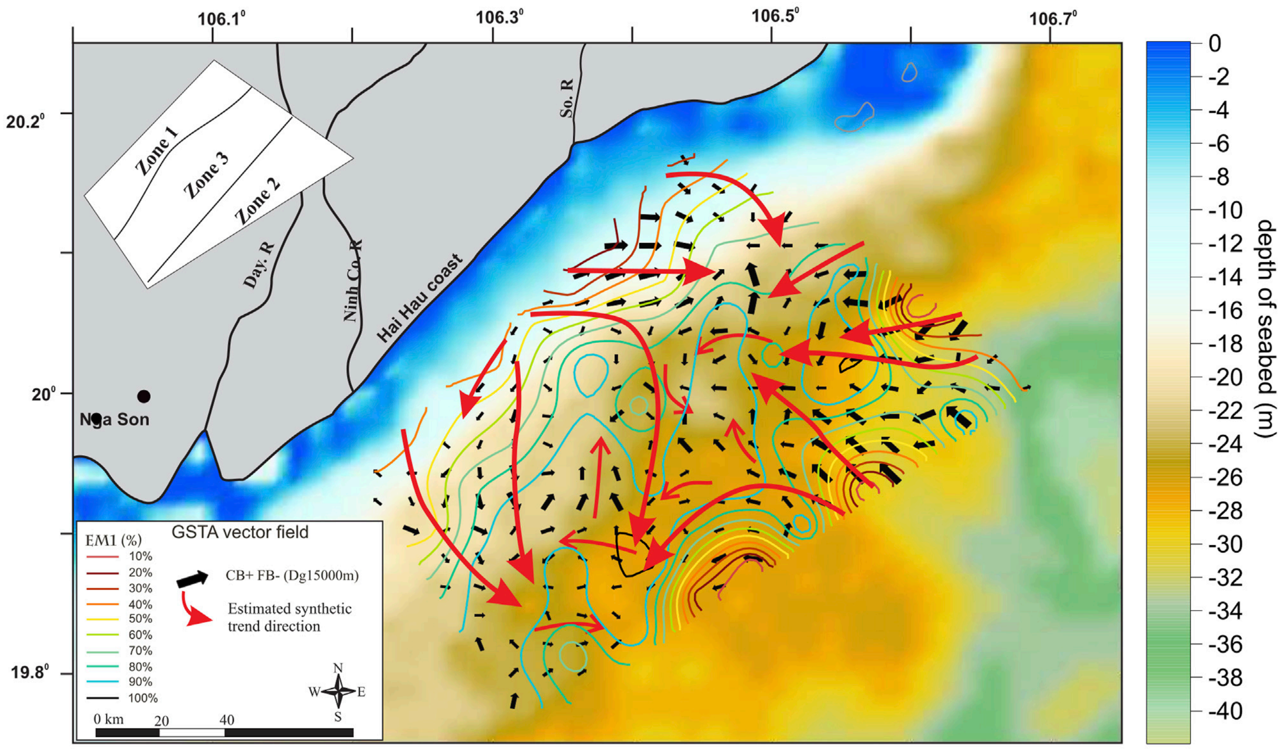

FIGURE 9
Spatial distribution of vectors and trends of general sediment transport, background of Gebco seabed depth, and contour line showing the relative content of EM1(%).

Conclusion

Five grain size end members (EM1–EM5) have been identified by the EMMAgeo model. EM1 (fine silt) is possibly originated from sediments eroded in the Hai Hau shore or delivered from the north (Ba Lat River mouth area). The source of EM2 (coarse silt) may be the coast of Hai Hau (for the nearshore-distributed part) and the offshore area (for the locally distributed part). EM3 (very coarse silt) is likely derived from the So River area. EM4+5 (fine-medium sand) is interpreted to have been transported from the Ba Lat River mouth and locally deposited at relatively deep locations.

The combination approach using EMMAgeo and GSTA predicted the transport mechanism of sediments at sampling sites. Sediments in the study area are supplied by three main sources, including erosion along the Hai Hau coast, sediment from the Ba Lat River mouth, and deeper water environments outside the study area. Continuous river–sea interaction is evident in the center of the study area. Sediments along the Hai Hau coast are eroded and carried to the sea; most of the fine-grained sediments (EM1+2+3) are transported away from the shore and deposited in the center of the study area under the influence of various dynamic processes. In addition, the fine-grained components in the center can also derive from the Ba Lat River mouth. A part of the sand sediment (EM4+5) from the Ba Lat River mouth is also transported in deep water areas (below 28 m water depth).

The combination of EMMA and GSTA proved a reliable picture of sediment transport in coastal areas. These two methods are based on same and simple information to get granulometric data. EMMA alone gives footprints of characteristic grain-size distributions, which then help GSTA to better identify the best trend case to compute the transport vector field. Because these two approaches are based on field data sets, the results of their application can be used by hydro-sedimentary numerical models to set and validate sediment transport.

Data availability statement

The original contributions presented in the study are included in the article/Supplementary Material, and further inquiries can be directed to the corresponding author.

Author contributions

NV, NH, and TT processed sediment samples, analyzed the grain sizes and the results from the Horiba LA960 device. MD and LA conducted data processing and used and presented EMMA model results. EP, MD, and TT processed, used, and analyzed GSTA model data and outlined the idea of model results. DH and DC reviewed the results of two models and considered the correlation with the collected documents.

Funding

The paper is supported by the projects coded UQĐTCB.03/20-21, ĐTĐLCN.59/22-C, and NVCC24.03/22-23.

Conflict of interest

The authors declare that the research was conducted in the absence of any commercial or financial relationships that could be construed as a potential conflict of interest.

Publisher's note

Supplementary material

The Supplementary Material for this article can be found online at: https://www.frontiersin.org/articles/10.3389/feart.2023.1099730/full#supplementary-material

References

Alexander, C. R., DeMaster, D. J., and Nittrouer, C. A. (1991). Sediment accumulation in a modern epicontinental-shelf setting: The Yellow Sea. *Mar. Geol.* 98, 51–72. doi:10.1016/0025-3227(91)90035-3

Asselman, N. E. M. (1999). Grain size trends used to assess the effective discharge for floodplain sedimentation, river Waal, The Netherlands. *J. Sediment. Res.* 69, 51–61. doi:10.2110/jsr.69.51

Blott, S. J., and Pye, K. (2001). Gradistat: A grain size distribution and statistics package for the analysis of unconsolidated sediments. *Earth Surf. Process Landf.* 26, 1237–1248. doi:10.1002/esp.261

Carriquiry, J., Sánchez, A., and Camacho-Ibar, V. (2001). Sedimentation in the northern Gulf of California after cessation of the Colorado River discharge. *Sediment. Geol.* 144, 37–62. doi:10.1016/s0037-0738(01)00134-8

Collins, J. D., O'Grady, P., Langford, R. P., and Gill, T. E. (2016). End-member mixing analysis (EMMA) apllied to sediment grainsize distributions to characterize formational processes of the main excavation block, unit 2, of the rimrock draw rockshelter (35ha3855), harney basin, eastern Oregon (USA). *Archaeometry* 59, 331–345. doi:10.1111/arcm.12243

Dietze, E., and Dietzel, M. (2019). Grain-size distribution unmixing using the R package EMMAgeo. *E&G Quat. Sci. J.* 68, 29–46. doi:10.5194/egqsj-68-29-2019

Dietze, E., Hartmann, K., Diekmann, B., Ijmker, J., Lehmkuhl, F., Opitz, S., et al. (2012). An end-member algorithm for deciphering modern detrital processes from lake sediments of lake Donggi Cona, NE Tibetan plateau, China. *Sediment. Geol.* 243-244, 169–180. doi:10.1016/j.sedgeo.2011.09.014

Duc, D. M., Nhuan, M. T., Tran, N., Tien, D. M., van Weering, T. C. E., and van den Bergh, G. D. (2007). Sediment distribution and transport at the nearshore zone of the Red River delta, Northern Vietnam. *J. Asian Earth Sci.* 29, 558–565. doi:10.1016/j.jseaes.2006.03.007

Duc, D. M., Thanh, D. X., Quynh, D. T., and McLaren, P. (2016). Analysis of sediment distribution and transport for mitigation of sand deposition hazard in Tam Quan estuary, Vietnam. *Vietnam. Environ. Earth Sci.* 75, 741. doi:10.1007/s12665-016-5560-2

Duc, D. M., Nghi, T., Nhuan, M. T., and Tien, D. M. (2003). Net sediment transport pathways inferred from grain-size analysis. *Vietnam J. Geol.* 276 5–6. Available at: http://www.idm.gov.vn/Data/TapChi/2003/276/t46.htm. Available at: http://www.idm.gov.vn/Data/TapChi/2003/276/t54.htm.

Duong Ngoc Tien (2012). Analysis of the sediment transport trend and changes of shoreline and bottom of the Day rivermouth using Mike model. Msc thesis of oceanography. Vietnamese: Hanoi University of Science.

Flemming, B. W. (1988). "Process and pattern of sediment mixing in a microtidal coastal lagoon along the west coast of South Africa," in *Tide-influenced sedimentary environments and facies*. Editors P. L. de Boer, A. van Gelder, and S. D. Nio (Dordrecht: Reidel), 275–288.

Flemming, B. W. (2007). The influence of grain-size analysis methods and sediment mixing on curve shapes and textural parameters: Implications for sediment trend analysis. *Sediment. Geol.* 202, 425–435, doi:10.1016/j.sedgeo.2007.03.018

Folk, R. L., and Ward, W. C. (1957). Brazos River bar: a study in the significance of grain size parameters. *J. Sediment. Petrol.* 27, 3–26.

Gao, S., Collins, M. B., Lanckneus, J., Moor, G. D., and Lancker, V. V. (1994). Grain size trends associated with net sediment transport patterns: An example from the Belgian continental shelf. *Mar. Geol.* 121, 171–185. doi:10.1016/0025-3227(94)90029-9

Gao, S., and Collins, M. (1992). Net sediment transport patterns inferred from grain-size trends, based upon definition of "transport vectors. *Sediment. Geol.* 80, 47–60.

Hoan, L. X., Hanson, H., Larson, M., Donnelly, C., and Nam, P. T. (2009). Modeling shoreline evolution at Hai Hau beach, Vietnam. *J. Coast. Res.* 25 (0), 000. doi:10.2112/08-1061.1

Huang, H. Q. (2010). Reformulation of the bed load equation of Meyer-Peter and Müller in light of the linearity theory for alluvial channel flow. *Water Resour. Res.* 46, W09533. doi:10.1029/2009WR008974

Hughes, S. A. (2005). *Use of sediment trend analysis (STA) for coastal projects ERDC/CHL chetn-VI-40*. Vicksburg, MS: US Army Corps of Engineers, 17.

Huu, V. C., Hoan, L. X., and Son, N. M. (2012). Calculation of waves and sediment transport in the nearshore Hai Hau - Nam Dinh. *J. Water Resour. Sci. Technol.* 2012, 7. Available at: https://www.vawr.org.vn/tinh-toan-song-va-van-chuyen-bun-cat-tai-vung-bien-ven-bo-hai-hau-nam-dinh.

Jia, J., Gao, S., and Xue, Y. (2003). Sediment dynamic processes of the Yuehu inlet system, Shandong peninsula, China. *Estuar. Coast Shelf Sci.* 57, 783–801. doi:10.1016/s0272-7714(02)00406-7

Khac Nghia, N., Dan, M. A., and Tuan, N. A. (2013). Evolution of Lach Giang estuary through analysis of historical documents, satellite images and political orientation to stabilize the coast. *J. Water Resour. Sci. Technol.* 2013, 16. Available at: https://www.vawr.org.vn/images/File/PGS.TS.%20Nguyen%20Khac%20Nghia.pdf.

Le Roux, J. P. (1994). Net sediment transport patterns inferred from grain-size trends, based upon definition of "transport vectors" - comment. *Sediment. Geol.* 90, 153–156. doi:10.1016/0037-0738(94)90022-1

Le Roux, J., and Rojas, E. (2007). Sediment transport patterns determined from grain size parameters: Overview and state of the art. *Sediment. Geol.* 202, 473–488. doi:10.1016/j.sedgeo.2007.03.014

Li, T., and Li, T. J. (2018). Sediment transport processes in the Pearl River Estuary as revealed by grain-size end-member modeling and sediment trend analysis. *Geo-Mar Lett.* 38, 167–178. doi:10.1007/s00367-017-0518-2

López-González, N., Alonso, B., Juan, C., Ercilla, G., Bozzano, G., Cacho, I., et al. (2019). 133,000 Years of sedimentary record in a contourite drift in the western alboran sea: Sediment sources and paleocurrent reconstruction. *Geosciences* 9 (8), 345. doi:10.3390/geosciences9080345

Masselink, G. (1992). Longshore variation of grain size distributions along the coast of the Rhone Delta, *South. France a test "Mc Laren Model." J. Coast. Res.* 8, 286–291.

Mather, S. J., Davies, J., Mc Donal, A., Zalasiewicz, J. A., and Marsh, S. (1996). The red River Delta of Vietnam. British Geological Survey Tecchnical Report WC/96/02, 41p.

Mathers, S., and Zalasiewicz, J. (1999). Holocene sedimentary architecture of the red River delta, Vietnam. *J. Coast. Res.* 15, 314–325.

McLaren, P., and Beveridge, P. (2006). Sediment trend analysis of the hylebos waterway: Implications for liability allocations. *Integr. Environ. Assess. Manag.* 2 (3), 262–272. doi:10.1002/ieam.5630020306

McLaren, P., and Bowles, D. (1985). The effects of sediment transport on grain-size distributions. *J. Sediment Pet.* 4:457–470.

McLaren, P., Hill, S. H., and Bowles, D. (2007). Deriving transport pathways in a sediment trend analysis (STA). *Sediment. Geol.* 202, 489–498. doi:10.1016/j.sedgeo.2007.03.011

McLaren, P. (1981). An interpretation of trends in grain size measures. *J. Sediment. Pet.* 51, 611–624.

Nghi, T., Nhan, T. T. T., Dien, T. N., Thanh, D. X., Dung, T. T., Thao, N. T. P., Truong, T. X., Tuan, D. M., and Lam, D. D. (2018). The Holocene – present shorelinemigration off Thai binh – NamDinh in relation to evolution of deltaic lobes and history of the So River. *VNU J. Sci. Earth Environ. Sci.* 34 (4), 2588–1094. Available at: https://js.vnu.edu.vn/EES/article/view/4346.

O'Shea, M., and Murphy, J. (2016). The validation of a new GSTA case in a dynamic coastal environment using morphodynamic modelling and bathymetric monitoring. *J. Mar. Sci. Eng.* 4, 27. doi:10.3390/jmse4010027

Ostrowski, R., Pruszak, Z., Różyński, G., Szmytkiewicz, M., and Van Ninh, P. (2009). Coastal processes at selected shore segments of south BalticSea and gulf of tonkin (south China sea). *Archives Hydro-Engineering Environ. Mech.* 56 (1–2), 3–28. Available at: http://www.ibwpan.gda.pl/storage/app/media/ahem/ahem56str003.pdf.

Paladino, Í. M., Mengatto, M. F., Mahiques, M. M., Noernberg, M. A., and Nagai, R. H. (2022). End-member modeling and sediment trend analysis as tools for sedimentary processes inference in a subtropical estuary. *Estuar. Coast. Shelf Sci.* 278, 108126. doi:10.1016/j.ecss.2022.108126

Paterson, G. A., and Heslop, D. (2015). New methods for unmixing sediment grain size data. *Geochem. Geophys. Geosyst.* 16, 4494–4506. doi:10.1002/2015GC006070

Pedreros, R., Howa, H. L., and Michel, D. (1996). Application of grain size trend analysis for the determination of sediment transport pathways in intertidal areas. *Mar. Geol.* 135, 35–49. doi:10.1016/s0025-3227(96)00042-4

Poizot, E., Méar, Y., and Biscara, L. (2008). Sediment trend analysis through the variation of granulometric parameters: A review of theories and applications. *Earth Sci. Rev.* 86, 15–41. doi:10.1016/j.earscirev.2007.07.004

Poizot, E., Mear, Y., Thomas, M., and Garnaud, S. (2006). The application of geostatistics in defining the characteristic distance for grain size trend analysis. *Comput. Geosci.* 32, 360–370. doi:10.1016/j.cageo.2005.06.023

Poizot, E., and Méar, Y. (2010). Using a GIS to enhance grain size trend analysis. *Environ. Model. Softw.* 25, 513–525. doi:10.1016/j.envsoft.2009.10.002

Prins, M. A., Bouwer, L. M., Beets, C. J., Troelstra, S. R., Weltje, G. J., Kruk, R. W., et al. (2002). ocean circulation and iceberg discharge in the glacial north atlantic: Inferences from unmixing of sediment size distributions. *Geology* 30, 555–558. doi:10.1130/0091-7613(2002)030<0555:ocaidi>2.0.co;2

Pruszak, Z., Szmytkiewicz, M., NguyenHung, M., and Pham Van Ninh (2002). Coastal processes in the red river delta area, Viet Nam. *Coast. Eng. J.* 44 (2), 97–126. doi:10.1142/s0578563402000469

Ríos, F., Cisternas, M., Le Roux, J., and Corréa, I. (2002). Seasonal sediment transport pathways in Lirquen Harbor, Chile, as inferred from grain-size trends. *Investe. Mar. Valpso.* 30 (1), 3–23. doi:10.4067/s0717-71782002000100001

Shore Protection Manual (1984). *Coastal engineering research center*. Vicksburg, Mississippi: US Army Corps of Engineers.

van Lancker, V., Lanckneus, J., Hearn, S., Hoekstra, P., Levoy, F., Miles, J., et al. (2004). Coastal and nearshore morphology, bedforms and sediment transport pathways at Teignmouth (UK). *Cont. Shelf Res.* 24, 1171–1202. doi:10.1016/j.csr.2004.03.003

Weltje, G. J., and Prins, M. A. (2007). Genetically meaningful decomposition of grain-size distributions. *Sed. Geol.* 202, 409–424. doi:10.1016/j.sedgeo.2007.03.007

Weltje, G. J., and Prins, M. A. (2003). Muddled or mixed? Inferring palaeoclimate from size distributions of deep-sea clastics. *Sediment. Geol.* 162, 39–62. doi:10.1016/s0037-0738(03)00235-5

Weltje, G. J. (1997). End-member modeling of compositional data: Numerical-statistical algorithms for solving the explicit mixing problem. *Math. Geol.* 29, 503–549. doi:10.1007/bf02775085

Frontiers in Earth Science

TYPE Original Research
PUBLISHED 31 March 2023
DOI 10.3389/feart.2023.1117132

OPEN ACCESS

EDITED BY
Jian Liu,
Qingdao Institute of Marine Geology (QIMG), China

REVIEWED BY
Maosheng Gao,
Qingdao Institute of Marine Geology (QIMG), China
Tianyuan Zheng,
Ocean University of China, China

*CORRESPONDENCE
Guanghui Zhan,
✉ zhangh2007@126.com

SPECIALTY SECTION
This article was submitted to Quaternary Science, Geomorphology and Paleoenvironment,
a section of the journal
Frontiers in Earth Science

RECEIVED 06 December 2022
ACCEPTED 13 March 2023
PUBLISHED 31 March 2023

CITATION
Zhan G, Li J, Wang H, Wen X and Gu H (2023), Origin and hydrochemical evolution of confined groundwater in Shanghai, China.
Front. Earth Sci. 11:1117132.
doi: 10.3389/feart.2023.1117132

Origin and hydrochemical evolution of confined groundwater in Shanghai, China

Guanghui Zhan[1,2]*, Jingzhu Li[1,2], Hanmei Wang[1,2], Xiaohua Wen[1,2] and Hua Gu[1,2]

[1]Shanghai Institute of Geological Survey, Shanghai, China, [2]Key Laboratory of Land Subsidence Monitoring and Prevention, MNR, Shanghai, China

Confined groundwater is an indispensable resource for the urban security of Shanghai, China, where multi-layer aquifer structures and human activities create a complex groundwater environment. An understanding of the hydrochemical characteristics and evolutionary mechanisms of groundwater is necessary for its protection and effective utilization and will be explored in this study. A total of 87 groundwater samples were collected from five confined aquifers. Hydrochemistry analysis methods such as Durov diagram, Gibbs model and Saturation index were used to determine the origin and hydrochemical evolution of the confined groundwater. The results show that the samples have two different origins, marine–continental and continental, which have different hydrochemical characteristics. Cl^- content of 7.5 meq L^{-1} was used as a demarcation index for the two origins. The groundwater with a marine–continental-origin is dominated by ancient seawater from which Na^+ and Cl^- are derived, whereas Ca^{2+}, Mg^{2+}, and HCO_3^- are derived mainly from carbonate dissolution. Groundwater with a continental-origin is dominated by the effects of water–rock interaction, where major ions are derived mainly from silicate weathering and carbonate dissolution. In both types of groundwater, SO_4^{2-} is mainly derived from insoluble sulfides that are present in low quantities, whereas SO_4^{2-} in the few samples with high insoluble sulfide content is derived from human activities. Cation exchange is another controlling factor regarding the hydrochemical composition of groundwater, and water from the two origins have different reaction modes as follows: reverse cation exchange is dominant in marine–continental groundwater, whereas positive cation exchange is more common in continental groundwater. Over the past century, saline water has been flowing into the groundwater funnel region due to human activities, which has resulted in changes in the hydrochemical composition. The recent influx of fresh groundwater and artificial recharge has caused groundwater salinization and mineral re-dissolution.

KEYWORDS

hydrochemistry, groundwater origin, Shanghai, water–rock interaction, ion source

1 Introduction

Confined groundwater is an important high-quality water resource for domestic and industrial purposes (Zhang et al., 2016), but its over-use causes serious problems. Globally, changes in the hydrochemical composition of groundwater threatens resources in many regions, especially in economically developed delta areas (Gan et al., 2018; Wang et al., 2022).

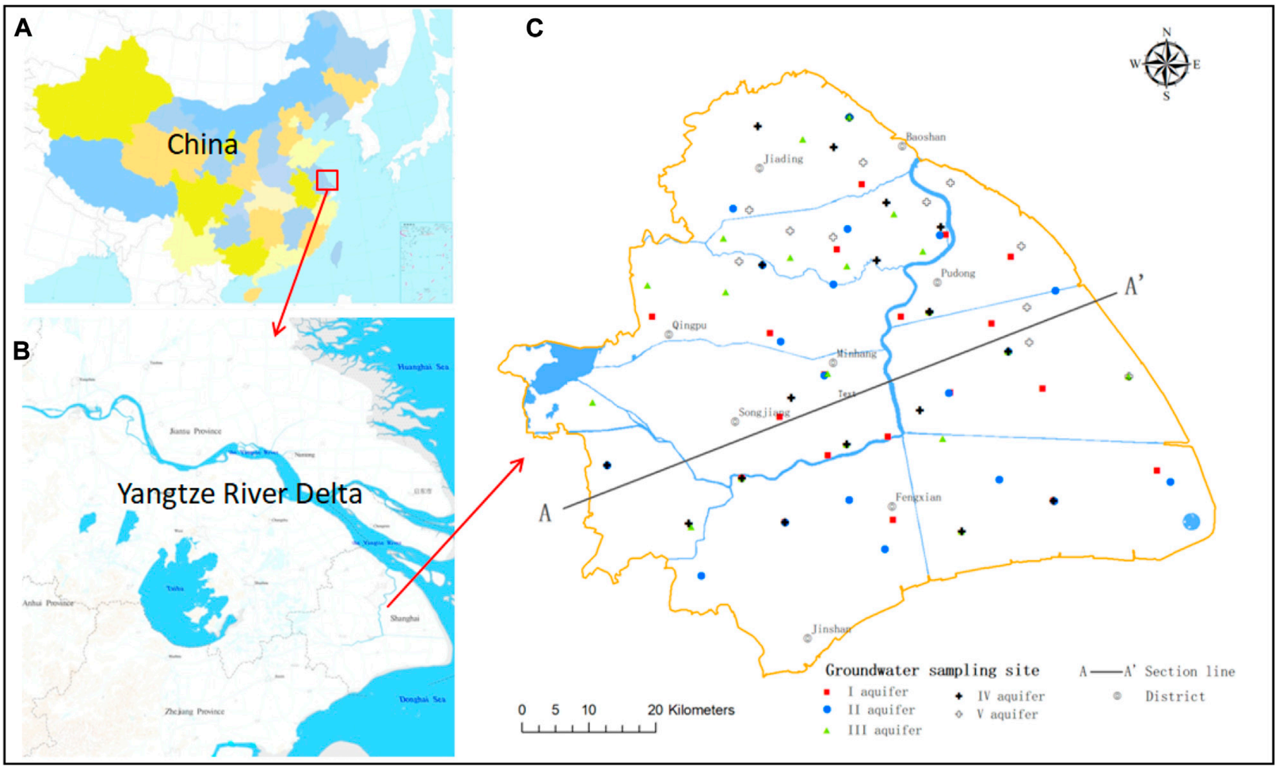

FIGURE 1
Map of the study area showing groundwater sampling points. **(A)** Map of China. **(B)** Map of the Yangtze River Delta. **(C)** Map of Shanghai.

Therefore, an understanding of the hydrochemical origins and controlling factors of groundwater is necessary for its development and protection.

The five confined aquifers in the Shanghai study area developed in an unconsolidated alluvial formation deposited under alternating marine and continental sedimentary environments. There is a weak hydraulic connection between the five aquifers, except where the aquifers are physically connected. Large quantities of high-quality groundwater are confined in Shanghai (Zhang et al., 1999), which has provided an enormous contribution to economic development over recent decades (Jang et al., 2012). However, over-exploitation and artificial recharge have greatly affected the groundwater environment, and its hydrochemical composition has considerably changed in some regions. Increasing attention had been focused on fluctuations in groundwater levels because of the serious land subsidence caused by groundwater exploitation (Huang et al., 2021; Li et al., 2021), but there have been few reports on the hydrochemical characteristics and evolutionary mechanisms of groundwater, and the use and protection of groundwater has received little attention. The origins of groundwater, hydrochemical characteristics, and its classification should be considered in detail to delineate groundwater boundaries and predict saline expansion/contraction (Yang et al., 2018; Li et al., 2022). The Yangtze River Delta is an ideal location to conduct such a study.

The aim of this study was to apply hydrochemical methods in (1) describing groundwater hydrochemical characteristics, 2) identifying sources of groundwater and establishing their demarcation index, 3) identifying the sources of major ions in groundwater, 4) explaining the hydrochemical evolution of the water of different origins, and 5) elucidating the influence of human activities on groundwater. As a result, these methods provide a scientific basis for groundwater utilization and protection planning.

2 Materials and methods

2.1 Study area

The study area is the mainland part of Shanghai in the flat alluvial plain of the Yangtze River Delta at the mouth of the Changjiang River with an area of 5,300 km^2 within 120°52′–122°12′E and 30°40′–31°53′N (Figure 1). Quaternary deposits are widely distributed in the area with a thickness of 250–350 m increasing W–E. The aquifers are comprised mainly sand and clay in loose Quaternary sediments and include aphreatic aquifers and five confined aquifers (Figure 2). This study focused on the latter.

Aquifers I–V were formed during the early to middle–late Pleistocene and their characteristics are shown in Table 1.

The groundwater system in the study area is not a stand-alone system and is part of the Yangtze River Delta system, where confined aquifers are the predominant type. In its natural state, groundwater

FIGURE 2
Cross-section showing hydrological conditions along the **(A,A′)** transect.

TABLE 1 Characteristics of aquifers in the study area.

Aquifer	I	II	III	IV	V
Depositional age	Q_3^2	Q_3^1	Q_2^2	Q_1^2	Q_1^1
Depositional environment	Coastal-fluvial	Coastal-fluvial	Coastal-fluvial	Fluvial	Fluvial
Lithology	Fine sand	Medium sand	Medium sand and coarse sand	Medium sand, coarse sand	Medium sand and gravel
Depth (m)	30–40	60–70	110–120	130–180	250–280
Thickness (m)	3–18	20–30	20–30	60–80	10–40
Water yield of a single well (m^3/d)	300–500	1,000–3000	1,000–3000	3000–5,000	1,000–3000

flows mainly NW–SE. In general, the groundwater is characterized by weak hydrodynamic conditions and a low flow rate. Recharge is mainly through lateral inflow, although artificial recharge has become an important source in recent decades, and discharge is mainly from anthropogenic extraction.

2.2 Sampling and analysis

For sampling, 87 wells were selected to provide a balanced regional distribution. Groundwater samples were collected in September 2018, and 19, 19, 19, 17, and 13 samples were collected from aquifers I–V, respectively (Figure 1).

Prior to filling, all sample bottles were rinsed three times with sample water. Samples for the cation analysis were collected in 500-mL HDPE bottles and then five drops of concentrated nitric acid were added; those for anion analysis were collected in 1000-mL glass bottles without preservatives. All samples were stored on ice in the field and transferred to 4°C storage until ready for analysis.

The concentrations of Na^+, K^+, Ca^{2+}, Mg^{2+}, Cl^-, and SO_4^{2-} were determined by ion chromatography, HCO_3^- was determined by acid–base titration, and total dissolved solid (TDS) concentrations were determined using gravimetric analysis (drying at 105 °C). The analysis accuracy was assessed through the ion-balance error of ±5%.

2.3 Durov diagram

The Durov diagram, which is used to study hydrochemical characteristics and facies (An et al., 2014; Gu et al., 2018), comprises two triangles, a central square, and two rectangles (Figure 5). The left and top triangles indicate the concentrations of cations and anions, respectively, the centrals square shows hydrochemical facies, and the right and bottom rectangles indicate TDS concentration and pH, respectively.

TABLE 2 Analysis results for confined groundwater samples.

Aquifer	Index	Unit	Min	Max	Mean	SD
I	pH	-	6.99	8.36	7.49	0.36
	K$^+$	mg/l	1.61	38.25	12.18	11.50
	Na$^+$	mg/l	154.64	2206.16	1,119.16	594.68
	Ca^{2+}	mg/l	62.20	958.43	334.36	220.97
	Mg^{2+}	mg/l	69.19	422.94	186.31	85.32
	HCO$_3^-$	mg/l	31.49	1,280.86	448.62	296.23
	CL$^-$	mg/l	550.24	5,942.06	2644.55	1,376.07
	SO$_4^{2-}$	mg/l	0.20	13.53	4.23	4.06
	TDS	mg/l	1,306	9690	4562	2206
II	pH	-	7.06	8.36	7.52	0.32
	K$^+$	mg/l	1.10	64.01	12.11	13.71
	Na$^+$	mg/l	35.12	2676.06	866.57	867.31
	Ca^{2+}	mg/l	35.28	584.68	240.95	155.66
	Mg^{2+}	mg/l	20.97	302.81	140.95	98.70
	HCO$_3^-$	mg/l	15.74	648.77	294.55	153.86
	CL$^-$	mg/l	4.49	5,518.66	2031.00	1864.13
	SO$_4^{2-}$	mg/l	0.67	28.58	6.56	6.84
	TDS	mg/l	316	8846	3475	2869
III	pH	-	6.92	9.42	7.86	0.66
	K$^+$	mg/l	1.21	81.03	12.97	20.06
	Na$^+$	mg/l	32.10	4727.98	870.89	1,347.78
	Ca^{2+}	mg/l	3.97	789.17	167.15	238.51
	Mg^{2+}	mg/l	8.37	414.43	116.45	149.88
	HCO$_3^-$	mg/l	39.04	687.66	282.55	152.07
	CL$^-$	mg/l	3.83	9310.29	1781.92	2773.69
	SO$_4^{2-}$	mg/l	0.20	1,131.02	64.26	258.43
	TDS	mg/l	250	16,522	3176	4648
IV	pH	-	7.30	9.38	8.04	0.56
	K$^+$	mg/l	1.32	19.38	4.20	4.18
	Na$^+$	mg/l	65.67	2007.69	298.84	456.31
	Ca^{2+}	mg/l	4.22	262.67	54.01	68.98
	Mg^{2+}	mg/l	9.81	263.52	44.02	59.83
	HCO$_3^-$	mg/l	21.97	416.88	252.28	129.67
	CL$^-$	mg/l	6.32	4437.07	519.81	1,051.50
	SO$_4^{2-}$	mg/l	0.20	55.38	7.31	13.38
	TDS	mg/l	246	7010	1,084	1,593
V	pH	-	7.50	9.09	8.22	0.45
	K$^+$	mg/l	1.83	18.79	5.59	4.58
	Na$^+$	mg/l	105.18	628.03	283.28	160.89
	Ca^{2+}	mg/l	6.37	91.21	25.45	23.05
	Mg^{2+}	mg/l	17.01	80.93	38.15	20.88
	HCO$_3^-$	mg/l	78.72	499.37	240.87	124.96
	CL$^-$	mg/l	65.23	1,114.87	421.01	362.02
	SO$_4^{2-}$	mg/l	0.20	192.27	23.02	54.78
	TDS	mg/l	342	1974	940	526

(Continued in next column)

TABLE 2 (*Continued*) Analysis results for confined groundwater samples.

2.4 Gibbs model

The Gibbs model is effective in elucidating hydrochemical processes (Gibbs, 1970; Gibbs, 1972). This model is based on groundwater hydrochemical processes being mainly controlled by water–rock interaction, evaporation, and precipitation (Farid et al., 2015; Wang et al., 2022). For this study area, the hydrochemical processes were adjusted to include rock–water interaction, marine-origin, and recharge (including lateral inflow and artificial recharge).

2.5 Saturation index

The saturation index (SI) is used to describe the solubility equilibrium of minerals in water (Rezaei et al., 2005). SI = log(IPA/Ksp), where IPA is the ionic activity product of dissolved mineral constituents and Ksp is the solubility product of the mineral. SI values of 0, >0, and <0 indicate saturated, supersaturated (precipitation may occur), and undersaturated (dissolution may occur) groundwater, respectively.

3 Results and discussion

3.1 Hydrochemical characteristics of confined groundwater

The ionic contents of the studied samples are shown in Table 2. The hydrochemical characteristics of aquifers I and II were generally similar, as were those of aquifers IV and V. The ion contents of aquifer III were the most variable with high standard deviation (SD) values, which indicated that the spatial distribution of groundwater is somewhat variable in terms of hydrochemical composition.

The pH values of groundwater were in the range of 6.99–8.36, 7.06–8.36, 6.92–9.42, 7.30–9.38, and 7.50–9.09 for aquifers I–V, respectively. Aquifers I–III were neutral to slightly alkaline, and aquifers IV–V were slightly alkaline with the pH increasing from aquifers I to V.

TDS concentrations had a range of 246–16522 mg L^{-1} and decreased from aquifers I to V (Figure 3). All groundwater samples in aquifer I were saline water with TDS >5000 mg L^{-1} in the west. In aquifer II, 68.4% of the samples were saline, with most in the southwest

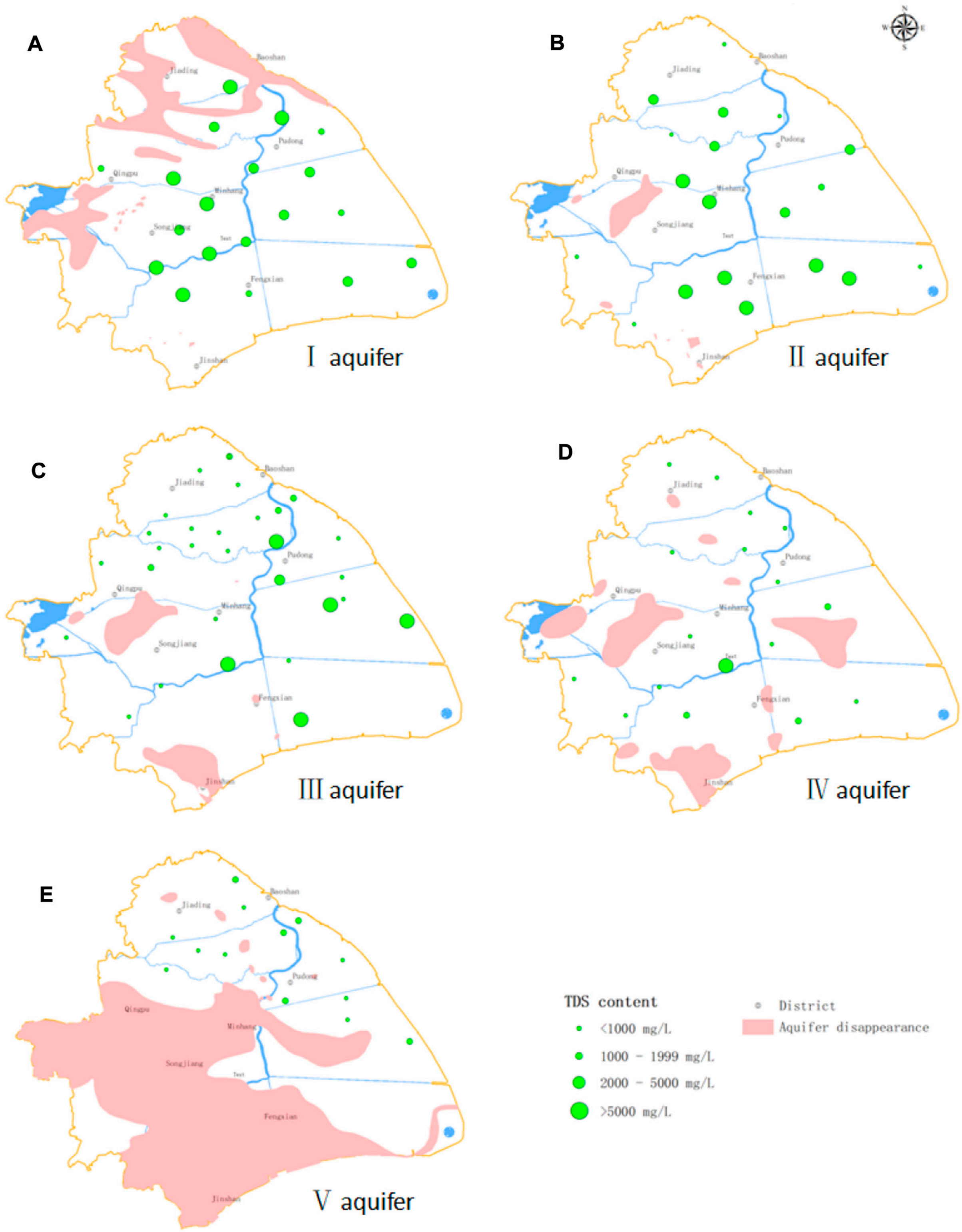

FIGURE 3
Spatial distribution of TDS in the study area. Dot sizes indicate TDS concentrations as follows: the larger the dot, the higher the TDS concentration. **(A)** TDS concentrations of all samples in aquifer I were >1000 mg L^{-1} and gradually increase from east to west; saline water was distributed throughout the aquifer. **(B)** In aquifer II, 68.4% of samples had TDS concentrations >1000 mg L^{-1}; saline water occupies most of the aquifer. **(C)** In aquifer III, groundwater TDS concentrations were markedly higher in the east than in the west. Additionally, saline water is mainly distributed in the eastern part of the aquifer, whereas fresh water is mainly distributed in the western part of the aquifer. **(D)** In aquifer IV, most samples have TDS concentrations <1000 mg L^{-1} with the exception of one sample from the area connecting aquifers III and IV that had TDS = 7010 mg L^{-1} and another from the same area in aquifer III that had TDS = 7654 mg L^{-1}. We infer that there is a close hydraulic connection between the groundwater of aquifers III and IV in this area. **(E)** The groundwater of aquifer V is mainly fresh water, but some brackish water with TDS of 1,000–2000 mg L^{-1} is also present.

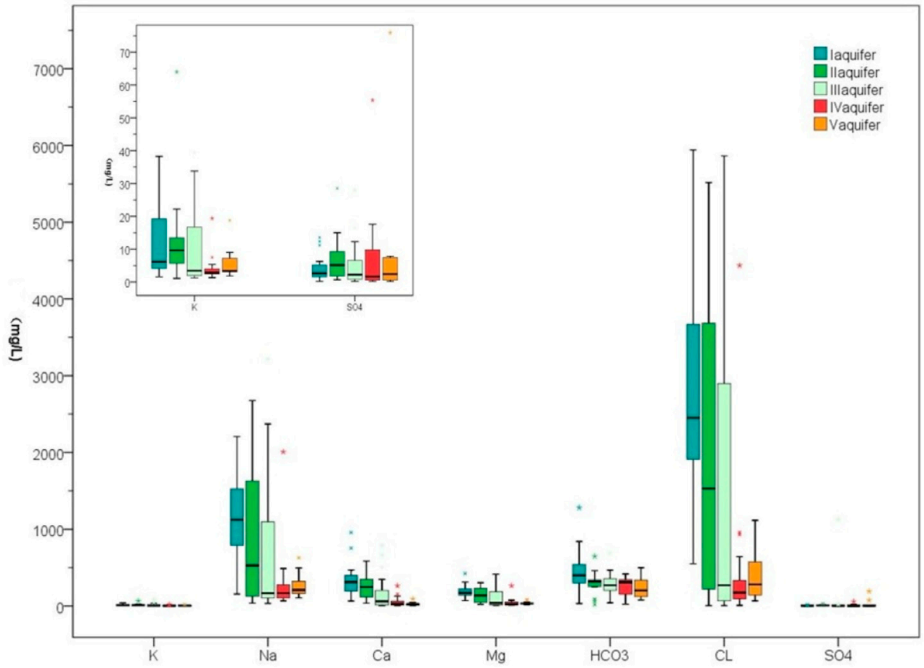

FIGURE 4
Ranges of major-ion concentrations in confined groundwater aquifers.

having TDS >5000 mg L^{-1}. There was a wide range of TDS concentrations in aquifer III, from 250 to 16522 mg L^{-1}, with fresh water predominating in the west and saline water in the east. In aquifers IV and V, most samples were fresh water. There were a few samples with TDS >2000 mg L^{-1} in the area connecting aquifers III and IV.

The range of concentrations of the major ions are shown in Figure 4. Na^+ was the dominant cation with an order of $Na^+ > Ca^{2+} > Mg^{2+} > K^+$. Of the anions, Cl^- had the highest concentrations with clear dominance among all major ions in aquifers I–III. The concentrations of K^+, Na^+, Ca^{2+}, Mg^{2+}, and Cl^- generally decreased from aquifers I to III but had similar concentrations in aquifers IV and V. Most samples had low $SO_4^{2-}$and HCO_3^-concentrations from all five aquifers (Table 2).

3.2 Hydrochemical facies of confined groundwater

The hydrochemical compositions and characteristics of the groundwater samples are indicated by the Durov diagram (Figure 5), where samples from aquifers I and II are concentrated on the Na^+ and Cl^- sides and those from aquifers III–V are scattered in the upper half of the central square. This indicates that the predominant hydrochemical facies of aquifers I and II are Cl–Na, whereas those of aquifers III–V are variable.

The hydrochemical facies of groundwater can also be described in terms of TDS as follows: for TDS of <1000 mg L^{-1}, hydrochemical facies were variable and included HCO_3·Cl–Na, Cl·HCO_3–Na, HCO_3·Cl–Na·Mg, and Cl·HCO_3–Na·Mg, which were mainly distributed in aquifers II–V. For a TDS of 1,000–2000 mg L^{-1}, the hydrochemical facies were Cl–Na, Cl–Na·Ca, and Cl–Na·Mg, and these are distributed mainly in aquifers I, IV, and V. For TDS of 2000–5000 mg L^{-1}, the hydrochemical facies were Cl–Na·Ca and Cl–Na, which were mainly distributed in aquifers I and II. For TDS >5000 mg L^{-1}, the hydrochemical facies were Cl–Na and distributed mainly in aquifers I–III.

3.3 Hydrochemical processes in confined groundwater

The Gibbs diagrams for all groundwater samples are shown in Figure 6. Most samples from aquifers I and II are plotted in the marine-origin domain, whereas those from aquifer III are plotted in both the marine-origin and rock–water-interaction domains, and those from aquifers IV and V are plotted in the rock–water-interaction domain. However, some samples from aquifers IV and V deviate from the Gibbs model (Figure 6A). Therefore, we speculate that other factors may affect the composition of groundwater, which makes Na^+ rich and Ca^{2+} poor. A similar pattern of evolution applies to aquifers I–III as discussed in the following section.

Quaternary strata studies (Qiu and Li., 2007) indicate that there were seven marine transgressions in Shanghai during the Quaternary period with aquifers I–III formed during transgression periods. The presence of groundwater of marine–continental- and continental-origin in the study area was verified. The distribution of the former may account for most of aquifers I and II, and the eastern portion of aquifer III. The latter applies to the remaining aquifers, including small portions of aquifers II and III and most of aquifers IV and V. Further evidence is provided in the following section based on an ion-ratio analysis.

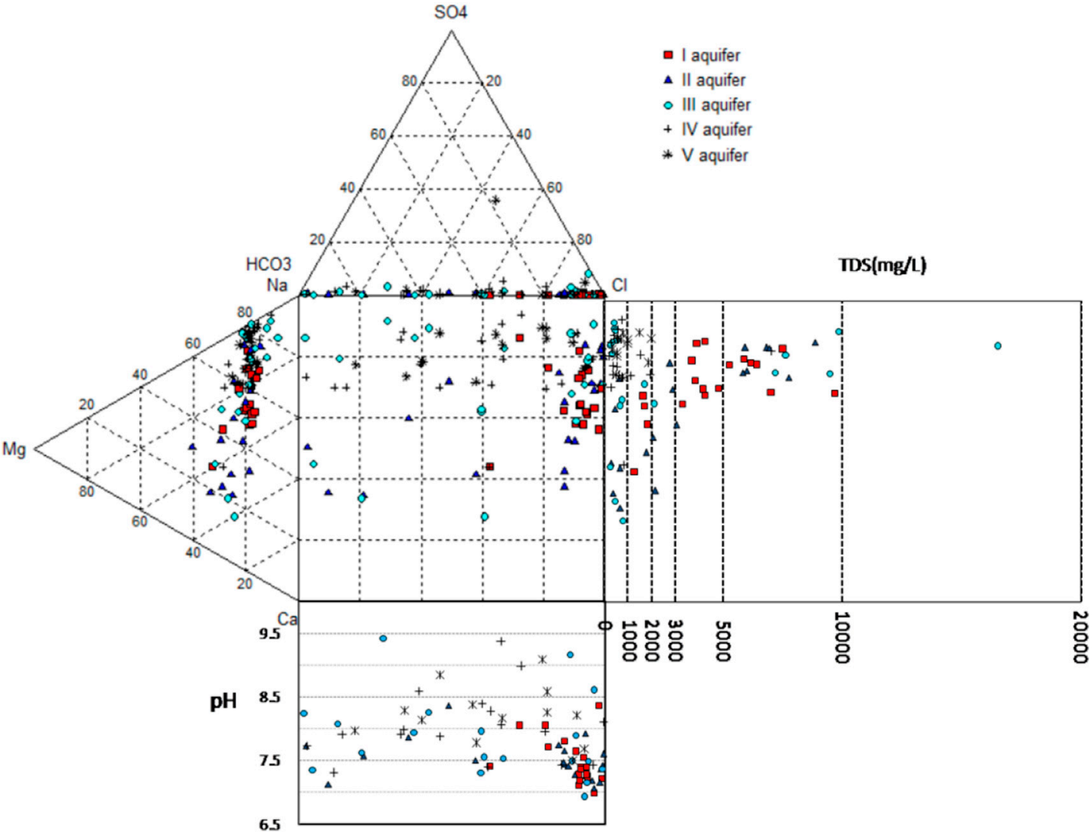

FIGURE 5
Durov diagram for confined groundwater samples.

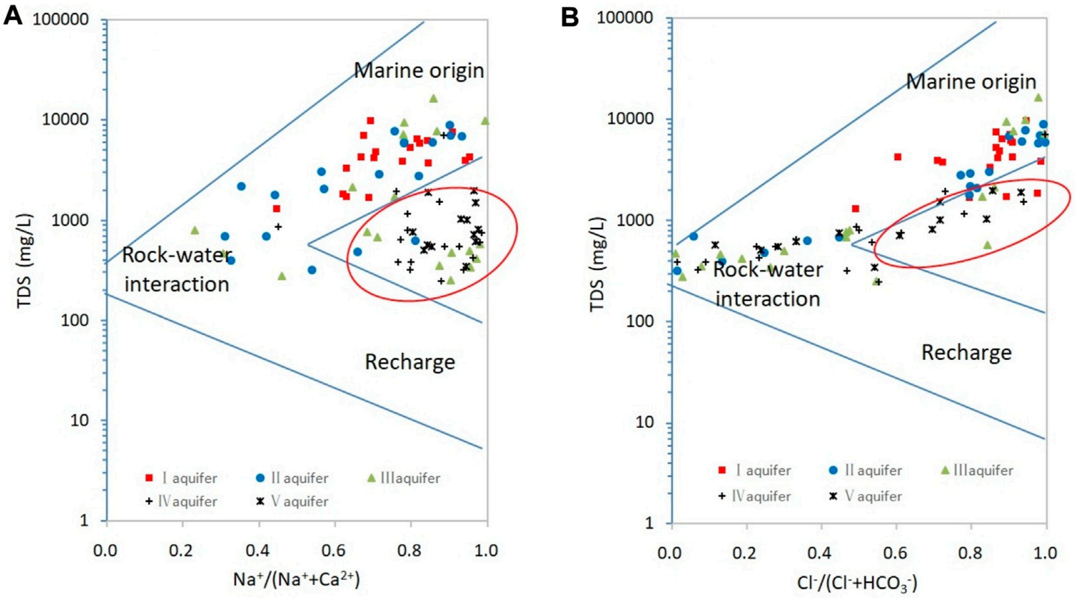

FIGURE 6
Gibbs diagrams for confined groundwater. The red circles indicate samples that deviate from the Gibbs model. **(A)** Gibbs diagrams of ions. **(B)** Gibbs diagrams of anions.

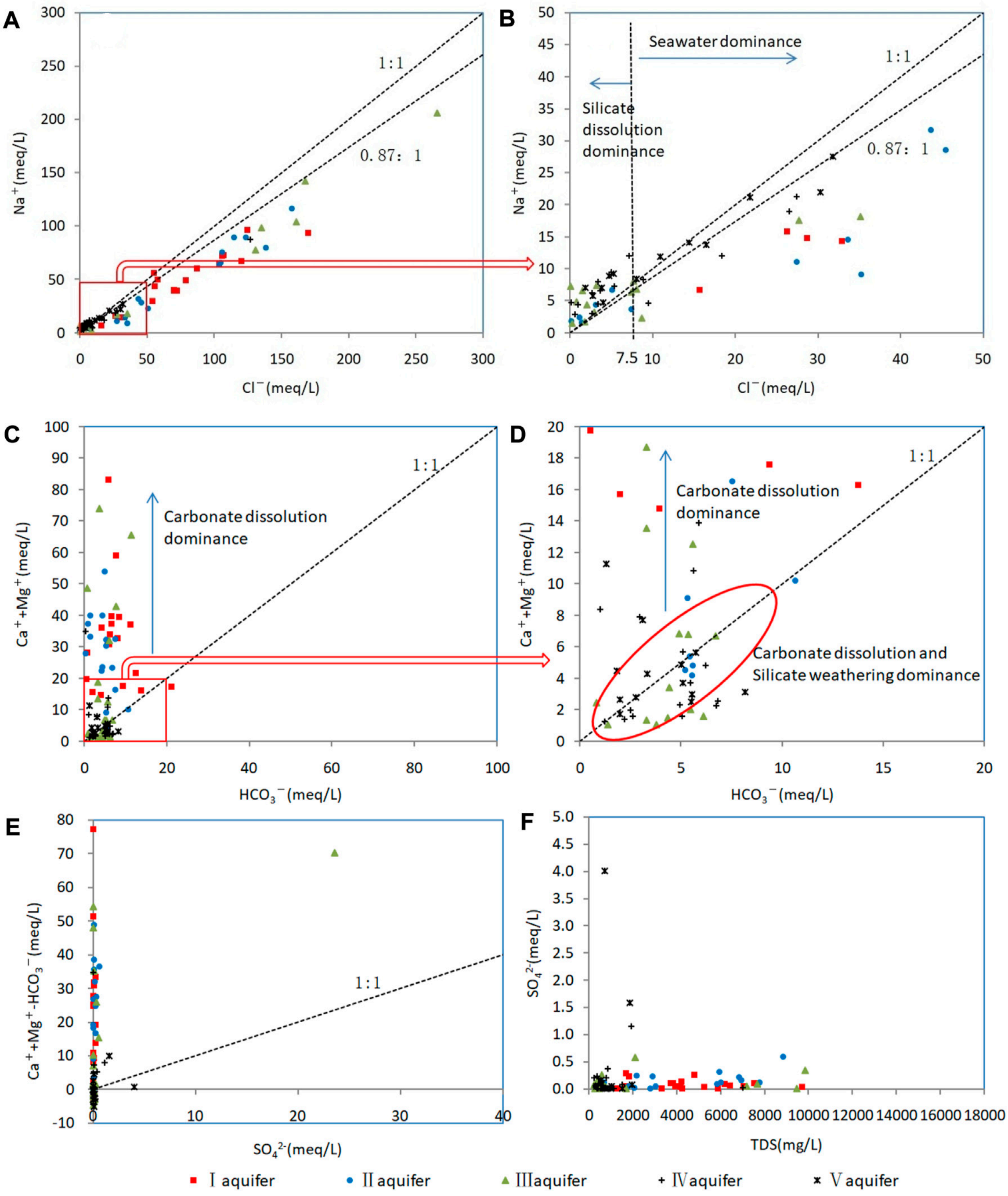

FIGURE 7
Relationships between ion contents of confined groundwater samples. **(A)** Relationship between Na^+ and Cl^- for all samples. **(B)** Relationship between Na^+ and Cl^- for samples with Na^+ and Cl^- concentration of <50 meq L^{-1}. **(C)** Relationship between (Mg^{2+}+Ca^{2+}) and HCO_3^- for all samples. **(D)** Relationship between (Mg^{2+}+Ca^{2+}) and HCO_3^- for samples with (Mg^{2+}+Ca^{2+}) and HCO_3^- concentration of <20 meq L^{-1}. **(E)** Relationship between (Mg^{2+}+Ca^{2+}−HCO_3^-) and SO_4^{2-} for all samples. **(F)** Relationship between SO_4^{2-} and TDS for all samples.

3.4 Sources of ions in confined groundwater

The Quaternary sediments in the study area are comprised sand and clay. X-ray diffraction and electron microscopy data for these sediments (Qiu and Li, 2007) indicate that the diagenetic minerals in the aquifers are predominantly silicate (quartz, feldspar, kaolinite, and illite) and carbonate (calcite and dolomite) rocks. Rock weathering and dissolution are naturally controlled by the hydrochemical composition of groundwater (Bau et al., 2004; Kim, 2010) through typical reactions as follows:

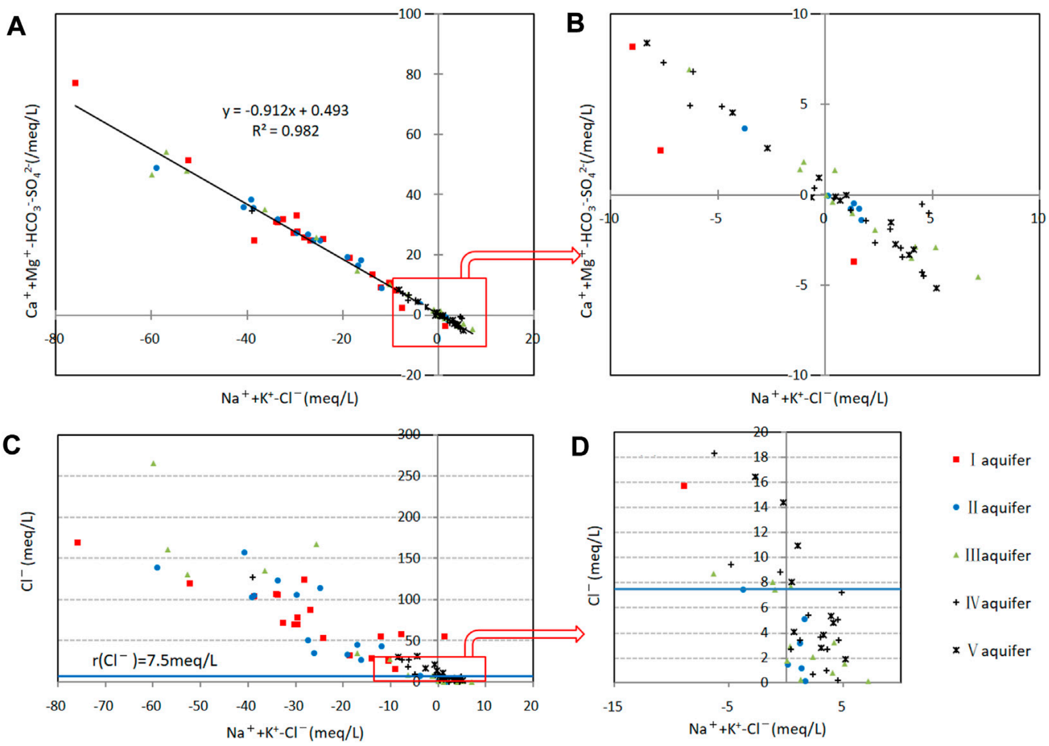

FIGURE 8
Cation-exchange analysis diagram of confined groundwater. **(A)** Relationship between (Mg^{2+}+Ca^{2+}−HCO_3^-−SO_4^{2-}) and (Na^++K^+−Cl^-) for all samples. **(B)** Relationship between (Mg^{2+}+Ca^{2+}−HCO_3^-−SO_4^{2-}) and (Na^++K^+−Cl^-) for samples with low concentrations. **(C)** Relationship between Cl^- and (Na^++K^+−Cl^-) for all samples. **(D)** Relationship between Cl^- and (Na^++K^+−Cl^-) for samples with low concentrations.

Silicate dissolution:

$$2Na_xK_{(1-x)}AlSi_3O_8 + 2CO_2 + 11H_2O \rightarrow 2xNa^+ + 2(1-x)K^+ + Al_2Si_2O_5(OH)_4 + 4H_4SiO_4 + 2HCO_3^- \quad (1)$$

Carbonate dissolution:

$$CaCO_3 + H_2O + CO_2 \rightarrow Ca^{2+} + 2HCO_3^- \quad (2)$$

$$CaMg(CO_3)^2 + 2H_2O + 2CO_2 \rightarrow Ca^{2+} + Mg^{2+} + 4HCO_3^- \quad (3)$$

Halite dissolution:

$$NaCl \rightarrow Na^+ + Cl^- \quad (4)$$

$$KCl \rightarrow K^+ + Cl^- \quad (5)$$

Ancient seawater is an important source of Na^+ and Cl^- in the groundwater of marine–continental-origin. The Na^+/Cl^- equivalence ratio in seawater is 0.87 (Kunwar and Kawamura, 2014). A ratio of <1 indicates that the groundwater is affected mainly by seawater, whereas ratios of >1 indicate that silicate dissolution is more important (Eq. 1) and a ratio of 1 indicates that halite dissolution is the primary source of these ions (Eqs 4, 5; Gianguzza et al., 2004; Panno et al., 2006).

Bivariate plots for Na^+ and Cl^- are shown in Figures 7A–B, which shows two groups of samples separated by the Cl^- = 7.5 meq L^{-1} line (Figure 7B). Samples from aquifers I and II are distributed mainly below the 0.87:1 line with Cl^- >7.5 meq L^{-1}, and samples from aquifers IV and V are distributed mainly above the 1:1 line with Cl^- <7.5 meq L^{-1}. Therefore, the Cl^- = 7.5 meq L^{-1} line acts as a demarcation index to identify groundwater origins in the study area. Some samples from the aquifer V plot near the 1:1 line with Cl^- >7.5 meq L^{-1} is due to halite dissolution rather than seawater. Using the demarcation index of Cl^- = 7.5 meq L^{-1}, it was determined that the proportions of continental-origin groundwater samples in aquifers I–V were 0%, 26.3%, 52.6%, 70.6%, and 84.6%, respectively.

Carbonate dissolution and silicate weathering are the primary sources of Ca^{2+}, Mg^{2+}, and HCO_3^- as indicated by the (Mg^{2+}+Ca^{2+})/HCO_3^- ratio (Kenoyer and Bowser, 1992; Kim, 2010): a ratio of <1 indicates that Ca^{2+} and Mg^{2+} were derived primarily from silicate weathering, and ratios of ≤1 indicate they were derived primarily from carbonate dissolution.

Most samples from aquifers I and II and the east part of aquifer III have (Mg^{2+}+Ca^{2+})/HCO_3^- ratios of >1 (Figure 7C), which suggests carbonate dissolution as a source of Ca^{2+} and Mg^{2+}. Most samples from aquifers IV and V and the west part of aquifer III have ratios of ≤1, which reflects the predominant contributions of silicate weathering and carbonate dissolution. Calcite and dolomite reach saturation or oversaturation in most samples (SI >−0.5; Figures 10C, D), which indicates that carbonate dissolution occurred throughout geological history. In summary, carbonate dissolution made the greatest contribution to marine–continental-origin groundwater, whereas both silicate weathering and carbonate dissolution contributed to continental-origin groundwater.

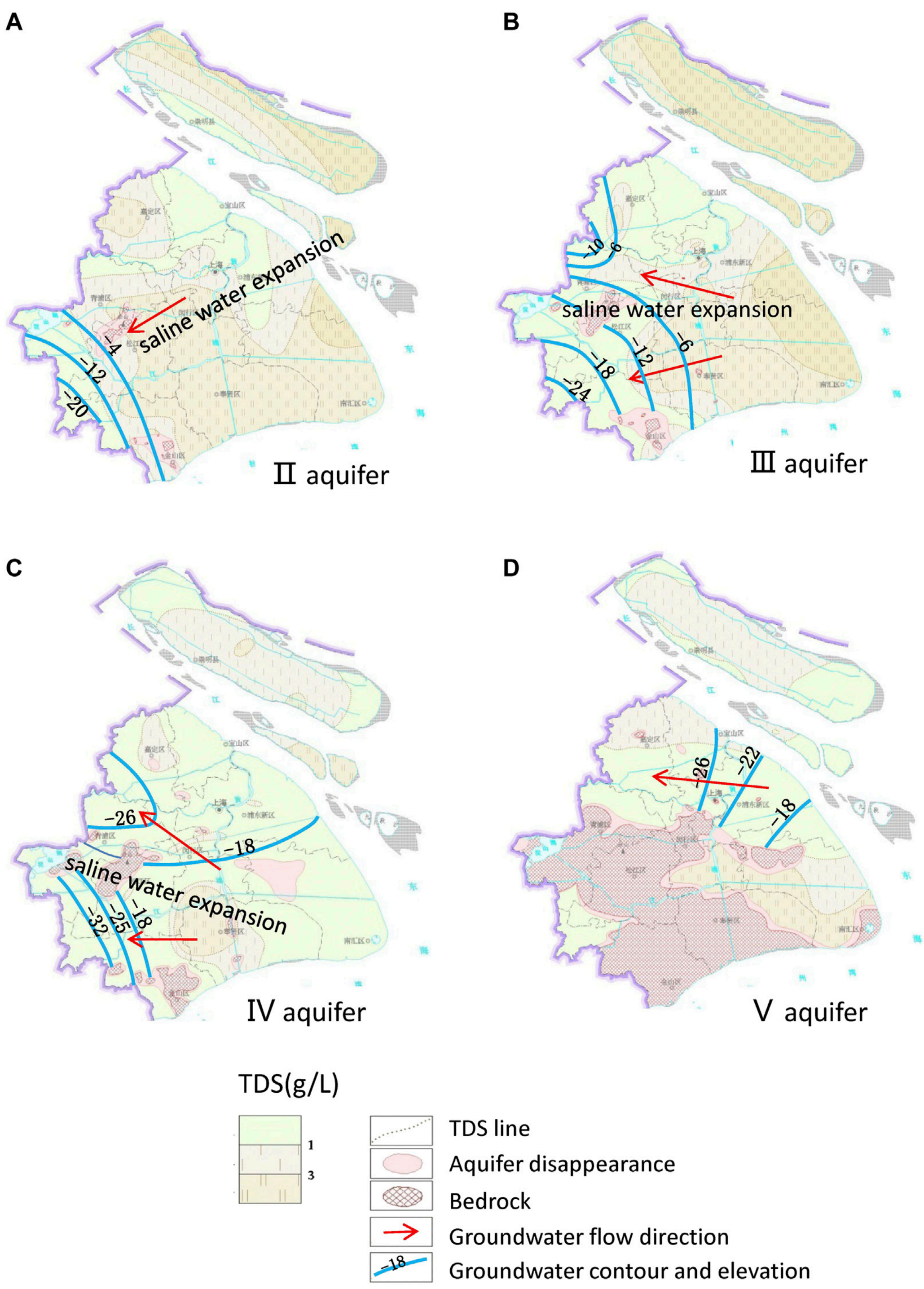

FIGURE 9
TDS and groundwater levels in the study area in 2009. TDS data are derived from Wei et al. (2010). Groundwater levels and flow directions are derived from Gong, (2009). **(A)** Groundwater funnels in aquifer II were mainly located in Songjiang in the southwest of the study area. **(B)** Groundwater funnels in aquifer III were mainly located in Songjiang and Qinpu in the western part of the study area. **(C)** Groundwater funnels in aquifer IV are similar to those in aquifer III. Saline recharge from aquifer III to aquifer IV in the area connecting the aquifers has been exacerbated by a decline in groundwater levels in aquifer IV. **(D)** Groundwater generally flowed from east to west due to the decline in groundwater levels in the west part of aquifer V.

In the absence of anthropogenic sources, SO_4^{2-} is derived mainly from evaporite deposits, such as gypsum, through hydrochemical reactions as follows:

$$CaSO_4 \rightarrow Ca^{2+} + SO_4^{2-} \tag{6}$$

$$MgSO_4 \rightarrow Mg^{2+} + SO_4^{2-} \tag{7}$$

The SO_4^{2-} content of most samples was low (Figure 7F), and the correlations between (Mg^{2+}+Ca^{2+}−HCO_3^-) and SO_4^{2-} were poor (Figure 7E). Furthermore, most samples were undersaturated in

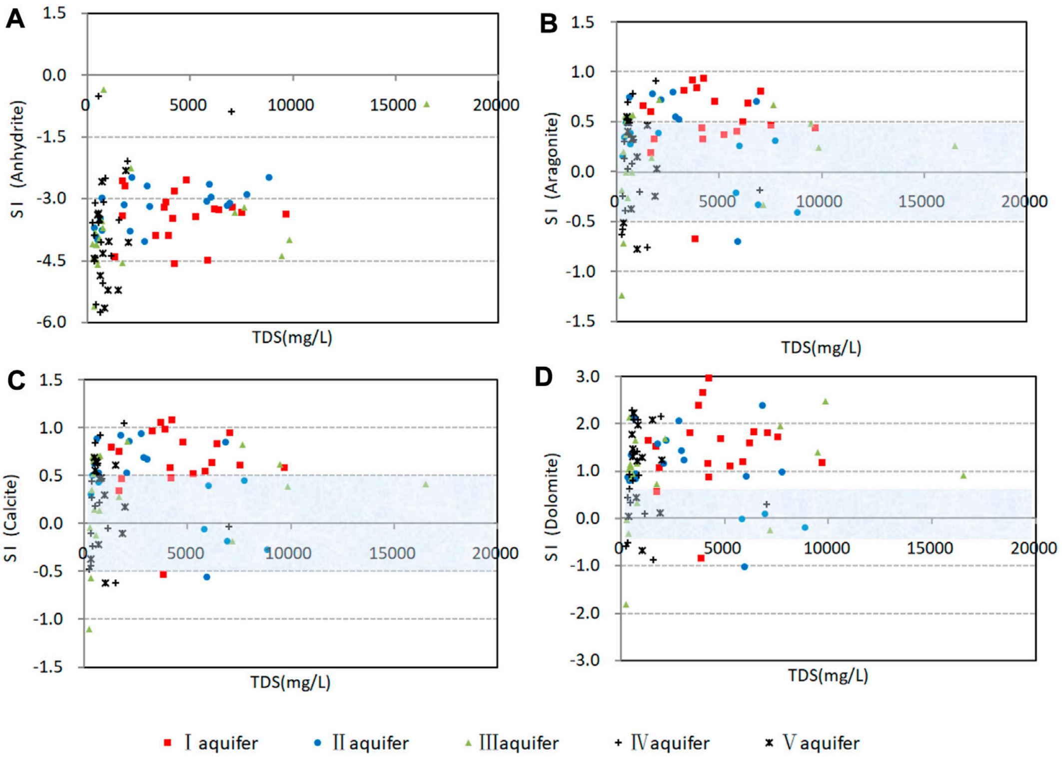

FIGURE 10
Saturation indices of confined groundwater in the study area. **(A)** Saturation indices values for anhydrite. **(B)** Saturation indices values for aragonite. **(C)** Saturation indices values for calcite. **(D)** Saturation indices values for dolomite.

gypsum (SI <−2; Figure 10A). Confined aquifers in the study area have excellent sealing properties, low mobility, and long retention times, so evaporite deposits such as gypsum are at low levels and SO_4^{2-} is mainly derived from insoluble sulfides (Lang et al., 2011), although the high SO_4^{2-} contents of some samples are attributable to anthropogenic activity.

3.5 Cation exchange

In terms of hydrochemical processes and ion sources, Ca^{2+}, Mg^{2}, and Na^{+} deviated slightly from the standard model, which implied that the groundwater was affected by other factors. Cation exchange commonly influences the evolution of groundwater composition (Tournassat et al., 2009; Zheng et al., 2021) through typical reactions as follows:

$$2Na^{+}\,(rock) + Ca^{2+}\,(water) \rightleftharpoons 2Na^{+}\,(water) + Ca^{2+}\,(rock) \quad (8)$$

$$2Na^{+}\,(rock) + Mg^{2+}\,(water) \rightleftharpoons 2Na^{+}\,(water) + Mg^{2+}\,(rock) \quad (9)$$

The reactions on the right are positive cation exchange, and those to the left are reverse cation exchange. The relationship between ($Mg^{2+}+Ca^{2+}-HCO_3^{-}-SO_4^{2-}$) and ($Na^{+}+K^{+}-Cl^{-}$) indicates the mechanism of cation exchange (Figure 8).

Changes in ($Mg^{2+}+Ca^{2+}-HCO_3^{-}-SO_4^{2-}$) and ($Na^{+}+K^{+}-Cl^{-}$) for the samples were opposite with a correlation coefficient of 0.98, which indicated a strong negative correlation. In general, the anion changes (Cl^{-}, HCO_3^{-}, SO_4^{2-}) in the groundwater were not significant, so this negative correlation mainly reflects (Ca^{2+}, Mg^{2+}) and (Na^{+}, K^{+}). A clear relationship between (Ca^{2+}, Mg^{2+}) and (Na^{+}, K^{+}) is thus noted with cation exchange playing a major role in controlling the hydrochemical compositions of groundwater.

The direction of cation exchange depends on the ionic adsorption energy and concentration. The energy decreases in the order of $Ca^{2+}>Mg^{2+}>K^{+}>Na^{+}$, so positive cation exchange is more common and leads to an increase in Na^{+} and K^{+} and a decrease in Ca^{2+} and Mg^{2+} concentrations in groundwater. However, 61% of the samples in the study area exhibited reverse cation exchange with negative ($Na^{+}+K^{+}-Cl^{-}$) and positive ($Mg^{2+}+Ca^{2+}-HCO_3^{-}-SO_4^{2-}$) values.

Reverse cation exchange is more common in water with Cl^{-} content of >7.5 meq L^{-1} (Figures 8C, D), whereas positive cation exchange is predominant with Cl^{-} <7.5 meq L^{-1}. This is consistent with the demarcation index for groundwater origins (Section 3.4). Reverse cation exchange is more significant in marine–continental-origin groundwater, and positive cation exchange is more significant in continental-origin groundwater with cation exchange explaining the deviation of some samples from the Gibbs model and why the Na^{+}/Cl^{-} ratio is below the 0.87:1 line.

3.6 Anthropogenic activity and hydrochemical evolution

As a drainage area of the Yangtze River Delta, aquifers in the study area have received freshwater recharge throughout geological history through lateral inflow, which compresses saline water within a certain range and limits its expansion and forms stable boundaries. However, boundaries and hydrochemical characteristics have changed over the past century due to groundwater exploitation.

Annual groundwater use exceeded 200 million m^3 in 1963, but it is currently decreasing each year. During the heavy-use periods, groundwater funnels develop due to excessive use, and saline water flows into the fresh water. Thus, continental-origin groundwater becomes marine–continental-origin groundwater (Figure 9). For example, saline water from the east flowed into a groundwater funnel to the northwest of Qingpu in aquifer III.

The expansion of saline water due to human activities over the past century is widespread and has serious implications for freshwater resources. Fortunately, Shanghai has adopted strict controls on groundwater exploitation with annual use limited to 2 million m^3. Artificial recharge has also been implemented. During the 13th Five Year Plan period, the annual artificial recharge was ~20 million m^3 and through this the groundwater level rises each year. However, artificial recharge has caused other problems, notably, desalination and mineral re-dissolution.

Saturation indices were calculated with respect to gypsum, aragonite, calcite, and dolomite in groundwater and are plotted in Figure 10. It is generally considered that groundwater is saturated at SI values of −0.5 to +0.5 (Liu, 2019). Most samples were supersaturated or saturated in aragonite, calcite, and dolomite (SI >−0.5; Figures 10B–D), which is consistent with weak hydrodynamic conditions in the study area. However, a few samples had SI values of <−0.5, which is possibly because of the influx of fresh groundwater and artificial recharge and resulted in the breakdown of hydrochemical equilibrium and renewed mineral dissolution (Kanagaraj and Elango, 2019).

4 Conclusion

The hydrochemical characteristics of groundwater were studied and trends in the study area were identified. These findings are valuable for planning groundwater protection and utilization in Shanghai.

Hydrochemical characteristics are dominated by the origin of groundwater. Two groundwater origins were identified: marine–continental- and continental-origin. For marine–continental-origin groundwater, major ions are primarily derived from ancient seawater and carbonate dissolution, and reverse cation exchange is common due to high concentrations of Na. Silicate weathering, carbonate dissolution, and positive cation exchange predominantly contribute to the hydrochemical composition of continental-origin groundwater.

TDS contents of 1,000 mg L^{-1} and hydrochemical facies do not accurately identify the origins of groundwater, but Cl^- content of 7.5 meq L^{-1} acts as a demarcation index for the two origins. This index can be used to determine the boundaries between the groundwater of the two origins and allows accurate monitoring and prediction of the advance/retreat of saline water.

We mainly focused on the relationship between groundwater and human activities, which is unavoidable in Shanghai. The study demonstrates that geogenic processes are not the only mechanisms controlling groundwater chemistry; anthropogenic activities also affect groundwater chemistry, and once the evolution of groundwater is disturbed, then recovery is difficult.

Data availability statement

The original contributions presented in this study are included in the article/Supplementary Material, and further inquiries can be directed to the corresponding author.

Author contributions

All authors listed have made a substantial, direct, and intellectual contribution to the work and approved it for publication.

Funding

This research was supported by a special project on Asian cooperation (Comparative study of geo-environment and geohazards in the Yangtze River Delta and Red River Delta) and a study of three-dimensional geological models and environmental physical fields of middle–shallow underground space.

Conflict of interest

The authors declare that the research was conducted in the absence of any commercial or financial relationships that could be construed as a potential conflict of interest.

Publisher's note

References

An, T. D., Tsujimura, M., Phu, V. L., Kawachi, A., and Ha, D. T. (2014). Chemical characteristics of surface water and groundwater in coastal watershed, mekong delta, vietnam. *Environ. Sci.* 20, 10. doi:10.1016/j.proenv.2014.03.085

Bau, M., Alexander, B., Chesley, J. T., Dulski, P., and Brantley, S. L. (2004). Mineral dissolution in the cape cod aquifer, Massachusetts, USA: I. Reaction stoichiometry and impact of accessory feldspar and glauconite on strontium isotopes, solute concentrations, and REY distribution. *Geochimica Cosmochimica Acta* 68 (6), 1199–1216. doi:10.1016/j.gca.2003.08.015

Farid, I., Zouari, K., Rigane, A., and Beji, R. (2015). Origin of the groundwater salinity and geochemical processes in detrital and carbonate aquifers: Case of chougafiya basin (central Tunisia). *J. Hydrology* 530, 508–532. doi:10.1016/j.jhydrol.2015.10.009

Gibbs, R. J. (1970). Mechanisms controlling world water chemistry. *Science* 170 (3962), 1088–1090. doi:10.1126/science.170.3962.1088

Gibbs, R. J. (1972). Water chemistry of the amazon river. *Geochimica Cosmochimica Acta* 36 (9), 1061–1066. doi:10.1016/0016-7037(72)90021-x

Gan, Y., Zhao, K., Deng, Y., Liang, X., Ma, T., and Wang, Y. (2018). Groundwater flow and hydrogeochemical evolution in the jianghan plain, central China. *Hydrogeology J.* 26 (5), 1609–1623. doi:10.1007/s10040-018-1778-2

Gianguzza, A., Milea, D., Millero, F. J., and Sammartano, S. (2004). Hydrolysis and chemical speciation of dioxouranium(vi) ion in aqueous media simulating the major ion composition of seawater. *Mar. Chem.* 85 (3-4), 103–124. doi:10.1016/j.marchem.2003.10.002

Gong, S. L. (2009). Change of groundwater seepage field and its influence on the development of land subsidence in shanghai. *Scispace* 20 (3), 1–5. doi:10.3969/j.issn.1007-1903.2009.01.001

Gu, X., Xiao, Y., Yin, S., Hao, Q., Liu, H., Hao, Z., et al. (2018). Hydrogeochemical characterization and quality assessment of groundwater in a long-term reclaimed water irrigation area, north China plain. *Water* 10 (9), 1209. doi:10.3390/w10091209

Huang, S., Yin, Y., Sun, R., and Tan, X. (2021). *In situ* anaerobic bioremediation of petroleum hydrocarbons in groundwater of typical contaminated site in shanghai, China: A pilot study. *Environ. Eng. Sci.* 38, 1052–1064. doi:10.1089/ees.2020.0534

Jang, C. S., Liu, C. W., and Chou, Y. L. (2012). Assessment of groundwater emergency utilization in taipei basin during drought. *J. Hydrology* 414, 405–412. doi:10.1016/j.jhydrol.2011.11.016

Kanagaraj, G., and Elango, L. (2019). Chromium and fluoride contamination in groundwater around leather tanning industries in southern India: Implications from stable isotopic ratio δ 53 cr/δ 52 cr, geochemical and geostatistical modelling. *Chemosphere* 220, 943–953. doi:10.1016/j.chemosphere.2018.12.105

Kenoyer, G. J., and Bowser, C. J. (1992). Groundwater chemical evolution in a sandy silicate aquifer in northern Wisconsin: 1. Patterns and rates of change. *Water Resour. Res.* 28 (2), 579–589. doi:10.1029/91WR02302

Kim, K. (2010). Plagioclase weathering in the groundwater system of a sandy, silicate aquifer. *Hydrol. Process.* 16 (9), 1793–1806. doi:10.1002/hyp.1081

Kunwar, B., and Kawamura, K. (2014). One-year observations of carbonaceous and nitrogenous components and major ions in the aerosols from subtropical okinawa island, an outflow region of Asian dusts. *Atmos. Chem. Phys.* 14 (4), 1819–1836. doi:10.5194/acpd-13-22059-2013

Lang, Y. C., Liu, C. Q., Li, S. L., Zhao, Z. Q., and Zhou, Z. H. (2011). Tracing natural and anthropogenic sources of dissolved sulfate in a karst region by using major ion chemistry and stable sulfur isotopes. *Appl. Geochem.* 26, S202–S205. doi:10.1016/j.apgeochem.2011.03.104

Li, C., Men, B-H., and Yin, S-Y. (2022). Analysis of groundwater chemical characteristics and spatiotemporal evolution trends of influencing factors in southern beijing plain. *Front. Environ. Sci.* 10, 913542. doi:10.3389/fenvs.2022.913542

Li, M. G., Chen, J. J., Xu, Y. S., Tong, D. G., and Shi, Y. J. (2021). Effects of groundwater exploitation and recharge on land subsidence and infrastructure settlement patterns in shanghai. *Eng. Geol.* 282, 105995. doi:10.1016/j.enggeo.2021.105995

Liu, C. W., and Wu, M. Z. (2019). Geochemical, mineralogical and statistical characteristics of arsenic in groundwater of the lanyang plain, taiwan. *J. Hydrology* 577, 123975. doi:10.1016/j.jhydrol.2019.123975

Panno, S. V., Hackley, K. C., Hwang, H. H., Greenberg, S., Krapac, I., Landsberger, S., et al. (2006). Characterization and identification of na-cl sources in ground water. *Ground water* 44 (2), 176–187. doi:10.1111/j.1745-6584.2005.00127.x

Qiu, J. B., and Li, X. (2007). *Quaternary Strata and sedimentary Environment in Shanghai*. Shanghai Chian: Shanghai Scientific and TechnicalPublishers.

Rezaei, M., Sanz, E., Raeisi, E., Ayora, C., Vazquez-Sune, E., and Carrera, J. (2005). Reactive transport modeling of calcite dissolution in the fresh-salt water mixing zone. *J. Hydrology* 311 (1-4), 282–298. doi:10.1016/j.jhydrol.2004.12.017

Tournassat, C., Gailhanou, H., Crouzet, C., Braibant, G., Gautier, A., and Gaucher, E. C. (2009). Cation exchange selectivity coefficient values on smectite and mixed-layer illite/smectite minerals. *Soil Sci. Soc. Am. J.* 73 (3), 928–942. doi:10.2136/sssaj2008.0285

Wang, S., Xie, Z., Wang, F., Zhang, Y., Wang, W., Liu, K., et al. (2022). Geochemical characteristics and quality appraisal of groundwater from Huatugou of the Qaidam Basin on the Tibetan plateau. *Front. Earth Sci.* 10, 874881. doi:10.3389/feart.2022.874881

Wei, Z. X., Zai, G. Y., and Yan, X. X. (2010). *Atlas of Shanghai urban Geology*. China: Geological Publishing House.

Yang, N., Wang, G., Shi, Z., Zhao, D., Jiang, W., Guo, L., et al. (2018). Application of multiple approaches to investigate the hydrochemistry evolution of groundwater in an arid region: Nomhon, northwestern China. *Water* 10 (11), 1667. doi:10.3390/w10111667

Zhang, X., Hui, Q., Wu, H., Chen, J., and Qiao, L. (2016). Multivariate analysis of confined groundwater hydrochemistry of a long-exploited sedimentary basin in northwest China. *J. Chem.* 2016, 1–15. doi:10.1155/2016/3812125

Zhangh, W., Qin, X., and Yi, L. (1999). Groundwater system and ITS characteristics in Shanghai region. *Carsologica Sin.* 1999(4), 343–351. doi:10.3969/j.issn.1001-4810.1999.04.007

Zheng, Z., Gla, B., Xs, B., Xz, B., Lei, W. B., Fu, H., et al. (2021). Geochemical controls on the enrichment of fluoride in the mine water of the shendong mining area, China. *Chemosphere* 284, 131388. doi:10.1016/j.chemosphere.2021.131388

frontiers | Frontiers in Earth Science

TYPE Original Research
PUBLISHED 09 May 2023
DOI 10.3389/feart.2023.1165809

OPEN ACCESS

EDITED BY
Jian Liu,
Qingdao Institute of Marine Geology (QIMG), China

REVIEWED BY
Xiting Liu,
Ocean University of China, China
Bo Liu,
Alfred Wegener Institute Helmholtz Centre for Polar and Marine Research (AWI), Germany

*CORRESPONDENCE
Ke Cao,
✉ 53932214@qq.com

RECEIVED 14 February 2023
ACCEPTED 17 April 2023
PUBLISHED 09 May 2023

CITATION
Sun T, Cao K, Yin P, Jiang X and Tian Y (2023), Authigenic pyrite and gypsum minerals in offshore Zhoushan sediments: morphology, formation, and environmental implications.
Front. Earth Sci. 11:1165809.
doi: 10.3389/feart.2023.1165809

Authigenic pyrite and gypsum minerals in offshore Zhoushan sediments: morphology, formation, and environmental implications

Tiantian Sun[1,2], Ke Cao[1,2]*, Ping Yin[1,2], Xuejun Jiang[1,2] and Yuan Tian[1,2]

[1]Qingdao Institute of Marine Geology, China Geological Survey, Ministry of Natural Resources, Qingdao, China, [2]Laboratory for Marine Geology, Qingdao National Laboratory for Marine Science and Technology, Qingdao, China

Offshore Zhoushan sediments are a potential area for shallow gas resources in China, where authigenic pyrite is widely distributed. Pyrite content, size distribution, and morphology are influenced by depositional conditions and are sensitive to environmental changes. This study investigated the authigenic pyrites or gypsums of core JC-1 offshore of Zhoushan. Scanning electron microscopy was used to observe the pyrites and identify various aggregations. Changes in lithology, chlorine content, and stable isotope values of organic matter were analyzed to indicate the evolution of ancient marine, floodplain estuary, tidal flat environments, and shallow marine sedimentary facies. The morphology and microcrystalline structure of these types of pyrites can be divided into spherical framboid aggregates, sub-euhedral aggregates, and microcrystalline euhedral pyrites with different sedimentary facies. Gypsum minerals and the coexistence of pyrite and gypsum were found in the enriched authigenic pyrites at the SMTZs. The sources of sulfate formed by authigenic gypsums may originate from overlying seawater and pyrite oxidation, whereas calcium ions may come from the dissolution of carbonate or calcareous shells caused by local environmental acidification. The various aggregations of pyrites observed may be related to SO_4-AOM in different environments. The findings suggest that authigenic gypsums form due to local environmental acidification and that the sources of the formed sulfate may be from overlying seawater and pyrite oxidation. This study provides a new perspective for understanding the responses of different sedimentary environments to sea level rise and climate change.

KEYWORDS

authigenic pyrite, gypsum minerals, sedimentary facies, environmental evolution, Offshore Zhoushan

1 Introduction

During early diagenetic processes, a variety of authigenic sulfide minerals are formed in marine sediments; these minerals can be roughly divided into two types: acid volatile sulfur (AVS; AVS=FeS + H_2S + 2/3 Fe_3S_4), mainly composed of iron monosulfide minerals (e.g., mackinawite), and chromium-reducible sulfur, mainly pyrites (CRS; CRS= FeS_2 + S^0 + 1/

3 Fe_3S_4). Overall, unstable iron monosulfide minerals eventually transform into diagenetically stable pyrite (Rickard and Luther, 2007; Taylor and Macquaker, 2011; Lin et al., 2016d; Liu et al., 2020a). The formation of authigenic pyrite in sediments is controlled by a combination of factors, including the degradation of organic matter, the sulfate content in pore water, and the active iron content. Thus, pyrite is an important tool for studying early diagenesis (Jørgensen, 1982; Berner, 1984; Böttcher and Lepland, 2000). Therefore, pyrite in marine sediments is an important sink for sulfur and iron and plays an important role in global C-S-Fe biogeochemical cycles (Berner, 1984; Liu et al., 2020a). Organoclastic sulfate reduction (OSR) is the dominant anaerobic mechanism of organic matter remineralization and sulfide (H_2S) formation, which then reacts with active iron to form iron sulfide and is buried in modern marine sediments (Liu et al., 2021).

Framboids are generally the most common morphological type of authigenic pyrite. They are zoned aggregates with radial overgrowths that surround the framboidal cores, fillings, and agglomerates (Amstutz et al., 1967). Variations in their morphological types reflect the difference between the physical and chemical conditions of the water body during its formation and the later diagenetic environments (Shevelkova et al., 1996). Authigenic pyrite is widely developed on the inner shelves of the Yellow Sea and the East China Sea. Early pioneering research on the distribution, morphological type, formation, and control factors of authigenic pyrite developing in the sea area indicated that its formation process and characteristics are closely related to the sedimentation process and are controlled by different factors, including organic matter content, system openness, anaerobic oxidation of methane (AOM), and sedimentation rate (Kang et al., 2014; Chang et al., 2020; Liu et al., 2022). In addition, pyrite abundance and morphological characteristics may be influenced by local depositional environments, particularly during physical reworking and bioturbation (Richardson et al., 2019; Liu et al., 2022). Therefore, diverse sedimentary environments and geological evolution can be recorded in the content, morphology, and other signals of authigenic pyrite, which provide good materials for studying the response mechanisms of authigenic pyrites to sedimentation environments.

As a typical evaporative salt mineral, authigenic gypsum ($CaSO_4{\cdot}2H_2O$) is widely found in evaporitic environments in arid climate conditions and semi-restricted basins, as well as in non-evaporative deep marine sediments and cold and dry polar environments. The oxidation of sulfides, the action of acidic sulfate solutions on calcareous rocks, and the hydration of anhydrite ($CaSO_4$) are the most common forms of non-evaporative gypsum (Vogel et al., 2010; Haffert et al., 2013; Lin et al., 2016a; Liu et al., 2018b). The coexistence of authigenic gypsum and pyrite was recently reported as a typical mineral assemblage in cold seeps (Lin et al., 2016a; Zhao et al., 2021; Dantas et al., 2022). The formation mechanism of authigenic gypsum is linked to the oxidation of authigenic pyrite and the evolution of the underlying methane seeps. Zhao et al. (2021) suggested that gypsum formation is likely associated with the downward migration of the sulfate–methane transition zone (SMTZ), which causes anaerobic pyrite oxidation at its original site of formation. Liu et al. (2020b) also found authigenic gypsum minerals in a location where a large amount of pyrite was formed in a study of authigenic minerals in EC2005 core samples from the East China Sea shelf. However, the mechanism of authigenic gypsum formation is not well understood. Additionally, authigenic pyrite–gypsum association is rare in marine sediments, mainly in the southwest Indian Ocean (Criddle, 1974), the southwest continental slope of Africa (Siesser and Rogers, 1976), the Madras sea area (Vijaykumar and Vaz, 1995), and Rías Baixas (Garcia-Gil, 2003). Additionally, Chinese researchers have identified gypsum-pyrite assemblages in the sediments of the South China Sea (Chen et al., 2007; Lin et al., 2012), which they suggested was related to Ca^{2+} enrichment caused by the dissolution of carbonate or biological shells by hydrogen sulfide released by the decomposition of organic matter or methane migration.

Offshore Zhoushan had a typical shallow depositional environment. During several transgressions and regressions in the Quaternary, sediments were formed in multiple layers with freshwater and marine sedimentary facies (Lin et al., 2004; Liu et al., 2022), and multiple sets of muddy, silty, and sandy sediments rich in organic matter were alternately deposited (Chen et al., 2020). After the last glaciation, offshore Zhoushan experienced depositional evolution from the river channel to the floodplain estuary and the present estuarine-shallow sea, with an increase in sea level (Lin et al., 2005). Based on recent high-resolution seismic surveys (Figure 1B), biogenic shallow gas (mainly methane) is widely developed in the sediments of offshore Zhoushan, with a water depth of approximately 0–25 m (Ni et al., 2013). Because of the methane, AOM may be the dominant process for sulfide production, which is finally preserved as authigenic pyrites (Liu et al., 2020a). Other researchers have used geochemical methods, mainly AOM and methanogenesis, to study the geochemical characteristics of sediments (He et al., 2020). We recently found abundant pyrites formed in the shallow gas enrichment area offshore of Zhoushan, which are probably related to AOM or OSR. The study of the evolution of the sedimentary environment by tracing differences in pyrite morphology and highly variable content is of great scientific importance because it can provide new ideas and avenues for understanding variable local environmental conditions. For instance, the sedimentary pyrites and C/S ratios of mud sediments on the East China Sea inner shelf indicate a late Pleistocene–Holocene environmental evolution (Liu et al., 2020a; Liu et al., 2022). However, little has been reported on the morphological characteristics and the constraints of authigenic pyrite in the offshore Zhoushan sediments. In this study, we selected, separated, and identified authigenic pyrite and gypsum minerals from sediment samples of core JC-1 in a shallow gas enrichment area offshore of Zhoushan. Combined with a comprehensive study on the total sulfur and grain size of bulk sediments and methane contents in the headspace, we explored the origin of pyrite and gypsum minerals to establish the diagenetic process for the observed morphology signals and their implications for environmental changes during deposition.

2 Materials and methods

2.1 Geological setting

Core JC-1 was located in the coastal area of Zhoushan (Figure 1). Controlled by the regional structure and various

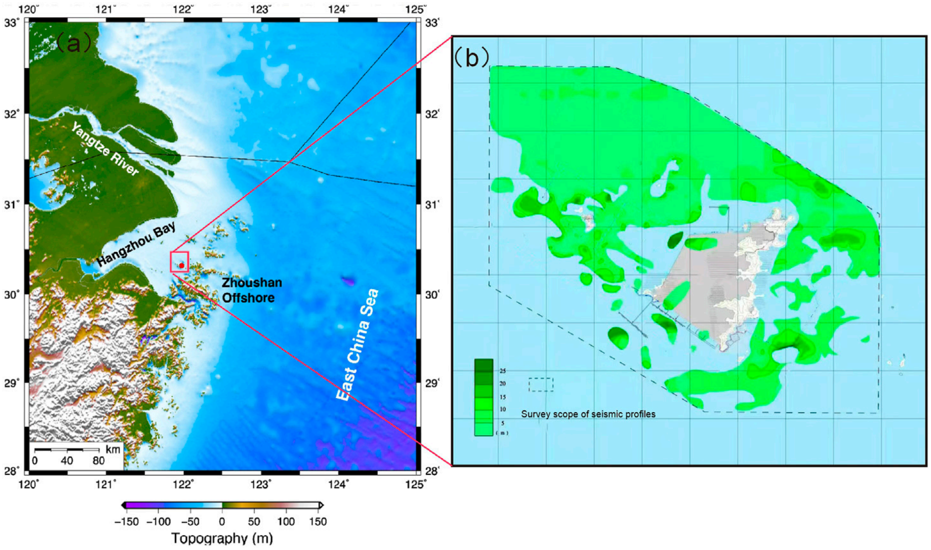

FIGURE 1
(A) Geological background map of the study area showing the location of core JC-1. **(B)** Seismic profile of the shallow gas distribution in the study area.

natural agents in the later stage, the island location in the research area is mainly in the form of long strips and is distributed in the southwest to the northeast direction (Chai et al., 2015). It lies on the inner shelf of the East China Sea (ECS) (Figure 1). The ECS is a typical river-dominated marginal sea characterized by the delivery of large amounts of terrigenous sediments from surrounding rivers, including the Yangtze and Qiantang rivers (Yang et al., 2016; Liu et al., 2018a). The distribution and dispersal patterns of terrigenous sediments in the ECS are modulated by oceanic and tidal currents, as well as sea level, which leads to the formation of variable sedimentary systems on the continental shelf (Liu et al., 2018a). A recent study showed an average preservation efficiency of terrigenous organic matter in the ECS inner shelf of approximately 24.7% ± 4.7% (Wu et al., 2013).

During the Last Glacial Maximum (LGM), the entire ECS inner shelf was exposed and represented a terrestrial fluvial environment (Li et al., 2014) because the global sea level was 120–135 m lower than the present sea level (Liu et al., 2022). With the rapid rise in sea level, transgressive system tracts were formed from 11 to 8 ka BP (Chen et al., 2020) and the incised valleys were filled. Consequently, the tide-dominated estuary face overlaid the fluvial sediments and was covered by a tide-dominated delta face. When the sea level reached its high point at ~7.5 ka (Li et al., 2014), the sedimentary environment evolved from shallow water to the current estuary due to the continuous input of sediments from the Yangtze River and local small rivers. According to the seismic profiles, biogenic shallow gas is widely distributed in the shallow mud sediments in the study area (Figure 1), where the total thickness of the Holocene sediments is >40 m (Lin et al., 2004; Hu et al., 2016; He et al., 2020). Owing to the comprehensive impact of terrestrial and marine material inputs, the sedimentation regime provides a solid basis for calculating the sedimentary indicators related to sedimentary pyrite.

2.2 Sample collection

In 2019, the Qingdao Institute of Marine Geology of the China Geological Survey performed a comprehensive geological survey of the central coastal zone of Zhejiang Province, using rotary drilling technology for coring construction near the Zhoushan offshore, in the ECS continental margin. The JC-1 core with a depth of 63 m below sea floor (mbsf) and a diameter of 108 mm was obtained, with a drilling and coring rate of approximately 100%. The geographical location of the study core is N 30°18′55.54″ and E 121°58′32.20″ (Figure 1). After the sediment core was drilled, it was sectioned, observed, photographed, and described on the deck. The total length of the core column at core JC-1 is 63 m. On the vertical profile, the samples showed a transition from gray-black to brown-yellow-brown from top to bottom, mainly composed of muddy sediments, with clear interlayer boundaries. The core sediment samples collected on the ship and the PVC pipes on the deck were divided into small sections approximately 2 m in length according to the number of times. The two ends were then sealed with plastic caps and tapes and stored in the deck cooler. At the end of the voyage, the samples were transported to the core library of the Qingdao Institute of Marine Geology of the China Geological Survey, where they were continuously sampled at 2 cm intervals. A total of 310 samples were collected.

Gas samples at 2–3-m intervals in the sediments were collected immediately after the core was drilled according to a previously published protocol (Jiang et al., 2023). Specifically, a 50-mL disposable sterile syringe, whose head was removed, was inserted into the sediment core. Then, 35 mL of fresh sediment sample in the syringe was placed into a 50-mL glass vial with a 10-mL sodium chloride saturated solution. The vial was quickly sealed with a butyl rubber stopper and aluminum cap. The sealed glass vials were kept in darkness and sent to the Qingdao Institute of Marine Geology,

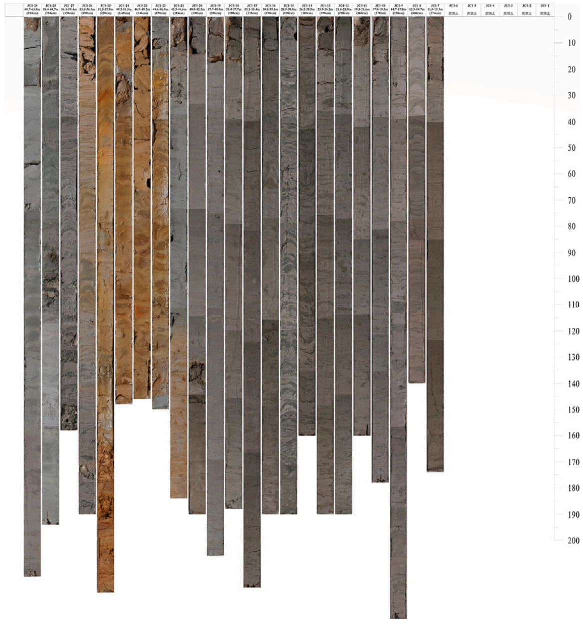

FIGURE 2
Sediment core JC-1 collected from offshore Zhoushan. Numbers JC1-1 to JC1-29 represent the number of each core segment from top to bottom.

China, for gas content and stable isotopic composition testing (described in Jiang et al., 2023).

Based on the sedimentary structure and grain size characteristics, four sedimentary zones were identified from the core bottom to the top. In the first sedimentary zone (Zone 1: 55–63 mbsf), the sediments were mainly dark gray and grayish-black. In the second sedimentary zone (Zone 2:40–55 mbsf), the sediments were mainly composed of massive yellowish-brown sands with numerous sand clumps and rusty-brown stains. In the third sedimentary zone (Zone 3:23–40 mbsf), the sediments were composed mainly of massive muddy sediments with a small number of sand clumps and horizontal bedding. In the fourth sedimentary zone (Zone 4:12–23 mbsf), the sediments were mainly composed of dark gray and clayey silt (Figure 2).

2.3 Pyrite identification

Authigenic mineral identification was performed at the laboratory at the Qingdao Institute of Marine Geology. An appropriate amount of the sample was fully immersed in water. The dispersed sediment sample was then placed in a water sieve with a 0.063 mm diameter and rinsed repeatedly with distilled water to separate clay and other components with particle sizes <0.063 mm. After drying the washed debris (mainly authigenic minerals, terrigenous debris, and biological shells) in a 60-C incubator for 24 h, the light and heavy minerals were separated with tribromomethane ($CHBr_3$, density is 2.89 g/mL) as the medium. After drying and weighing, the authigenic minerals were observed under a solid-state microscope and manually selected. The extracted authigenic pyrite was sectioned and observed under an optical microscope.

Representative minerals were selected for scanning electron microscopy. We secured a properly sized sample to the metal table with a conductive adhesive and observed the morphology on the machine after carbon spraying. The scanning electron microscope instrument used in this study was obtained from the test room at the Qingdao Institute of Marine Geology. The thermal field emission scanning electron microscope manufactured by a Japanese company was Hitachi S4800, equipped with a Brooke Quantax-200 energy spectrum. The test conditions were as follows: working distance: 8.5 mm; voltage: 15 kV.

2.4 Grain size analysis

Approximately 0.5 mL of bulk sediment was used to digest the organic matter fraction for grain size analyses. Excessive H_2O_2 solution was removed by heating and evaporation before 0.5% of sodium hexametaphosphate was added to completely disperse the sample. Finally, $Na_4P_2O_7{\cdot}10H_2O$ was added to each sample before measuring to prevent aggregate formation. The grain size was measured using a laser particle size analyzer (Mastersize-2000, Malvern Instruments Ltd., United Kingdom) at the Qingdao Institute of Marine Geology, China Geological Survey. The volume percentages of the sand (63–2000 µm), silt (4–63 µm), and clay fractions (<4 µm) were calculated.

3 Results

3.1 Morphology and mineralogy of authigenic pyrites

Most of the handpicked pyrite particles (aggregates with particle sizes >0.063 mm) from the core sediments were the most common authigenic minerals in the shallow gas enrichment area offshore of Zhoushan. The most common morphological types of pyrite aggregate observed under SEM were tubular, cubic, irregular, and spherical and filled with the shells of foraminifera and other organisms (Figure 3). The pyrite shapes and particle sizes varied significantly among the different layers. Overall, the particles were mainly spherical aggregates with a smaller diameter in Zone 4 (12–23 mbsf; Figures 3D, F) and tubular shapes with variations in both diameter and length in Zone 3 (23–40 mbsf; Figures 3A–C). In the deep zone of Zone 1, the pyrite mainly formed irregular aggregates with euhedral crystals (50–63 mbsf). The authigenic pyrite particles had a black metallic luster, a few particles in different zones were fragile, and the internal fresh section was red, which may have been related to pyrite oxidation. Careful SEM observation of the authigenic pyrite-filled foraminiferal shells revealed carbonation in most of the shells (Figure 3). While some foraminiferal shells contained only scattered spherical authigenic pyrite, others had their outer circumference tightly wrapped in spherical shapes, with no growth holes observed in the shell, for smoother flow.

The SEM-EDS analysis of selected parts of the handpicked pyrites showed variable shapes (Figure 4). In general, authigenic pyrite particles consist of finer crystals and have a variety of crystal forms, including spherical, sub-euhedral, and euhedral.

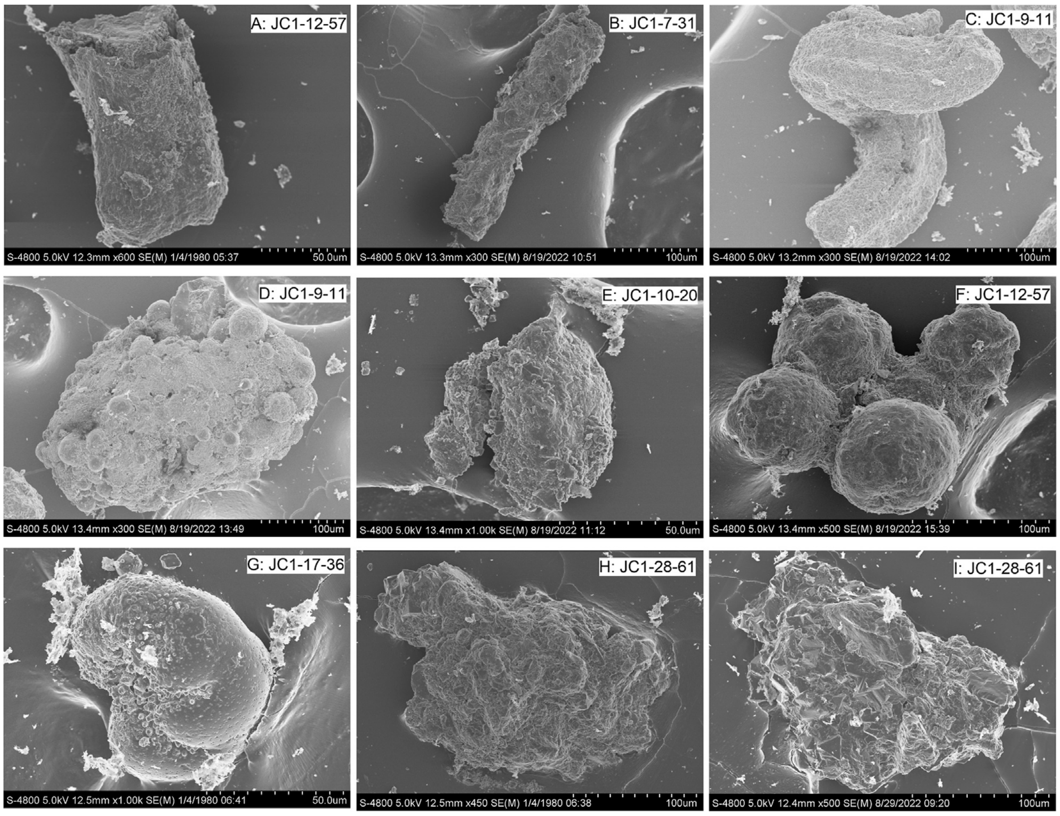

FIGURE 3
SEM micrographs of the morphology of pyrite aggregation in the JC-1 site. **(A)** Long strip pyrite aggregates. **(B)** Selected SEM photographs of authigenic pyrite tubes. **(C)** Curved rod-shaped pyrite. **(D)** Pyrite aggregate formed by the polymerization of spherical pyrite. **(E)** Well-developed pyrite framboids. **(F)** Pyrite aggregate formed by the polymerization of spherical pyrite. **(G)** Foraminifera-filled pyrite aggregates. **(H)** Well-developed pyrite framboids with euhedral microcrystals. **(I)** Accretive pyrite aggregates formed by the disorderly accumulation of numerous octahedral microcrystals.

The irregular aggregates are composed of euhedral-shaped microcrystals approximately 40 μm in size (Figure 4B). In the same spherical and pyrite framboids, the size and diameter of microcrystals are relatively uniform, but the particle size of different framboids varies widely, from about 0.1 to 4 μm (Figures 4C, F–I). The observation results in multiple zones of core JC-1 showed certain differences in the aggregate and crystal morphologies of authigenic pyrite in different layers. The massive tubular pyrites were composed of pyrite framboid and sub-euhedral crystals approximately 20–40 μm in size (Figures 3A–C; Figures 4F, I). Overall, they presented a tree-like shape, indicating that they were microchannels for fluid migration in sediments (Figures 3A, E). Morphologically, pyrite framboid crystals of uniform size continued to grow from the pores, making the structure more compact and showing the growth characteristics of different periods.

EDS spectra were used to test the authigenic pyrites selected under a microscope for some individuals. The results showed two distinct narrow Fe and S peaks, with a mass content almost completely coincided with the standard peak spectrum of FeS_2 (Figure 5; Figure 7). The EDS mode may have experienced elemental interference from the surrounding matrix or other minerals during the pyrite analysis; thus, other elements such as oxygen (O) and silicon (Si) could have been captured in the EDS spectra. The pyrite particles in the same sample were observed under a scanning electron microscope. Therefore, while authigenic pyrite particles were present in the sediments, their content distribution was uneven at different depths.

3.2 Gypsum morphology and the coexistence of authigenic gypsum and pyrite

In addition to pyrite, gypsum was a relatively common authigenic mineral in the core JC-1 sediments in the study area. Most of the gypsum crystals handpicked from the core sediments were aggregations of granular spherical shapes, and some coexisted with authigenic gypsum and pyrite (Figures 6D–G). The gypsum crystals were mainly in the form of microspheres and elongated rod-shaped gypsum and were mostly distributed as rosette clusters or aggregates. The SEM-EDS results of the gypsums (Figure 7) showed that the rosette clusters were mainly composed of Ca, O, and S, which are the spectral peaks of gypsum. In addition to authigenic gypsum, irregular and massive authigenic carbonates (Figure 7) were also found on the large granular pyrite. The particles often showed a flat crystal surface, about 100 μm in size.

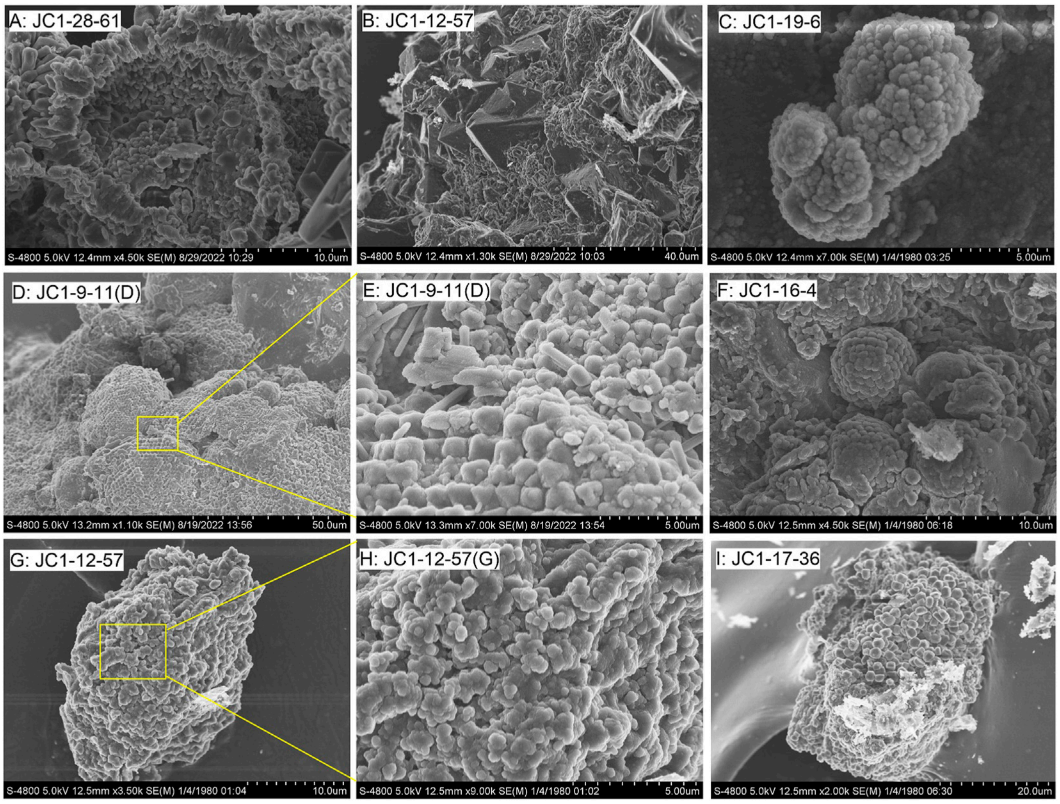

FIGURE 4
Selected SEM photographs of authigenic pyrites. **(A)** Pyrite pyritohedron with a spherical framboid in the center. **(B)** Well-developed pyrite framboids with octahedral microcrystals. **(C)** Well-developed pyrite framboids. **(D)** Euhedral pyrite. **(E)** Enlarged view of the box in **(D)** showing octahedral pyrite and surrounding elongated pyrite microcrystals. **(F)** Spherical pyrite growing around framboid pyrite. **(G)** Framboid pyrite aggregates. **(H)** Enlarged view of the box in **(G)**. **(I)** Well-developed pyrite framboids with euhedral microcrystals.

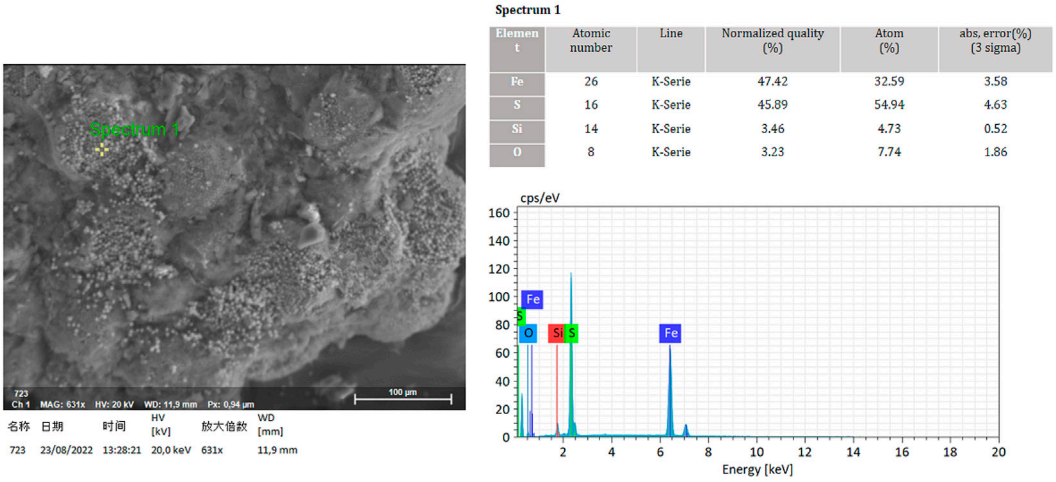

名称	日期	时间	HV [kV]	放大倍数	WD [mm]
723	23/08/2022	13:28:21	20,0 keV	631x	11,9 mm

Spectrum 1

Element	Atomic number	Line	Normalized quality (%)	Atom (%)	abs, error(%) (3 sigma)
Fe	26	K-Serie	47.42	32.59	3.58
S	16	K-Serie	45.89	54.94	4.63
Si	14	K-Serie	3.46	4.73	0.52
O	8	K-Serie	3.23	7.74	1.86

FIGURE 5
EDS analysis of pyrite showing Fe and S at the major content (sample number JC1-12-57).

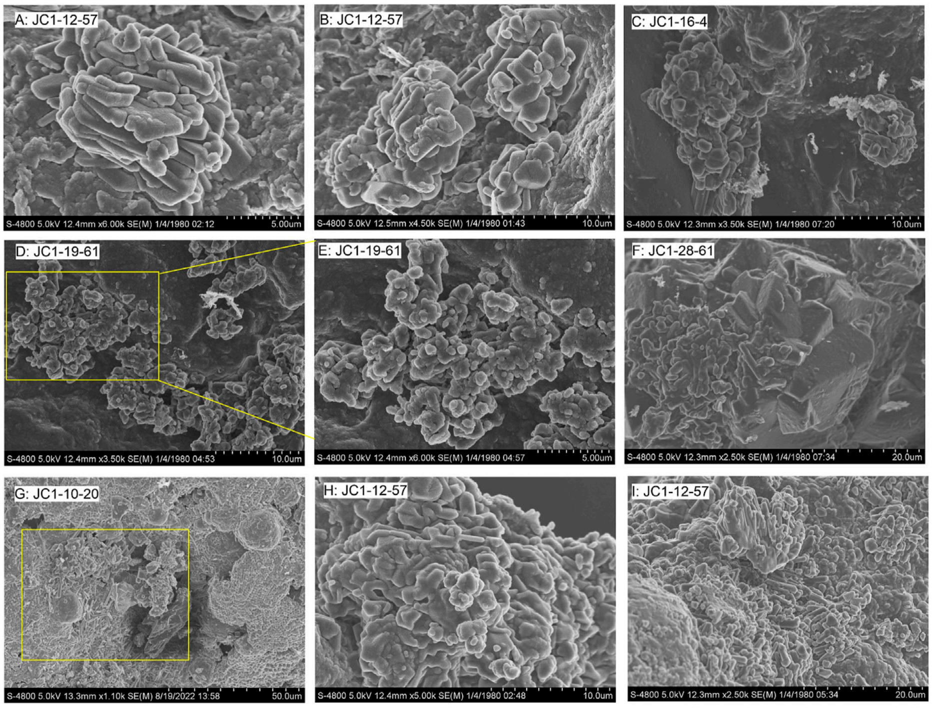

FIGURE 6
Morphology of gypsum from the JC-1. **(A)** Elongated rod-like gypsum aggregates. **(B)** Spherical and elongated rod-shaped gypsum aggregate. **(C)** Cluster-like gypsum aggregate. **(D)** Cluster-like gypsum aggregates. **(E)** Enlarged diagram of the box in the figure showing rosette clusters. **(F)** Tufted gypsum and pyrite growing around an octahedron. **(G)** Cluster-like gypsum growing around spherical pyrite. **(H)** Rosette forming pyrite–gypsum symbiosis. **(I)** Elongated rosette gypsum aggregates.

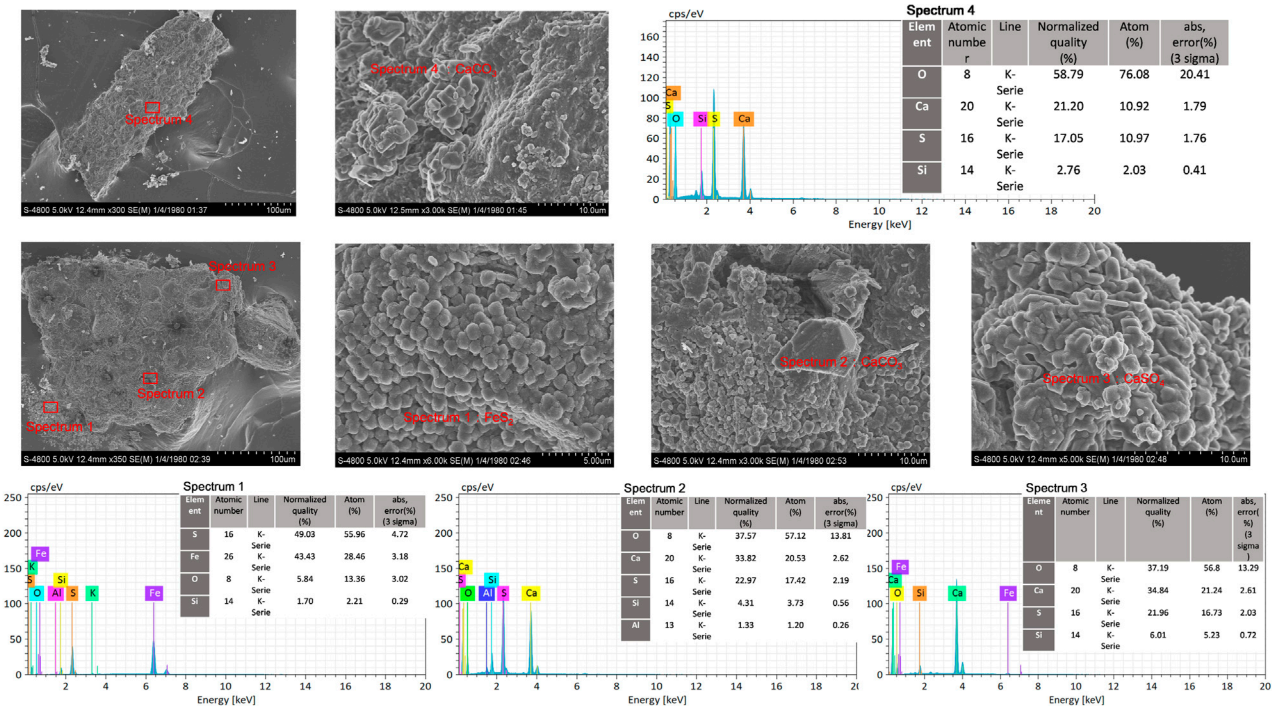

Spectrum 4

Element	Atomic number	Line	Normalized quality (%)	Atom (%)	abs, error(%) (3 sigma)
O	8	K-Serie	58.79	76.08	20.41
Ca	20	K-Serie	21.20	10.92	1.79
S	16	K-Serie	17.05	10.97	1.76
Si	14	K-Serie	2.76	2.03	0.41

Spectrum 1

Element	Atomic number	Line	Normalized quality (%)	Atom (%)	abs, error(%) (3 sigma)
S	16	K-Serie	49.03	55.96	4.72
Fe	26	K-Serie	43.43	28.46	3.18
O	8	K-Serie	5.84	13.36	3.02
Si	14	K-Serie	1.70	2.21	0.29

Spectrum 2

Element	Atomic number	Line	Normalized quality (%)	Atom (%)	abs, error(%) (3 sigma)
O	8	K-Serie	37.57	57.12	13.81
Ca	20	K-Serie	33.82	20.53	2.62
S	16	K-Serie	22.97	17.42	2.19
Si	14	K-Serie	4.31	3.73	0.56
Al	13	K-Serie	1.33	1.20	0.26

Spectrum 3

Element	Atomic number	Line	Normalized quality (%)	Atom (%)	abs, error(%) (3 sigma)
O	8	K-Serie	37.19	56.8	13.29
Ca	20	K-Serie	34.84	21.24	2.61
S	16	K-Serie	21.96	16.73	2.03
Si	14	K-Serie	6.01	5.23	0.72

FIGURE 7
Microcrystal morphology and structure characteristics of pyrite–gypsum intergrowth in the sediments of the study area and energy spectrum (EDS) analysis of gypsum showing that its main chemical components are Ca, O, and S. The irregular and tubular pyrite are from samples JC1-10-20 and JC1-28-61, respectively.

3.3 Pyrite content and gypsum distribution

In this study, the sediment samples were first pretreated by sieving and washing. Authigenic minerals were then identified and selected under SEM. Some samples showed the presence of gypsum particles. Because almost all of the samples were consumed, it is difficult to analyze the content of the gypsum particles in the sediment using chemical methods. Therefore, in this study, the presence of gypsum was observed using SEM and verified by EDS. We observed gypsum in five samples from core JC-1 (Figure 9), with a distribution of 17–20 mbsf, 31 mbsf, 38 mbsf, and 61 mbsf. The coexistence of pyrite and gypsum was also found at the 17.5 mbsf, 38 mbsf, and 61 mbsf depths.

The relative contents of hand-picked pyrite in coarse-grained heavy minerals (>63 μm) are shown in Figure 9 and Supplementary Table S2. Pyrite is in high abundance at ~17 bmsf, ~39 bmsf, and ~60 bmsf. The pyrite contents increased significantly (0.76 wt.%) at 17.5 mbsf, followed by a decrease to a low value (0.09 wt.%) at 30.9 mbsf. The relative pyrite contents then increased again, up to 0.58 wt.% at 37.8 mbsf, before finally dropping to low values (0.02 wt.%). Generally, the relative contents of pyrite within the coarse fraction remained at high abundance in the deeper portion of 59–62 mbsf.

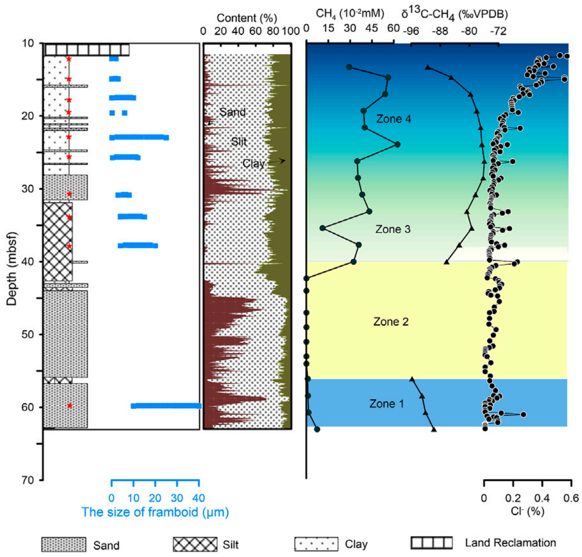

FIGURE 8
Lithological distribution of the sediment core from JC-1.

4 Discussion

4.1 Characteristics of pyrite induced by the anaerobic oxidation of methane

The diagenetically stable pyrite in marine and freshwater sediments has a widespread distribution, making it an essential indicator of local environmental conditions. This is due to the varying pyrite morphologies, high content, and variable sulfur isotopic compositions observed in different sediment (Lin et al., 2017; Rickard et al., 2017; Liu et al., 2019; Miao et al., 2021; Liu et al., 2022). The morphological characteristics and crystal shapes of pyrite are controlled by the nature of the supersaturated conditions, which vary between different pathways of pyrite formation (Shevelkova et al., 1996; Taylor and Macquaker, 2011; Rickard, 2012).

The high reactive Fe content in this study are shown in Figure 9 and Supplementary Table S1 facilitated the formation of early diagenetic authigenic pyrite during and after sediment deposition. The significant peaks of total sulfur (TS) and pyrite content in the samples suggest that the coarse fraction's relative pyrite content was the primary inorganic sulfide in the sediments are shown in Figure 9 and Supplementary Table S1. The offshore core JC-1 in Zhoushan contained a considerable amount of framboidal pyrite, which occurred as spheroidal, cubic, irregular particles, and tubular or rod-shaped monomers. These pyrite characteristics resemble those of authigenic pyrite reported in the sediments of the East and Yellow seas (Chen, 1981; Chang et al., 2020). Nevertheless, the pyrite morphology and size varied significantly at different depths. For instance, at 60 mbsf in Zone 1 of core JC-1, framboid overgrowth was observed, with a framboid mean size of >20 μm. This suggested that the pyrite framboids formed during the earliest stages of diagenesis (Richardson et al., 2019). In strongly reduced environments, authigenic pyrite often has unique morphological features, such as a long growth time, and it mostly occurs as large framboidal pyrite aggregates or organism-filling aggregates (Miao et al., 2021). Therefore, the mean size and shape of the pyrite particles may suggest that the pyrites in Zone 1 were early diagenetic framboids that precipitated under reduced conditions. Similar findings were observed in Zones 4 and 3. As shown in Figure 7, the mean size of the framboid particles gradually decreased from Zone 3 to Zone 4, accompanied by a gradual transition from tubular or rod-shaped pyrite to smaller spherical particles. Additionally, most of the pyrite particles in the two zones were smaller and had a relatively wider size distribution at 17.5 mbsf and 37.8 mbsf, reflecting an anoxic environment with strongly reduced conditions. The formation of authigenic pyrite in the mud sediments of the East China Sea (Liu et al., 2020a) and the northern continental slope of the South China Sea (Lin et al., 2016b; Lin et al., 2016c) is associated with methane fluids. Given the widespread distribution of biogenic CH$_4$ offshore of Zhoushan (He et al., 2020), the authigenic pyrite may have formed during early diagenesis via the SO$_4$-AOM pathway in an anoxic environment.

According to the investigation and analysis of shallow gas data in the study area, free CH$_4$ gases with extremely low δ^{13}C-CH$_4$ values (all < - 72 ‰ VPDB) were seen at 12–40 mbsf and 55–63 mbsf shallow gas-bearing layers in the sediments of core JC-1 are shown in Figure 8 and Supplementary Table S2. In this case, methane gas in the sediments underwent SO$_4$-AOM in the SMTZ, resulting in framboidal pyrite formation. A large amount of framboidal pyrite composed of microcrystals with relatively wider size distributions was observed at 17.5 mbsf, 37.8 mbsf, and 60 mbsf layers, which is considered to be an effective indicator of SMTZ positions (Miao et al., 2021). Microbial methanogenesis of organic matter in the mud sediments produced biogenic methane, which has been vertically distributed in multiple layers within a hundred meters of the seabed during the Holocene and late Pleistocene (Chen et al., 2004; Hu et al., 2016). Since the Quaternary, the sedimentation rate of estuarine

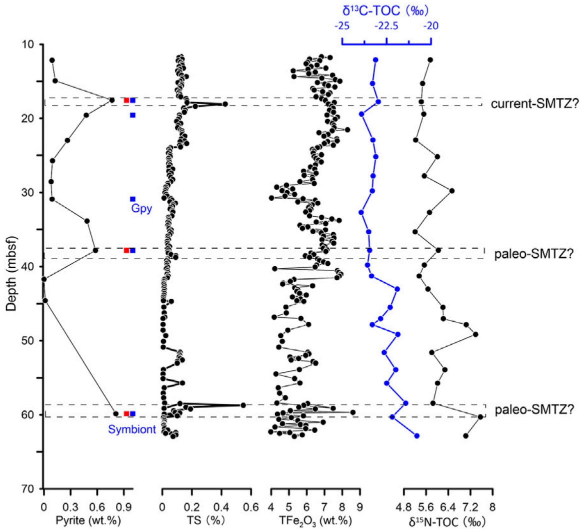

FIGURE 9

TS, TFe_2O_3, and relative content of pyrite in hand-picked coarse-grained (coarser than 63 μm) heavy minerals, and the stable isotopes values of organic matter (δ^{13}C-TOC and δ^{15}N-TOC) in sediment from core JC-1.

facies in the coastal areas of the Qiantang River and offshore Zhoushan has been 4–5 mm/a and has been a long-term process of stable sedimentation. This continuous and rapid sedimentation leads to the sufficient and sustained production of biogenic methane in sediments (Chen et al., 2004). Moreover, multiple transgression-regression processes during the geological history period have made the sediment pore water in the study area rich in certain sulfate concentrations (Li et al., 2014; Dong et al., 2018; Liu et al., 2020a), with a multilayer distribution, providing a material basis for the SO_4-AOM of biogenic methane in the sediment. As a result, extensive development of framboid pyrite occurred in multiple SMTZs and was deposited in the sediment, resulting in large and variable early diagenetic framboid deposits.

The sediments of core JC-1 were also rich in gypsum. The results of the statistical analysis showed that gypsum was mainly enriched in the methane gas-bearing zones. The gypsum enrichment positions were located near or below the pyrite enrichment positions, which were closely associated with pyrite (Figure 6; Figure 9). In the sedimentary environment of core JC-1, the gypsum in the sediments cannot be the result of evaporation. The research core was located offshore of Zhoushan, with a water depth of approximately 60 m. Based on the stratigraphic distribution of gypsum, gypsum was not found in any of the samples with pyrite. In addition, because of the low-temperature preservation environment after core column collection, gypsum crystals could not form during sample processing and sediment storage in core JC-1 (Lin et al., 2016a; Liu et al., 2018b). The gypsums exhibited good self-shaped crystals under SEM. The crystal surface was complete and smooth, had a relatively stable aggregate shape, and did not exhibit obvious wear or erosion (Figure 6), indicating that the gypsum crystals were *in situ* (Vogel et al., 2010; Lin et al., 2016a). Most importantly, we found that the aggregate shape characteristics of gypsum differed in the JC-1 sediment at different depths; some were individual rosette clusters, while others were wrapped with pyrite to form the coexistence of pyrite and gypsum. The differences in gypsum crystal morphology may be related to the speed of mineral precipitation or differences in the chemical conditions in local microenvironments (Vogel et al., 2010; Haffert et al., 2013).

4.2 Sedimentary environmental factors

Sea-level change is the primary driver of changes in the evolution of Late Pleistocene and Holocene shelf environments (Lambeck et al., 2014; Li et al., 2014; Dong et al., 2018; Liu et al., 2022). During the Last Glacial Maximum (LGM; 26.5–19.0 ka), the entire ECS inner shelf was exposed and represented a floodplain–estuary environment due to the lowest sea level (Li et al., 2014). Sea level rise after the LGM (23–15.4 ka) led to the gradual inundation of continental shelf areas worldwide (Lambeck et al., 2014; Li et al., 2014), followed by a rapid sea-level rise during 14.0–12.9 ka in the ECS inner shelf (Dong et al., 2018). The Younger Dryas (YD; 12.5–11.5; Lambeck et al., 2014) was a dramatic cooling event during the transition from the LGM to the Holocene, which led to a transgressive–regressive cycle and represented a tidal flat environment. The global sea-level rise during the last deglaciation (15.4–7.0 ka) oscillated but has slowed since 7.0 ka, as documented in the sediments of the ECS (Liu et al., 2021). The offshore area of Zhoushan is one of the major estuaries along the ECS, where abundant shallow gas reservoirs have been developed (Figure 1; Chen et al., 2004; He et al., 2020). Based on previous studies (Lin et al., 2004; Lin et al., 2010), the 63-m-long sediment core was divided into four sedimentary facies, or zones (ancient marine, floodplain-estuary, tidal flat environment, and present shallow marine), according to the changes in lithology and geochemical data (Figure 7). In Zone 1, a certain amount of elemental chlorine (Figure 8) indicated a marine environment. The lithological characteristics of Zone 1 are dominated by dark gray and grayish-black sediments (Figure 2; Chen et al., 2004), indicating that the Late Pleistocene strata are in a sulfidic environment and have good conditions for microbial methanogenesis. Researchers have frequently employed stable isotopes of δ^{13}C-TOC and δ^{15}N-TOC to differentiate terrestrial and marine organic matter sources (Middelburg and Nieuwenhuize, 1998; Wu et al., 2007; Yuan et al., 2017). The higher δ^{13}C-TOC (−21.7‰ on average) and δ^{15}N-TOC (6.6‰ on average) values in Zone 1 indicated a greater proportion of marine organic carbon (C4) inputs (Yuan et al., 2017; Liu et al., 2020a), which also corresponded to a marine sedimentary environment. Sulfate is a major salt in marine sediments, and anaerobic sulfidic conditions are conducive to the occurrence of SO_4-AOM, resulting in pyrite formation. We found more abundant hand-picked pyrites with high TS and wider size in Zone 1 (Figure 9), which represented an indicator of the marine environment. During the SO_4-AOM process, the HS^- product reacts with reactive Fe in the sediment to produce FeS and release H^+, which in turn is converted to pyrite. H^+ enrichment dissolves carbonates or biological shells, resulting in the enrichment of Ca^{2+} ions.

Therefore, when combined with sulfate in pore water in a marine environment, gypsum precipitates, which also occurs with pyrite. Based on the pyrite and gypsum content and the existence of pyrite and gypsum, the paleo-SMTZ (~60 mbsf) can be inferred. In Zone 2, the sediments were mainly composed of massive yellowish-brown sands with many sand clumps and rusty-brown stains, which are typical features of the floodplain–estuary deposits. Furthermore, the seawater chlorine content decreased to a relatively stable level, as was also indicated by the floodplain–estuary deposits. We also noticed that the lithological characteristics and grain sizes from Zone 1 to Zone 2 experienced retrogressive aggradation as recorded in the sedimentary sequence, with progressively yellowish, coarse grains (Figure 2). The δ^{13}C-TOC (−22.5‰ on average) and δ^{15}N-TOC (6.2‰ on average) values in Zone 2 indicated a more significant proportion of terrestrial organic carbon inputs. The stable isotope values of terrestrial and marine organic matter overlap over a large range (Wu et al., 2007). Therefore, during the Zone 2 stage, core JC-1 sediments experienced a transition from a marine environment to a terrestrial environment due to sea-level changes during the LGM (Li et al., 2014; Liu et al., 2022), which can be divided into a transgressive lag and a floodplain estuary. Changes in sedimentary environments characterized by varying inputs of terrestrial matter and the presence of coarse sand sediments can be used to infer predictable changes in the quality of organic matter (Sun et al., 2020). Based on the absence of methane, low levels of TS content, and nearly imperceptible pyrite (as shown in Figure 9), the organic matter in this zone can be inferred to consist of refractory organic matter, which is more resistant to decomposition compared to marine sources (Zhao et al., 2021; Liu et al., 2022).

During the end of deposition in Zone 2, the intrusion of seawater began to affect the study area, as evidenced by the multiple peaks in chlorine content (Lambeck et al., 2014; Li et al., 2014). The stable isotope values of organic matter (δ^{13}C-TOC and δ^{15}N-TOC) suggest a mixture of marine and terrestrial sources in the sediments during this period. In Zone 3, the lithological characteristics consist of massive mud sediments with a few sand clumps and horizontal bedding, which indicate tidal facies. Previous research showed that the study area receives significant terrestrial inputs from rivers such as the Yangtze and Qiangtang rivers, with an ample supply of reactive iron (Sun et al., 2020; Zhao et al., 2021; Chang et al., 2022). The presence of abundant iron oxides did not restrict the formation of sedimentary pyrite (Figure 9). With the appearance of hand-picked pyrite aggregates and seawater intrusion, microbial sulfate reduction may have been limited during transgressive intervals. However, gypsum minerals (Figure 8) were also identified, possibly related to the oxidation of authigenic pyrites (Liu et al., 2018b; Zhao t al., 2021). Although seawater is unsaturated relative to gypsum in Zone 3, various processes can lead to increased Ca^{2+} and SO_4^{2-} in pore water. Iron sulfide oxidation is a relatively common process that can lead to an increased sulfate content of pore water (Liu et al., 2018b). Based on the sedimentary structure and grain size characteristics of core JC-1, horizontal stratification was relatively obvious without significant bioturbation or strong physical reworking in Zone 3. Simultaneously, the presence of many tubular pyrites indicates underflow activities such as methane diffusion (Figure 3). The sedimentary environment is mostly anaerobic, and the anaerobic oxidation of deposited iron sulfides (Zhao et al., 2021) and the disproportionation reaction of S intermediates (Pirlet et al., 2010) predominantly affect pore water SO_4^{2-}. Simultaneously, the anaerobic oxidation of deposited iron sulfides can lead to the acidification of local pore water, which, in turn, leads to the dissolution of calcareous biological shells (Pirlet et al., 2010; Liu et al., 2018b; Zhao et al., 2021). The increased Ca^{2+} and SO_4^{2-} content jointly promoted gypsum precipitation.

From Zone 3 to Zone 4, the chlorine content diffused from the tidal facies to shallow marine environments with a concave downward decrease (Figure 8). The sea level was relatively stable during the deposition of Zone 4 and the sediments in the marine environment consisted of dark gray and clayey silt with a relatively uniform grain size distribution (Figure 8). However, we noticed that the grain size increased sharply at a depth of ~15.5 mbsf, which may be related to strong physical reworking and surface reclamation of sediments, as demonstrated by the surface sediments with alternating light yellow and dark gray colors. In Zone 4, the TS and handpicked pyrite had relatively high contents, with a peak of ~17 mbsf. The shallow surface sediments of the original seabed did not contain methane before reclamation; however, after reclamation, this layer contained a considerable amount of biogenic methane. The downward infiltration of seawater may have caused the SO_4-AOM to shift upward and become shallow, and the ~17 mbsf position may be the current SMTZ position. In general, the handpicked pyrites were mainly spherical aggregates with smaller diameters and narrow size distributions, which may also support our speculation that authigenic pyrite was newly formed at the current SMTZ position (Zhao et al., 2021). We also found some gypsum particles and the coexistence of pyrite and gypsum at ~17 mbsf (Figure 8), which may be related to AOM (Dantas et al., 2022). However, the mechanism of sufficient SO_4^{2-} provided by diffusing from the overlying seawater and sulfide oxidation, leading to gypsum formation, cannot be ruled out (Liu et al., 2018b). Therefore, the use of multiple indicators, such as stable S and O isotopes, is recommended to reveal the formation mechanisms of sedimentary authigenic minerals.

4.3 Evolution mechanism of authigenic pyrite and the coexistence of pyrite and gypsum

Love and Amstutz (1966) suggested that pyrite framboid was the main form of pyrite in the early diagenetic stage. Due to changes in environmental conditions, they may further grow and evolve into euhedral crystals in later stages; the specific evolution sequence can be expressed as spherical → sub-euhedral → microcrystalline euhedral → euhedral pyrite. Analysis of the distribution of authigenic pyrite, gypsum, and methane in core JC-1 showed that the morphological characteristics of authigenic pyrite represent the sedimentary evolution process. The coexistence of authigenic pyrite and gypsum may be related to the distribution and migration of shallow gases. Additionally, authigenic gypsum forms as a result of contributions from both seawater and pyrite oxidation, while Ca^{2+} is derived from local seawater acidification due to the oxidation process of authigenic pyrite. Therefore, we propose a simple depositional evolution model for offshore Zhoushan, which explains the formation process of authigenic pyrite and gypsum at the research site since the LGM (Figure 10).

(a) Mud sediments were deposited offshore in Zhoushan before changes in sea level and inland climate. Methanogenesis in mud sediments released a large amount of biogenic methane that

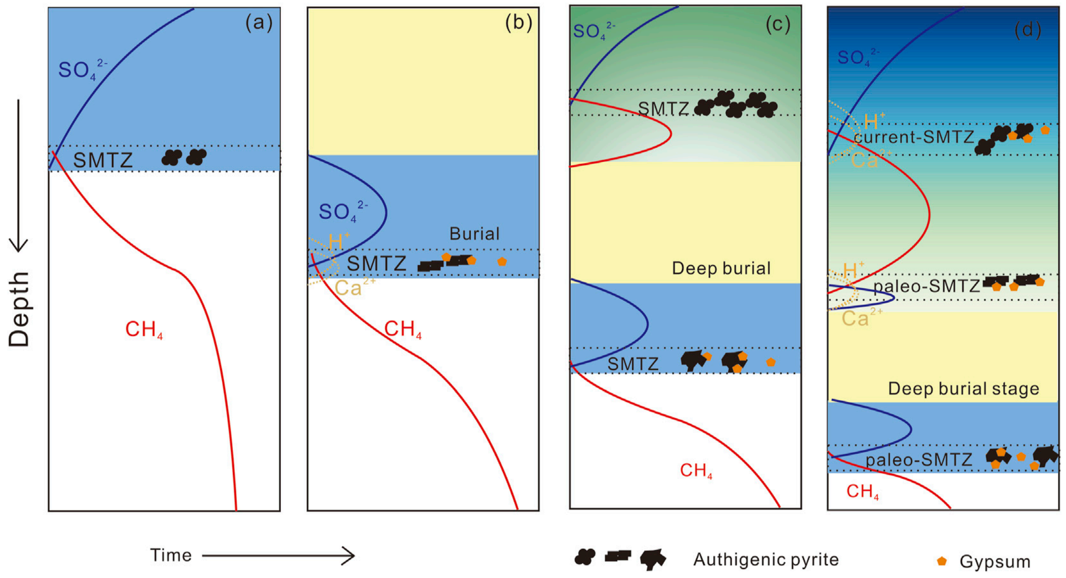

FIGURE 10
Simple diagenetic model for authigenic pyrite and gypsum precipitated in the JC-1 core. No scale reference. **(A–D)** Represent different depositional stages. Black dotted line, SMTZ; blue background, marine sedimentary environment; yellow background, floodplain–estuary depositional conditions; light green to dark blue background, tidal facies to shallow marine environments.

acted on the SMTZ, strengthened SO_4-AOM, and promoted the enrichment of diagenetic framboid particles. However, owing to the consumption of a large amount of sulfate by the enhanced AOM, the sulfate content in the pore water was limited and it was difficult to form gypsum precipitation at this stage.

(b) During the LGM, the entire ECS inner shelf was exposed, including the Zhoushan offshore (Li et al., 2014), resulting in the formation of floodplain and estuary deposits. The organic matter at this time was refractory, which is more difficult to decompose than marine sources (Zhao et al., 2021). The methane content of the upward diffusion was significantly reduced to zero, and the SMTZ subsequently migrated deeper. At this point, the sulfate concentration in the pore water at its original position began to increase. As the SO_4-AOM process advanced, HS^- reacted with reactive Fe in the sediment to produce FeS and release H^+, which was in turn converted into pyrite. H^+ enrichment dissolved carbonates or biological shells, resulting in the enrichment of Ca^{2+} ions. Therefore, it combined with pore-water sulfate in the marine environment to precipitate gypsum, which occurred with pyrite in the SMTZ. Simultaneously, the diagenetic pyrites began to transform into sub-euhedral structures.

(c) Sea level rise after the LGM led to the gradual inundation of continental shelf areas (Lambeck et al., 2014; Li et al., 2014). The study area was influenced by seawater intrusion, and sediments began to form tidal facies deposits under the influence of tidal currents. The formation time of the upper pyrite was later than that of the deeper pyrite; however, the formation mechanism of the pyrites was the same. Organoclastic sulfate reduction may also have occurred, which requires more indicators to be explored. During this stage, the upper pyrite was enriched in the shallow SMTZ; the presence of many tubular pyrites gradually evolved into an irregular microcrystalline euhedral shape close to the deeper position of the paleo-SMTZ. The sedimentary environment was mostly anaerobic, and the anaerobic oxidation of deposited pyrites (Liu et al., 2018b) and the disproportionation reaction of S intermediates (Pirlet et al., 2010) affected the pore water SO_4^{2-}. Simultaneously, the anaerobic oxidation of deposited iron sulfides led to the acidification of local pore water, which in turn led to the dissolution of calcareous biological shells (Pirlet et al., 2010; Liu et al., 2018b; Zhao et al., 2021). The increased Ca^{2+} and SO_4^{2-} content jointly promoted gypsum precipitation.

(d) The sea level tended to be relatively stable. The Holocene mud depocenter then began to develop, forming the present shallow marine environments (Lin et al., 2005). The downward infiltration of seawater may have caused the SO_4-AOM to shift upward and become shallow, forming the current SMTZ position. Spherical pyrite aggregates with smaller diameters, gypsum particles, and the coexistence of pyrite and gypsum were newly formed at the current SMTZ position, which may be related to ongoing SO_4-AOM. The formation mechanism of these authigenic minerals was the same as that in the deep part; however, the formation time was later. Simultaneously, authigenic pyrites in the deeper paleo-SMTZs continued to form and evolve into massive tubular or irregular pyrites. Additional work is needed to confirm the differences in authigenic pyrite in different zones.

5 Conclusion

The morphology and formation mechanisms of authigenic pyrite and gypsum show great potential in tracing depositional evolution history during the glacial–interglacial cycle in offshore Zhoushan. A variety of authigenic minerals were found in the sediment of core JC-1, which may be related to SO_4-AOM. Thus, the morphology, size distribution, and content of authigenic pyrite in different zones can indicate the evolution of the depositional environment. Additionally, gypsum minerals and the coexistence of pyrite and gypsum were found in the enriched authigenic pyrites at the SMTZs. The sources of sulfate formed by authigenic gypsums may originate from overlying seawater and pyrite oxidation, whereas calcium ions may come from the dissolution of carbonate or calcareous shells caused by local environmental acidification. The results of this study provide a new perspective for better understanding the responses of different sedimentary environments to sea level rise and climate change. However, using coarse-grained heavy minerals to calculate pyrite content may result in bias due to the sorting effect of particle size. In addition, the C-S-Fe cycle in continental shelf sediments is very complex; thus, we only provide a new mineralogy perspective. More detailed work is needed to limit the fate of authigenic minerals. We suggest using multiple indicators, such as ^{34}S isotopes of iron sulfides and/or chemical sequential extraction methods, to obtain the relative contents of various types of iron-bearing minerals in bulk sediments and further explore their potential in tracking sedimentary environment evolution.

Data availability statement

The original contributions presented in the study are included in the article/Supplementary Material. Further inquiries can be directed to the corresponding author.

Author contributions

TS was responsible for manuscript writing and performing tests. KC, YT, and PY provided the study samples. PY revised the text and provided comments. TS and XJ identified the minerals. All authors contributed to the article and approved the submitted version.

Funding

This work was financially supported by the Postdoctoral Foundation of Qingdao (grant QDBSH20220202138), the National Natural Science Foundation of China (grant 42176091), the China-ASEAN Cooperation in Marine Geoscience Research and National Key Research, and Development Plan Project (no. 2019YFE0127200).

Acknowledgments

The authors are grateful to the editors and reviewers for their constructive comments on our manuscript.

Conflict of interest

The authors declare that the research was conducted in the absence of any commercial or financial relationships that could be construed as a potential conflict of interest.

The handling editor JL declared a shared affiliation with the authors TS, KC, PY, XJ, and YT at the time of review.

Publisher's note

Supplementary material

The Supplementary Material for this article can be found online at: https://www.frontiersin.org/articles/10.3389/feart.2023.1165809/full#supplementary-material

References

Amstutz, G. C., Park, W. C., Schot, E. H., and Love, L. G. (1967). Orientation of framboidal pyrite in shale. *Miner. Deposita* 1 (4), 317–321. doi:10.1007/BF00205204

Berner, R. (1984). Sedimentary pyrite formation: An update. *Geochimica Cosmochimica Acta* 48 (4), 605–615. doi:10.1016/0016-7037(84)90089-9

Böttcher, M., and Lepland, A. (2000). Biogeochemistry of sulfur in a sediment core from the west-central Baltic Sea: Evidence from stable isotopes and pyrite textures. *J. Mar. Syst.* 25 (3), 299–312. doi:10.1016/S0924-7963(00)00023-3

Chai, X., Hu, B., Wei, N., Mu, Q., He, J., and He, S. (2015). Distribution, sources and assessment of heavy metals in surface sediments of the Hangzhou Bay and its adjacent areas [J]. *Huanjing Kexue Xuebao/Acta Sci. Circumstantiae* 35, 3906–3916. doi:10.13671/j.hjkxxb.2015.0138

Chang, X., Liu, X., Wang, H., Zhuang, G. C., Ma, Z., Yu, J., et al. (2022). Depositional control on the sulfur content and isotope of sedimentary pyrite from the southeast coast of China since MIS5. *Front. Mar. Sci.* 9, 1005663. doi:10.3389/fmars.2022.1005663

Chang, X., Zhang, M., Gu, Y., Wang, H., and Liu, X. (2020). Formation mechanism and controlling factors of authigenic pyrite in mud sediments on the shelf of the Yellow Sea and the East China Sea (in Chinese with English abstract) [J]. *Chin. J.* 35 (13), 1306–1320. doi:10.11867/j.issn.1001-8166.2020.105

Chen, Q. (1981). Study on authigenic pyrites in sediments of the South huanghai sea [J]. *Acta Geol. Sinica Transl. Chin.* 55 (3), 232–244. doi:10.19762/j.cnki.dizhixuebao.1981.03.007

Chen, S., Sun, J., Shen, C., and Du, X. (2004). Clustered components analysis for functional MRI. *Mar. Geol. Quat. Geol.* 24 (2), 85–98. doi:10.1109/TMI.2003.819922

Chen, Y., Deng, B., and Zhang, J. (2020). Shallow gas in the Holocene mud wedge along the inner East China Sea shelf. *Mar. Petroleum Geol.* 114, 104233. doi:10.1016/j.marpetgeo.2020.104233

Chen, Z., Yan, W., Chen, M. H. J. M. G., and Leung, K. (2007). A simple *in vitro* model to study the stability of acylglucuronides. *Mar. Geol. Quat. Geol.* 27 (2), 91–95. doi:10.1016/j.vascn.2006.03.008

Criddle, A. J. (1974). "A preliminary description of microcrystalline pyrite from the nannoplankton ooze at site 251, Southwest Indian Ocean," in *Proceedings of the Environmental Science, Geology* (London, United Kingdom: Department Of Mineralogy, British Museum (Natural History)). doi:10.2973/DSDP.PROC.26.126.1974

Dantas, R., Hassan, M., Cruz, F., and Jovane, L. (2022). Evidence for methane seepage in South Atlantic from the occurrence of authigenic gypsum and framboidal pyrite in deep-sea sediments. *Mar. Petroleum Geol.* 142, 105727. doi:10.1016/j.marpetgeo.2022.105727

Dong, J., Li, A., Liu, X., Wan, S., Feng, X., Lu, J., et al. (2018). Sea-level oscillations in the East China Sea and their implications for global seawater redistribution during 14.0–10.0 kyr BP. *Palaeogeogr. Palaeoclimatol. Palaeoecol.* 511, 298–308. doi:10.1016/j.palaeo.2018.08.015

Garcia-Gil, S. (2003). A natural laboratory for shallow gas: The Ras Baixas (NW Spain). *Geo-Marine Lett.* 23 (3), 215–229. doi:10.1007/s00367-003-0159-5

Haffert, L., Haeckel, M., Liebetrau, V., Berndt, C., Hensen, C., Nuzzo, M., et al. (2013). Fluid evolution and authigenic mineral paragenesis related to salt diapirism – the Mercator mud volcano in the Gulf of Cadiz. *Geochimica Cosmochimica Acta* 106, 261–286. doi:10.1016/j.gca.2012.12.016

He, X., Tan, L., Duan, X., Yin, P., Xie, Y., Yang, L., et al. (2020). Carbon cycle within the sulfate-methane transition zone in the marine sediments of Hangzhou Bay [J]. *Mar. Geol. Quat. Geol.* 40 (3), 51–60. doi:10.16562/j.cnki.0256-1492.2020021401

Hu, X., Gu, Z., Zhang, X., Zhao, L., Xing, Z., Liu, C., et al. (2016). Development of a novel monoclonal antibody to human inducible co-stimulator ligand (ICOSL): Biological characteristics and application for enzyme-linked immunosorbent assay. *Mar. Geol. Quat. Geol.* 36 (1), 151–157. doi:10.1016/j.intimp.2016.04.019

Jiang, W., Cao, K., Duan, X., He, X., Yin, P., Chen, J., et al. (2023). Influence of sedimentary environment evolution on fingerprint characteristics of methane isotopes: A case study from hangzhou bay. *J. Geophys. Res. Biogeosciences* 128, 1–14. doi:10.1029/2022JG007357

Jørgensen, B. B. (1982). Mineralization of organic matter in the sea bed—the role of sulphate reduction. *Nature* 296 (5858), 643–645. doi:10.1038/296643a0

Kang, X., Liu, S., and Zhang, G. (2014). Reduced inorganic sulfur in the sediments of the Yellow Sea and East China sea. *Acta Oceanol. Sin.* 33 (9), 100–108. doi:10.1007/s13131-014-0499-1

Lambeck, K., Rouby, H., Purcell, A., Sun, Y., and Sambridge, M. (2014). Sea level and global ice volumes from the last glacial maximum to the Holocene. *Proc. Natl. Acad. Sci. U. S. A.* 111 (43), 15296–15303. doi:10.1073/pnas.1411762111

Li, G., Li, P., Liu, Y., Qiao, L., Ma, Y., Xu, J., et al. (2014). Sedimentary system response to the global sea level change in the East China Seas since the last glacial maximum. *Earth-Science Rev.* 139, 390–405. doi:10.1016/j.earscirev.2014.09.007

Lin, C., Gu, L., Li, G., Zhao, Y., and Jiang, W. (2004). Geology and formation mechanism of late Quaternary shallow biogenic gas reservoirs in the Hangzhou Bay area, eastern China. *Aapg Bull. - AAPG Bull.* 88 (5), 613–625. doi:10.1306/01070403038

Lin, C. M., Li, Y. L., Zhuo, H. C., Shurr, G., Ridgley, J., Zhang, Z. P., et al. (2010). Features and sealing mechanism of shallow biogenic gas in incised valley fills (the Qiantang River, eastern China): A case study. *Mar. Petroleum Geol.* 27 (4), 909–922. doi:10.1016/j.marpetgeo.2009.11.006

Lin, C-M., Zhuo, H-C., and Gao, S. (2005). Sedimentary facies and evolution in the Qiantang River incised valley, eastern China. *Mar. Geol.* 219 (4), 235–259. doi:10.1016/j.margeo.2005.06.009

Lin, Q., Wang, J., Su, P., and Hu, G. (2016a). Formation mechanism of authigenic gypsum in marine methane hydrate settings: Evidence from the northern South China Sea. *Deep Sea Res. Part I Oceanogr. Res. Pap.* 115, 210–220. doi:10.1016/j.dsr.2016.06.010

Lin, Q., Wang, J., Sun, F., and Lin, R. (2016b). Enhanced framboidal pyrite formation related to anaerobic oxidation of methane in the sulfate-methane transition zone of the northern South China Sea. *Mar. Geol.* 379, 100–108. doi:10.1016/j.margeo.2016.05.016

Lin, Z., Lu, Y., Xu, L., Gong, J., Lu, H., Teichert, B., et al. (2016c). Stable isotope patterns of coexisting pyrite and gypsum indicating variable methane flow at a seep site of the Shenhu area, South China Sea. *J. Asian Earth Sci.* 123, 213–223. doi:10.1016/j.jseaes.2016.04.007

Lin, Z., Peckmann, J., Lu, Y., Xu, L., Strauss, H., Zhou, H., et al. (2016d). How sulfate-driven anaerobic oxidation of methane affects the sulfur isotopic composition of pyrite: A sims study from the South China sea. *Chem. Geol.* 440, 26–41. doi:10.1016/j.chemgeo.2016.07.007

Lin, Z., Strauss, H., Lu, Y., Gong, J., Xu, L., Lu, H., et al. (2017). Multiple sulfur isotope constraints on sulfate-driven anaerobic oxidation of methane: Evidence from authigenic pyrite in seepage areas of the South China Sea. *Geochimica Cosmochimica Acta* 211, 153–173. doi:10.1016/j.gca.2017.05.015

Lin, Z., Sun, X., Yang, L., and Xu, L. (2012). Formation mechanism of authigenic gypsum in marine methane hydrate settings: Evidence from the northern South China Sea [J]. *Mineral. Deposits* 115 (31), 1–2. doi:10.16111/j.0258-7106.2012.s1.218

Liu, X., Fike, D., Li, A., Dong, J., Xu, F., Zhuang, G. C., et al. (2019). Pyrite sulfur isotopes constrained by sedimentation rates: Evidence from sediments on the East China Sea inner shelf since the late Pleistocene. *Chem. Geol.* 505, 66–75. doi:10.1016/j.chemgeo.2018.12.014

Liu, X., Li, A., Dong, J., Lu, J., Huang, J., and Wan, S. (2018a). Provenance discrimination of sediments in the Zhejiang-Fujian mud belt, East China Sea: Implications for the development of the mud depocenter. *J. Asian Earth Sci.* 151, 1–15. doi:10.1016/j.jseaes.2017.10.017

Liu, X., Li, A., Dong, J., Zhuang, G-C., Xu, F., and Wan, S. (2018b). Nonevaporative origin for gypsum in mud sediments from the East China Sea shelf. *Mar. Chem.* 205, 90–97. doi:10.1016/j.marchem.2018.08.009

Liu, X., Li, A., Fike, D., Dong, J., Xu, F., Zhuang, G. C., et al. (2020a). Environmental evolution of the East China Sea inner shelf and its constraints on pyrite sulfur contents and isotopes since the last deglaciation. *Mar. Geol.* 429, 106307. doi:10.1016/j.margeo.2020.106307

Liu, X., Li, A., Ma, Z., Dong, J., Zhang, K., Xu, F., et al. (2020b). Constraint of sedimentary processes on the sulfur isotope of authigenic pyrite (in Chinese with English abstract) [J]. *Chin. J.* 38 (1), 124–137. doi:10.14027/j.issn.1000-0550.2019.073

Liu, X., Zhang, M., Li, A., Dong, J., Zhang, K., Gu, Y., et al. (2022). Sedimentary pyrites and C/S ratios of mud sediments on the East China Sea inner shelf indicate late Pleistocene-Holocene environmental evolution. *Mar. Geol.* 450, 106854. doi:10.1016/j.margeo.2022.106854

Liu, X., Zhang, M., Li, A., Fan, D., Dong, J., Jiao, C., et al. (2021). Depositional control on carbon and sulfur preservation onshore and offshore the Oujiang Estuary: Implications for the C/S ratio as a salinity indicator. *Cont. Shelf Res.* 227, 104510. doi:10.1016/j.csr.2021.104510

Love, L. G., and Amstutz, G. C. (1966). Review of microscopic pyrite from the devonian chattanooga shale and rammelsberg banderz [J]. *Fortschr Mineral.* 43, 273–309.

Miao, X., Feng, X., Liu, X., Li, J., and Wei, J. (2021). Effects of methane seepage activity on the morphology and geochemistry of authigenic pyrite [J]. *Mar. Petroleum Geol.* 133, 105231. doi:10.1016/j.marpetgeo.2021.105231

Middelburg, J., and Nieuwenhuize, J. (1998). Carbon and nitrogen stable isotopes in suspended matter and sediments from the Schelde Estuary. *Mar. Chem.* 60 (3), 217–225. doi:10.1016/S0304-4203(97)00104-7

Ni, Y., Dai, J., Zou, C., Liao, F., Shuai, Y., and Zhang, Y. (2013). Geochemical characteristics of biogenic gases in China. *Int. J. Coal Geol.* 113, 76–87. doi:10.1016/j.coal.2012.07.003

Pirlet, H., Wehrmann, L., Brunner, B., Frank, N., Jan, D., Rooij, D., et al. (2010). Diagenetic formation of gypsum and dolomite in a cold-water coral mound in the Porcupine Seabight, off Ireland: Diagenetic gypsum in a cold-water coral mound. *Sedimentology* 57 (3), 786–805. doi:10.1111/j.1365-3091.2009.01119.x

Richardson, J., Keating, C., Lepland, A., Hints, O., Bradley, A., and Fike, D. (2019). Silurian records of carbon and sulfur cycling from Estonia: The importance of depositional environment on isotopic trends. *Earth Planet. Sci. Lett.* 512 (4), 71–82. doi:10.1016/j.epsl.2019.01.055

Rickard, D., and Luther, G. (2007). Chemistry of iron sulfides. *Chem. Rev.* 107 (2), 514–562. doi:10.1021/cr0503658

Rickard, D., Mussmann, M., and Steadman, J. (2017). Sedimentary sulfides. *Sediment. Sulfides J. Elem.* 13 (2), 117–122. doi:10.2113/gselements.13.2.117

Rickard, D. (2012). "Sulfidic sediments and sedimentary rocks," in *Developments in Sedimentology*. School of Earth and Ocean Sciences Cardiff University Wales (United Kingdom: Elsevier), 767–801. doi:10.1016/B978-0-444-52989-3.20001-9

Shevelkova, A. N., Sal'nikov, Y. I., Kuz'mina, N. L., Ryabov, A., Wilkin, R., Barnes, H. L., et al. (1996). The size distribution of framboidal pyrite in modern sediments: An indicator of redox conditions. *Geochimica Cosmochimica Acta* 60 (20), 3897–3912. doi:10.1016/0016-7037(96)00209-8

Siesser, W. G., and Rogers, J. J. S. (1976). Authigenic pyrite and gypsum in South West African continental slope sediments. *Environ. Sci. Geogr. Geol.* 23, 567–577. doi:10.1111/J.1365-3091.1976.TB00068.X

Sun, X., Fan, D., Liao, H., and Tian, Y. (2020). Fate of organic carbon burial in modern sediment within Yangtze River estuary. *J. Geophys. Res. Biogeosciences* 125 (2), 1–20. doi:10.1029/2019JG005379

Taylor, K., and Macquaker, J. (2011). Iron minerals in marine sediments record chemical environments. *Elements* 7 (2), 113–118. doi:10.2113/gselements.7.2.113

Vijaykumar, P., and Vaz, G. (1995). Occurrence of authigenic gypsum in a deep sea core off Madras [J]. *J. - Geol. Soc. India* 45, 483–486.

Vogel, M., Des Marais, D., Parenteau, M., Jahnke, L., Turk-Kubo, K., and Kubo, M. (2010). Biological influences on modern sulfates: Textures and composition of gypsum deposits from Guerrero Negro, Baja California Sur, Mexico [J]. *Sediment. Geol. - Sediment. Geol.* 223 (3), 265–280. doi:10.1016/j.sedgeo.2009.11.013

Wu, Y., Dittmar, T., Ludwichowski, K-U., Kattner, G., Zhang, J., Zhu, Z., et al. (2007). Tracing suspended organic nitrogen from the Yangtze River catchment into the East China sea. *Mar. Chem.* 107, 367–377. doi:10.1016/j.marchem.2007.01.022

Wu, Y., Eglinton, T., Yang, L., Deng, B., Montluçon, D., and Zhang, J. (2013). Spatial variability in the abundance, composition, and age of organic matter in surficial sediments of the East China sea: Spatial variability in the abundance. *J. Geophys. Res. Biogeosciences* 118, 1495–1507. doi:10.1002/2013jg002286

Yang, Z., Guo, R., Shi, X., He, S., Wang, L., Dai, M., et al. (2016). Bioaugmentation of Hydrogenispora ethanolica LX-B affects hydrogen production through altering indigenous bacterial community structure [J]. *Bioresour. Technol.* 211, 97. doi:10.1016/j.biortech.2016.03.097

Yuan, H-W., Chen, J., Ye, Y., Lou, Z. H., Jin, A. M., Chen, X. G., et al. (2017). Sources and distribution of sedimentary organic matter along the Andong salt marsh, Hangzhou Bay. *J. Mar. Syst.* 174, 78–88. doi:10.1016/j.jmarsys.2017.06.001

Zhao, B., Yao, P., Bianchi, T., and Yu, Z. (2021a). Controls on organic carbon burial in the eastern China marginal seas: A regional synthesis. *Glob. Biogeochem. Cycles* 35 (4), 1–27. doi:10.1029/2020GB006608

Zhao, J., Wang, J., Phillips, S., Liang, J., Su, P., Lin, Q., et al. (2021b). Non-evaporitic gypsum formed in marine sediments due to sulfate-methane transition zone fluctuations and mass transport deposits in the northern South China Sea. *Mar. Chem.* 233, 103988. doi:10.1016/j.marchem.2021.103988

Frontiers in Earth Science

TYPE Original Research
PUBLISHED 21 June 2023
DOI 10.3389/feart.2023.1186661

OPEN ACCESS

EDITED BY
Ying Zhao,
Ludong University, China

REVIEWED BY
Tianyuan Zheng,
Ocean University of China, China
Xuejing Wang,
Tianjin University, China

*CORRESPONDENCE
Maosheng Gao,
✉ gaomsh66@sohu.com

RECEIVED 15 March 2023
ACCEPTED 09 June 2023
PUBLISHED 21 June 2023

CITATION
Gao M, Sun Q, Dang X, Hou G, Guo F, Liu Z, Chang X and Zhao G (2023), Hydrogeochemical characteristic and recognization of saline groundwater formation and evolution in silty coast of the Yellow Sea and Bohai Sea, Eastern China.
Front. Earth Sci. 11:1186661.
doi: 10.3389/feart.2023.1186661

Hydrogeochemical characteristic and recognization of saline groundwater formation and evolution in silty coast of the Yellow Sea and Bohai Sea, Eastern China

Maosheng Gao[1,2]*, Qiming Sun[1,2,3], Xianzhang Dang[1], Guohua Hou[1,2], Fei Guo[4], Zhenlin Liu[1,5,6], Xinyue Chang[1] and Guangming Zhao[1,2]

[1]Qingdao Institute of Marine Geology, CGS, Qingdao, China, [2]Laboratory for Marine Geology, Pilot National Laboratory for Marine Science and Technology, Qingdao, China, [3]Hubei Key Laboratory of Yangtze Catchment Environmental Aquatic Science, School of Environmental Studies, China University of Geosciences, Wuhan, China, [4]Institute of Marine Science and Technology, Shandong University, Qingdao, China, [5]Chinese Academy of Geological Sciences, Beijing, China, [6]Faculty of Engineering, China University of Geosciences, Wuhan, Hubei, China

Saline groundwater is a valuable unconventional water resource in silty coastal zone, which contain complex and fragile sedimentary and hydrological environments that are widely distributed and vulnerable to human activities. Coastal groundwater salinization along the eastern coast of China since the late Pleistocene is thought to be a response to global environmental change. Previous studies have shown a spatial and temporal link between the development of saline groundwater and deposition of marine strata. However, groundwater salinization is becoming an increasing problem in coastal zone, and the hydrogeochemical characteristics and cause of the groundwater salinization or desalinization remain poorly understood. In this study, we compared the hydrogeochemical characteristics and relationships between saline groundwater and the sedimentary environment in two representative, muddy coastal zone of the Yellow Sea coast (YSC) and Bohai Sea coast (BSC). Our monitoring results show that the groundwater varies from fresh water, to brackish water, saltwater, and brine moving offshore of the BSC, with total dissolved solid (TDS) concentrations of 203–184,196 mg/L. In contrast, brine is absent from the YSC, where the TDS concentrations range from 280 to 41,690 mg/L. The relationships between δ^2H and δ^{18}O values indicate that freshwater–seawater–brine and freshwater–seawater mixing are the main processes leading to enrichment in TDS in the BSC and YSC, respectively. Based on the relationship between the major cations, Cl^-, and Cl/Br ratios, the results show that the groundwater salinity is primarily due to saltwater intrusion and secondly to water–rock interactions (i.e., evaporitic salt dissolution and cation exchange). The regression curves on plots of Na–Cl and (Ca+Mg)–(CO_3+SO_4) have negative slopes (–0.33 and –0.34, respectively) for the groundwater samples from the BSC and YSC, indicating the Na in groundwater exchange for Ca due to seawater or residual seawater intrusion. The saline groundwater (or brine) samples with reverse ion exchange indicate that seawater or residual seawater has invaded the aquifer, and in which Na^+ is replacing Ca^{2+} and Mg^{2+}. These results enhance our understanding of the formation and evolution of saline groundwater, and provide insights into groundwaters in other silty coastal zones.

KEYWORDS

silty coast, saline groundwater, hydrogeochemical characteristic, TDS, seawater intrusion

1 Introduction

The interactions between the ocean, land and human activities can affect muddy groundwater environments, making these areas more vulnerable to geological disasters (Wang et al., 2020). Coastal zone can be classified into five types: sandy, silty, bedrock, biological, and artificial coasts (Yang, 2004). Silty coasts are characterized by silty clay and clayey silt (Wang et al., 2003), and have been widely developed and utilized due to their broad expanse and flat terrain. Frequent changes in global sea level have led to the formation of saline groundwaters in silty coastal zone (Han et al., 2014; Larsen et al., 2017). Due to population growth and industrialization, water resources in silty coastal zone are becoming increasingly scarce and urgently needed. Understanding the formation and evolution of saline groundwater might contribute to preventing seawater intrusion and the protection of scarce freshwater resources.

Silty coastal zone has complex hydrogeological environments due to the presence of various types of groundwater, such as freshwater (total dissolved solids [TDS] < 1 g/L), brackish water (TDS: 1–3 g/L), saline groundwater (TDS: 3–50 g/L), and brine (TDS ≥ 50 g/L). For example, the groundwater varies from freshwater to brine on the coast of the Louisiana Gulf in the USA (Hanor and Mercer, 2010), Rhine-Meuse delta in the Netherlands (Griffioen et al., 2016), and the Burdekin delta in Australia (Fass et al., 2007). The complex sedimentary environment, as well as the variable hydrodynamic and hydrogeochemical conditions of silty coastal zone, hinder studies of the salinization mechanisms of groundwater (Cary et al., 2013). The salinization mechanisms of coastal groundwater include: 1) modern seawater intrusion (Reilly and Goodman, 1985; Andersen et al., 2005; Werner et al., 2013); 2) marine transgressive–regressive events associated with ancient sea water intrusion (Kooi et al., 2000; Santucci et al., 2016; Li et al., 2021); (3)evaporitic salt infiltration (Guan et al., 2010; Yang et al., 2016); 4) water–rock interactions (Merchán et al., 2015; Sun et al., 2023); 5) pollution by industrial and domestic waste water (Perrin et al., 2011; Cary et al., 2013); 6) extreme weather events such as storm surges and tsunamis (Yu et al., 2016).

Despite numerous studies of saline groundwater, the formation mechanisms of different types of groundwater remain unclear. Currently, the methods used for identifying the source and migration of water–salt include mainly (bio) geochemical analysis (major and trace elements, microorganisms, and isotopes ratios) and numerical simulations. Although (bio) geochemical analysis can provide information regarding the source, supply, and migration of water and salt, it cannot accurately quantify the contribution from different sources or predict the evolution of groundwater under complex environmental conditions. In contrast, numerical simulation can quantify the hydrodynamic and hydrogeochemical changes on different spatial and temporal scales, but provide limited insights into the formation mechanisms of saline groundwater.

Saline groundwater occurs widely in eastern coastal areas of China, including Hebei, Shandong, and Jiangsu provinces, where groundwater has been utilized for centuries, with brine being used for salt production on the northern coast of Shandong Province (Han et al., 1996). Previous studies have investigated saline groundwaters in these silty coastal zones. Zhao et al. (1993) proposed that changes in the Holocene sea level controlled the distribution of saline groundwater beneath the Jiangsu alluvial plain. Zhang X. et al. (2017) found that deep saline groundwater beneath the Jiangsu alluvial plain was mainly formed by leaching of salt from ancient marine strata. Ge (2018) investigated the salinity sources in porewater from the Jiangsu alluvial plain, and showed that the salinity was mostly derived from Holocene seawater, with the deep porewater salinity due mainly to contributions from late Pleistocene seawater. By simulating the porewater migration, Li et al. (2021) showed that saltwater in weak permeable layers was the potential cause of groundwater salinization.

The Bohai Sea coast (BSC) has more types of groundwater and a more complex evolution as compared with the Yellow Sea coast (YSC). Sun et al. (2006); Sun (2007) found that overexploitation of groundwater had caused various modes of seawater intrusion in BSC, including facial, stripped, veined, and leakage types (Zuo and Wan, 2006; Fei et al., 2009; Shi et al., 2014). Along the southern coast of Laizhou Bay, previous studies have focused mainly on the sedimentary environment (Han et al., 1999; Li et al., 1999; Liu et al., 2003), water–rock interactions (Zhang and Chen, 1996; Sun et al., 2023), and saltwater (brine) intrusion (Han D. et al., 2011; Han F. et al., 2011; Han et al., 2014). Early studies considered that the coastal brine was formed by the evaporation and concentration of ancient seawater stranded by marine transgressive–regressive events since the late Pleistocene (Han and Wu, 1982; Zhang and Chen, 1996; Wang et al., 2003). However, further research has questioned this hypothesis (Han et al., 1996; Xu et al., 2011; Yang et al., 2016; Sun et al., 2023). Although the previous studies linked the source of the saltwater to marine transgressive–regressive events, the proposed formation mechanisms vary widely. From the perspective of regional water circulation, there have been few studies of the saline groundwater (brine) characteristics and salinization, and most researches on groundwater salinization is focused on the two end-members mixing model of saline–fresh water, the mixing of the three end-members (freshwater–seawater–brine) and the hydrogeochemical evolution of saline groundwater remain poorly understood (Han D. et al., 2011; Han F. et al., 2011;

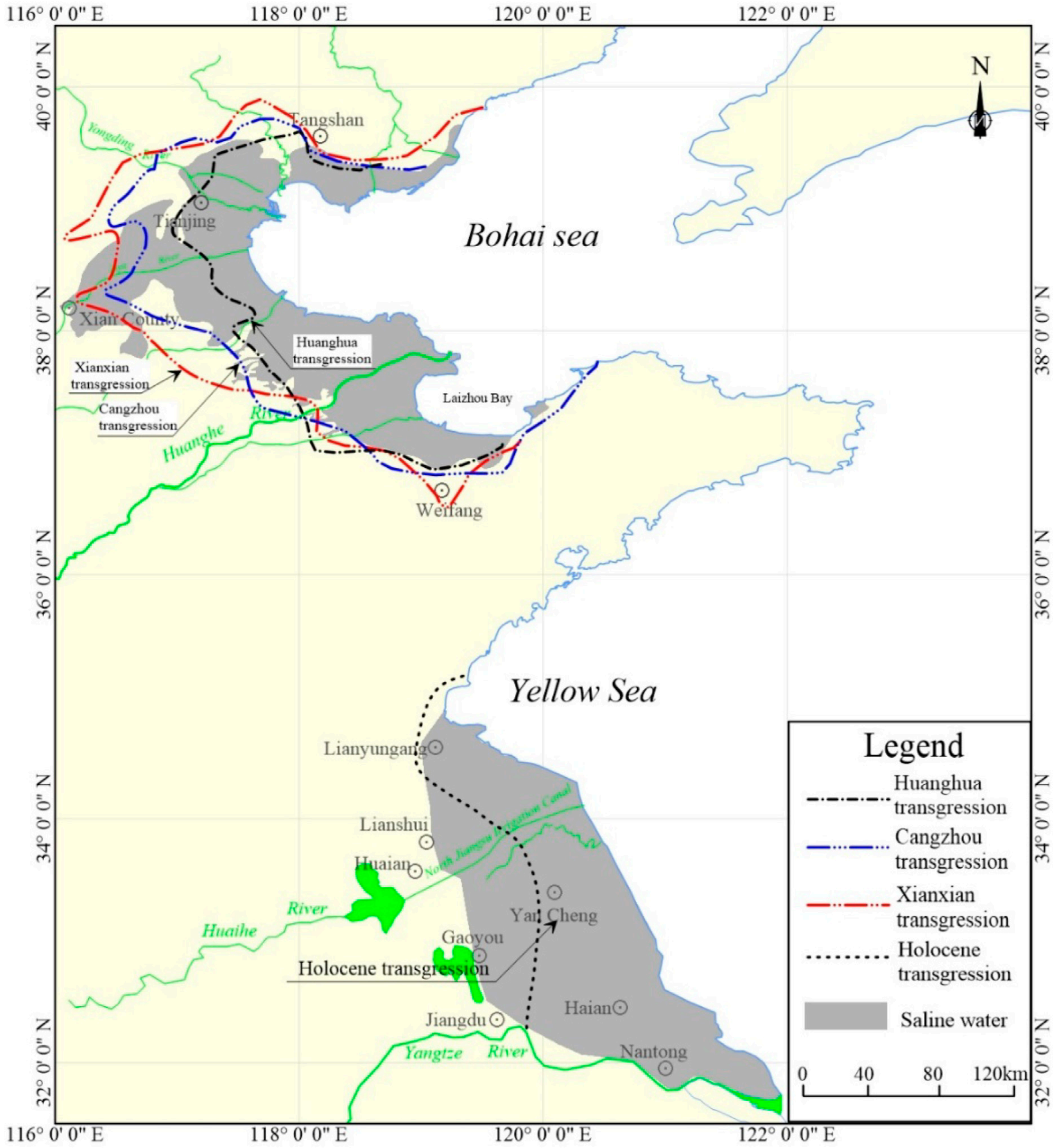

FIGURE 1
Saline groundwater and three marine transgressions in coast of eastern China (Modified from Xue, 2009; Hou et al., 2021).

Han et al., 2014; Hu et al., 2015; Dang, et al., 2022; Sun et al., 2023). Given this shortcoming, it is necessary to better understand the formation and evolution of saline groundwater in silty coastal zone (Gao et al., 2015).

Our research objectives were as follows: 1) to clarify the relationship between saline groundwater and the sedimentary environment in silty coastal zone; 2) to identify the water and salt sources in saline groundwater and the controlling factors on the hydrochemical evolution; and 3) to compare the formation and evolution of saline groundwater in the YSC and BSC.

2 Materials and methods

2.1 Regional setting

The distribution of saline groundwater in the silty coast of eastern China is mainly concentrated in coastal zone of Hebei, Tianjin, Shandong, and Jiangsu Provinces (Figure 1). These regions have an elevation below 30 m and a slope ratio <0.13‰. The climate is influenced by monsoon variations in BSC, with an average annual temperature of 8°C–12°C, showing warm-dry conditions and high evaporation rates. Specifically, the annual average evaporation is

TABLE 1 Distribution range and characteristics of transgression stratum in the Yellow Sea and Bohai Sea (modified by Li, 1986).

Transgression stratum	Distribution range and thickness	Epoch	Aquifer
I	Northern coast of Bohai Sea is the thickest (0–35 m or 0–25 m), west bank of Yellow Sea is the thinnest (0–16 m and 10–15 m)	Holocene	Shallow groundwater, confined aquifer
II	Northeast coast of Bohai Sea is the thickest (45–80 m), alluvial plain in northern Jiangsu, and the thinnest in western coast of Bohai Sea (20–45 m)	Late Pleistocene	Middle confined aquifer
III	Northeast coast of Bohai Sea is the thickest (98–161 m), western coast of Bohai Sea is the shallowest (40–70 m), and sedimentary thickness of the alluvial plain in northern Jiangsu is 40–62 m	Middle Pleistocene	Deep confined aquifer

1–4 times higher than annual average precipitation (Sun et al., 2006). The annual average precipitation of YSC is 1,050 mm, and the annual average evaporation is 951–1,120 mm (Li et al., 2021).

The North China depression belongs to the China-North Korea Paraplatform, while the Lower Yangtze depression falls within the Yangtze Paraplatform, as determined by their geological structures. The secondary depressions and uplifts are predominantly oriented in the NE direction. Since the Cenozoic period, these structures have been in a decline stage, while the surrounding mountains ranges have experienced relatively upward movement (Li, 1986). Due to extensive sedimentation, all uplifts and depressions have been buried by thick layers of sedimentary formations. In particular, the Quaternary strata are characterized by a thickness of 500–600 m. The major coastal rivers in the study area including the Yellow, Huaihe, Haihe and Luanhe rivers.

The sedimentary environment of saline groundwater in the silty coast is complex, and microscopic hydrogeochemical behavior occurs at the interfaces of seawater/saltwater, saltwater/brine, and freshwater/saltwater. Such behavior could lead to changes in the chemical type of groundwater, which in turn affects the intensity of groundwater circulation. The saline groundwater significantly impedes normal industrial and agricultural production. Conversely, the overexploited fresh groundwater has changed the hydrodynamic conditions of local groundwater. This has resulted in saltwater intrusion into freshwater aquifers, causing geological disasters such as groundwater salinization and soil secondary salinization, which seriously threatens the sustainable development of the coastal ecological environment.

2.2 Sedimentary environment

The BSC and YSC have been the sites of deposition of three marine sediment layers since the last glacial period (Qing and Zhao, 1985). These layers are closely linked to changes in global sea level, and correspond to the Cangzhou (Qp_3^1; 110–70 ka B.P.), Xianxian (Qp_3^3; 40–25 ka B.P.), and Huanghua (Q_h^2, 7–2.5 ka B.P.) transgressions. The general distribution and thickness of each sediment layer are provided in Table 1. The largest transgressive event occurred during the middle Holocene, with the boundary extending to the west coast of Yellow Sea (i.e., the northern Jiangsu alluvial plain). Coeval ancient or invasive seawater is stored in these alternating continental–marine facies sedimentary strata. The sedimentary environment along these silty coasts varies greatly due to the combined effects of tectonic activity, sea level rise, topography, and paleoclimate. The sedimentary environment has undergone major changes, especially during the early stages of the regressions. As such, the groundwater consists of multiple types and is stratified.

The distribution of saline groundwater along the eastern coast of China is mainly controlled by the topography. Groundwater flow onto alluvial fans at mountain fronts penetrates into the relatively low alluvial plain and finally flows into the river delta. The northern saltwater area is mainly the Luxi Plain, and the southern saltwater area is the low hilly area from southwest Shandong Province to the Yangtze River, which is mainly the alluvial plain in northern Jiangsu Province. Although saltwater in northern Jiangsu Province is not connected with that in the northern China, there is exchange of saline groundwater between the saltwater in northern Jiangsu Province and that in northern China due to the effects of former Yellow River and geological structure.

In Cangzhou in Hebei Province, a saltwater layer along the Binhai–South Canal is sourced from the Holocene to lower Pleistocene strata, and the salt water to the west of the South Canal–Ziya River occurs only in the Holocene and Upper Pleistocene strata. The depth of the saltwater layer ranges from 20 to 280 m. Based on the burial conditions and hydraulic properties, the groundwater is typically divided into shallow and deep saline groundwaters. The shallow groundwater is <60 m deep and mostly Holocene saltwater. The deep groundwater is >60 m deep and mostly late middle Pleistocene saltwater (Li, 1986). From the land to ocean, the groundwater exhibits obvious zonation: HCO_3–Ca·Mg → HCO_3–Ca·Na → HCO_3·Cl–Na·Ca → Cl·SO_4–Na → Cl–Na. The shallow groundwater beneath the alluvial plain in northern Jiangsu Province is mainly saltwater. The deeply confined aquifer was mainly recharged by precipitation during the late Pleistocene cold periods, and the shallow groundwater was mainly recharged by precipitation during the Holocene warm period. The salinity is mainly derived from ancient residual seawater that has undergone strong evaporation.

The distribution of saline groundwater is closely associated with coastline changes. For example, since the Holocene transgression, there have been several high sea-level stands (Figure 2). A comparison of the changes of the saline groundwater with the shoreline, seawater intrusion, and stratigraphy (Table 1) shows that the saltwater distribution is related to changes in the seawater intrusion and coastline. For example, the Yellow and Bohai Seas expanded to the surrounding inland plains. The distribution of saltwater (and marine transgressive strata) is

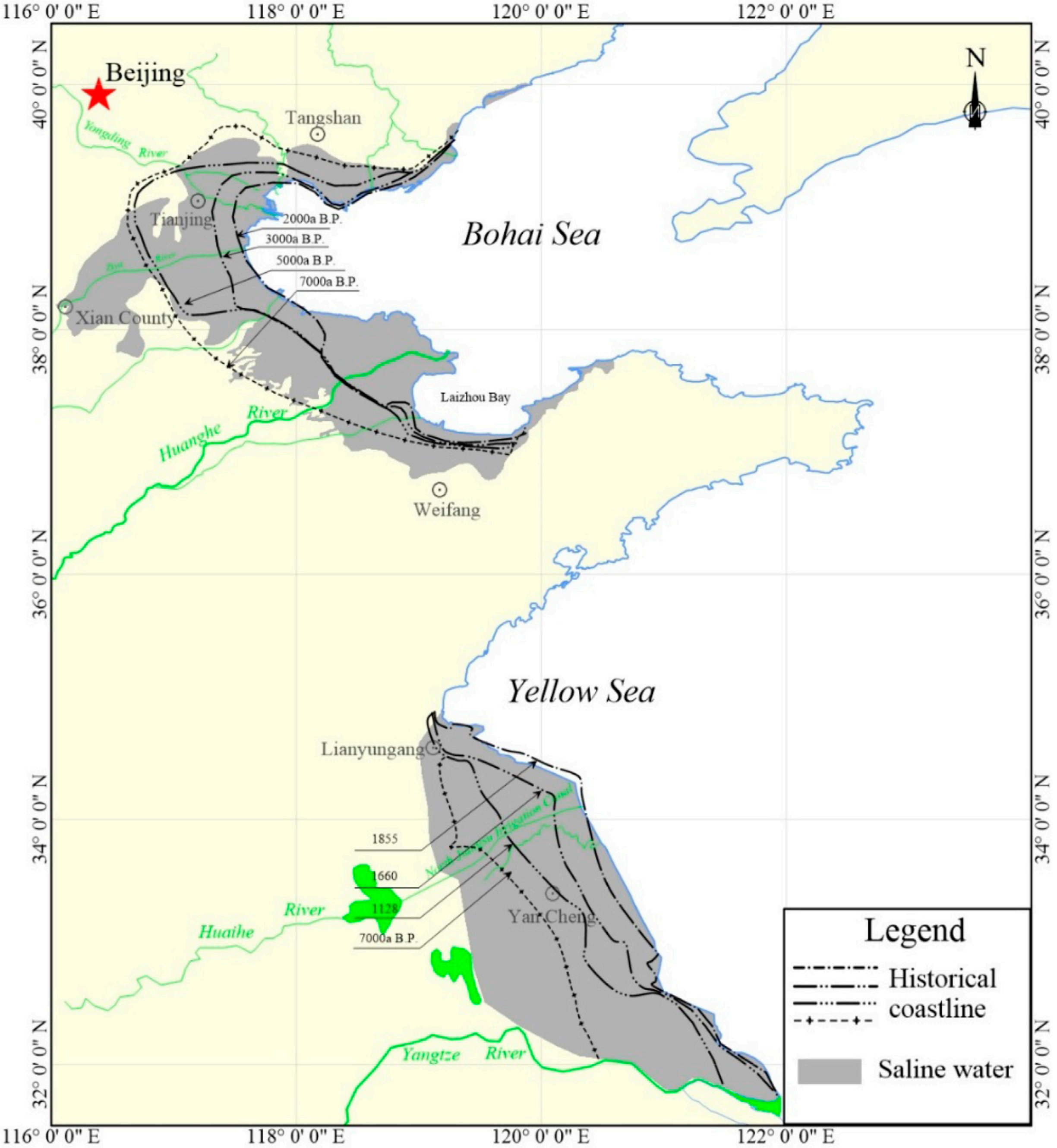

FIGURE 2
Transition of coastlines and distribution of saline groundwater.

greatest in the western BSC and YSC, and smallest along the northeast BSC and YSC (Figure 2). From the mountain front → central alluvial plain → river delta, the saltwater layer occurs in Holocene → late Pleistocene to Holocene → lower Pleistocene to Holocene strata, due to the temporal relationship between seawater intrusion and transgression. There is also a strong correlation between the saltwater chemistry and transgressive strata. From the ocean to land, the hydrochemical characteristics vary as follow: Cl–Na → SO_4·Cl–Na·Mg → HCO_3–Ca·Na. The TDS concentrations also change from high to low.

2.3 Dating and methods

A total of 139 samples were collected (Figure 3), including 124 groundwater samples, 12 surface water samples, one local rainwater sample, and two seawater samples, during four sampling campaigns from October 2016 to June 2020. Groundwater samples were divided into shallow groundwater samples (depth < 30 m) and deep groundwater samples (depth > 30 m), which were obtained from unconfined and confined aquifers, respectively. The surface water included eight samples from the YSC and four samples from the BSC.

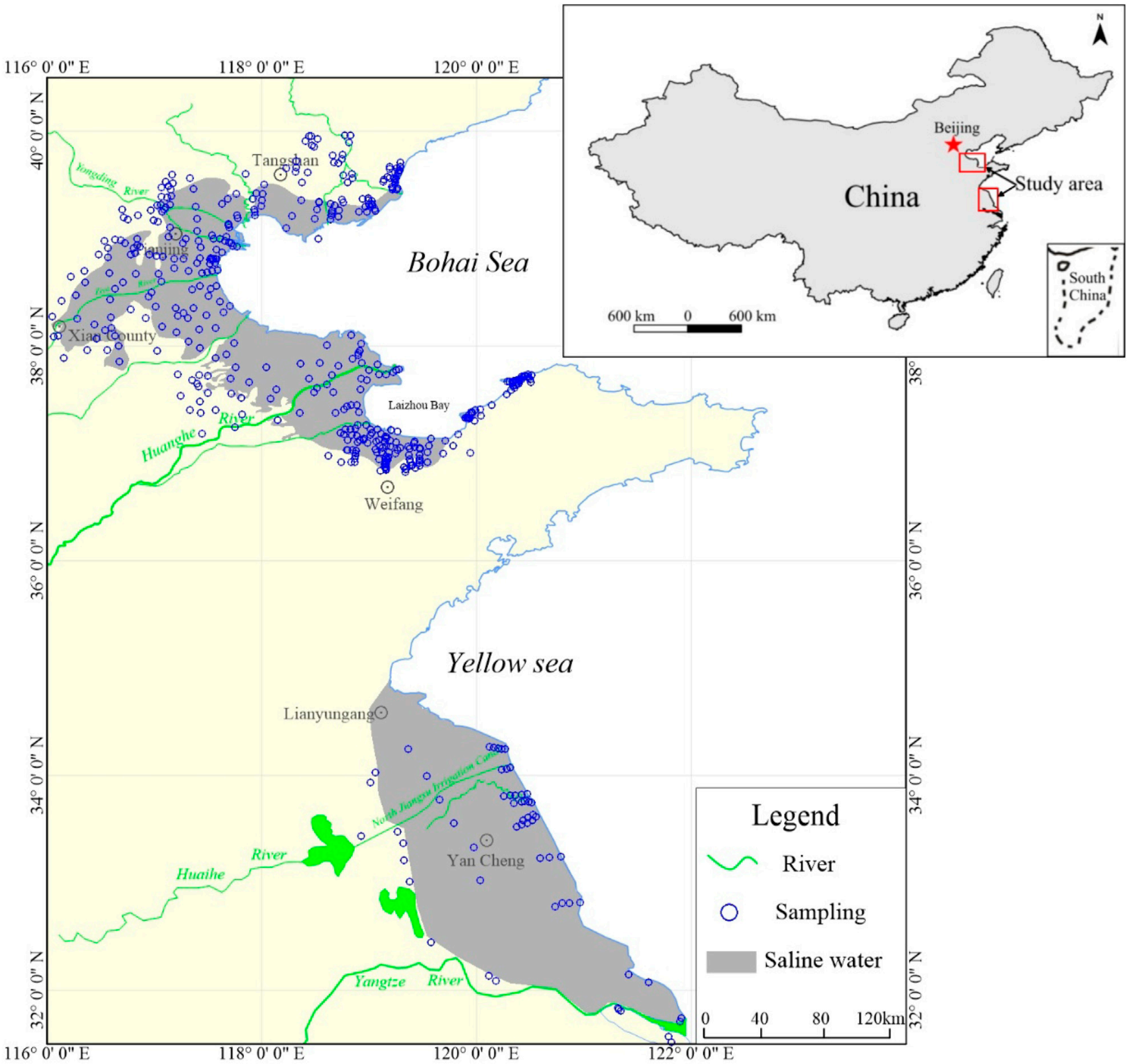

FIGURE 3
Distribution of saline groundwater and location of sampling points.

All samples were filtered through a 0.22 μm filtration membrane, cationic analysis samples are pretreated with a 6 mmol/L nitrate water at pH < 2. Stable isotope (δ^2H, δ^{18}O) testing samples were filled with 10 mL brown glass bottle, and the hydrochemical test samples were filled with 500 mL plastic bottle.

Groundwater sampling depths and pH values were measured *in situ* using Eureka Manta+ (Water quality Multiprobe Sonde). The concentrations of K^+, Na^+, Ca^{2+}, Mg^{2+}, and Br^-ions were measured using inductively coupled plasma analysis (ICAP–7400), while SO_4^{2-} and Cl^-ions were determined using ion chromatography (ICS–600). The HCO_3^- concentrations of samples were measured using titration. The TDS is obtained by evaporating the water at 105°C–110°C and weighing the total amount of the resulting dried residue, or is calculated by all dissolved component concentrations summed minus one-half of the bicarbonate. The water samples were tested at the Experimental & Testing Center of Marine Geology, Ministry of Natural Resources, China, using high-temperature pyrolysis-isotope ratio mass spectrometry. The values of δ^{18}O and δ^2H were calculated with respect to Vienna Standard Mean Ocean Water (VSMOW), and the uncertainties in δ^2H and δ^{18}O were ± 1.0‰ and ± 0.2‰, respectively.

At the same time, this study collected 239 hydrochemical data and 172 isotope data (δ^{18}O and δ^2H) in BSC and YSC published papers (Han et al., 1996; Xue et al., 2000; Han D. et al., 2011; Han F. et al., 2011; Han et al., 2014; Du et al., 2015; Yang et al., 2016; Zhang Y. et al., 2017).

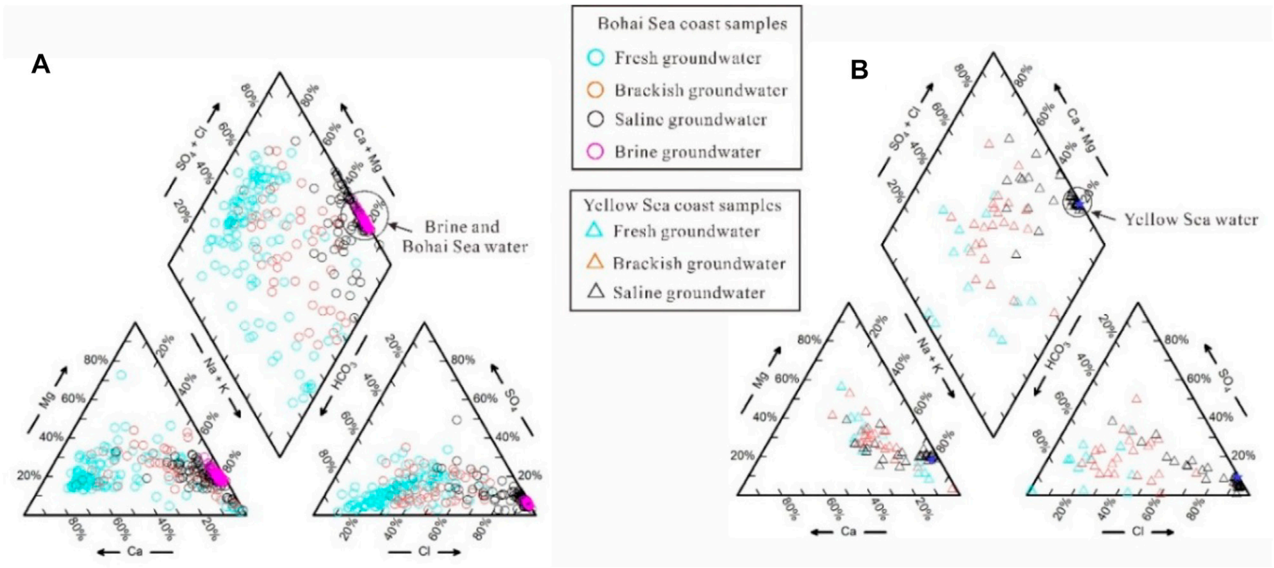

FIGURE 4
Piper triplex diagram [**(A)** BSC, **(B)** YSC].

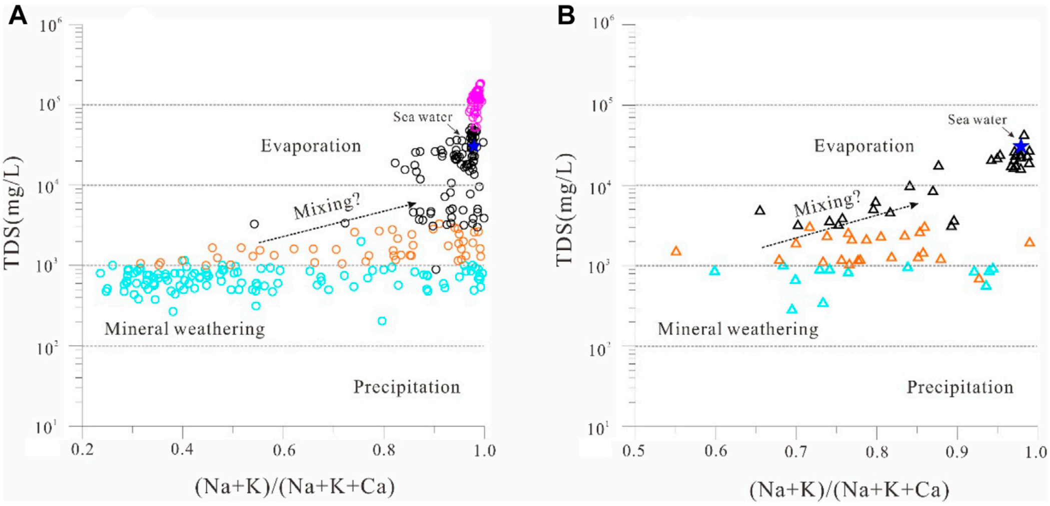

FIGURE 5
Gibbs diagram [**(A)** BSC, **(B)** YSC].

3 Results

3.1 Hydrochemistry

The TDS concentrations of groundwater in the BSC and YSC range from 204 to 184,196 mg/L and 280 to 41,690 mg/L, respectively. The distribution of groundwater chemical types included (Zhou, 2013): freshwater, brackish water, saline water, and brine, with a predominance of freshwater–brackish water–saline water–brine from land to ocean in the BSC, and freshwater–brackish water–saltwater in the YSC. As mentioned earlier, the hydrogeochemical types exhibit distinct zonation in the silty coasts. In the BSC, the freshwater is mainly HCO_3–Ca, HCO_3–Ca·Mg, HCO_3–Na; brackish water is HCO_3–Na and Cl–Na; saltwater and brine is Cl–Na (Figure 4A). In the YSC, freshwater is HCO_3–Ca and HCO_3–Na, brackish water is HCO_3–Na, HCO_3–Mg, and Cl–Na, and saltwater is Cl–Na (Figure 4B).

Gibbs diagrams are frequently used to characterize the primary factors that influence the chemical composition of groundwater, including rainfall, mineral weathering, and evaporation (Rajmohan et al., 2021; Yang et al., 2021). Figure 5 illustrates that mineral weathering is the dominant control on freshwater chemistry.

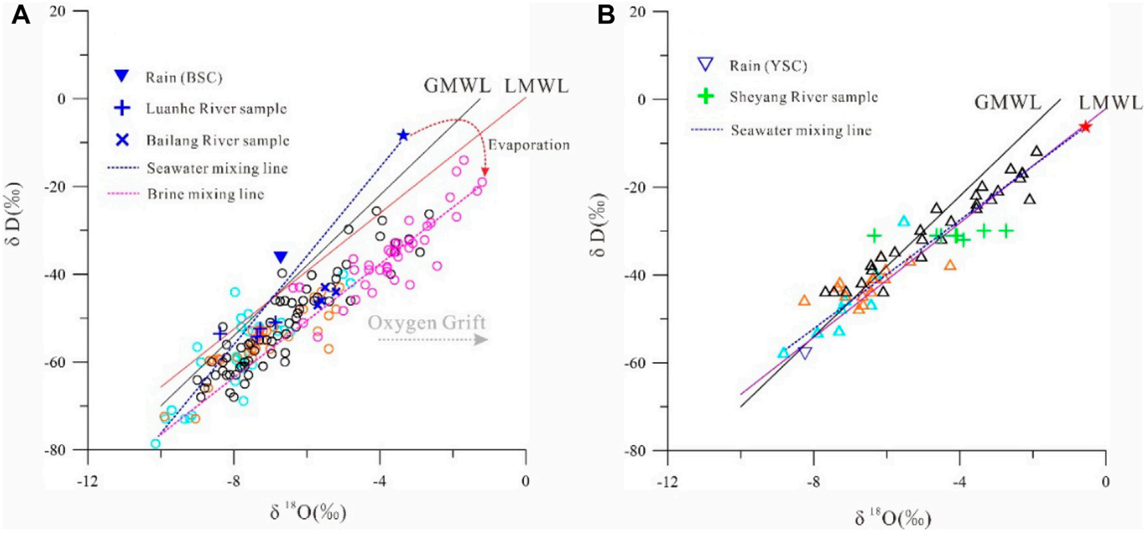

FIGURE 6
Relationships of Hydrogen and Oxygen isotope in various water samples [**(A)** BSC, **(B)** YSC].

Mineral dissolution and precipitation can modify the cationic components during runoff, such as calcium feldspar weathering to kaolinite and sodium feldspar weathering to montmorillonite, resulting in a broad distribution range of (Na+K)/(Na+K+Ca) in fresh groundwater (Figure 5). With increasing TDS concentrations, (Na+K)/(Na+K+Ca) decreases in saline water, indicating that seawater intrusion has progressively become the main factor. Brine samples along the BSC locate in the upper right corner of the Gibbs diagram (Figure 5A), indicating that they are controlled by strong evaporative concentration (Xu et al., 2021).

3.2 Isotopes

Stable isotopes can record the processes of recharge, mixing, and evaporation in coastal groundwaters. The global meteoric water line (GMWL; $\delta^2H = 8\cdot\delta^{18}O + 10$) was taken from Craig (1961), and the local meteoric water line (LMWL; $\delta^2H = 6.6\ \delta^{18}O + 0.3$) for the BSC is based on H–O isotope data for rainfall at Tianjin Station, which is located ~100 km from the study area (IAEA/WMO, 2006). The LMWL ($\delta^2H = 8.5\cdot\delta^{18}O + 17.7$) for the YSC is based on data from Nanjing Station (IAEA, 2011) (Figure 6). For the BSC, H–O isotope data deviate to the right of the GMWL and LMWL (Figure 6A), indicating that atmospheric precipitation has undergone evaporation or mixing with other waters before entering the aquifer. Many seasonal rivers, such as the Mihe and Weihe rivers, flow into the Bohai Sea. Affected by evaporation, isotopic fractionation of the river water is likely to occur. Most of the freshwater and brackish water isotopic compositions are similar to those of river water, indicating groundwater is closely linked to surface rivers. The freshwater with stable isotopic compositions that plot at the bottom left of Figure 6 may be related to groundwater recharge under cold conditions during the late Pleistocene (Han D. et al., 2011; Han F. et al., 2011; Li et al., 2017; Dang et al., 2020).

Given that the retention time of underground brine along the BSC ranges from 2 to 7 ka B.P. (Han et al., 2014; Dang et al., 2022), the saline groundwater is likely to be due to infiltration of ancient seawater after evaporation and salt concentration during Holocene transgression. In the BSC, the saline groundwater samples have a wide range of δ^2H and $\delta^{18}O$ values, which plot mostly along a seawater and brine mixing line, indicative of the freshwater–seawater–brine end-members. Fresh groundwater from the YSC plots mainly near the GMWL and LWML (Figure 6B), and the isotopic composition is similar to that of rainwater, indicating the freshwater is mainly derived from atmospheric precipitation. With increasing TDS concentrations, the isotope values gradually become enriched, and the brackish water and saltwater samples plot along the local seawater mixing line (Mao et al., 2020).

Figures 7, 8 show the relationships between Na^+, Mg^{2+}, Ca^{2+}, SO_4^{2-}, Br^-, and Cl^-concentrations in the water samples. On plots of Na–Cl (Figure 7A), Mg–Cl (Figure 7B), and Br–Cl (Figure 8A), the saltwater samples plot near the seawater–freshwater mixing line, and saltwater with higher TDS concentrations than seawater plots near the seawater evaporation line, indicating that the salinity is related to seawater and residual seawater after evaporation. The Cl/Br ratio of seawater is 655 (Siemann, 2003), and the Cl/Br ratio of terrestrial freshwater is generally <<655. The Cl/Br ratio is often used to identify the salinity source of coastal groundwater (Liu et al., 2017). As shown in Figure 8B, some of the saltwater and brine samples deviate from the seawater Cl/Br ratio line. NaCl precipitation occurs after seawater evaporation reaches halite saturation, and Br is not easy to precipitate, due to its stable chemical properties; thus, the Cl/Br ratio of residual seawater decreases (Figure 8B). However, during recharge by atmospheric precipitation, evaporitic salts in marine strata are easily dissolved into groundwater, resulting in increasing Cl/Br ratios (Cartwright et al., 2004; 2006). In plots of SO_4–Cl and Ca–Cl (Figures 7C, D), the water samples deviate from mixing or evaporation lines, particularly the Cl/Br ratios of the freshwater and

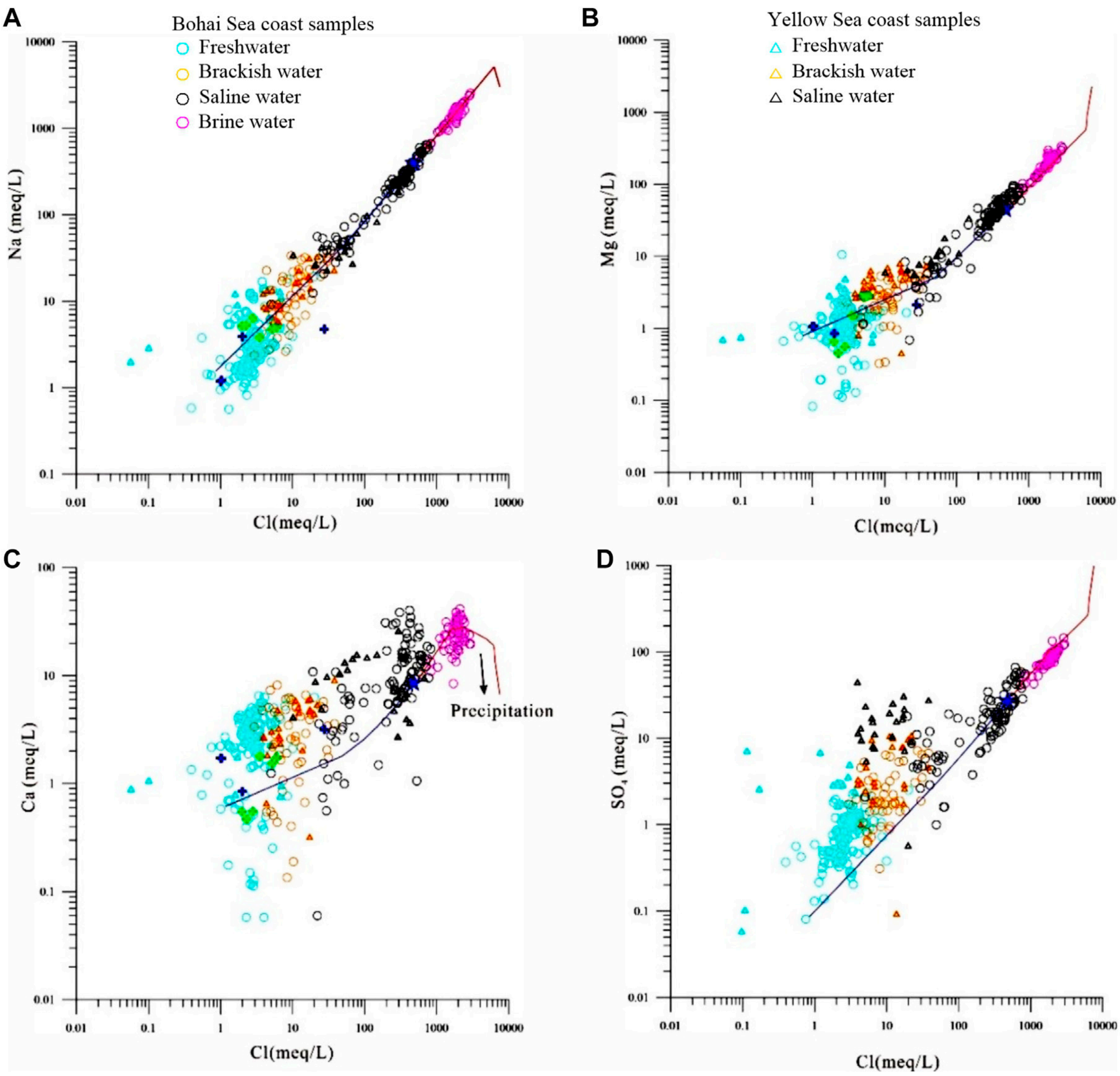

FIGURE 7
Relationship between major ions (A is Na^+, B is Mg^{2+},C is Ca^{2+}, D is $SO_4{}^{2-}$) and chloride ions in various water samples (blue is simulation mixing curve of seawater and fresh water, and the red is evaporation line of seawater in BSC).

brackish water samples, which deviate significantly from the seawater ratio (Figure 8B). This indicates that mixing with seawater or concentrated saltwater, in combination with hydrogeochemical effects such as mineral precipitation–dissolution, and ion exchange may have modified the groundwater composition during its formation and evolution.

4 Discussion

4.1 Hydrochemical process

In general, Ca dominates terrestrial groundwater, and the Ca/Mg ratio is >1 (Abu-alnaeem et al., 2018). Magnesium in saline groundwater is only exceeded in concentration by Cl and Na, and the Ca/Mg ratio is much lower than that of terrestrial freshwater. Due to seawater intrusion, groundwater Ca/Mg ratios will change significantly. Most of the Ca/Mg ratios are >1 in the fresh groundwater samples (Figure 9A), indicative of mineral weathering and groundwater recharge and runoff. The dissolution of gypsum increases the Ca and SO_4 contents, which also explains why the freshwater and brackish water samples are located above the seawater mixing line in plots of SO_4–Cl and Ca–Cl (Figures 7C, D); Weathering of silicate minerals such as plagioclase means that some freshwater samples plot above the 1:1 line of Ca-containing minerals (gypsum, calcite, and mica) (Figure 9B). With increasing Cl contents, the Ca/Mg ratios of the brackish water and saltwater samples approach that of seawater (Figure 9A), indicating seawater intrusion. The Ca/Mg ratios of the saltwater and brine samples are less than that of seawater. The salinity of the brine reflects that of residual seawater after evaporation.

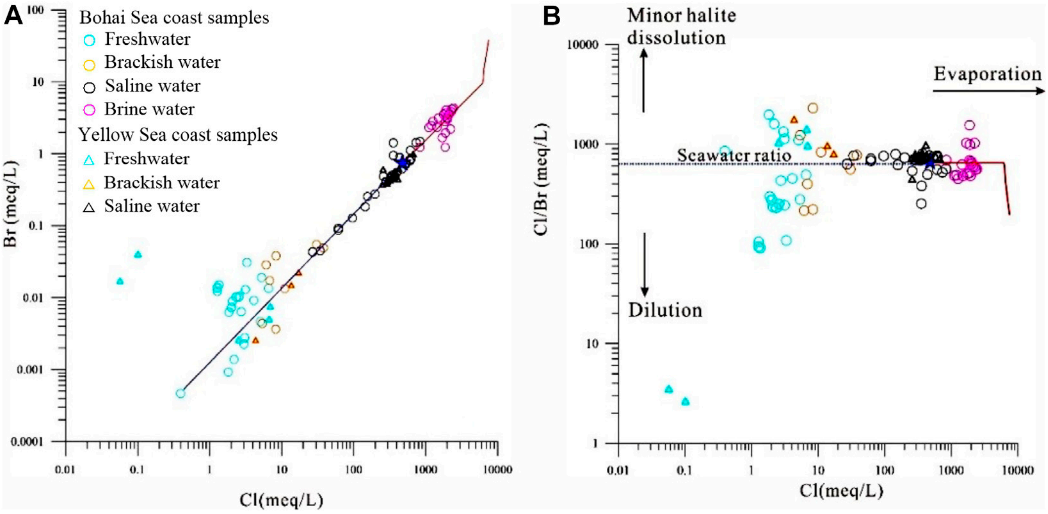

FIGURE 8
Correlation diagram of bromine and chlorine in underground water samples [**(A)** Bromine and chlorine, **(B)** Bromine/chlorine and chlorine).

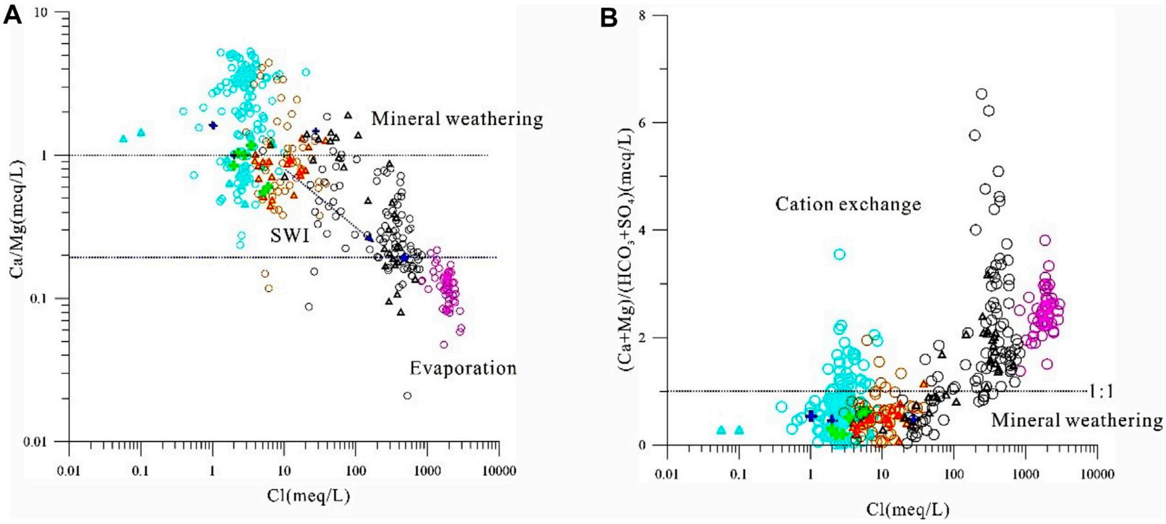

FIGURE 9
Relationship between Ca/Mg and Cl [**(A)**. Ca/Mg and Cl **(B)**. $(Ca+Mg)/(HCO_3+SO_4)$ and Cl].

When the seawater evaporated, Ca-containing minerals such as calcite and muscovite were precipitated (Wang, 2021). The Ca^{2+} in the residual seawater was consumed, and the Ca/Mg ratios of the residual seawater decreased.

When the salinity changes significantly, such as aquifer desalination or seawater intrusion, there may be ion exchange between the groundwater and clay minerals in the aquifer medium (Eq. 1), and a reverse ion exchange (RIE) process may also occur (Eq. 2) (Nogueira et al., 2019; Rajmohan et al., 2021).

$$\mathrm{Na\,(K)-Clay+Ca^{2+}\,(Mg^{2+})_{aq}=2Na^{+}\,(K^{+})_{aq}+Ca\,(Mg)-Clay,} \tag{1}$$

$$\mathrm{Ca\,(Mg)-Clay+2Na^{+}\,(K^{+})_{aq}=Ca^{2+}\,(Mg^{2+})_{aq}+Na\,(K)-Clay,} \tag{2}$$

The relationships between Na–Cl and $(Ca+Mg)–(HCO_3+SO_4)$ can well be indicative of cation exchange. If cation exchange is the cause of enrichment of Na^+ or Ca^{2+} (Mg^{2+}) in groundwater, then the water samples should plot near the equilibrium line with a slope of about −1 (Xiao et al., 2014). As shown in Figure 10A, the slopes of the groundwater regression curves are −0.33 and −0.34 for the BSC and YSC, respectively. The saltwater (brine) samples are located in the RIE field, indicating that seawater or residual seawater has infiltrated down into the aquifer and undergone exchange

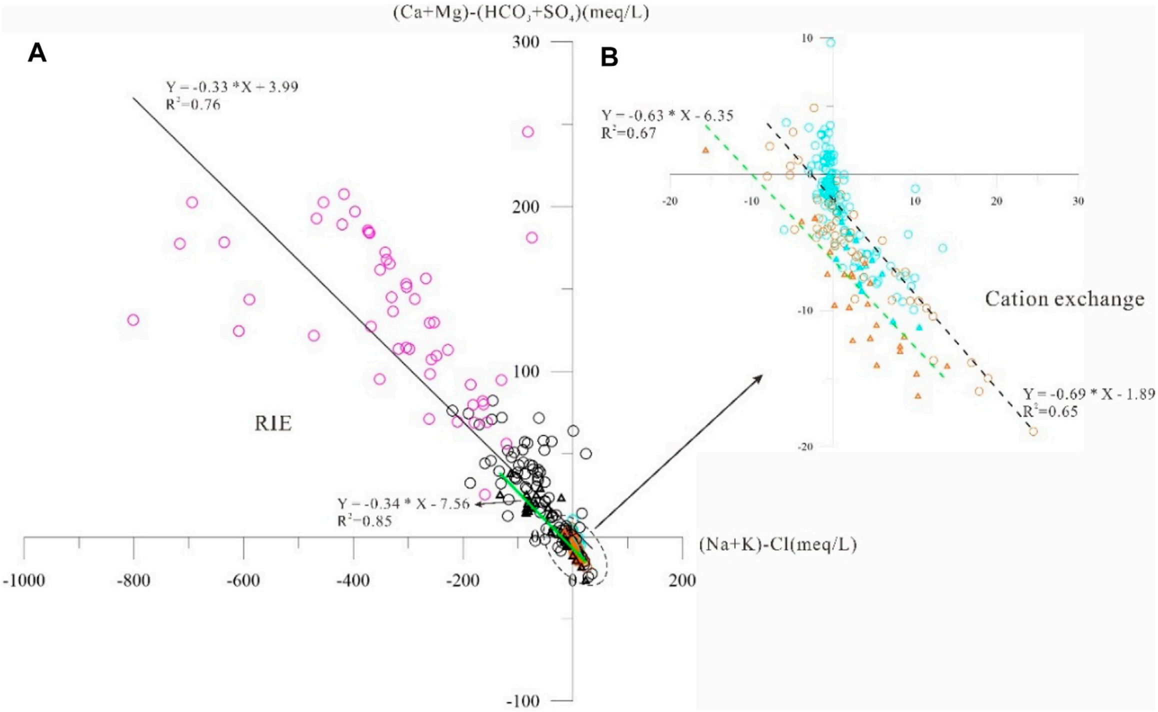

FIGURE 10
Relationship between (Na−Cl) and (Ca+Mg)−(HCO_3+SO_4) in coastal groundwater [**(A)**. all water samples, **(B)**. fresh and brackish water samples].

between Na^+ (K^+) and Ca^{2+} (Mg^{2+}) via interactions with clay during seawater intrusion. This also explains why the (Ca+Mg)/(HCO_3+SO_4) value is >1 for the saltwater and brine samples. The slopes of the regression curves for the freshwater and brackish water samples are −0.69 and −0.63 in the BSC and YSC, respectively (Figure 10B). Most water samples plot in the cation exchange area, indicating that the freshwater and brackish water samples have undergone cation exchange processes. After a regressive event, freshwater (i.e., river water and atmospheric precipitation) can recharge a saltwater aquifer, and Ca^{2+} (Mg^{2+}) is exchanged with the Na^+ adsorbed in the marine sediments, enriching Na^+ in the groundwater and resulting in Ca^{2+} or Mg^{2+} consumption. The (Ca+Mg)/(HCO_3+SO_4) values of the freshwater and slightly saline water samples are <1 (Figure 9B).

4.2 Groundwater formation mechanisms

Douglas et al. (2000) and Han and Currell (2018) proposed that coastal multi-type groundwaters are part of a complex system formed in numerous stages during ocean–land interactions, with mixing between two or three end-members. Chloride ions and oxygen isotopes in groundwater do not participate in reaction processes and can be used to examine mixing processes and saltwater (brine) evolution. Figure 11A shows the relationship between $\delta^{18}O$ values and Cl^-contents of the various BSC groundwater samples. Seawater–freshwater and brine-freshwater mixing lines were constructed based on conservation of mass. The saltwater and brine samples plot between the two mixing lines, and the water samples with a lower salinity than seawater plot near the seawater–freshwater mixing line. With increasing Cl^-, the groundwater samples gradually approach the saltwater–freshwater mixing line.

Since the late Pleistocene, the study area has experienced marine transgression–regression events in the silty coastal zone (Gao et al., 2016). Saltwater intrusion can occur in sand barrier–lagoon facies and other places, and the groundwater was salinized by seawater–freshwater mixing. As the sea level became stable, rivers began to prograde towards the ocean. Due to river sand transport and waves, the sand barrier–lagoon environment changed under the mild–arid paleoclimatic conditions, especially at the delta front. After evaporation, the concentrated saltwater in this semi-closed environment infiltrated the aquifer, and underwent cation exchange and mixing, which increased its salinity. The “seawater-brine-freshwater” end-members mixing occurred in this groundwater aquifer (Dang et al., 2022). Due to a marine regression, lateral infiltration of river waters and fresh groundwater is considered to have been the main saltwater dilution process in the Vietnam delta (Kwong and Jiao, 2016; Larsen et al., 2017; Van Lam et al., 2019). Due to the shallow channels submerged by seawater, frequent flooding events help to wash away ancient saltwater. However, due to mixing with river water and groundwater, mineral dissolution (gypsum) and RIE can occur. The brackish and freshwater samples of the present study have low Cl^-contents like the river water samples (Figure 11A), and similar stable isotopic composition.

A plot of $\delta^{18}O$ *versus* Cl^-in the YSC shows saltwater plots mainly near the seawater mixing line, and brackish water and freshwater

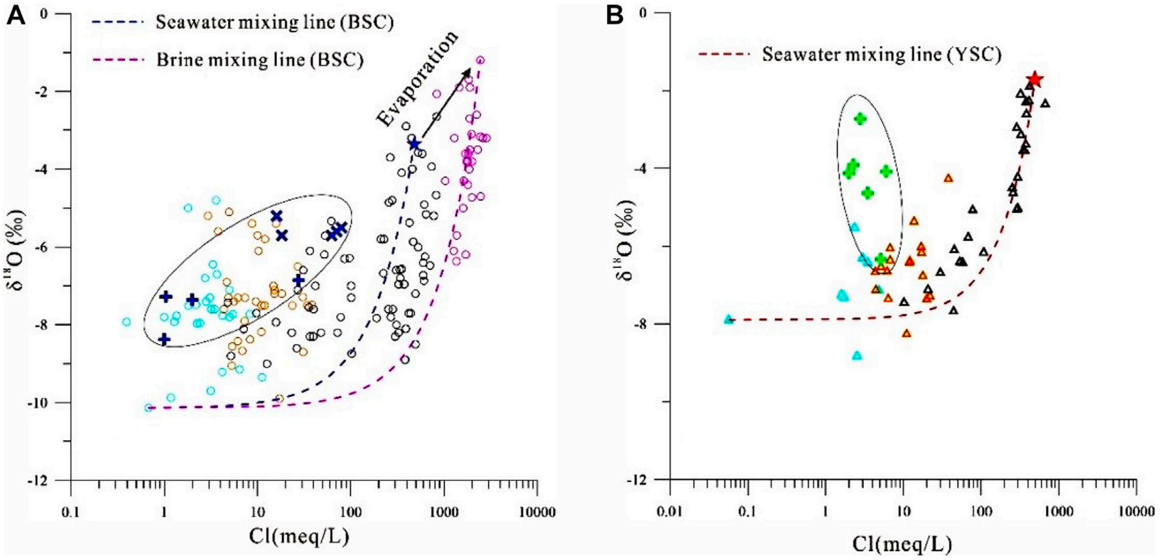

FIGURE 11
Relationship between δ18O and Cl of various water samples [**(A)** BSC, **(B)** YSC].

plot close to the river water samples (Figure 11B), indicating that the groundwater has undergone similar salinization and dilution processes. Brine has not yet been documented in the YSC. During a regression, parts of the YSC formed barrier–lagoons (Zhang et al., 2010). However, a large amount of freshwater (Yellow and Yangtze rivers) enters the ocean, which has promoted the transformation of lagoons into freshwater lakes (Ling, 2005). At the same time, the southern Yangtze River provides the material that has formed the tidal sand formations in the YSC (Li et al., 1998). Tidal sands are conducive to cation exchange (Figure 10B). In general, the groundwater is saltwater, but it does not have a high salt concentration due to the lack of stable and semi-enclosed lagoonal evaporitic environments in the YSC.

5 Conclusion

Saline groundwater occurs in complex and fragile sedimentary environments, and is widely distributed and susceptible to human activities in silty coastal zone. We investigated saline groundwaters in the BSC and YSC. Since the late Pleistocene, there have been three or more large-scale marine transgressive–regressive events along the eastern coast of China. The groundwater composition was found to be controlled by mineral weathering, seawater intrusion, and residual seawater that formed after evaporation. The dissolution of evaporitic salts in marine strata was also a contributor to groundwater salinity. Three end-member mixing (seawater, concentrated salt water (brine), freshwater) occurs in the BSC, whereas saline groundwater is mainly formed by two end-member mixing (seawater and freshwater) in the YSC. Brine has not yet been observed in the YSC, which may be due to the large amount of freshwater and lack of semi-enclosed environments, such as barrier–lagoon systems. The study highlights the complexity of groundwater evolution in silty coastal zones due to ocean-land interactions and human activities. Overall, this study provides valuable insights into the complex geochemical and hydrological processes that govern saline groundwater occurrence in the silty coastal zone. The findings have important implications for managing and conserving freshwater resources in vulnerable coastal zones.

Data availability statement

The datasets presented in this article are not readily available because the authors do not have permission to share data. Requests to access the datasets should be directed to gaomsh66@sohu.com.

Author contributions

MG performed "Writing–Original Draft and Review"; QS contributed to "Writing–Editing"; XD contributed to "Writing–Editing"; GH contributed to "Investigation"; FG contributed to "Software"; ZL helped perform "Methodology"; XC contributed to "Visualization". GZ contribution to "Software". All authors contributed to the article and approved the submitted version.

Funding

This study was financially supported by the National Natural Science Foundation of China (U2106203, 41977173, and 42076070), the National Geological Survey Project of China Geology Survey (No. DD20221775, DD20211401), the China-ASEAN maritime cooperation fund (Cooperative researches on the marine geo-environments and geo-hazards in the Yangtze River and the Red

River deltas), and National Natural Science Foundation Shandong Province of China (ZR2020MD079).

Conflict of interest

The authors declare that the research was conducted in the absence of any commercial or financial relationships that could be construed as a potential conflict of interest.

Publisher's note

References

Abu-Alnaeem, M. F., Yusoff, I., Ng, T. F., Alias, Y., and Raksmey, M. (2018). Assessment of groundwater salinity and quality in Gaza coastal aquifer, Gaza Strip, Palestine: An integrated statistical, geostatistical and hydrogeochemical approaches study. *Sci. Total Environ.* 615, 972–989. doi:10.1016/j.scitotenv.2017.09.320

Andersen, M. S., Nyvang, V., Jakobsen, R., and Postma, D. (2005). Geochemical processes and solute transport at the seawater/freshwater interface of a sandy aquifer. *Geochimica Cosmochimica Acta* 69 (16), 3979–3994. doi:10.1016/j.gca.2005.03.017

Cartwright, I., Weaver, T. R., and Fifield, L. K. (2006). Cl/Br ratios and environmental isotopes as indicators of recharge variability and groundwater flow: An example from the southeast murray basin, Australia. *Chem. Geol.* 231, 38–56. doi:10.1016/j.chemgeo.2005.12.009

Cartwright, I., Weaver, T. R., Fulton, S., Nichol, C., Reid, M., and Cheng, X. (2004). Hydrogeochemical and isotopic constraints on the origins of dryland salinity, Murray Basin, Victoria, Australia. *Appl. Geochem.* 19 (8), 1233–1254. doi:10.1016/j.apgeochem.2003.12.006

Cary, L., Casanova, J., Gaaloul, N., and Guerrot, C. (2013). Combining boron isotopes and carbamazepine to trace sewage in salinized groundwater: A case study in cap bon, Tunisia. *Appl. Geochem.* 34, 126–139. doi:10.1016/j.apgeochem.2013.03.004

Craig, H. (1961). Standard for reporting concentrations of deuterium and oxygen-18 in natural waters. *Science* 133 (3467), 1833–1834. doi:10.1126/science.133.3467.1833

Dang, X., Gao, M., Wen, Z., Hou, G., Jakada, H., Ayejoto, D., et al. (2022). Saline groundwater evolution in the Luanhe river delta (China) during the Holocene: Hydrochemical, isotopic, and sedimentary evidence. *Hydrology Earth Syst. Sci.* 26 (5), 1341–1356. doi:10.5194/hess-26-1341-2022

Dang, X., Gao, M., Wen, Z., Jakada, H., Hou, G., and Liu, S. (2020). Evolutionary process of saline groundwater influenced by palaeo-seawater trapped in coastal deltas: A case study in Luanhe river delta, China. *Coast. Shelf Sci.* 244, 106894. doi:10.1016/j.ecss.2020.106894

Douglas, M., Clark, I. D., Raven, K., and Bottomley, D. (2000). Groundwater mixing dynamics at a Canadian Shield mine. *J. Hydrology* 235 (1-2), 88–103. doi:10.1016/S0022-1694(00)00265-1

Du, Y., Ma, T., Chen, L., Shan, H., Xiao, C., Lu, Y., et al. (2015). Genesis of salinized groundwater in Quaternary aquifer system of coastal plain, Laizhou Bay, China: Geochemical evidences, especially from bromine stable isotope. *Appl. Geochem.* 59, 155–165. doi:10.1016/j.apgeochem.2015.04.017

Fass, T., Cook, P. G., Stieglitz, T., and Herczeg, A. L. (2007). Development of saline ground water through transpiration of sea water. *Groundwater* 45 (6), 703–710. doi:10.1111/j.1745-6584.2007.00344.x

Fei, Y., Zhang, Z., Song, H., Qian, Y., Chen, J., and Meng, S. (2009). Discussion of vertical variations of saline groundwater and mechanism in North China Plain. *Water Resour. Proctection* 25 (6), 3–10. (in Chinese).

Gao, M., Hou, G., and Guo, F. (2016). Conceptual model of underground brine formation in the silty coast of Laizhou Bay, Bohai Sea, China. *J. Coast. Res.* 74, 157–165. doi:10.2112/SI74-015.1

Gao, M., Zheng, Y., Liu, S., Wang, S., Kong, X., Zhao, J., et al. (2015). Paleogeographic condition for origin of underground brine in southern coast of Laizhou Bay, Bohai Sea. *Geol. Rev.* 61 (2), 393–400. (in Chinese).

Ge, Q. (2018). *The formation and Geochemical evolution of porewater in the coastal clay-rich aquitards-a case study in north Jiangsu coastal plain. Doctoral dissertation.* China University of Geosciences. (in Chinese).

Griffioen, J., Verweij, H., and Stuurman, R. (2016). The composition of groundwater in Palaeogene and older formations in The Netherlands. A synthesis. *Neth. J. Geosciences* 95 (3), 349–372. doi:10.1017/njg.2016.19

Guan, H., Love, A. J., Simmons, C. T., Makhnin, O., and Kayaalp, A. S. (2010). Factors influencing chloride deposition in a coastal hilly area and application to chloride deposition mapping. *Hydrology Earth Syst. Sci.* 14 (5), 801–813. doi:10.5194/hess-14-801-2010

Han, D., and Currell, M. J. (2018). Delineating multiple salinization processes in a coastal plain aquifer, northern China: Hydrochemical and isotopic evidence. *Hydrology Earth Syst. Sci.* 22 (6), 3473–3491. doi:10.5194/hess-22-3473-2018

Han, D., Kohfahl, C., Song, X., Xiao, G., and Yang, J. (2011a). Geochemical and isotopic evidence for palaeo-seawater intrusion into the south coast aquifer of Laizhou Bay, China. *Appl. Geochem.* 26 (5), 863–883. doi:10.1016/j.apgeochem.2011.02.007

Han, D. M., Song, X. F., Currell, M. J., Yang, J. L., and Xiao, G. Q. (2014). Chemical and isotopic constraints on evolution of groundwater salinization in the coastal plain aquifer of Laizhou Bay, China. *J. Hydrology* 508, 12–27. doi:10.1016/j.jhydrol.2013.10.040

Han, F., Wu, J., Zhang, Y., Lu, Y. m., Liu, L. l., Chen, Y. x., et al. (2011b). Melatonin ameliorates ischemic-like injury-evoked nitrosative stress: Involvement of HtrA2/PED pathways in endothelial cells. *J. Nanjing Univ. Nat. Sci.* 47 (3), 281–291. (in Chinese). doi:10.1111/j.1600-079X.2010.00838.x

Han, M., Zhao, M., Li, D., and Cao, X. (1999). Study on the ancient channels and the relationship between the ancient channels and the sea (salt) water intrusion of the south coastal plain of Laizhou Bay. *J. Nat. Disasters* 8 (2), 73–80. (in Chinese).

Han, Y., Meng, G., and Wang, S. (1996). *Quaternary underground brine in the coastal areas of the northern China.* Beijing: Science Press. (in Chinese).

Han, Y., and Wu, H. (1982). The origin of underground brine in the coastal plain of Laizhou Bay. *Geol. Rev.* 28 (2), 126–131. (in Chinese).

Hanor, J. S., and Mercer, J. A. (2010). Spatial variations in the salinity of pore waters in northern deep water Gulf of Mexico sediments: Implications for pathways and mechanisms of solute transport. *Geofluids* 10 (1-2), 83–93. doi:10.1111/j.1468-8123.2009.00271.x

Hou, G., Gao, M., Dang, X., and Chen, G. (2021). Water and salt sources and salinization of shallow saline groundwater in the coastal area of Yancheng, Jiangsu. *Mar. Geol. Quat. Geol.* 41 (4), 48–59. (in Chinese).

Hu, Y., Li, H., Li, Y., Shi, P., Yang, J., Hu, Z., et al. (2015). Hydrogeochemical recognization of seawater intrusion process at the typical profile in Laizhou Bay. *Geol. Surv. Res.* 38 (1), 41–50. (in Chinese).

IAEA (International Atomic Energy Agency) (2011). Global network of isotopes in precipitation. Available at: http://www-naweb.iaea.org/napc/ih/IHS_resources_gnip.ht-ml.

IAEA/WMO: Global Network of Isotopes in Precipitation (2006). *Global network of isotopes in precipitation. The GNIP database.* Vienna. Available at: http://www-naweb.iaea.org/napc/ih/IHS_resources_gnip.html.

Kooi, H., Groen, J., and Leijnse, A. (2000). Modes of seawater intrusion during transgressions. *Water Resour. Res.* 36 (12), 3581–3589. doi:10.1029/2000WR900243

Kwong, H. T., and Jiao, J. J. (2016). Hydrochemical reactions and origin of offshore relatively fresh pore water from core samples in Hong Kong. *J. Hydrology* 537, 283–296. doi:10.1016/j.jhydrol.2016.03.050

Larsen, F., Tran, L. V., Van Hoang, H., Tran, L. T., Christiansen, A. V., and Pham, N. Q. (2017). Groundwater salinity influenced by Holocene seawater trapped in incised valleys in the Red River delta plain. *Nat. Geosci.* 10 (5), 376–381. doi:10.1038/ngeo2938

Li, C., Zhang, J., and Yang, S. (1998). Characteristics and paleoenvironmental evolution of onshore tidal sandbodies in North Jiangsu Plain. *Sci. China* 28 (5), 418–424. (in Chinese).

Li, D., Han, M., Zhao, M., and Jiang, A. (1999). A study of the shallow-buried paleochannel zones and their relations with sea(salt)-water intrusion on the south coast plain of Laizhou Bay. *Acta Oceanol. Sin.* 21 (6), 64–71. (in Chinese).

Li, F. (1986). Discussion on underground saline water and sea intrusion in coastal plain of Yellow Sea and Bohai Sea. *Acta Oceanol. Sin.* 8 (4), 456–465. (in Chinese).

Li, J., Gong, X., Liang, X., Liu, Y., Yang, J., Meng, X., et al. (2021). Salinity evolution of aquitard porewater associated with transgression and regression in the coastal plain of Eastern China. *J. Hydrology* 603, 127050. doi:10.1016/j.jhydrol.2021.127050

Li, J., Liang, X., Jin, M., Yang, J., Ma, B., and Ge, Q. (2017). Origin and evolution of aquitard porewater in the Western coastal plain of Bohai Bay, China. *Groundwater* 55 (6), 917–925. doi:10.1111/gwat.12590

Ling, S. (2005). Study on models of the changes about sheyang lake in historical period. *J. Chin. Hist. Geogr.* 20 (3), 73–79. (in Chinese).

Liu, E., Zhang, Z., Shen, J., and Yang, L. (2003). Sedimentary characteristic of Weihe palaeochannel since late Pleistocene and their control to modern salt-water intrusion. *Geol. J. China Univ.* 9 (1), 47–53. (in Chinese).

Liu, S., Tang, Z., Gao, M., and Hou, G. (2017). Evolutionary process of saline-water intrusion in Holocene and late Pleistocene groundwater in southern Laizhou Bay. *Sci. Total Environ.* 607, 586–599. doi:10.1016/j.scitotenv.2017.06.262

Mao, C., Tan, H., Song, Y., and Rao, W. (2020). Evolution of groundwater chemistry in coastal aquifers of the Jiangsu, east China: Insights from a multi-isotope (δ2H, δ18O, 87Sr/86Sr, and δ11B) approach. *J. Contam. Hydrology* 235, 103730. doi:10.1016/j.jconhyd.2020.103730

Merchán, D., Auqué, L. F., Acero, P., Gimeno, M. J., and Causapé, J. (2015). Geochemical processes controlling water salinization in an irrigated basin in Spain: Identification of natural and anthropogenic influence. *Sci. Total Environ.* 502, 330–343. doi:10.1016/j.scitotenv.2014.09.041

Nogueira, G., Stigter, T. Y., Zhou, Y., Mussa, F., and Juizo, D. (2019). Understanding groundwater salinization mechanisms to secure freshwater resources in the water-scarce city of Maputo, Mozambique. *Sci. Total Environ.* 661, 723–736. doi:10.1016/j.scitotenv.2018.12.343

Perrin, J., Mascré, C., Pauwels, H., and Ahmed, S. (2011). Solute recycling: An emerging threat to groundwater quality in southern India. *J. Hydrology* 398 (1-2), 144–154. doi:10.1016/j.jhydrol.2010.12.024

Qing, W., and Zhao, S. (1985). The sedimentary model and quaternary transgression in the continental shelf of China. *Quat. Sci.* 01, 27–34.

Rajmohan, N., Masoud, M. H., and Niyazi, B. A. (2021). Impact of evaporation on groundwater salinity in the arid coastal aquifer, Western Saudi Arabia. *Catena* 196, 104864. doi:10.1016/j.catena.2020.104864

Reilly, T. E., and Goodman, A. S. (1985). Quantitative analysis of saltwater-freshwater relationships in groundwater systems—a historical perspective. *J. Hydrology* 80 (1-2), 125–160. doi:10.1016/0022-1694(85)90078-2

Santucci, L., Carol, E., and Kruse, E. (2016). Identification of palaeo-seawater intrusion in groundwater using minor ions in a semi-confined aquifer of the Río de la Plata littoral (Argentina). *Sci. Total Environ.* 566, 1640–1648. doi:10.1016/j.scitotenv.2016.06.066

Shi, J., Li, G., Liang, X., Chen, Z., Shao, J., and Song, X. (2014). Evolution mechanism and control of groundwater in the North China plain. *Acta Geosci. Sin.* 35 (5), 8–18. (in Chinese).

Siemann, M. G. (2003). Extensive and rapid changes in seawater chemistry during the phanerozoic: Evidence from Br contents in basal halite. *Terra* 15 (1), 243–248. doi:10.1046/j.1365-3121.2003.00490.x

Sun, Q., Gao, M., Wen, Z., Hou, G., Dang, X., Liu, S., et al. (2023). Hydrochemical evolution processes of multiple-water quality interfaces (fresh/saline water, saline water/brine) on muddy coast under pumping conditions. *Sci. Total Environ.* 857, 159297. doi:10.1016/j.scitotenv.2022.159297

Sun, X. (2007). *Sustainable utilization study of groundwater resources in Circum-Bohai-Sea region. Doctoral dissertation*. China University of Geosciences. (in Chinese).

Sun, X., Xu, J., Yang, Q., Shi, P., Zhong, X., Zhang, S., et al. (2006). Character and prevention strategies of sea (saline) water intrusion in Circum-Bohai-Sea region. *Geol. Surv. Res.* 29 (003), 203–211. (in Chinese).

Van Lam, N., Van Hoan, H., and Duc Nhan, D. (2019). Investigation into groundwater resources in southern part of the Red River's delta plain, Vietnam by the use of isotopic techniques. *Water* 11 (10), 2120. doi:10.3390/w11102120

Wang, X. (2021). Equilibrium between dolomitization and dedolomitization of a global set of surface water samples: A new theoretical insight on the dolomite inorganic formation mechanism. *Mar. Chem.* 235, 104017. doi:10.1016/j.marchem.2021.104017

Wang, Y., Gan, Y., Deng, Y., and Xie, X. (2020). Land-ocean interactions and their eco-environmental effects in the coastal zone: Current progress and future perspectives. *Bull. Geol. Sci. Technol.* 39 (1), 1–10. doi:10.19509/j.cnki.dzkq.2020.0101

Wang, Z., Meng, G., and Wang, S. (2003). Geochemistry modeling of quaternary subsurface brine in the south coast of the Laizhou Bay, Bohai Sea. *Mar. Geol. Quat. Geol.* 23 (1), 49–53. (in Chinese).

Werner, A. D., Bakker, M., Post, V. E., Vandenbohede, A., Lu, C., Ataie-Ashtiani, B., et al. (2013). Seawater intrusion processes, investigation and management: Recent advances and future challenges. *Adv. water Resour.* 51, 3–26. doi:10.1016/j.advwatres.2012.03.004

Xiao, G., Yang, J., Hu, Y., Du, D., Xu, Q., Qin, Y., et al. (2014). Hydrogeochemical recognition of seawater intrusion processes in Yang River and Dai River coastal plain of Qinhuangdao city. *Saf. Environ. Eng.* 21 (02), 32–39. (in Chinese).

Xu, B., Yu, Z., Liu, D., Jiang, X., Chen, H., Yao, Q., et al. (2011). Study of formation of high dissolved uranium in underground brines at the south coast of Laizhou Bay. *Periodical Ocean Univ. China* 41 (11), 5. (in Chinese).

Xu, X., Xiong, G., Chen, G., Fu, T., Yu, H., Wu, J., et al. (2021). Characteristics of coastal aquifer contamination by seawater intrusion and anthropogenic activities in the coastal areas of the Bohai Sea, eastern China. *J. Asian Earth Sci.* 217, 104830. doi:10.1016/j.jseaes.2021.104830

Xue, C. (2009). Historical changes of coastlines on west and south coasts of Bohai Sea since 7000 a B.P. *Sci. Geogr. Sin.* 29 (2), 217–222. (in Chinese).

Xue, Y., Wu, J., Ye, S., and Zhang, Y. (2000). Hydrogeological and hydrogeochemical studies for salt water intrusion on the south coast of Laizhou Bay, China. *Groundwater* 38 (1), 38–45. doi:10.1111/j.1745-6584.2000.tb00200.x

Yang, F., Liu, S., Jia, C., Gao, M., Chang, W., and Wang, Y. (2021). Hydrochemical characteristics and functions of groundwater in southern Laizhou Bay based on the multivariate statistical analysis approach. *Estuar. Coast. Shelf Sci.* 250, 107153. doi:10.1016/j.ecss.2020.107153

Yang, Q., Wang, R., Xu, S., Li, W., Wang, Z., Mei, J., et al. (2016). Hydrogeochemical and stable isotopic characteristics of brine in Laizhou Bay. *Geol. Rev.* 62 (2), 343–352. (in Chinese).

Yang, Z. (2004). *Marine geology*. Shandong Education Press. [in Chinese].

Yu, X., Yang, J., Graf, T., Koneshloo, M., O'Neal, M. A., and Michael, H. A. (2016). Impact of topography on groundwater salinization due to ocean surge inundation. *Water Resour. Res.* 52 (8), 5794–5812. doi:10.1002/2016WR018814

Zhang, X., Miao, J., Hu, B. X., Liu, H., Zhang, H., and Ma, Z. (2017a). Hydrogeochemical characterization and groundwater quality assessment in intruded coastal brine aquifers (Laizhou Bay, China). *Environ. Sci. Pollut. Res.* 24, 21073–21090. doi:10.1007/s11356-017-9641-x

Zhang, Y., and Chen, H. (1996). Characteristics of sedimentary seawater and its formation environment in post-late Pleistocene strata on the south of Laizhou Bay. *Acta Oceanol. Sin.* 18 (6), 8–16. (in Chinese).

Zhang, Y., Fu, C., Mao, L., Gong, X., and Li, X. (2017b). Hydrochemical characteristic and formation mechanism of the groundwater in Yancheng, Jiangsu Province. *Resour. Environ. Yangtze Basin* 26 (4), 598–605. (in Chinese).

Zhang, Z., Xie, L., and Zhang, Y. (2010). Sedimentary records of the MIS3 marine transgression event in the North Jiangsu Plain, China. *Quat. Sci.* 30 (5), 883–891. (in Chinese).

Zhao, J., Liang, J., and Cai, S. (1993). Relationship between brackish water formation and water-bearing medium in northern Jiangsu alluvial Plain. *Hydrogeology Eng. Geol.* (03), 25–27. (in Chinese).

Zhou, X., Li, Y., Liu, S., Yang, Q., Su, X., Zhou, L., et al. (2013). Ultra-deep sequencing enables high-fidelity recovery of biodiversity for bulk arthropod samples without PCR amplification. *Hydrogeology Eng. Geol.* 40 (5), 4–10. (in Chinese). doi:10.1186/2047-217X-2-4

Zuo, W., and Wan, L. (2006). Characteristics of down-movement of the fresh-saline groundwater interface in the plain region of Tianjin. *Hydrogeology Eng. Geol.*, 33(2), 13–18. (in Chinese).

Frontiers in Earth Science

TYPE Original Research
PUBLISHED 25 July 2023
DOI 10.3389/feart.2023.1237831

OPEN ACCESS

EDITED BY
Alessandro Amorosi,
University of Bologna, Italy

REVIEWED BY
Jingrui Li,
Qingdao National Laboratory for Marine Science and Technology, China
Dongdong Dong,
Chinese Academy of Sciences (CAS), China

*CORRESPONDENCE
Jing Feng,
✉ fengjing200272@163.com
Haiyan Cheng,
✉ chenghaiyan_2005@163.com

RECEIVED 10 June 2023
ACCEPTED 13 July 2023
PUBLISHED 25 July 2023

CITATION
Jiang S, Dong C, Feng J, Cheng H, Yang J, Li M, Wang J, Chen X and Zhou Y (2023), Geological hazards in the Oujiang estuary in the Zhejiang Province, China: type, distribution, and origin.
Front. Earth Sci. 11:1237831.
doi: 10.3389/feart.2023.1237831

Geological hazards in the Oujiang estuary in the Zhejiang Province, China: type, distribution, and origin

Shenghui Jiang[1], Chao Dong[2], Jing Feng[3]*, Haiyan Cheng[4]*, Jiaojiao Yang[2], Meina Li[3], Jianqiang Wang[2], Xuanbo Chen[2] and Yubo Zhou[2]

[1]Key Lab of Submarine Geosciences and Prospecting Techniques, MOE and College of Marine Geoscience, Ocean University of China, Qingdao, China, [2]Zhejiang Institute of Hydrogeology and Engineering Geology, Ningbo, China, [3]Qingdao Institute of Marine Geology, China Geological Survey, Qingdao, China, [4]Qingdao Geological Exploration Institute of China Metallurgical Geology Administration, Qingdao, China

Introduction: As our understanding of the ocean and its uses continues to advance, countries worldwide with ocean access are implementing new marine strategies. For example, understanding marine geological disasters can help develop the use of ocean resources and oceanic engineering.

Methods: Therefore, this study used recent data from the Oujiang Estuary, a nearshore area in China, to determine its geological hazards.

Results: The geological hazards were classified as active or restricted based on topography, geomorphology, shallow seismic profile, single-channel seismic profile, and geological drilling data. Active geological hazards primarily include shallow gas and active sand waves, whereas restrictive geological hazards include irregularly buried bedrock, erosion channels, steep submarine slopes, and buried paleochannels. We also evaluated the distribution characteristics and scope, such as the vertical distribution of shallow gas based on the seismic profiles, drilling rock facies, methane, and carbon dioxide contents in the top air, and the isotope values. We found that shallow gas was vertically distributed among multiple layers. The main gas-bearing layers were the clayey silt and sandy (silt) clay layers of the early Holocene and late Pleistocene strata. The shallow gas content was relatively low in the coarse sediment layer at the bottom of the late Pleistocene succession. Generally, the Holocene and late Pleistocene deposits do not contain gas, and the gas content in the middle and late Pleistocene strata (at greater depths) is relatively low.

Discussion: The combined effects of the regional geological structure, sea level changes, modern hydrodynamics, and human activities have formed the geological environment of the Oujiang Estuary.

KEYWORDS

oujiang estuary, geological hazards, shallow gas, origin, marine structures

1 Introduction

Marine geological hazards are an important research branch in the geological hazards field, becoming a marginal discipline with the exploration and development of nearshore oil and gas and seabed mineral resources (Wang et al., 2014; Feng et al., 2017; Qiao et al., 2022). Marine geological disasters are phenomena or events caused by external geological effects, such as waves, ocean currents, and storm surges, or internal geological effects, such as earthquakes, faults, and volcanic activities, threatening human life and property (Ye, 2011; Liu et al., 2014; Qiu et al., 2018).

Marine geological hazards can be classified in many ways but are generally deemed active or restricted based on the activity level of the potential geological hazards (Bao and Jiang, 1993; Sun et al., 2010; Chen S. et al, 2020). Active geological hazards can move, causing direct damage to marine engineering and the natural environment under internal and external forces, such as shallow gas, pockmarks, submarine landslides, active faults, active sand waves, liquefaction of sand and soil, bottom heave, coastal erosion and accretion, and landslides. Restricted geological hazards, also called restrictive geological conditions, cannot move; instead, they restrict certain marine engineering projects. If ignored, they pose hidden dangers in marine engineering. Examples include buried paleochannels, depressions, steep underwater slopes, irregularly shallow buried bedrock, and troughs.

The Oujiang Estuary is situated along the coast of Wenzhou City in Zhejiang Province, China, and is one of the most important river mouths in the region, with more than 200 large and small islands in the estuary area. This region is rich in marine resources, including ports, tidal flats, fisheries, and tourism, making it a key area for economic development. However, the area's marine geological environment is complex and influenced by various dynamic conditions, including Oujiang River runoff, waves, tides, and currents, resulting in the formation of a series of shoal–channel geomorphic systems in the coastal area outside the estuary that hold potential for various geological disasters. Therefore, this study investigated the marine geological hazards in this area to provide basic data for further studies of marine environmental evolution, ocean development, and ocean engineering construction (Yang et al., 2022).

2 Materials and methods

2.1 Geological setting

The Oujiang Estuary is in the central part of the Wenzhou metropolitan area and is its main axis, situated between the Yangtze River Delta and Pearl River Delta economic zones in the northern part of the West Coast Economic Zone (Zhang et al., 2020). It is also located at the intersection of the middle section of the Yellow Sea coastline and the Oujiang golden waterway "T." The nearshore terrain of the Oujiang Estuary is relatively complex, with many islands in the region, dense shoals, and intersecting shoal channels. River erosion and tidal currents mainly affect the section within the estuary. The northern mouth of the Oujiang River is more strongly eroded than the southern mouth, with a water depth generally less than 15 m, while the southern mouth has a water depth of generally less than 10 m; the average depth is approximately 7–8 m (Shang et al., 2018). The section outside the mouth of the estuary is affected by open terrain, island reef distribution, and tidal erosion, resulting in considerable changes in the terrain, with strong tidal currents between the islands. Generally, a good waterway forms when the depth is more than 20 m, and sediment accumulates around the waterway, forming shoals in some local areas. The terrain is generally less than 5 m deep, with isobaths developing around the islands.

This area is in the Southeast Zhejiang Uplift of the South China Fold Belt, which has been an active continental margin since the Mesozoic period, manifesting as strong fault movement and large-scale calc-alkaline magmatic activity. The fault structure is highly developed, with dominant regional deep and large faults oriented in the northeast and northwest directions, constituting the basic structural framework of this area (Xu et al., 2007).

2.2 Seismic profiles and boreholes

Shallow- and single-channel seismic profiles were acquired for the Oujiang Estuary in 2017 and 2018 (Figure 1). Shallow seismic profiles were obtained using a sub-bottom profiling high-resolution acoustic system (AAE Technologies, Great Yarmouth, United Kingdom) with an electric spark source as the seismic source. Single-channel seismic measurements were conducted using a G.I air gun with a maximum source capacity of 210 in^3 (Sercel. Carquefou Cedex, France), and the receiving cable was a SIG model 16.48.65 receiving cable (SIG, Bouvron, France). Before the marine geophysical survey, method-related and technical experiments were conducted in the Oujiang Estuary. The parameters for the shallow seismic profile were experimentally determined, including the excitation energy (typically selected at 800 J), band-pass filtering (100–5000 Hz), and the timely adjustment of seabed tracking (based on the strength of the reflection signal). The data were recorded in SGY format with a printing range of 200 ms. The parameters for the air gun operations were: source capacity: 90 in^3; air pressure: 1600–1800 psi; streamer drag length: 40 m; and source drag length: 35 m. Seabed tracking was promptly adjusted based on the strength of the reflection signal, and the data were recorded in the SGY format with a recording range of 500 ms. The seismic profiles of the study area were interpreted based on recognition markers of the seismic reflection interfaces. The distribution patterns were determined by identifying the characteristics and ranges of various geological factors of disasters in the seismic profiles based on their reflection features.

2.3 Core data and chart data collection

In 2019, two geological boreholes, DSJ3 and DSJ4, were drilled along the seismic profile using an XY-2 drilling rig and the rotary sampling method (Figure 1). DSJ3 reached a depth of 200.3 m, with an average recovery rate of 95.54% in the mud layer and 90.74% in the sand layer. DSJ4 reached a depth of 182.9 m, with an average recovery rate of 95.52% in the mud layer and 83.68% in the sandy layer. The recovered rock cores were then stored in a laboratory for photography, preservation, description, and sampling. Intact shells were selected from the cores for accelerator mass spectrometry ^{14}C dating at Beta Analytic (Miami, FL, USA). Grain size and paleomagnetic samples were collected at approximately 30–35 cm intervals. Grain size analyses were completed at the China University of Geosciences, whereas paleomagnetic testing was conducted at the East China Mineral Resources Supervision and Testing Center of the Ministry of Natural Resources.

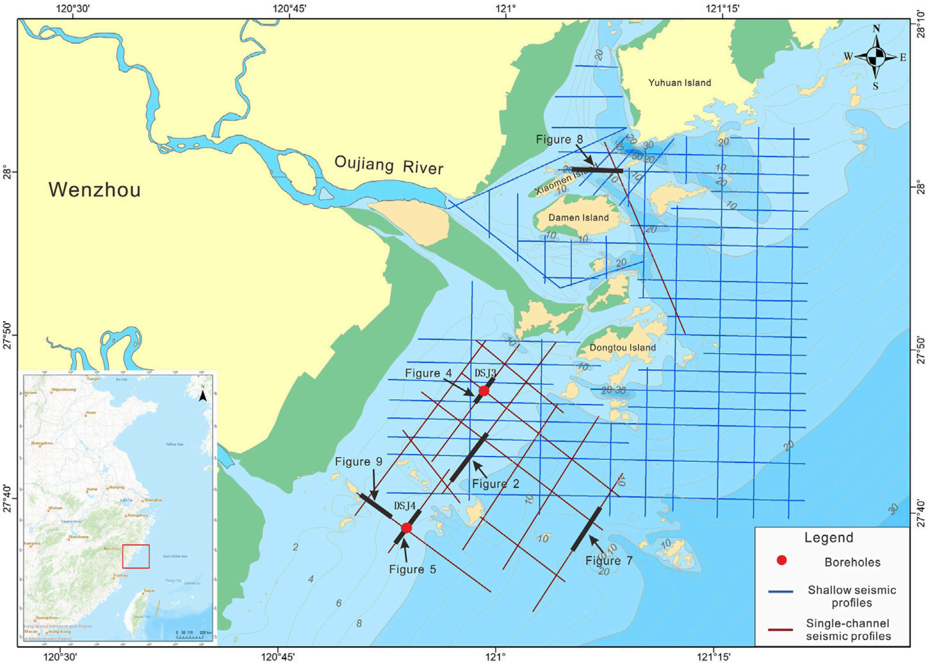

FIGURE 1
Seismic profile and borehole locations in the Oujiang Estuary offshore area. Red circles represent boreholes, blue lines represent shallow seismic profiles, and red lines represent single-channel seismic profiles.

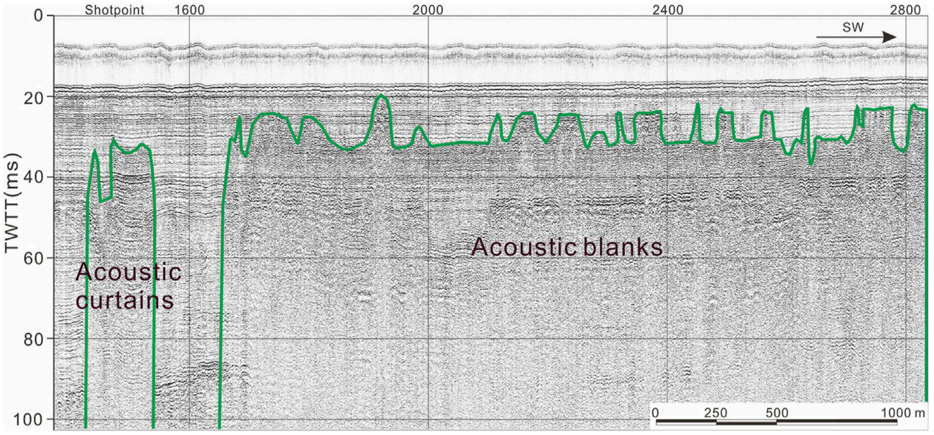

FIGURE 2
Acoustic blanks, acoustic curtains, and acoustic disturbance from the shallow seismic profile in the Oujiang Estuary. SW: Southwest; TWTT: Two-way travel time.

Chart data were collected from four historical datasets from 1979, 1986, 2002 and 2011 to reflect the morphological evolution of active sand waves according to changes in water depth.

3 Results

The geological hazards in the study were classified as active or restricted based on the degree of geological activity of the potential hazards.

3.1 Active geological hazards

3.1.1 Shallow gas

In the sedimentary succession, gas can decrease the seismic wave propagation velocity and cause rapid attenuation of the reflected wave energy, resulting in little or no energy reflection (Benites, et al., 2015). This event forms a "reflection blurry zone," shielding sedimentary reflection information. Seismic reflection characteristics mainly manifest as "acoustic blanks," "acoustic

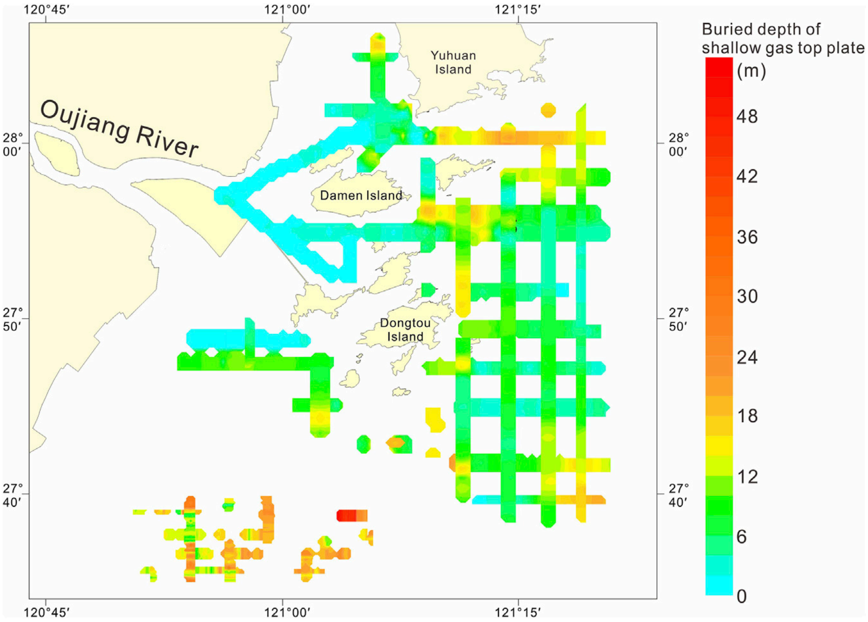

FIGURE 3
Distribution and buried depth of shallow gas along seismic lines in the study area.

curtains," "acoustic disturbances," and other phenomena (Figure 2). If shallow gas escapes from the seabed, it can form special micro-landforms, such as "pockmarks" and "mud volcanoes" on the seafloor (Dondurur et al., 2011; Chen Y. et al., 2020). Thus, the shallow gas feature results of the area were projected onto a plane to obtain the shallow gas distribution and burial depth of the top plate (Figure 3). The study area had a widespread distribution of shallow gas in the sea, and the distribution had relatively evident regional variation, mainly distributed northeast of the study area. The burial depth of a shallow gas top plate is generally between 5 and 30 m, but mostly within 12 m, with a maximum burial depth of over 50 m. The burial depth of the shallow gas in the southwest region of the study area was relatively large, ranging from 3 to 52 m, whereas the burial depth in the northeast region was generally shallow, with a maximum burial depth of approximately 30 m. No obvious seafloor "pockmarks" were observed on the seismic profiles in the study area, indicating that shallow gas did not overflow, or the overflow was minimal, and it was not enough to affect the micro-landform morphology.

The vertical distribution characteristics of shallow gas at the drilling site were obtained based on the seismic profiles, core samples, and methane (CH_4) content in the top air and interstitial water samples. The seismic profile of the DSJ3 borehole revealed that the gas-bearing top plate of the shallow gas was approximately 12 m, and the CH_4 content in the top air sample was almost zero at a depth of 11 m or less, consistent with the analysis results of the two (Figure 4). The lithology of this section is silty clay, corresponding to the middle-late Holocene succession. Within a depth range of approximately 11–100 m, the deposits are generally gas-bearing, corresponding to the early Holocene and late Pleistocene strata. The shallow gas content is roughly divided into three sections: 1) 11–43 m, relatively high gas content and corresponding to the clayey silt layer of the Holocene and late Pleistocene; 2) 43–80 m, low content of gas; and 3) 80–100 m, a small or non-existent gas content in the coarse sediment layer, such as the medium-fine sand layer.

An obvious "reflection blurry zone" was not observed at the DSJ4 location, but the seismic profile revealed a more obvious "reflection blurry zone" approximately 500 m southeast along the seismic profile (Figure 5). The buried depth at the top of the blurry zone was consistent with the buried depth of the CH_4 content greater than zero in the top air sample. Moreover, the overall CH_4 content at DSJ4 was lower than that at DSJ3 based on the content in the top air sample. Therefore, DSJ4 likely has a low shallow gas content, reflected in the single-channel seismic profile of the air gun. Furthermore, the CH_4 content was the highest in the clayey and sandy silt deposits of the early Holocene and late Pleistocene, with a burial depth of approximately 27–75 m. In strata deeper than 75 m, the CH_4 content was generally low.

Based on the borehole data, shallow gas was vertically distributed among multiple layers. The main gas-bearing layers were the clayey silt and sandy (silt) clay layers of the early Holocene and late Pleistocene strata. The shallow gas content in the coarse sediment layer at the bottom of the late Pleistocene deposits was relatively low. Generally, the Holocene and late Pleistocene strata do not contain gas, and the gas content in the middle and late Pleistocene deposits at greater depths is relatively low. Based on the engineering characteristics of the drilling sample analyses, the main gas-bearing rock types were clayey silt and silty clay layers, which are not conducive to the large-scale storage and accumulation of gas. Also, the gas pressure and volume were generally low. The single-channel seismic results did not reveal the "pockmark" phenomenon on the seafloor, indicating that shallow gas did not overflow or the overflow was small; thus, it

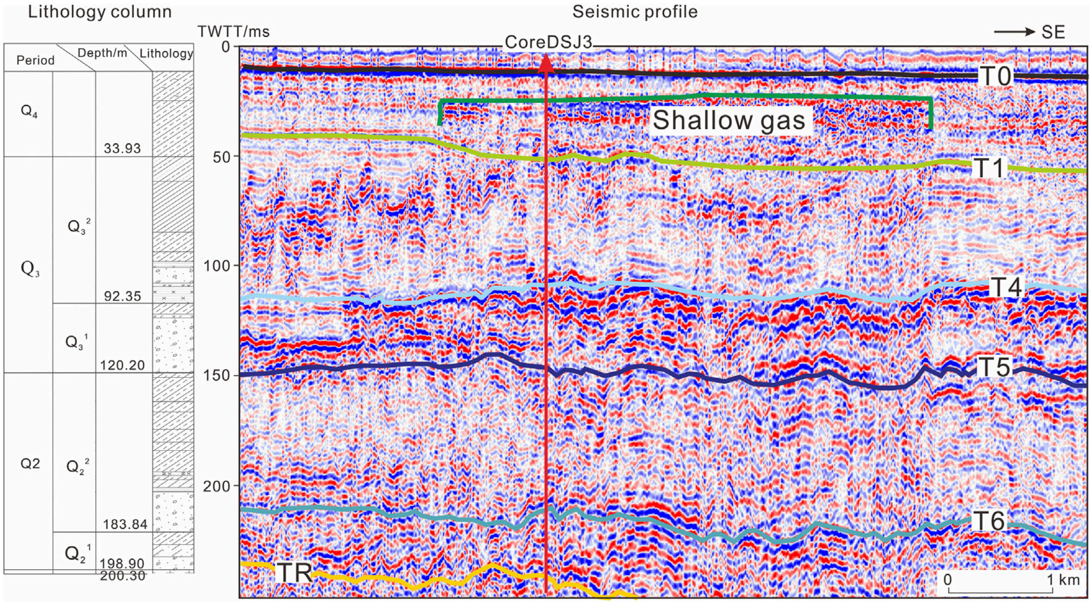

FIGURE 4
Comparisons between the single-channel seismic unit division and core DSJ03 lithology. SE: Southeast.

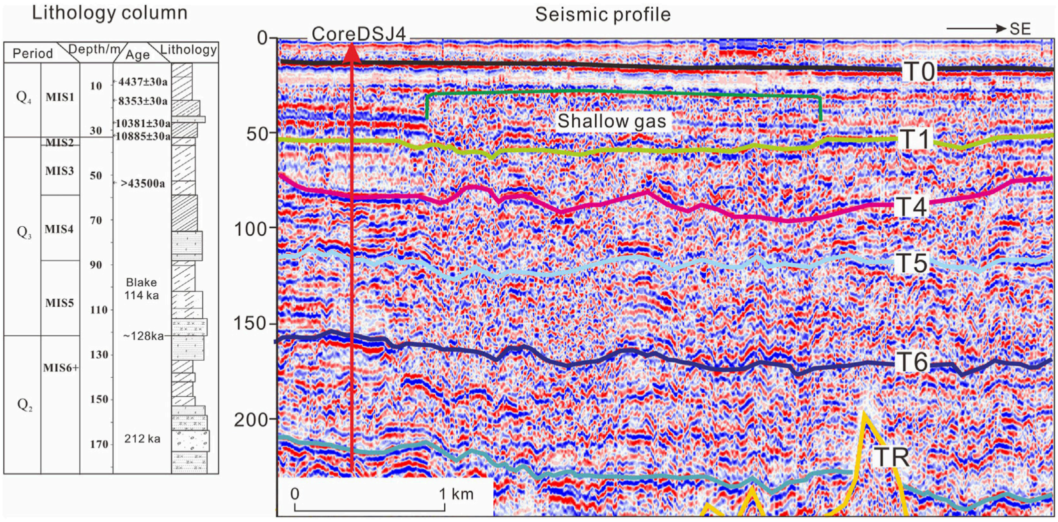

FIGURE 5
Comparisons between the single-channel seismic unit division and core DSJ04 lithology. SE: Southeast.

was not enough to affect the micro-geomorphic features. Most of the gas was isolated from the viscous soil layer in the form of small bubbles. Overall, the possibility of a large-scale blowout in the study area is believed to be low; however, the possibility of locally high instantaneous gas pressure cannot be excluded.

3.1.2 Active sand waves

Larger-scale active sand waves in the study area were mainly distributed in the shallow sea area of the northern mouth of the Oujiang River, the west side of the Damao Island's triangular sand, the Zhongsha and Chongshan sand waves on the south side, and sporadically distributed in the Qitouyang Sea area at the southern mouth of the Oujiang River (Figure 6). Among these, triangular sand wave was the largest in scale, with a triangular shape resembling a horseshoe. During low tide, shallow sand waves were exposed, which extended in two directions, northwest and southeast, and were mainly composed of medium-to fine-sand sediment. In recent years, the sand waves have eroded near the river mouth, the

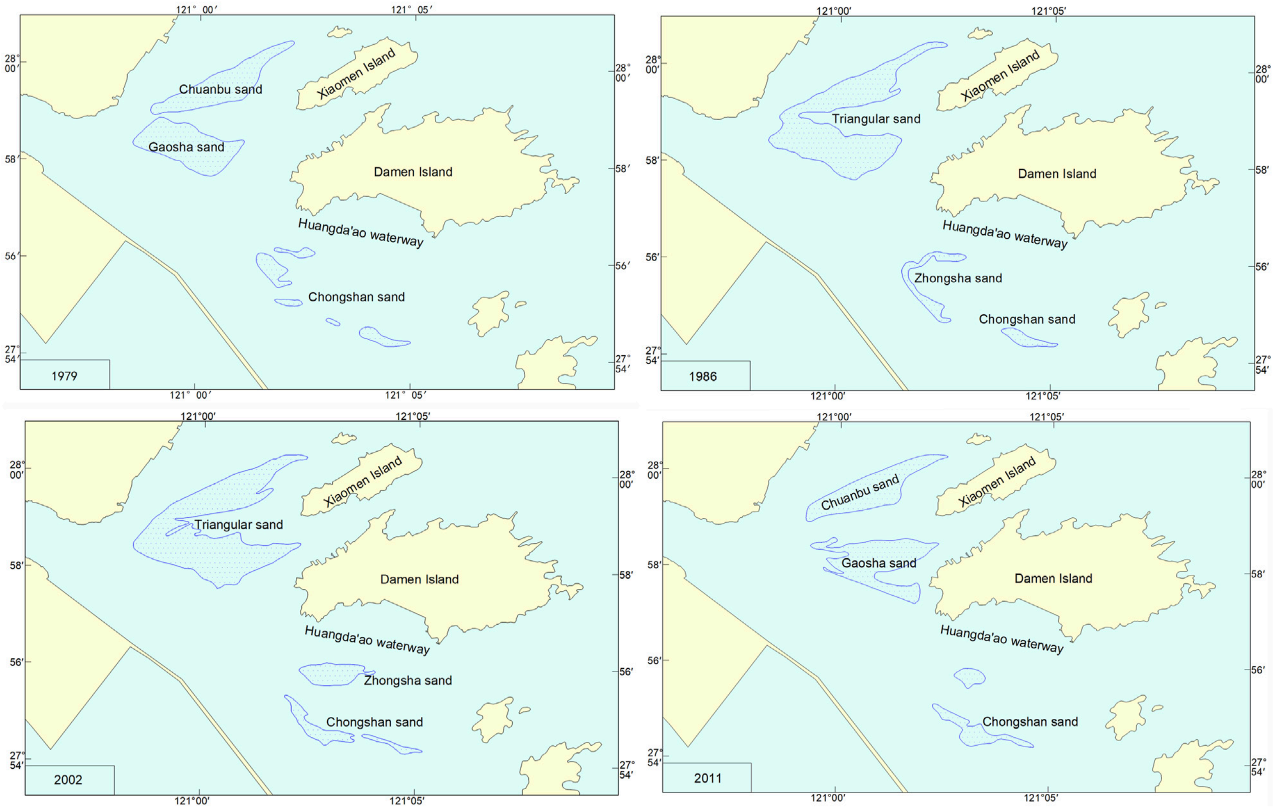

FIGURE 6
Location and morphological evolution of active sand waves in the Oujiang Estuary from 1979 to 2011.

TABLE 1 Active sand wave changes from 1979 to 2011 (km^2).

Active sand waves	Year			
	1979	1986	2002	2011
Triangular sand	9.36	10.99	12.86	10.14
Zhongsha sand	1.16	1.34	1.64	0.58
Chongshan sand	0.89	0.64	1.59	1.54

terrain has deepened, the 0 m line range has shrunk, and the tidal current has cut through the middle of the sand wave, dividing the triangular sand into Chuanbu sand and Gaosha sand waves.

On a smaller scale, the Zhongsha and Chongshan sand waves are located on the southern side of the Huangda'ao Waterway. Since 1979, Zhongsha gradually formed from a series of smaller-scale tidal sand bodies, with southeastern and northwestern axis lengths of 2.6 km and 2.3 km, respectively. In recent years, owing to the completion of the Lingni Dyke, the range of the mid-water channel has narrowed, the main axis of the tidal current has shifted northward, the flow rate has increased, and the shallow water of Zhongsha has eroded, and by 2011, the 0 m line continued extending toward the Chongshan sand wave, and the southern end of Zhongsha merged with Chongshan sand (Table 1). Therefore, the Chongshan sand wave scale expanded and continued to develop.

3.1.3 Erosion channels

Natural erosion and scouring of surface sediments on the seabed form erosion channels, which are mainly distributed in narrow areas between islands with strong tides or water currents. Steep channels are often accompanied by steep slopes prone to landslides. Waterways are large channels that serve as water transportation routes and play an important role in local economic development. However, there are significant constraints on certain offshore engineering projects, such as laying submarine cables and oil pipelines. Erosion channel slopes are generally steep, which can easily cause sediment on the slope to collapse, undermining the foundation of buildings and causing pipelines, cables, and other structures to break or deform. Therefore, erosion channels pose a hidden danger to offshore engineering construction.

Erosion channels are identifiable from a single seismic profile and were the main topographic features in the study area. They were characterized by deep-cut channels and a generally small-scale distribution, mainly located in tidal channels between the islands (Figure 7).

3.2 Restricted geological hazards

3.2.1 Irregular shallow-buried bedrock

In a single seismic profile, bedrock is mainly characterized by medium to low frequency, strong amplitude, and medium to low

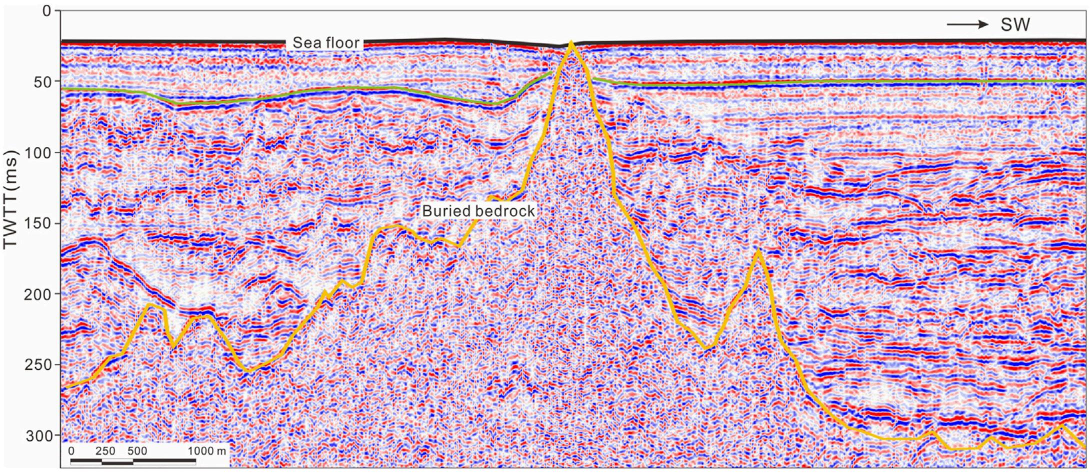

FIGURE 7
The single-channel seismic profile reveals irregular shallow buried bedrock. SW: Southwest; TWTT: Two-way travel time.

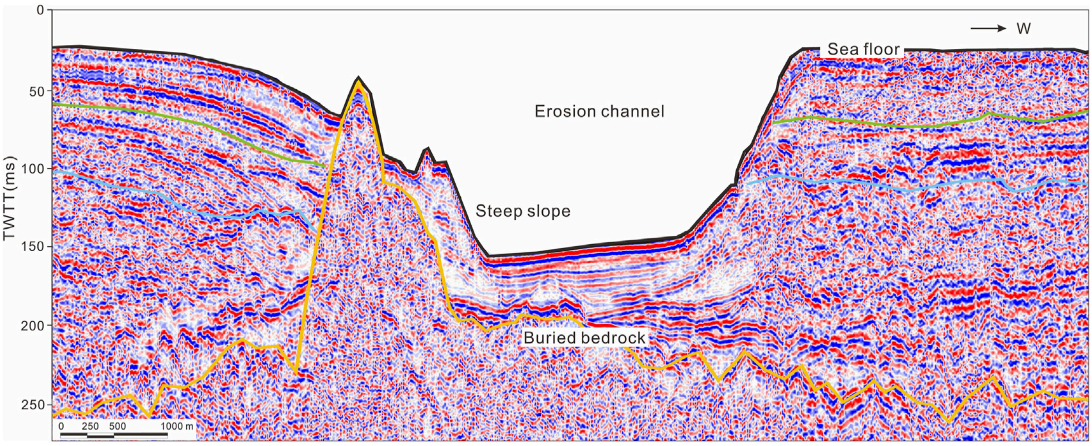

FIGURE 8
The single-channel seismic profile reveals irregular shallow buried bedrock, steep slopes, and erosion channels. TWTT: Two-way travel time; W: West.

continuity reflection features. We identified irregular reflection morphology with high and low undulations, and the bedrock surface protrusions often exhibited strong reflections in the form of conical or pointed peaks (Figure 8). Also, the internal reflections were blurry and chaotic, with no clear layering, and some diffraction waves were observed. The shallow bedrock in the study area mainly appeared in areas close to the bedrock coast and islands, with limited regional distribution. Bedrock outcrops in some local sea areas became reefs and were primarily distributed in areas with large seabed undulations. In this study, in a single seismic profile, we observed 11 bedrock outcrops ranging from 3.5 to 28.5 m in depth.

3.2.2 Steep submarine slopes

Steep submarine slopes are large and prone to instability and landslides/tipping under external disturbances, potentially causing catastrophic consequences for underwater facilities, such as underwater pipelines, cables, pipe networks, and anchorages, and is a safety hazard for submarine slope stability (Wang et al., 2019).

Steep submarine slopes have distinguishing features in the data, such as in a single seismic profile and depth measurements. Steep slopes are usually characterized by an intensive arrangement of terrain contours, and their linear shapes and positions can be clearly seen on three-dimensional topographic maps. Single seismic profiles mainly manifest as significant distortions of the seabed reflection waveform or sudden changes in water depth. Based on the characteristics of steep slopes in the Wenzhou Sea, slopes greater than 6° were defined as submarine steep slopes. The study area is densely populated, with islands and waterways prone to forming deep trench-shore slopes. Therefore, the steep slopes in the study area were mainly erosion-steep

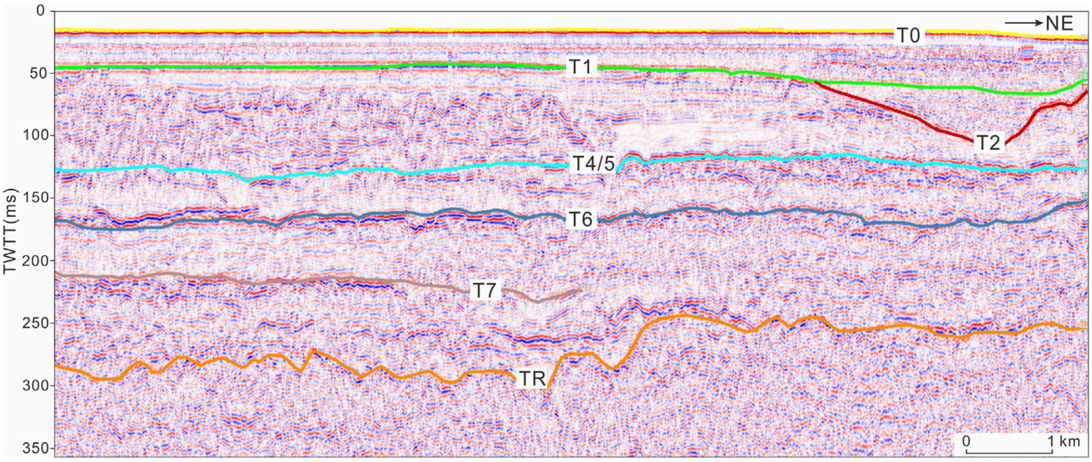

FIGURE 9
The single-channel seismic profile reveals a late and middle Pleistocene paleo-channel. Note: Figure 1 shows the location of the profile. NE: Northeast; TWTT, two-way travel time. T0-T7: seismic interfaces. TR: bedrock.

slopes, and their extension direction was consistent with the direction of the isobaths. In total, 59 steep submarine slopes were identified through a single seismic survey, with slopes >6°. The maximum slope was 20.8°, and the steep submarine slopes in the study area were distributed on both sides of the scouring grooves in the tidal channels between the islands (Figure 8).

3.2.3 Buried paleo-channel

In a single seismic profile, buried paleochannel sediments show various types of reflections, such as complex wave-like cluttered reflections, sub-parallel reflections, high-angle inclined interlaced reflections, and pre-fill reflections at different angles, some of which can be subdivided into multiple filling stages cut by each other (Qiu et al., 2012).

A comparative analysis of single-channel seismic interpretation results and drilling data suggests that three periods of paleo-channels have developed in the survey area since the early Pleistocene period (Figure 9). The locally developed late Pleistocene paleo-channel (T2 interface) extends towards the south of the Oujiang Estuary. The single-channel seismic profile cut down the lower marine succession as a basement, with internal reflections exhibiting subparallel and progradational reflections. The ancient early-late Pleistocene river channel (T6 interface) has been extensively developed on a larger scale. In the single-channel seismic profile, the basement was a strongly eroded interface with local fluctuations showing downward erosion and internal reflections exhibiting sub-parallel, chaotic, and oblique-cross reflections. In the drilling logs, the filling layers inside the paleo-channel demonstrate the basic characteristics of fluvial facies with an upward vertical fining trend. The ancient late-middle Pleistocene river channel (T7 interface) was widely developed. In the single-channel seismic profile, the basement is a strongly eroded interface identifiable by fewer overall fluctuations, whereas the internal reflections exhibit subparallel, chaotic, and oblique cross reflections. In the drilling logs, the filling layers inside the paleo-channel demonstrated the basic characteristics of fluvial facies with an upward vertical fining trend.

4 Discussion

Geological hazards in the study area result from geological structures and various external dynamic forces. Geological structures determine and influence the overall pattern of modern land-sea interactions and the distribution of coastal morphology and types. Thus, various external forces shape modern landforms, which, in turn, affect the types and scope of the geological hazard distribution (Figure 10).

4.1 Regional geological structure

The Wenzhou region is in the southeastern part of the Zhejiang Province, and the regional geological structures of this area have undergone long and complex processes to become their current form (Wang et al., 2010). Overall, two different structural systems control the landform in this area: the north-northeast and northwest directional structural systems (Figure 11). The north-northeast faults control the uplift of the western area to form high mountains and V-shaped valleys and control the formation of plain terrain in the east since the Quaternary period. Specifically, the main structural framework is composed of the Wenzhou-Zhenhai deep fault in the north-northeast, the Pingyang-Putuo deep fault, the Chun'an-Wenzhou major fault in the northwest, and the Taishun-Huangyan major fault in the northeast, which affect the area via volcanic activity, magma intrusion, and the formation and development of sedimentary basins.

4.2 Sea level change

Large-scale sea transgression and regression also cause significant fluctuations in the shoreline and have important influences on the formation of modern coastal morphology and changes in hydrodynamic conditions, material sources, and sedimentary environments. Since the late Pleistocene period, the

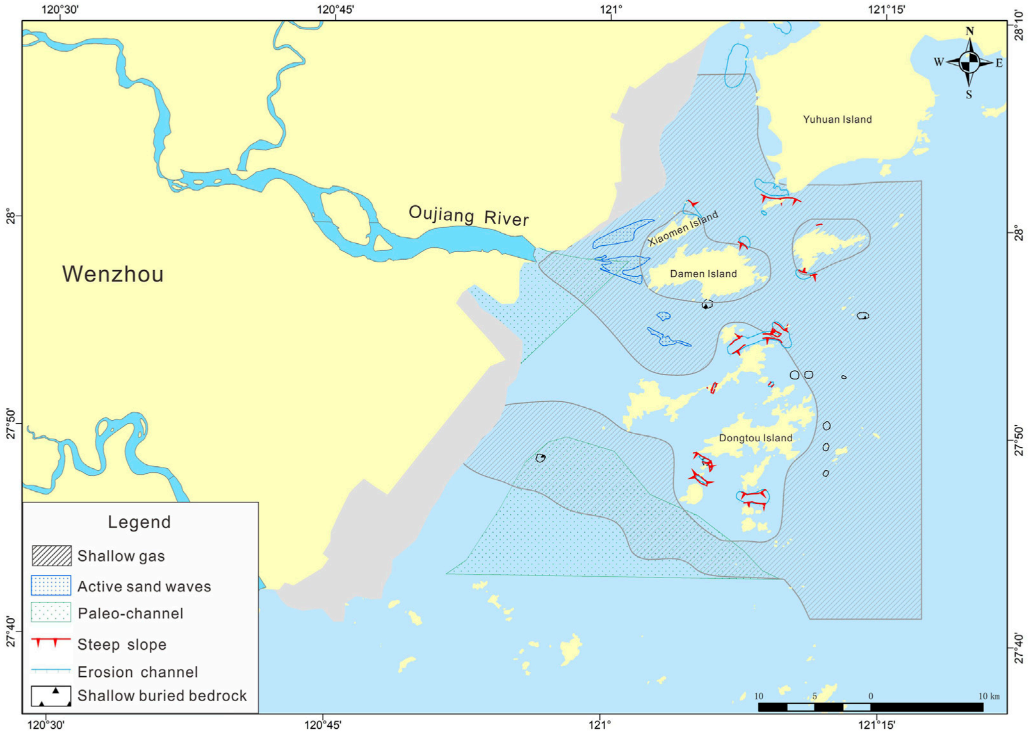

FIGURE 10
Geographical hazard map of the Oujiang Estuary.

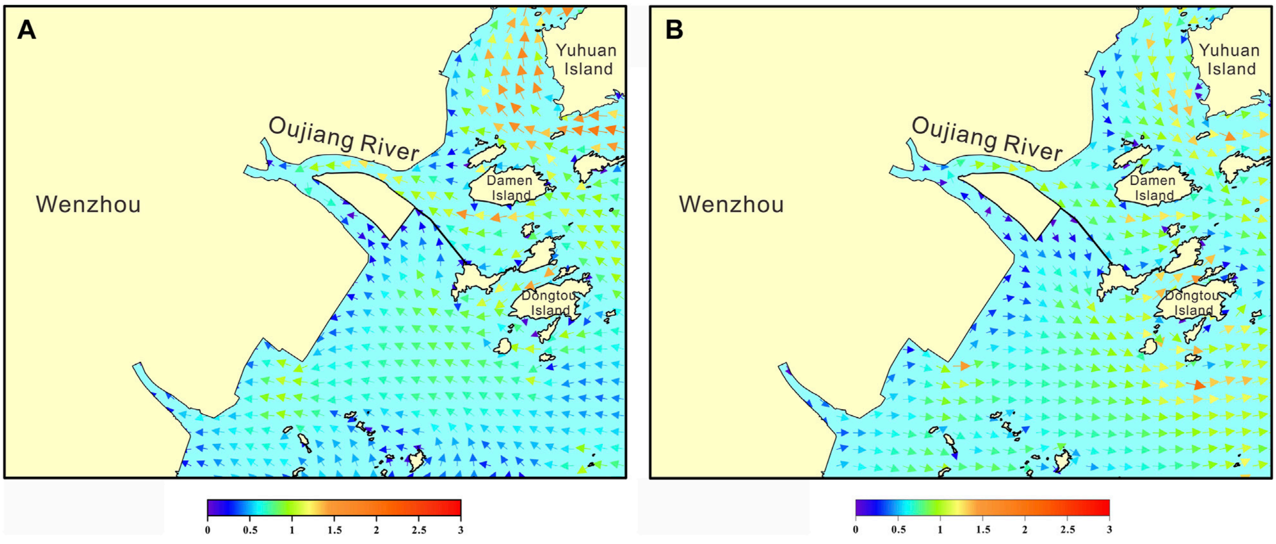

FIGURE 11
Local tidal current fields in the Oujiang River estuary at maximum flood **(A)** and ebb **(B)** moment (spring tide) (unit: m/s).

sea level in the Wenzhou coastal area has fluctuated, gradually stabilizing towards its current state during the middle Holocene period. The rise and fall of the sea level have caused constant erosion, transportation, and sedimentation accumulation in the paleo-channel and the seabed active sand waves, affecting the morphological evolution of the paleo-channel, active sand waves, and erosion gullies.

In addition, abundant amounts of terrestrial organic matter within the overlying fill of the paleo-channel have been buried by allochthonous sediment owing to the frequent sea level changes;

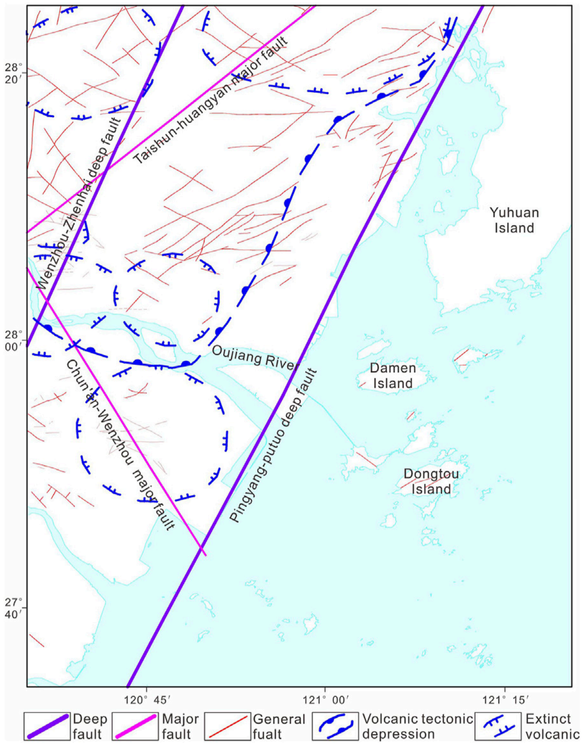

FIGURE 12
Regional geological structure map in the Oujiang Estuary.

consequently, oxygen isolation has occurred, and a rapid transition to a reduced environment is possible. Additionally, sediment cover-layers act as traps for dissolved substances that supply organic matter, which, in its immature stage, is biochemically decomposed by anaerobic bacteria to produce methane or biogas, commonly associated with shallow gases in paleo-channels. Based on its genesis, shallow gas can be divided into two types: biogenic and thermogenic gas (Zhang et al., 2008; Toth et al., 2014). Biogenic gas is formed by organic matter in shallow deposits under anoxic conditions through bacterial reduction. Thermogenic gas is formed by the thermal decomposition of organic matter in deep strata, often in a supercritical state (high-pressure gas chamber), that sometimes rises, migrating and accumulating as shallow gas along rock pore spaces, fissures, and fault planes. In recent years, most domestic and foreign experts have used an δ13C1 vale of less than −55‰ as the empirical characteristic boundary value to distinguish between biogenic, thermogenic, and sub-biogenic gas methane carbon isotopes (Verweij et al., 2018). However, our isotope analysis of the DSJ3 and DSJ4 wells indicated that the δ13C1 values were between −97.69‰ and −70.74‰, suggesting that the shallow gas in the study area is a typical biogenic gas generated through a CO_2 reduction reaction (Weschenfelder et al., 2016).

4.3 Modern dynamics

Based on tectonic movement and sea level changes, modern marine dynamic conditions, such as rivers, waves, currents, and

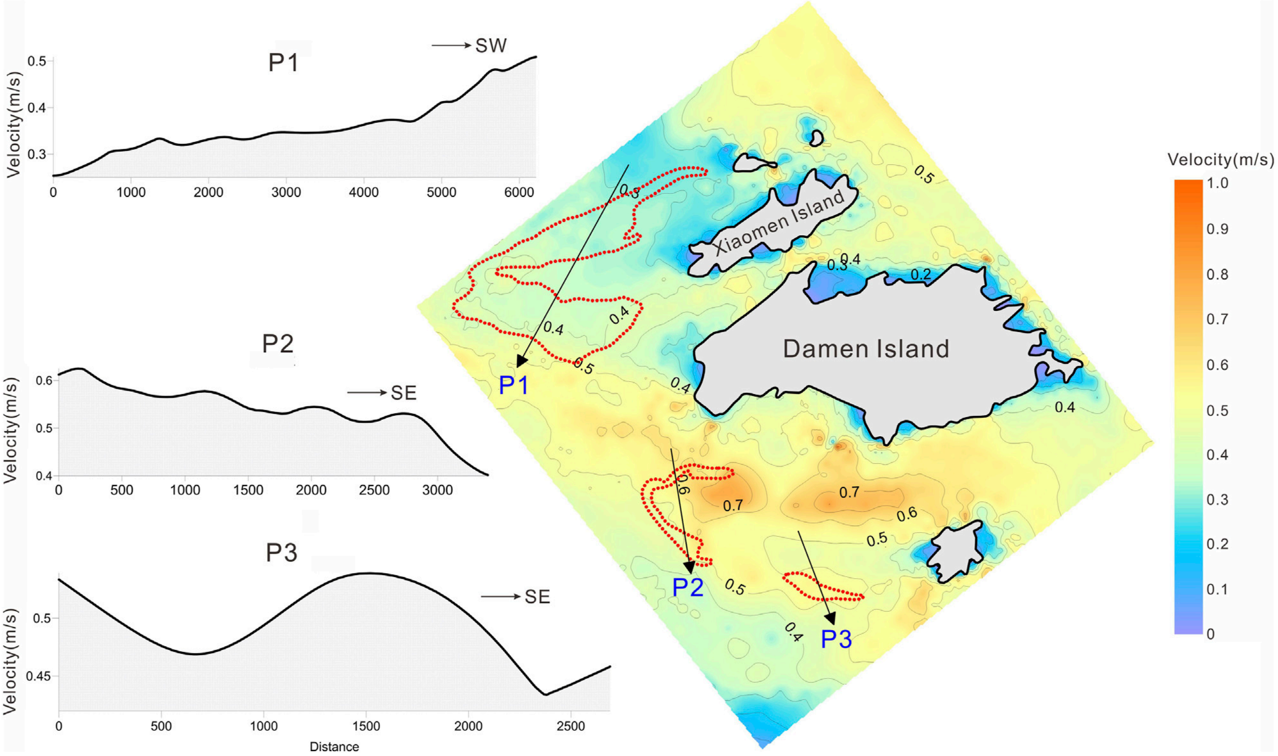

FIGURE 13
Vertical mean velocity distributions in the Oujiang Estuary. P: Profile, SW:Southwest, SE: Southeast.

tides, continually reshape and construct topography and are important factors controlling dynamic changes in topography and sediment sources (Figure 12). The development and evolution of the Oujiang Estuary coastal zone topography are continually influenced by the combined action of river inflow, nearshore circulation systems, and wave and tidal forces and play a significant role in the dynamic adjustment of active geological hazards (Wu et al., 2018).

The area had an extensive tidal range and fast flow, forming a typical tidal sandbody. Based on the tidal flow data measured on site from the Oujiang Estuary, which has active sand waves, the discriminant coefficient of the tidal flow was <0.5, indicating an irregular semidiurnal shallow sea tidal flow (Figure 13). Tidal waves are generally controlled by the M2 tide with a semidiurnal tidal current; the direction of the flood flow is northwest, whereas the ebb flow direction is southeast. Based on the tidal flow velocity distribution, the average tidal flow velocity in the triangular sand area was generally 0.3–0.4 m/s (Liu and Xia, 2007). In addition, the flow velocity in the sand wave area from north to south increased gradually and was generally <0.5 m/s. Finally, the average tidal flow velocity was generally 0.5–0.7 m/s in the middle sand and Zhongshan sand wave areas, and the rising flow velocity was slightly lower than the ebb flow velocity (Zhuang et al., 2008; Ye et al., 2016). Based on sediment grain size data in the sand wave area, the median grain size of sediment that makes up the sand waves was 0.30–0.42 mm, classified as medium sand. The sediment particles in the study area can be transported under the action of tidal current, resulting in higher mobility of sand waves.

4.4 Human activity

Human activity is an inevitable factor in the evolution of geological hazards. In recent decades, with the continuous social economic development, existing land resources have limited further development of Wenzhou City. The government has shifted its focus to the Oujiang Estuary, actively implementing development and remediation projects, such as enclosing and channel construction. Wenzhou City has completed projects such as the Ou-Fei Shoal partial enclosure, Zhaoyuanao harbor area partial enclosure, Wenzhou Shoal enclosure phase 1, Xiaomen Island northern enclosure, Dameng Island Huangao enclosure, and Dongtou Islands enclosure. High-intensity coastal engineering development and other human activities have altered the local hydrodynamic action and sediment deposition balance, causing disturbances in natural geological processes and ultimately leading to the formation, development, and evolution of marine geological disasters (Zhang et al., 2020).

The Wenzhou Shoal Enclosure Project commenced in 2003 (Zheng, 2010). The first phase of the project, Lingni Dike, located along the northern edge of Wenzhou Shoal, was completed and opened to traffic in 2006. The dike effectively intercepted the suspended sediment transport pathway between Wenzhou Shoal and the Middle Channel, leading to a predominantly oscillating flow in the tidal currents of both channels (Xu et al., 2017). Within this interaction, various degrees of slow flow, diversion, and convergence exist, resulting in the complexity of tidal channel fluctuations and the diversity of sediment erosion and deposition at the mouth of the Ou River, ultimately leading to the amalgamation of Zhongsha Shoal and Chongshan sand wave due to erosion and migration (Figure 6).

5 Conclusion

The main geological hazards in the Oujiang Estuary include shallow gas, active sand waves, shallow-buried irregular bedrock, erosion channels, steep submarine slopes, and buried paleo-channels. The seismic profiles and borehole data revealed the vertical distribution characteristics of the shallow gas; the main gas-bearing layers in the early Holocene and late Pleistocene strata were clayey silt and silt (sand) clay layers, and the shallow gas content in the coarse sedimentary layer at the bottom of the late Pleistocene was relatively low. There was no gas content in the middle-late Holocene succession, and the gas content in the deep middle Pleistocene succession was relatively small.

Moreover, the hazardous geology in the study area resulted from the geological structure and various external dynamic forces. The geological structure determines and influences the overall pattern of modern land and sea and the distribution of coastal contours and types. Various external forces (including sea-level changes, modern hydrodynamics, and human activities) have shaped modern landforms, affecting the distribution and evolution of hazardous geology.

Data availability statement

The original contributions presented in the study are included in the article/supplementary material, further inquiries can be directed to the corresponding authors.

Author contributions

SJ and CD contributed to conception and design of the study. JF and YZ organized the database. JY performed the statistical analysis. HC and SJ wrote the first draft of the manuscript. SJ, JW, and XC wrote sections of the manuscript. All authors contributed to the article and approved the submitted version.

Funding

This study was funded by the Comprehensive Geological Survey of Key Coastal Zone in Zhejiang Province (Wenzhou Key Area) (No. 2018009) and Shandong Provincial Natural Science Foundation (No. ZR2021MD049).

Conflict of interest

The authors declare that the research was conducted in the absence of any commercial or financial relationships that could be construed as a potential conflict of interest.

Publisher's note

References

Bao, C., and Jiang, Y. (1993). Types and characteristics of potential subbottom geological hazards in nearshore zone of China. *Trop. Oceanol.* 18 (3), 25–31.

Benites, M., Alves, D. P., Maly, M. D., and Jovane, L. (2015). Shallow gas occurrence in a Brazilian ria (Saco do Mamangua, Rio de Janeiro) inferred from high-resolution seismic data. *Cont. Shelf Res.* 108, 89–96. doi:10.1016/j.csr.2015.08.022

Chen, S., Wang, Z., Zhang, Y., Zhang, Z., Zhao, W., and Zhong, W. (2020a). Characteristics and origin of disaster geological bodies in the northern outer shelf of the East China Sea and its adjacent areas. *Geol. China.* 47 (5), 1512–1529.

Chen, Y., Deng, B., and Zhang, J. (2020b). Shallow gas in the Holocene mud wedge along the inner East China Sea shelf. *Mar. Petrol. Geol.* 114, 104233. doi:10.1016/j.marpetgeo.2020.104233

Dondurur, D., Cifci, G., Drahor, M. G., and Coskun, S. (2011). Acoustic evidence of shallow gas accumulations and active pockmarks in the Izmir Gulf, Aegean sea. *Mar. Pet. Geol.* 28, 1505–1516. doi:10.1016/j.marpetgeo.2011.05.001

Feng, J., Zhao, T., Sun, Y., Gao, X., and Li, P. (2017). Analysis on acoustic detection of geo-hazard factors in Bohai Strait. *Comput. Tech. Geophys. Geochem. Explor.* 37 (1), 96–102.

Liu, D., Hu, T., Huang, P., and Ji, Y. (2014). Classification and distribution of marine geo-hazards factors in zhoushan islands. *Trans. Oceanol. Limnol.* 3, 153–160.

Liu, Z., and Xia, D. (2007). *Tidal current sediment body in offshore China*. Beijing: Ocean Press.

Qiao, P., Chen, S., Zhang, Y., Xu, C., Kong, X., and Yu, K. (2022). Types and formation mechanism of main geological hazards in the Western continental shelf area of the East China Sea. *J. Hebei Geo Univ.* 45 (3), 63–72.

Qiu, J., Liu, J., Kong, X., Zhang, Y., Yue, B., Zhang, J., et al. (2012). Characteristics and distribution of geo-hazard factors in the Western south Yellow Sea. *Mar. Geol. Quart. Geol.* 32 (1), 27–34. doi:10.3724/sp.j.1140.2012.01027

Qiu, J., Liu, J., Yue, N., Wang, S., and Mai, D. D. (2018). Distribution and characteristics of hazardous geological features in the marine coastal and offshore areas of Zhejiang Province, East China Sea. *J. Ocean. Univ. China* 17 (6), 1318–1324. doi:10.1007/s11802-018-3671-y

Shang, S., Fan, D., Yin, P., Vurr, G., Zhang, M., and Wang, Q. (2018). Late quaternary environmental change in Oujiang delta along the northeastern zhe-min uplift zone (southeast China). *Palaeogeogr. Palaeogclimatol. Palaeoecol.* 492, 64–80. doi:10.1016/j.palaeo.2017.12.012

Sun, J., Zhang, W., and Jia, J. (2010). Hazardous geology and its relationship with environmental evolution in the Pearl River Estuary. *J. Trop. Oceanogr.* 29 (1), 104–110.

Toth, Z., Spiess, V., and Jensen, J. (2014). Seismo-acoustic signatures of shallow free gas in the Bornholm basin, Baltic sea. *Cont. Shelf Res.* 88, 228–239. doi:10.1016/j.csr.2014.08.007

Verweij, J., Nelskamp, S., Ten Veen, J., De Bruin, G., Geel, K., and Donders, T. (2018). Generation, migration, entrapment and leakage of microbial gas in the Dutch part of the Southern North Sea Delta. *Mar. Pet. Geol.* 97, 493–516. doi:10.1016/j.marpetgeo.2018.07.034

Wang, H., Zhang, W., Li, C., Lei, W., Yang, D., Liang, T., et al. (2014). Single amino acid substitution of VP1 N17D or VP2 H145Y confers acid-resistant phenotype of type Asia1 foot-and-mouth disease virus. *Mar. Sci.* 38 (7), 103–111. doi:10.1007/s12250-014-3426-x

Wang, J., Zhang, G., Chen, D., Wang, X., Wang, Z., Dong, D., et al. (2019). Geological hazards in lingshui region of qiongdongnan basin: Type, distribution and origin. *Mar. Geol. Quart. Geol.* 39 (4), 87–95.

Wang, Z., Xu, H., Zhan, Q., Saito, Y., He, Z., Xie, J., et al. (2010). Lithological and palynological evidence of late quaternary depositional environments in the subaqueous Yangtze delta, China. *Quat. Res.* 73, 550–562. doi:10.1016/j.yqres.2009.11.001

Weschenfelder, J., Klein, A., Green, A., Aliotta, S., de Mahiques, M., Neto, A., et al. (2016). The control of palaeo-topography in the preservation of shallow gas accumulation: Examples from Brazil, Argentina and south Africa. *Estuar. Coast Shelf Sci.* 172, 93–107. doi:10.1016/j.ecss.2016.02.005

Wu, X., Xing, L., Zhang, T., and Xiang, R. (2018). Mid–late Holocene changes in sedimentary organic matter on the inner shelf of the East China Sea. *J. Asian Earth Sci.* 154, 248–254. doi:10.1016/j.jseaes.2017.12.006

Xu, H., Wang, J., and Zhou, H. (2017). Preliminary study on the mechanism of the erosion-deposition adjustment in the tidal inlet out of the Oujiang Estuary. *J. Mar. Sci.* 35 (2), 33–43.

Xu, X., O'Reilly, S., Griffin, W., Wang, X., Pearson, N., and He, Z. (2007). The crust of cathaysia: Age, assembly and reworking of two terranes. *Precambrian Res.* 158, 51–78. doi:10.1016/j.precamres.2007.04.010

Yang, J., ChenLiuXu, Z., Song, W., Wang, S., et al. (2022). Acoustic stratigraphy of the quaternary in the south of the Oujiang River estuary. *Mar. Geol. Front.* 38 (8), 11–19.

Ye, W., Zhang, G., Zhu, Z., Huang, D., Han, Y., Wang, L., et al. (2016). Methane distribution and sea-to-air flux in the East China sea during the summer of 2013: Impact of hypoxia. *Deep Sea Res. Part II Top. Stud. Oceanogr.* 124, 74–83. doi:10.1016/j.dsr2.2015.01.008

Ye, Y. (2011). Review of the development of marine hazard geology and its future prospects. *J. Mar. Sci.* 29 (4), 1–7.

Zhang, G., Zhang, J., Liu, S., Ren, J., Xu, J., and Zhang, F. (2008). Methane in the changjiang (Yangtze River) estuary and its adjacent marine area: Riverine input, sediment release and atmospheric fluxes. *Biogeochemistry* 91, 71–84. doi:10.1007/s10533-008-9259-7

Zhang, Z., Zhou, L., Chen, Y., Liang, L., and Bao, X. (2020). Study on the accumulative effects of reclamation on hydrodynamic force in Qujiang estuary. *Trans. Oceanol. Limnol.* 2, 64–71.

Zheng, J. (2010). *Study on dynamical characteristics of the water environment during estuarine reclamation*. Beijing: Tsinghua University.

Zhuang, Z., Cao, L., Liu, S., and Hu, G. (2008). Activity level and balance signs of subaqueous dunes (waves) in the continental shelf. *J. Ocean. Univ. China* 38 (6), 1001–1007.

frontiers | Frontiers in Earth Science

TYPE Original Research
PUBLISHED 17 August 2023
DOI 10.3389/feart.2023.1238920

EDITED BY
Bo Li,
University of Wollongong, Australia

REVIEWED BY
Fajin Chen,
Guangdong Ocean University, China
Selvaraj Kandasamy,
Central University of Kerala, India

*CORRESPONDENCE
Lilei Chen,
✉ llchen@qnlm.ac
Duanxin Chen,
✉ chenduanxin07@qdio.ac.can

RECEIVED 12 June 2023
ACCEPTED 07 August 2023
PUBLISHED 17 August 2023

CITATION
Tong G, Chen L, Zhang G, Liu J, Chen B, Xu G, Liu M, An Y and Chen D (2023), High-resolution record of temporal change in organic matter burial over the past ~8,600 years on the northwestern continental slope of the South China Sea. *Front. Earth Sci.* 11:1238920.
doi: 10.3389/feart.2023.1238920

High-resolution record of temporal change in organic matter burial over the past ~8,600 years on the northwestern continental slope of the South China Sea

Gang Tong[1,2], Lilei Chen[3]*, Guangxu Zhang[4], Jian Liu[1], Bin Chen[1], Gang Xu[1], Ming Liu[5], Yuhui An[5] and Duanxin Chen[4]*

[1]Qingdao Institute of Marine Geology, CGS, Qingdao, China, [2]School of Ocean Sciences, China University of Geosciences, Beijing, China, [3]Deep-sea Multidisciplinary Research Center and Laboratory for Marine Geology, Laoshan Laboratory, Qingdao, China, [4]Institute of Oceanology, Chinese Academy of Sciences, Qingdao, China, [5]College of Marine Geosciences, Ocean University of China, Qingdao, China

Sedimentary organic matter (SOM) on continental slopes in marine regions can sensitively record climatic and environmental changes. In this study, total organic carbon content (TOC), total nitrogen content (TN), and their stable isotope compositions ($\delta^{13}C$ and $\delta^{15}N$) for sediments of core G02 were investigated (at ~24.2-year resolution) to reveal the temporal variations in organic matter sources and the main controls on the sources and distribution of buried organic matter on the northwestern continental slope of the South China Sea over the last ~8600 years. Results of a $\delta^{13}C$ binary mixing model reveal that ~82.3 ± 3% of SOM is derived from marine autochthonous sources. We suggest that the carbon and nitrogen contents and compositions of SOM are governed by distinct factors. The more positive $\delta^{15}N$ values before the *Pulleniatina* Minimum Event occurrence are ascribed to stronger subsurface water intrusion by the Kuroshio Current, which led to enhanced subsurface denitrification and in turn counteracted the effect of mixing with surface water caused by the East Asian winter monsoon. Sedimentary $\delta^{13}C$ values show a fluctuant decrease during ca. 8.6–3.0 cal kyr BP and a conspicuous increase during ca. 3.0–1.4 cal kyr BP. These changes are attributed to the decrease of marine productivity induced by the continuous weakening East Asian monsoon effect and the decrease of terrigenous organic carbon input induced by the weakened Indian summer monsoon precipitation, respectively. Since ca. 1.4 cal kyr BP, human activities have become the dominant factor in controlling the production and distribution of organic carbon. The results provide an important basis for understanding of source-sink processes of organic matter and the factors influencing these processes on continental slopes in low-latitude marginal seas.

KEYWORDS

South China Sea continental slope, sedimentary organic matter, denitrification, Asian monsoon changes, human activity

1 Introduction

Although continental marginal seas account for only 10% of the ocean surface area, they contain more than 80% of oceanic buried organic carbon (OC) (Hedges and Keil, 1995; Allison et al., 2007; Hu et al., 2016). Sedimentary organic matter (SOM) in marginal seas comprises a complex mixture of organic compounds originating from two main sources (Hu et al., 2014; Ge et al., 2019): terrestrial organic matter (OM) transported by river runoff, and marine OM produced by marine primary producers in the euphotic zone (EZ) (Huang et al., 2021). The nature of OM that becomes buried in a marginal sea is controlled by a combination of terrestrial sediment supply, aquatic productivity, and coastal hydrodynamics (Wang et al., 2021). Determining the sources, burial process, and ultimate fate of OM in marginal sea environments is essential for understanding regional biogeochemical processes and the global carbon cycle.

The South China Sea (SCS), the largest marginal sea of the western Pacific Ocean (Figure 1A), receives a huge amount of detritus from surrounding rivers (e.g., the Pearl, Mekong, and Red rivers) (Li et al., 2022a; Liu et al., 2023). Previous studies of the composition and distribution of sediments of the northern South China Sea (NSCS) have used element isotopes, biomarkers, and clay minerals (Liu et al., 2016; Yang et al., 2018; Chow et al., 2021). Those studies determined that sediments in the NSCS record a number of global events, including the 8.2 ka event, Last Glacial Maximum, and Younger Dryas (Wu et al., 2017; Li C. et al., 2019), suggesting a climatic teleconnection between the NSCS and the global climate system. The NSCS has the potential to provide valuable information on the strength and distribution of the Asian monsoon, the intensity of the western boundary current, and the

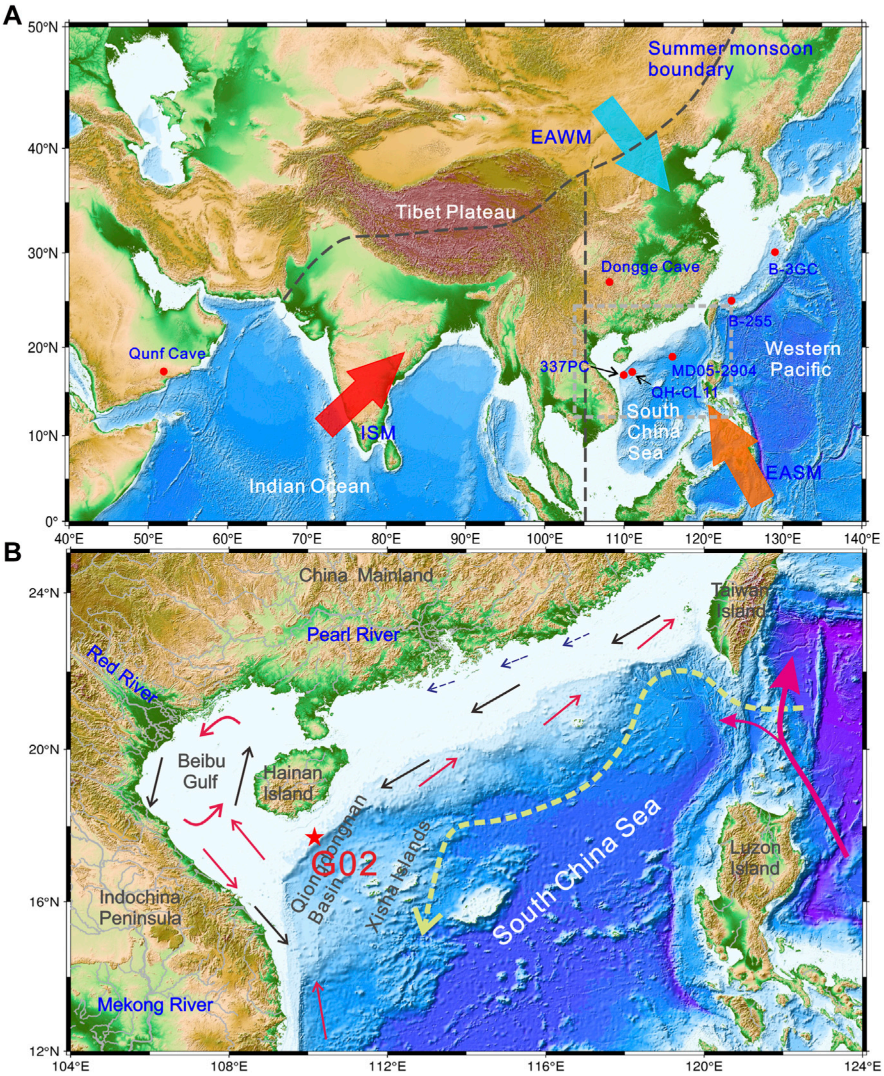

FIGURE 1
(A) Map showing regional atmospheric systems and locations of cores in the Asian region. The blue arrow represents the East Asian winter monsoon (EAWM), the red arrow represents the Indian summer monsoon (ISM), and the orange arrow represents the East Asian summer monsoon (EASM). Red dots indicate the locations of cores referred to in this paper. **(B)** Topography and the main components of ocean circulation of the South China Sea (SCS). The thick red line with arrows indicates the Kuroshio Current, the dashed yellow line with the arrow depicts the SCS deep current, blue lines with arrows represent the Guangdong Coastal Current, black lines with arrows indicate winter surface currents, and red lines with arrows depict summer surface currents, red pentagram represents the location of core G02.

intrusion of the North Pacific Intermediate Water (Zheng et al., 2016; Yang et al., 2017). However, uncertainty persists regarding the cycling processes of OM in the water column, and the interpretation of paleoenvironmental records is complicated by the multitude of factors that control the nature and distribution of OM in and around the NSCS. The complex topography and dynamic transport mechanisms in the margin of the NSCS, together with heterogeneous sources of particulate organic carbon (POC), have led to pronounced temporal and spatial variations in the elemental and isotopic compositions of SOM in the NSCS. The exchange of surface water with deep water through the Luzon Strait and Taiwan Strait may have been enhanced after the opening of the Taiwan Strait (Higginson et al., 2003), resulting in an increasing influence of deep water in the NSCS. In addition, monsoonal precipitation affects river flow and alters the input of OM from terrestrial sources. Furthermore, the original marine SOM record may be complicated by post-deposition biogeochemical processes (e.g., diagenesis and denitrification). The influence of sea-level change on variation in OM burial has decreased during the Holocene, whereas the influence of ocean current systems, monsoons, and human activity has increased (Wan et al., 2015; Wu et al., 2021; Wang et al., 2022). Therefore, high-resolution SOM records are urgently needed for the NSCS.

Most geochemical studies of the NSCS have focused on the area around the Pearl River and Beibu Gulf (Lin et al., 2006; Huang et al., 2018; Zhou et al., 2022). In comparison, few systematic studies have produced high-resolution sedimentary records from the northwestern continental slope of the SCS to elucidate the sources and distribution of OM there.

In this study, we analysed core sediments from the Qiongdongnan Basin on the northwestern continental slope of the SCS (Figure 1B) for AMS ^{14}C dating, grain size, total organic carbon (TOC), total nitrogen (TN), $\delta^{13}C$, and $\delta^{15}N$. Results of the analyses allow the sources of OM in sediments of the NSCS to be determined and the drivers of marine OM burial since the Holocene to be identified. The study provides insights into the relationship between OM burial and regional climate variation.

2 Regional setting

The SCS is the largest marginal sea in the western Pacific and is bounded by mainland China, the Indochina Peninsula, and island arcs (Figure 1B). Solar radiation received by the sea leads to a high sea surface temperature throughout the year, which generates strong vertical stratification of the water. The NSCS has a huge continental shelf that receives sediments transported by East Asian rivers such as the Pearl and Red rivers. The northern continental slope of the SCS has an important role in sediment transport and accumulation, and contains a paleoenvironmental record corresponding to its function as a connecting zone between the northern continental shelf and the central deep-sea basin of the SCS. The SCS is located in the tropical region and has a typical tropical monsoon climate influenced by the Asian monsoon (Wang et al., 1999). The surface water circulation of the SCS varies seasonally, with a seasonal surface current directed in opposite directions during summer and winter between Taiwan Island and Hainan Island. Year-round cyclonic circulation occurs in the Beibu Gulf near the Red River Estuary, in which the Qiongzhou Strait, with a westward flow of water, plays a key role. The deep-water current from the western Pacific Ocean is the only deep-water input into the SCS and reaches the deep-sea basin east of the Xisha Islands, from where it flows southward (Liu et al., 2016). The Kuroshio intrusion has a strong influence on surface water masses in the SCS by altering temperature and salinity and contributing to the N and C biogeochemical cycles.

3 Materials and methods

3.1 Sampling

A 3.55-m-long gravity core, G02, was retrieved from the Qiongdongnan Basin in the northwestern continental slope of the SCS (17.572°N, 110.272°E, water depth of 200 m; Figure 1B) in June 2018 by Yuexia Fishery guidance ship 20026, using a gravity corer with an automatic clutch and reverse catcher. After retrieval, the core was split, described, and subsampled in the laboratory. Core G02 shows only minor along-core changes in lithology and sedimentary facies. The lithology is dominated by grey-brown clayey silt with low contents of sand-sized components. The core was subsampled into 1-cm-thick samples, which were stored immediately at −20°C until analysis for organic geochemistry.

3.2 AMS ^{14}C dating of core sediments

Ten milligrams of planktonic foraminifera with intact shells and without black spots were selected from the >63 μm fraction in core samples. These samples were shipped to the Beta Analytic Testing Laboratory (Miami, Florida, United States) for analysis. Raw radiocarbon dates were subsequently transformed into calendar ages using the Calib 8.2 calibration program, which employs the MARINE20 calibration curve (Heaton et al., 2020) with a local marine reservoir age correction ($\Delta R = -159 \pm 49$ years). ΔR represents the mean of three site ΔRs from the ocean reservoir database: No. 406 (112.3°N, 16.7°E), No. 407 (112.3°N, 16.4°E), and No. 410 (106.5°N, 10.8°E). An age–depth model was constructed by Bayesian analysis using the *Undatable* program in Matlab 2016b software (Lougheed and Obrochta, 2019) (Figure 2A).

3.3 Grain-size analysis

Pretreatment of samples was performed prior to conducting grain-size analysis. Samples were reacted in 10% H_2O_2 for 24 h to remove OM, followed by the addition of 0.5 HCl until biological carbonate was completely removed. Each sample was rinsed several times with ionized water and then treated by adding a dispersant of 0.5% sodium hexametaphosphate solution. The remaining solids were analysed using a Mastersize-2000 laser particle-size analyser. The measurement range was 0.02–2000 μm with a size resolution of 0.01 μm, and the measurement error was within 3% (Xu et al., 2016).

3.4 Analysis of organic matter

Samples were ground to a particle size of <75 μm and then soaked in 0.4 mol/L HCl for 12 h at room temperature to eliminate excess inorganic carbonates. The remaining solids were rinsed four times with deionized water, freeze-dried, and transferred to tin

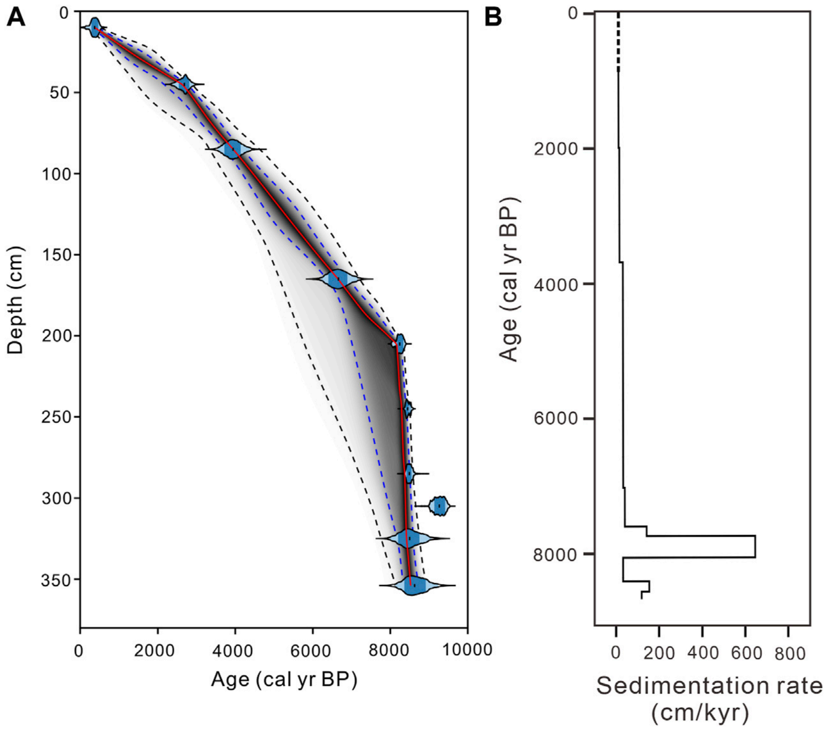

FIGURE 2
(A) Depth-age model for sediments of core G02. The shaded areas represent the 1σ uncertainties of calendar ages obtained with Undatable software using Bayesian statistical age modelling. **(B)** Sedimentation rate of core G02.

TABLE 1 AMS ^{14}C data from core G02.

Depth (cm)	Material	AMS ^{14}C age (yr BP)	1σ cal BP	Calendar age (cal yr BP)	Code no. (Beta)
10.0	*Globorotalia menardii*	1470 ± 30	758–911	833	528043
45.5		3410 ± 30	2977–3173	3078	528044
85.0		4290 ± 30	4086–4292	4194	528045
165.5		6280 ± 30	6408–6592	6502	528046
205.5		7130 ± 30	7336–7490	7416	528047
245.5	Mixed planktonic foraminifera	7390 ± 30	7571–7723	7651	528048
285.5		7440 ± 30	7617–7777	7701	528049
305.5		8010 ± 30	8205–8358	8283	541102
325.5		8110 ± 30	8313–8472	8391	541103
354.5		8290 ± 30	8491–8696	8597	528050

capsules. Analyses of TOC and TN were performed using a Euro EA 3000 elemental analyser with a standard deviation of ±0.02% dry wt (n = 6) for TOC and ± 0.002% dry wt (n = 6) for TN. Analyses of stable isotopes were determined using an elemental analyser/stable isotope ratio mass spectrometer (FLASH EA 1112 series coupled with Thermo Fisher Delta V continuous flow isotopic ratio mass spectrometer) at Center for Isotope Geochemistry and Geochronology, Laoshan Laboratory with a standard deviation of ± 0.1‰ for δ^{13}C and ± 0.1‰ for δ^{15}N (n = 6).

4 Results

4.1 Geochronology of core G02

AMS ^{14}C dating results are presented in Table 1. Interpolation of the results indicates that the earliest (lowermost) sediments deposited in core G02 have an age of ~8.6 cal kyr BP, with a mean sedimentation rate in the core of ~40 cm/kyr. Overall, the calculated sedimentation rate is higher in the lower part of the core

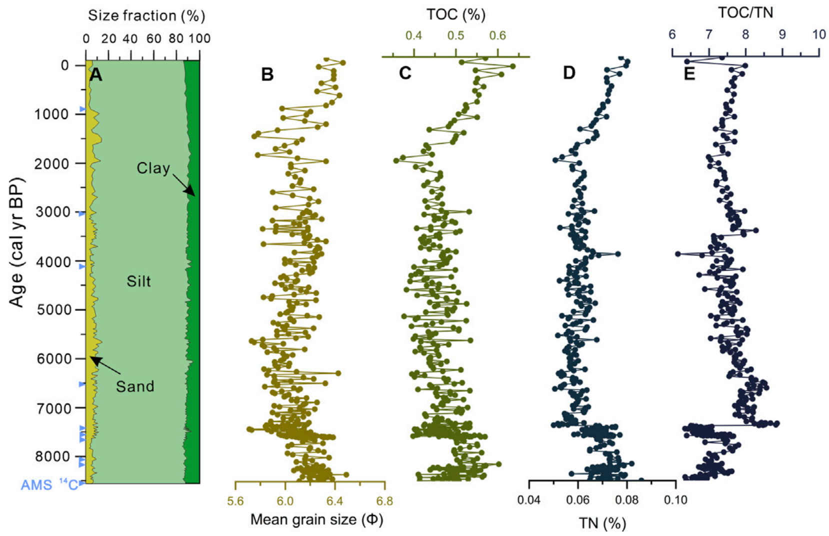

FIGURE 3
Temporal variations in mean grain size, sedimentary organic matter (SOM), and lithology in core G02. **(A)** Sediment size composition; **(B)** Mean grain size; **(C)** total organic carbon (TOC); **(D)** total nitrogen (TN); and **(E)** TOC/TN ratio.

than in the upper part. A sedimentation rate of ~180 cm/kyr is calculated for the period 8.6–8.3 cal kyr BP. An abrupt increase in sedimentation rate is observed during 8.3–7.7 cal kyr BP, reaching ~800 cm/kyr. After that, the sedimentation rate is stable at ~35 cm/kyr during 7.6–4.2 cal kyr BP and decreases slightly to 15 cm/kyr after 4.2 cal kyr BP (Figure 2B).

4.2 Grain-size characteristics

Sediment in core G02 was mainly composed of homogeneous grey to dark-grey clayey silt, which constitutes 63.31%–88.99% of the core, with a mean value of 81.86%. The proportions of sand and clay range from 5.15% to 14.45% and from 4.96% to 14.40%, with mean values of 6.41% and 11.75%, respectively (Figure 3A; Supplementary Table S1). The mean grain size (Mz) of sediments in core G02 varies mainly from 5.8 to 6.4 Φ. The Mz showed a gradual coarsening trend from 8.6 cal kyr BP to ~5.6 cal kyr BP due to a significant increase of sand content. Then the Mz was relatively stable (fluctuating around 6) from ~5.6 cal kyr BP to ~1.4 cal kyr BP followed by a slight increase of amplitude fluctuation over the last ~1.4 kyr, there is a clear trend of refinement (Figure 3B; Supplementary Table S1).

4.3 Contents of organic carbon and nitrogen

Contents of TOC and TN range from 0.36% to 0.64% and from 0.05% to 0.08%, with mean values of 0.48% and 0.06%, respectively (Figures 3C, D; Supplementary Table S1). The pattern of TN content through the core is similar to that of TOC, with both being uniform in the lower part of the core and showing a small increase in the upper part. Values of $\delta^{13}C$ and $\delta^{15}N$ for sediments of core G02 range from −21.97‰ to −20.63‰ and from 5.12‰ to 6.25‰, with mean values of −21.20‰ and 5.74‰, respectively (Supplementary Table S1). Both $\delta^{13}C$ and $\delta^{15}N$ display multi-decadal to centennial fluctuations. $\delta^{13}C$ values fluctuate irregularly in the bottom part of the core (355–205 cm core depth) and decrease slowly upwards from 205 to 100 cm core depth (7.3–4.6 cal kyr BP). In the uppermost 100 cm of the core, $\delta^{13}C$ values increase sharply during 3.0–1.4 cal kyr BP and then decrease from 1.4 cal kyr BP. The most obvious feature of the $\delta^{15}N$ values is the large fluctuations from 113 to 78 cm core depth (4.0–5.0 cal kyr BP), with substantial variation in values below and above the fluctuating interval. Values of TOC/TN for core G02 are quite uniform, ranging from 6.2 to 8.9, with a mean value of 7.4 (Figure 3E; Supplementary Table S1).

5 Discussion

5.1 Provenance of sedimentary organic matter

$\delta^{13}C$ and $\delta^{15}N$ can be used to identify the source and distribution of OM in sediment (Selvaraj et al., 2015; Ye et al., 2017; Mackensen and Schmiedl, 2019). Because of different photosynthetic mechanisms, the stable isotope $\delta^{13}C$ and $\delta^{15}N$ values of OM produced by different vegetation types exhibit specific ranges, allowing the sources of OM to be traced in sediment cores (Amir et al., 2021 and references therein). Terrestrial plants are generally divided into C3 and C4 plants. $\delta^{13}C$ values for C3 plants range from −30‰ to −23‰ (mean −27‰), whereas $\delta^{13}C$ values for C4 plants range from −19‰ to −10‰ (mean −13‰). $\delta^{13}C$ values of freshwater plants are close to those of C3 plants, generally ranging from −30‰ to −25‰, and $\delta^{13}C$ values of marine phytoplankton range from −22‰ to −19‰. Similar to $\delta^{13}C$, TOC/TN ratios have been used to differentiate the sources of OM. Terrestrial plants contain large amounts of lignin and cellulose, resulting in higher TOC/TN ratios in comparison with marine plants. In general, TOC/TN ratios of C3 plants exceed 15 and TOC/TN ratios of C4 plants exceed 30. OM produced by marine plants has TOC/TN ratios of <8. In addition, bacterial activity

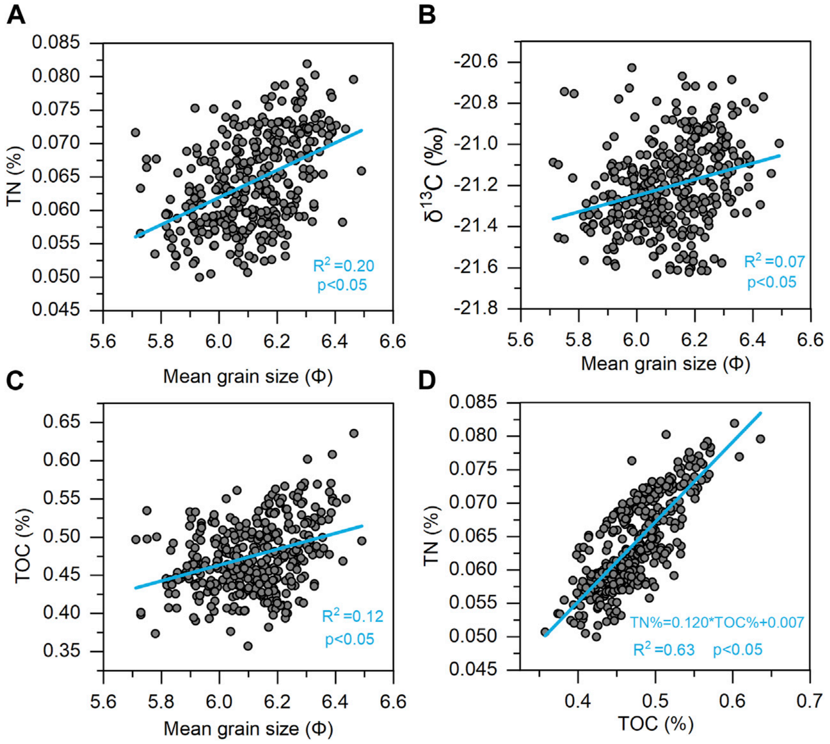

FIGURE 4
Correlation plots for **(A)** TN *vs*. mean grain size, **(B)** δ^{13}C *vs*. mean grain size, **(C)** TOC *vs*. mean grain size, **(D)** TN *vs*. TOC.

can alter TOC/TN ratios by introducing more nitrogen into sediment, with TOC/TN ratios in areas of higher bacterial abundance typically ranging from 4 to 6 (Lamb et al., 2006; Lu et al., 2021).

Controls on the fractionation of C isotopes and on TOC/TN ratios include early diagenesis, clay sorption, and sediment grain size. Fine-grained minerals have a greater ability to adsorb OM owing to their larger specific surface area, and therefore TOC and TN contents are higher in fine-rather than coarse-grained sediments (Zhang et al., 2022). δ^{13}C also vary according to grain-size fraction, and the stable isotope content of the fine-grained fraction is markedly higher than that of the coarse-grained fraction (Kienast et al., 2005). A plot of Mz values of sediment in core G02 *versus* TOC, TN and δ^{13}C values (Figures 4A–C) reveals substantial scatter, suggesting that sediment Mz has minimal or no effect on TOC, δ^{13}C and is only marginally correlated with TN. The use of TOC/TN ratios of SOM to determine the sources of OM in coastal settings requires consideration of the potential interference of inorganic nitrogen that is adsorbed by clay minerals in the form of $NH4^+$ during deposition, which leads to below-normal TOC/TN ratios. The linear correlation between TOC and TN in core G02 does not have a significant positive TN intercept (Figure 4D), suggesting that inorganic nitrogen may not be an important contribution and that TN more likely reflects the predominant contribution of organic N. In turn, this indicates that the small amount of inorganic nitrogen absorbed by clay minerals is not sufficient to influence the source identification of SOM. It is generally accepted that δ^{13}C is more conservative than TOC/TN ratios in the identification of sources of OM (Hu et al., 2012; Liu et al., 2023). Although early diagenesis has some influence on TOC/TN ratios, the combination of δ^{13}C values and TOC/TN ratios has been effectively applied to constrain OC sources (Liu et al., 2023).

Both δ^{13}C values and TOC/TN ratios of core G02 are consistent with the characteristics of marine OM. The distribution of sample data in diagrams of δ^{13}C *vs*. TOC/TN ratio and δ^{13}C *vs*. δ^{15}N further indicate that the source of SOM from core G02 was a mixture of *in situ* generated marine OM and imported terrestrial OM, with a dominant marine authigenic source and a minor amount of terrestrial OM from C3 plants and freshwater phytoplankton (Figures 5A, B). This mixed source appears to reflect the typical pattern of OM distribution in the continental slope; i.e., compared with the continental shelf, the continental slope is further from the estuary and the transport of terrestrial OM to the continental slope is more difficult, meaning that terrestrial OM accounts for a smaller proportion of the core sediment. On the basis of previous studies of the northwestern SCS continental slope, it is hypothesized that terrestrial OM on this continental slope is sourced mainly from the Red River (Wan et al., 2015; Li et al., 2022b). This interpretation is supported by the Red River being the main source of sediments on the northwestern SCS continental slope, and that Red River sediment can be transported to the southeastern Qiongdongnan Basin under surface and gravity-flow transport (Li et al., 2022a). It is generally considered to be difficult for sediments from the Pearl River and Taiwan Island to reach the northwestern SCS owing to the long distance involved, and only small amounts of sediment are transported to the sea from Hainan Island on account of the absence of large rivers on the island (Li et al., 2022a). Combining the above evidence, we consider that the terrestrial OM in core G02 originated predominantly from the Red River.

To obtain a more accurate understanding of the relative proportions of OM derived from marine and terrestrial sources and their temporal trends, quantitative estimation was performed using a δ^{13}C binary mixing model. Such models are commonly

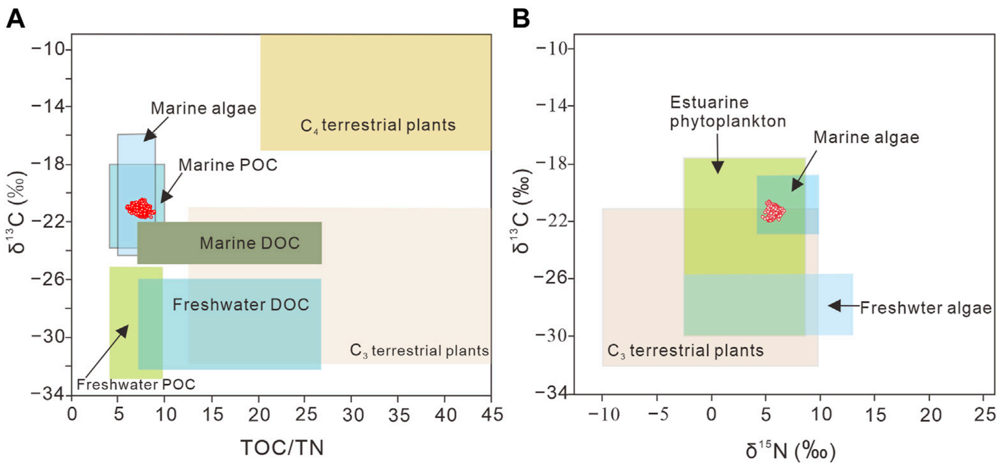

FIGURE 5
Organic matter (OM) source discrimination plots. **(A)** δ^{13}C *vs.* TOC/TN; **(B)** δ^{13}C *vs.* δ^{15}N. Red circles depict core G02 samples from this study. Reference values for various end-members are from Goñi et al. (2003), Lamb et al. (2006), Xia et al. (2015), Ho et al. (2021), and references therein. (POC and DOC denote particulate organic carbon and dissolved organic carbon, respectively).

utilized in studies of marginal seas to estimate the ratio of OM derived from terrestrial sources (OC_T) to OM derived from marine (OC_M) sources (Selvaraj et al., 2015; Chen et al., 2017; Zhou et al., 2022; Liu et al., 2023). The formulation is as follows:

$$\delta^{13}C = f_M \times \delta^{13}C_M + f_T \times \delta^{13}C_T$$

$$f_M + f_T = 1$$

where f_M and f_T represent the ratios of marine and terrestrial OC within TOC, respectively.

The global average δ^{13}C value of the ocean and oceanic phytoplankton (−20‰) is commonly used as the marine OC endmember (Yu et al., 2021) and was also adopted in this study. Considering that the Red River serves as the primary material source in the northwestern SCS continental slope. Thus, the δ^{13}C value of −26.8‰ for surface sediments of rivers on the Red River Delta was selected as the terrestrial OC endmember (Tue et al., 2019).

The binary model analysis shows that from 8.6 cal kyr BP, the proportion of marine OM ranged from 76.0% to 90.8%, with a mean of 82.3%. From 8.6 to 3.0 cal kyr BP, there was an overall increase in terrestrial input. During 3.0–1.4 cal kyr BP, a sharp decline occurred in the proportion of terrestrial-derived OM, with levels decreasing from 23.6% to 9.2%. From 1.4 cal kyr BP, the proportion of marine autochthonous OM decreased and the proportion of terrestrial OM input showed a slight increase.

5.2 Influence of subsurface water intrusion on δ^{15}N values of sediments in the NSCS

5.2.1 Potential factors affecting δ^{15}N values in sediment

The δ^{15}N value of sediment is highly sensitive to the oceanic nitrogen cycle and can be used to study the process of nitrogen cycling and its controlling mechanisms in the ocean (Gaye et al., 2009; Ren et al., 2012). The supply of nitrogen from various external and internal sources into the EZ, such as atmospheric nitrogen deposition, upwelling, lateral intrusion, and remineralization, modulates the biogeochemical of oligotrophic oceans and complicates nitrogen dynamics in the upper water column (Yang et al., 2017; Li M. et al., 2019). If OM is well-preserved in the sediment, dynamics of nitrogen can leave distinguishable signatures in the time series of the δ^{15}N values. Sediment δ^{15}N values during the Middle Holocene are higher than those of the Late Holocene (Figure 6H). The variations in δ^{15}N values within core G02 may be a function of several independent factors, such as variations in sediment grain size, diagenesis, nitrate isotopic composition, the degree of nitrate utilization, and denitrification (Altabet, 2001; Wang et al., 2022).

Our analyses reveal that the variation in grain size within core G02 is negligible and that it bears no correlation to changes in δ^{15}N ($R^2 = 0.02$, $p<0.05$). Therefore, the variability in δ^{15}N values cannot be attributed to variation in particle size. Selective degradation of OM during early diagenesis can change the nitrogen isotope signals of OM. This phenomenon is typically more pronounced in environments with lower sedimentation rates, such as the open ocean (Tesdal et al., 2013). In the present study, core G02 records a shallow water depth of 200 m and a high sedimentation rate of 40 cm/kyr. In this case, the N isotopic signatures of OM can be preserved in sediments with little isotopic alteration during sinking through the water column and subsequent burial. Therefore, in our analysis and interpretation of the δ^{15}N variation in the core, we ignore the potential influence of early diagenesis during sedimentation (Yang et al., 2017).

The utilization of nitrate in seawater has a substantial influence on δ^{15}N values. The assimilation of nutrients by phytoplankton preferentially uses the lighter nitrogen isotope (^{14}N), owing to the Rayleigh fractionation effect, and $^{15}NO_3^-$ is utilized only when $^{14}NO_3^-$ is deficient (Altabet, 2001). In seawater with sufficient nitrate or strong upwelling, it is difficult for phytoplankton to fully utilize $^{14}NO_3^-$, resulting in negative δ^{15}N values in sediments (Gaye et al., 2013). Previous studies have found that

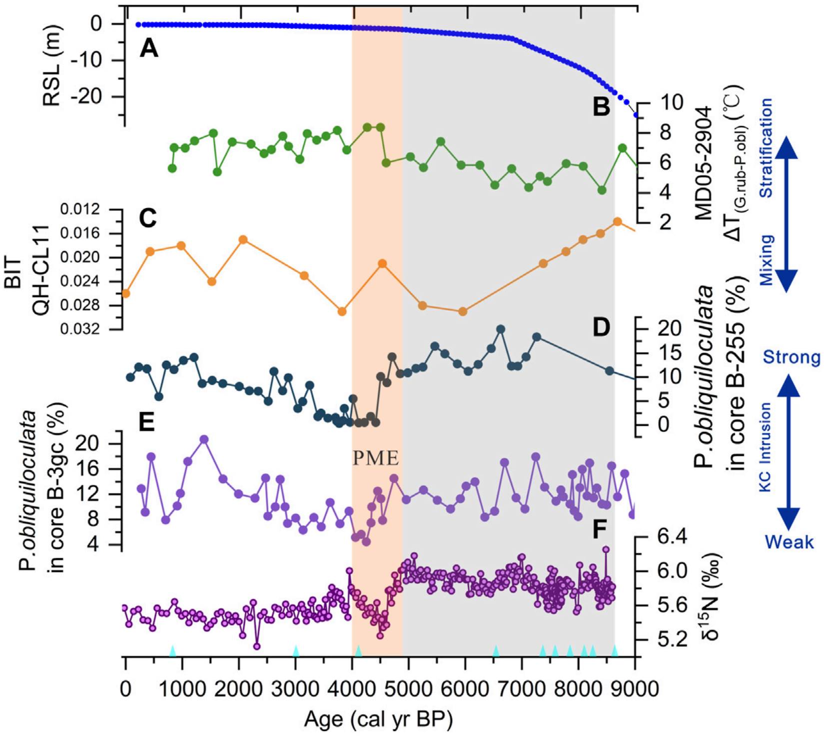

FIGURE 6
Comparison of results for core G02 with those of other environmental proxies. The gray bar and orange bar represent periods of enhanced and weakened Kuroshio Current (KC) intrusion, respectively. **(A)** Global relative sea level (RSL) (Lambeck et al., 2014); **(B)** The water temperature difference between layers ($\Delta T_{(G-P)}$) of core MD05-2904 (Steinke et al., 2011); **(C)** The ratio of brGDGTs to isoGDGTs (BIT) results (Wang et al., 2023b); **(D–E)** abundance of *P. obliquiloculata* in cores B-3gc and B-255 (Jian et al., 2000); and **(F)** temporal variation in $\delta^{15}N$ within core G02 (this study). PEM = *Pulleniatina* Minimum Event.

the SCS constitutes a typical oligotrophic oceanic regime and that nitrate is an important limiting control on primary productivity in this sea (Lin et al., 2010; Yan et al., 2022). Hence, nitrate in the NSCS is generally considered to be completely depleted (Takahashi and Hori, 1984; Kienast, 2000; Liu et al., 2020). Consequently, nitrate utilization is unlikely to have regulated the variation in sediment $\delta^{15}N$ values in core G02.

In nitrate-depleted water, nitrate in the EZ is almost completely consumed, and phytoplankton are unable to distinguish between $^{14}NO_3^-$ and $^{15}NO_3^-$. The $\delta^{15}N$ value of OM is governed primarily by the isotopic composition of nitrate in seawater rather than by the nitrogen isotopic fractionation that occurs during phytoplankton uptake (Higginson et al., 2003). Recent research conducted in the NSCS has revealed similar $\delta^{15}N$ values for nitrate in the EZ and subsurface layer, demonstrating that subsurface nitrate serves as the primary source of new N to support export production (Yang et al., 2017). The nitrogen isotopic signature of upwelled nitrate in the subsurface may become imprinted on settling particulate organic matter that is ultimately buried in sediment (Yang et al., 2022). This altered nature of subsurface water may explain the variation in $\delta^{15}N$ values of core G02 sediments. Denitrification reactions facilitated by denitrifying bacteria are known to influence the $\delta^{15}N$ values of subsurface water (Yang et al., 2017). Denitrification is the process by which heterotrophic bacteria convert NO_3^- to NO_2 or N_2 under anaerobic conditions and leads to an increase in $\delta^{15}N$ values of nitrate in seawater (Li C. et al., 2019). Denitrification is promoted by conditions of higher TOC content, warmer temperature, lower dissolved oxygen, and lower salinity (Kienast, 2000; Guo et al., 2020). Subsurface water in the NSCS is characterized by anoxia and relatively high nitrate content, favouring the occurrence of bacterial denitrification (Yang et al., 2017; Jurikova et al., 2022). Numerous studies have demonstrated that *in situ* denitrification is responsible for the depletion of dissolved nitrate and the corresponding high $\delta^{15}N$ values in subsurface hypoxic water (e.g., Chen et al., 2019; Yan et al., 2022). Therefore, we infer that the variation in $\delta^{15}N$ values in core G02 sediments may have been caused by stronger subsurface water denitrification during the Middle Holocene and weaker denitrification during the Late Holocene. It is worth noting that anaerobic ammonia oxidation is coupled to denitrification and may have the same effect on $\delta^{15}N$ (Wu et al., 2020), which needs to be further investigated in the future.

5.2.2 Response of sedimentary $\delta^{15}N$ values to lateral intrusion of the Kuroshio

Here, we explore the specific drivers of temporal changes in denitrification in the study area. A previous study of the Arabian Sea has shown that the decrease in sediment $\delta^{15}N$ associated with denitrification is the low dissolved oxygen concentrations in subsurface waters, with specific mechanisms related to vertical convection between surface water and subsurface waters (Banakar et al., 2005). Strong thermoclines and haloclines prevent the vertical mixing of water, making it difficult for oxygen-rich water to be transported downwards from the surface layer (Chen et al., 2019). Winter monsoon controlled sea surface temperature (SST) and wind strength are the main factors affecting the exchange of surface and subsurface seawater. Strong East Asian winter monsoon (EAWM) increases the depth of the mixed layer, thickens the thermocline and halocline, enhances vertical mixing of surface and subsurface seawater, and increases dissolved oxygen concentrations in the subsurface layer. Weak EAWM leads to shallower thermocline and halocline depth, weak vertical mixing and stronger stratification (Steinke et al., 2010; Zhang et al., 2022). The lack of large-scale upwelling in the northwestern SCS, where seawater stratification is common, suggests that it is possible that the variation in δ^{15}N values in sediments of core G02 has been at least partly controlled by the upper water column stratification (Lin et al., 2010; Wu et al., 2017; Zhu et al., 2020; Wang et al., 2023a). A recent study has reconstructed the upper vertical structure of the SCS during the Holocene using ΔT (water temperature difference between layers) and BIT index (the ratio of brGDGTs to isoGDGTs) (Wang et al., 2023b). A decrease in ΔT and an increase in the BIT index indicate enhanced stratification (Figures 6B, C), as has been identified for the Late Holocene in the NSCS (Steinke et al., 2011). The inferred increase in stratification would have led to a positive shift in δ^{15}N during the Late Holocene, which contradicts our results for core G02. This suggests that other factors have influenced the intensity of seawater denitrification in the subsurface water of the NSCS during 7.3–4.8 cal kyr BP, which exceeded the variation in δ^{15}N caused by ventilation between the upper and lower water layers.

Besides vertical surface and subsurface ventilation, lateral intrusion can also affect denitrification. Bulk sediment δ^{15}N records from modern water column denitrification zones like the eastern tropical Pacific show strong links between hydrography and denitrification rates (Dubois et al., 2011). Hydrographic variability in the NSCS is influenced predominantly by the western Pacific Ocean (Du et al., 2021; Yang et al., 2022). In particular, the nature of the surface and subsurface waters of the NSCS depends on the intensity of intrusion of the Kuroshio Current through the Luzon Strait (Liu et al., 2016). The lateral intrusion of the Kuroshio Current affects heat and salinity in the SCS, and also the biogeochemical cycling of N and C owing to the low salinity and high content of dissolved OC in Kuroshio water (Yan et al., 2022). Although few studies have examined the evolution of the Kuroshio intrusion in the NSCS, especially regarding the intensity and location of the intrusion (Du et al., 2021; Yang et al., 2022), It has been shown that the geochemical record of northern continental slope of the SCS is strongly influenced by the intensity of the Kuroshio (Li et al., 2021; Wang et al., 2023a). Records from cores B-3gc and B-255 from the western Pacific Ocean show a pronounced increase in the abundance of the planktonic foraminifer *P. obliquiloculata*, a marker species of the Kuroshio Current, at 7.3 cal kyr BP, followed by an abrupt decrease at ~4.6 cal kyr BP—Termed as the *Pulleniatina* Minimum Event (Figures 6D, E; Jian et al., 2000). In addition, Du et al. (2021) reported a westward shift and intensification of the Kuroshio Current in the Middle Holocene. A marked positive shift in δ^{15}N values is recorded in our core G02 before ~4.8 cal kyr BP (Figure 6H), which coincides with enhanced Kuroshio intrusion, and δ^{15}N values become negative for the period 4.8–4.2 cal kyr BP, corresponding to weakening of the SCS branch of the Kuroshio Current intrusion. These results suggest a causal link between intrusion of the Kuroshio Current and variations in δ^{15}N.

Intrusion of the Kuroshio Current into the NSCS occurs predominantly as subsurface water, with minimal surface water intrusion (Xu et al., 2018). In contrast to the high level of dissolved oxygen in the subsurface layer of the NSCS, the Kuroshio Current has very low levels of dissolved oxygen in the subsurface layer (Hosoda et al., 2021). Before 4.8 cal kyr BP, the intrusion of the high-salinity, low-oxygen Kuroshio Current into the NSCS intensified, reducing the dissolved oxygen concentration of NSCS subsurface water over the northwestern continental slope of the SCS via exchange. In addition, the nitrate supplied by the current resulted in an increase in the abundance of denitrifying bacteria. Although vertical ventilation may be stronger during this period compared with 4.8–0 cal kyr BP, the more pronounced Kuroshio intrusion is inferred to have led to higher δ^{15}N values in NSCS subsurface water and therefore also affected the sediment nitrogen isotope composition. Unfortunately, few studies have examined subsurface nitrate in the SCS branch of the Kuroshio Current. Further seasonal field studies on water column nitrate and its stable isotope composition should be conducted to determine the spatial variations in nitrate isotope compositions and the exact mechanisms by which invasion of the Kuroshio Current influences the biochemical cycling of nitrogen in the NSCS.

5.3 Control of variation in δ^{13}C by the monsoon

Previous research on the SCS has revealed that the geochemical record of OC during glacial-interglacial cycles is primarily influenced by climate change manifested by variations in monsoon intensity, on shorter time scales, the interannual variability is predominantly attributed to changes in upwelling and circulation strengths, which are primarily associated with the monsoon and El Niño (Liu et al., 2002). The composition of OC in the marginal marine environment is governed by the relative proportions of contributions from terrestrial and marine sources (Yang et al., 2011). δ^{13}C exhibits a fluctuating but negative trend in core G02 after ~8.6 cal kyr BP, indicating an increase in the proportion of terrestrial OC or a decrease in the proportion of marine OC. Since 8.6 cal kyr BP, the NSCS has undergone minimal sea-level change (Zong, 2004), effectively ruling out the possibility of sea-level-induced changes in terrestrially sourced input. In addition, the Mz of core G02 did not change significantly during the Middle Holocene, suggesting little change in the transport capacity of currents. We hypothesize that the changes occurring after 8.6 cal kyr BP are more likely to be influenced by monsoon variations, as inferred from various paleoclimate records from monsoonal regions elsewhere. There are two monsoon-related possibilities to explain these changes: increased OM inputs to the river and a decrease in marine biomass production.

The productivity of tropical marine areas is primarily controlled by the supply of nutrients in the upper layer of seawater. In regions with higher average water temperatures, the thicker thermocline makes it difficult for nutrients to reach the upper layer of seawater, thereby reducing marine productivity. In areas with more pronounced seasonal variations, the lower SST in winter weaken

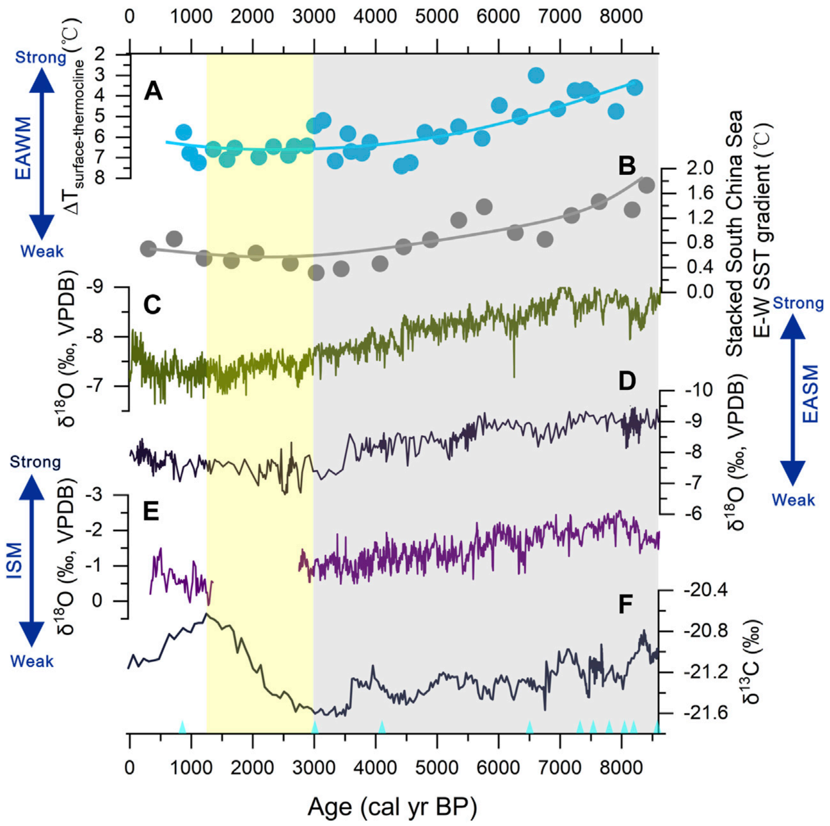

FIGURE 7
Comparison of EAWM, EASM and ISM proxy records with $\delta^{13}C$ records from GO2 cores during the last 8.6 cal kyr BP. **(A–B)** EAWM proxies in South China Sea including SST gradient between west and east (Huang et al., 2011) and between surface and thermocline waters (Steinke et al., 2011); **(C)** $\delta^{18}O$ record of Dongge Cave stalagmite (Dykoski et al., 2005); **(D)** $\delta^{18}O$ record of Dongge Cave stalagmite (Wang et al., 2005); **(E)** $\delta^{18}O$ of Qunf Cave stalagmite (Fleitmann et al., 2003); and **(F)** $\delta^{13}C$ *vs.* depth for core G02.

the stratification of seawater, leading to algal blooms. Therefore, changes in temperature can affect the structure of seawater and subsequently impact marine productivity (Ge et al., 2019). Additionally, surface wind patterns can also influence the structure of the upper water column. Generally, higher wind speeds at the sea surface result in stronger mixing of seawater, leading to higher primary productivity (Li et al., 2021). Marine primary productivity in the NSCS has obvious seasonal characteristics. Liu et al. (2002) using SeaWiFS data and shipboard data revealed that the primary production of the whole basin has a strong peak in winter and a slightly weaker peak in summer, which is mainly controlled by the EAWM and East Asian summer monsoon (EASM).

Variations in the strength of the Holocene EAWM and EASM on multiple time scales have been investigated using various records, including marine sediments, stalagmites, and lake sediments (Jing et al., 2009; Wang et al., 2010; Sandeep et al., 2017; Band et al., 2018; Li et al., 2018; Li et al., 2022). Huang et al. (2011) found that the EAWM has weakened significantly since the Holocene, using the east-west SST gradient record from the NSCS (Figure 7A); Steinke et al. (2011) reached the same conclusion using the SST gradient between surface and thermocline waters (Figure 7B). The stalagmite $\delta^{18}O$ record from Dongge Cave shows that a long-term gradual weakening of the EASM intensity starting at around 8.0 cal kyr BP (Figures 7C, D; Dykoski et al., 2005; Wang et al., 2005). In a word, since the Holocene, especially since the Middle Holocene, both EAWM and EASM have shown a weakening trend. We therefore suggest that the decrease in the proportion of marine OC before ca. 3.0 cal kyr BP is related to the decline in marine primary productivity under East Asian monsoon control.

The decrease in $\delta^{13}C$ continued until approximately 3.0 cal kyr BP and was followed by a rapid increase in $\delta^{13}C$ values during 3.0–1.4 cal kyr BP. The pronounced increase in $\delta^{13}C$ suggests an increase in the proportion of marine OM and a corresponding decrease in the contribution of terrestrial OM during this period. By this time, the EAWM have stabilised, so marine productivity is unlikely to be the main cause of the decline in the proportion of OC from terrestrial sources. The summer monsoon was still in a weakening phase (Huang et al., 2016; Huang et al., 2018), and indeed many studies suggest that it was not until 5.1 cal kyr BP that the Indian summer monsoon began to weaken at an accelerated rate (Fleitmann et al., 2003; Kohn, 2010; Chen et al., 2015; Griffiths et al., 2020). We believe that the decrease in monsoon precipitation due to the continued weakening of the summer monsoon led to a decrease in the flow of the Red River, which affected the transport of Red River material to the ocean and further led to a decrease in the proportion of terrestrial OC, which was also reflected in the sediment sedimentation rate.

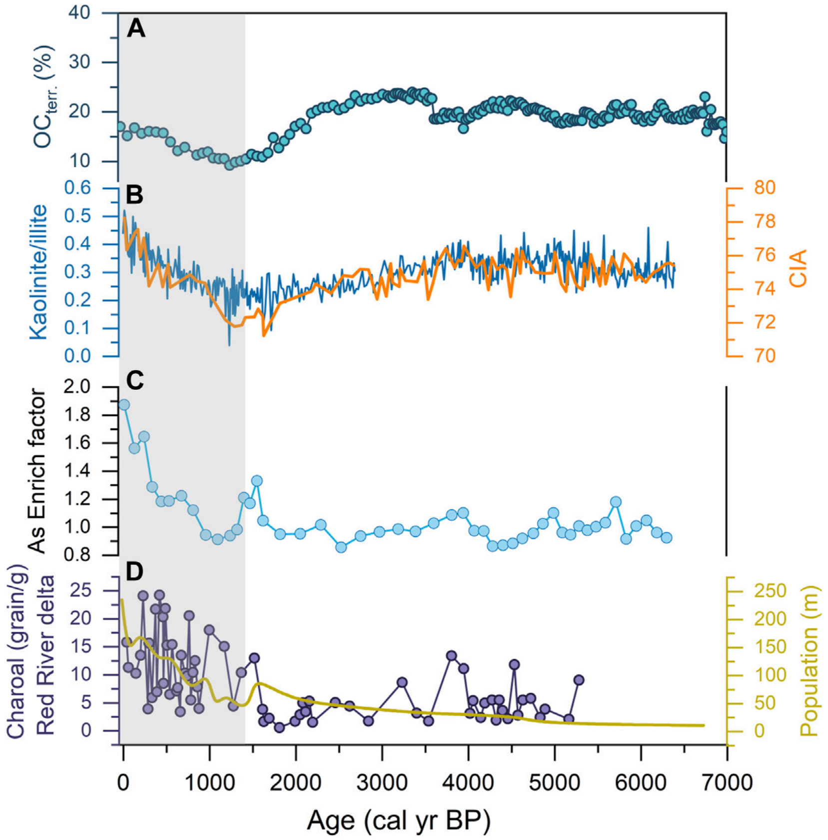

FIGURE 8
Comparison of the record of core G02 with other records for the period since 7000 cal yr BP. The vertical gray band indicates the period dominated by human activity. **(A)** Temporal variation of the proportion of terrestrial organic carbon in TOC in core G02; **(B)** chemical index of alteration (CIA) (orange line) and kaolinite/illite (K/I) (blue line) of cores from the terrestrial northwestern Southeast Qiong basin (Wan et al., 2015); **(C)** enrichment (enrich) factor of As for core 337PC from the northwestern Southeast Qiong basin (Wan et al., 2015); and **(D)** pollen record of the Erhai Sea (Shen et al., 2006) (purple points and line) and temporal change in the population of ancient/historical China (Li et al., 2009b) (yellow line).

5.4 Human disturbance over the past 1400 years

The negative shift in the trend of δ^{13}C values in the Late Holocene part of core G02 and the marked increases in TOC and TN content are interpreted as reflecting an increase in the input of terrestrial OM. Results based on the binary mixing model show that the proportion of terrestrial OC starts to increase after about 1.4 cal kyr BP, increasing from 9.2% to 17.2% of TOC (Figure 8A). A significant weakening trend in the Indian summer monsoon during the Late Holocene has been identified by several studies using data from lake sediments, stalagmites, and other proxies (Fleitmann et al., 2003; Wang et al., 2005; Chen et al., 2015), implying that the increase in terrestrial OC at that time cannot be attributed to strong monsoonal precipitation.

Over the past ~1.4 kyr, temporal variation in terrestrial OC content is consistent with temporal patterns of the chemical index of alteration, the kaolinite/illite ratio, the charcoal record from the Red River delta, and the population in ancient China (Figures 8B, D). We interpret that human activity dominated the variation in input of terrestrial OM after 1.4 cal kyr BP. The population increased steadily during the Late Holocene, and it is known from archaeological information that large-scale human migration from southern China into the lower reaches of the Red River occurred after approximately 2.0 cal kyr BP (Li et al., 2009a; Wan et al., 2015). Prior to this time, fishing and foraging were the main modes of production, whereas the southward migration of population corresponded to the introduction of the use of iron and farming techniques that greatly increased the ability to transform natural environments, primitive agriculture characterized by slash-and-burn cultivation and shifting cultivation began to develop, and metal mining and smelting also developed in parallel, as shown by the record of sulphur-related metallic elements (e.g., As) and their enrichment factors (Figure 8C). Human activity may have affected terrestrial OC inputs in two ways. First, the exposure of rocks by deforestation, farming, and mining stimulated more intense chemical and physical weathering, with eroded products being transported as sediments into marginal seas by rivers. Second, humans may have produced more OM by growing crops, and this OM was transported to marginal seas by rivers (Strong et al., 2013; Huang et al., 2018).

It is noted that the grain size of core G02 shows a clear fining trend through the Late Holocene (Figure 3A), suggesting that the transport capacity of overland flow decreased and that the intensity of the monsoon weakened (Wang et al., 2021). Fine-grained sediments play an influential role in the transport and burial of

OM (Goñi et al., 2008; Wang et al., 2021). Accordingly, we propose that fine-grained sediments also contributed to the increase in terrestrial OM content in core G02 during the Late Holocene. The increase in terrestrially sourced OM content started to stabilize at approximately 500 cal yr BP. We speculate that this change corresponds to the effects of the Little Ice Age, a major cooling event that occurred during 550–150 cal yr BP, when temperatures reached their lowest point during the last 10,000 years (Chen et al., 2015; Fan, 2023). This event may have resulted in reduced plant growth in the Red River basin, thereby slowing the increase in terrestrial OM input, as recorded in core G02.

In summary, we interpret that the impact of human activity on OM production in the Red River basin has increased since 1.4 cal kyr BP but that climatic variation has also been influential. The relative importance of these two factors needs to be more closely investigated in future studies.

6 Conclusion

The high-resolution (~24.2 years) multi-proxy analyses including grain size, TOC, TN, and stable isotopes ($\delta^{13}C$ and $\delta^{15}N$) of a 355 cm sediment core (G02) collected from the northwestern continental slope of the SCS reveal the role of local or remote forcing factors in controlling $\delta^{13}C$ and $\delta^{15}N$ variations since the past ~8600 years. Values of $\delta^{13}C$ and C/N indicate mixed marine and terrestrial sources of OM in the studied core. A $\delta^{13}C$ binary mixing model reveals that the source of OM in core G02 is mainly marine OM (82.3 ± 3%), with the remainder being terrestrial OM. Variations in $\delta^{13}C$ and $\delta^{15}N$ throughout the core are poorly correlated, suggesting that C and N isotopes respond to different factors. Through the period 8.6–4.6 cal kyr BP, $\delta^{15}N$ values of core G02 increased substantially. After excluding several potential determinants of change in $\delta^{15}N$ values, we infer that this change reflected an increasing degree of intrusion of low-oxygen subsurface water by the Kuroshio Current into the NSCS. The low-oxygen environment enhanced the denitrification of bacteria and resulted in positive $\delta^{15}N$ values of SOM. The continuous weakening of the East Asian monsoon and Indian summer monsoon resulted in negative $\delta^{13}C$ values during 8.6–3.0 cal kyr BP and positive $\delta^{13}C$ values during 3.0–1.4 cal kyr BP in the G02 core sediments, respectively. Since 1.4 cal kyr BP, human activity has played an increasingly important role in governing OC production and burial.

Data availability statement

The raw data supporting the conclusion of this article will be made available by the authors upon reasonable request.

Author contributions

GT and LC designed the study. DC and GZ collected samples in the field. LC and YA performed experiments on particle size and isotopes. GT wrote the manuscript. JL, GX, BC, DC, and ML revised the manuscript. All authors contributed to the article and approved the submitted version.

Funding

This work was financially supported by the National Natural Science Foundation of China (Grant Nos 41906062, 41906066, 42076070, and 42176071), Natural Science Foundation of Shandong Province, China (Grant Nos ZR2020MD069 and ZR2020MD079) and Asia Cooperation Fund (Comparative Study of Geoenvironment and Geohazards in the Yangtze River Delta and the Red River Delta).

Acknowledgments

We thank Hongying Song from the Center for Isotope Geochemistry and Geochronology, Laoshan Laboratory, Qingdao, China, for her help in isotope analysis. We also thank Shiwen Zheng and Jingbo Chen from College of Marine Geosciences, Ocean University of China, Qingdao, China, for their assistance in planktonic foraminifera selecting and sediment grain-size analysis.

Conflict of interest

The authors declare that the research was conducted in the absence of any commercial or financial relationships that could be construed as a potential conflict of interest.

Publisher's note

Supplementary material

The Supplementary Material for this article can be found online at: https://www.frontiersin.org/articles/10.3389/feart.2023.1238920/full#supplementary-material

References

Allison, M. A., Bianchi, T. S., McKee, B. A., and Sampere, T. P. (2007). Carbon burial on river-dominated continental shelves: impact of historical changes in sediment loading adjacent to the Mississippi River. *Geophys. Res. Lett.* 34 (1), L01606. doi:10.1029/2006gl028362

Altabet, M. A. (2001). Nitrogen isotopic evidence for micronutrient control of fractional NO_3^- utilization in the equatorial Pacific. *Limnol. Oceanogr.* 46 (2), 368–380. doi:10.4319/lo.2001.46.2.0368

Amir, M., Paul, D., and Malik, J. N. (2021). Geochemistry of Holocene sediments from Chilika Lagoon, India: inferences on the sources of organic matter and variability of the Indian summer monsoon. *Quat. Int.* 599 (600), 148–157. doi:10.1016/j.quaint.2020.08.050

Banakar, V. K., Oba, T., Chodankar, A. R., Kuramoto, T., Yamamoto, M., and Minagawa, M. (2005). Monsoon related changes in sea surface productivity and water column denitrification in the Eastern Arabian Sea during the last glacial cycle. *Mar. Geol.* 219 (2–3), 99–108. doi:10.1016/j.margeo.2005.05.004

Band, S., Yadava, M. G., Lone, M. A., Shen, C. C., Sree, K., and Ramesh, R. (2018). High-resolution mid-holocene Indian summer monsoon recorded in a stalagmite from the kotumsar Cave, Central India. *Quat. Int.* 479, 19–24. doi:10.1016/j.quaint.2018.01.026

Chen, F., Xu, Q., Chen, J., Birks, H. J. B., Liu, J., Zhang, S., et al. (2015). East Asian summer monsoon precipitation variability since the last deglaciation. *Sci. Rep.* 5 (1), 11186. doi:10.1038/srep11186

Chen, F., Zhou, X., Lao, Q., Wang, S., Jin, G., Chen, C., et al. (2019). Dual isotopic evidence for nitrate sources and active biological transformation in the Northern South China Sea in summer. *PLOS ONE* 14 (1), e0209287. doi:10.1371/journal.pone.0209287

Chen, L., Liu, J., Xing, L., Krauss, K. W., Wang, J., Xu, G., et al. (2017). Historical changes in organic matter input to the muddy sediments along the Zhejiang-Fujian Coast, China over the past 160 years. *Org. Geochem.* 111, 13–25. doi:10.1016/j.orggeochem.2017.06.003

Chow, C. H., Shih, Y. Y., Chien, Y. T., Chen, J. Y., Fan, N., Wu, W. C., et al. (2021). The wind effect on biogeochemistry in eddy cores in the northern South China sea. *Front. Mar. Sci.* 8, 717576. doi:10.3389/fmars.2021.717576

Du, S., Xiang, R., Liu, J., Yan, H., Sha, L., Liu, J. P., et al. (2021). Variable Kuroshio current intrusion into the northern South China Sea over the last 7.3 kyr. *Palaeogeogr. Palaeoclimatol. Palaeoecol.* 562, 110093. doi:10.1016/j.palaeo.2020.110093

Dubois, N., Kienast, M., Kienast, S., Normandeau, C., Calvert, S. E., Herbert, T. D., et al. (2011). Millennial-scale variations in hydrography and biogeochemistry in the Eastern Equatorial Pacific over the last 100 kyr. *Quat. Sci. Rev.* 30 (1-2), 210–223. doi:10.1016/j.quascirev.2010.10.012

Dykoski, C., Edwards, R., Cheng, H., Yuan, D., Cai, Y., Zhang, M., et al. (2005). A high-resolution, absolute-dated Holocene and deglacial Asian monsoon record from Dongge Cave, China. *Earth Planet. Sci. Lett.* 233 (1–2), 71–86. doi:10.1016/j.epsl.2005.01.036

Fan, K. (2023). The little ice age and the fall of the ming dynasty: a review. *Climate* 11 (3), 71. doi:10.3390/cli11030071

Fleitmann, D., Burns, S. J., Mudelsee, M., Neff, U., Kramers, J., Mangini, A., et al. (2003). Holocene forcing of the Indian monsoon recorded in a stalagmite from southern Oman. *Science* 300 (5626), 1737–1739. doi:10.1126/science.1083130

Gaye, B., Nagel, B., Dähnke, K., Rixen, T., Lahajnar, N., and Emeis, K. C. (2013). Amino acid composition and δ^{15}N of suspended matter in the Arabian Sea: implications for organic matter sources and degradation. *Biogeosciences* 10 (11), 7689–7702. doi:10.5194/bg-10-7689-2013

Gaye, B., Wiesner, M. G., and Lahajnar, N. (2009). Nitrogen sources in the South China Sea, as discerned from stable nitrogen isotopic ratios in rivers, sinking particles, and sediments. *Mar. Chem.* 114 (3–4), 72–85. doi:10.1016/j.marchem.2009.04.003

Ge, Q., Xu, D., Ye, L., Yang, K., and Yao, Z. (2019). Linking monsoon activity with river-derived sediments deposition in the northern South China sea. *J. Ocean Univ. China* 18 (5), 1098–1104. doi:10.1007/s11802-019-4155-4

Goñi, M. A., Monacci, N., Gisewhite, R., Crockett, J., Nittrouer, C., Ogston, A., et al. (2008). Terrigenous organic matter in sediments from the Fly River delta-clinoform system (Papua New Guinea). *J. Geophys. Res.* 113 (F1), F01S10. doi:10.1029/2006JF000653

Goñi, M. A., Teixeira, M. J., and Perkey, D. W. (2003). Sources and distribution of organic matter in a river-dominated estuary (Winyah Bay, SC, USA). *Estuar. Coast. Shelf Sci.* 57 (5–6), 1023–1048. doi:10.1016/S0272-7714(03)00008-8

Griffiths, M. L., Johnson, K. R., Pausata, F. S. R., White, J. C., Henderson, G. M., Wood, C. T., et al. (2020). End of green sahara amplified mid-to late Holocene megadroughts in mainland Southeast Asia. *Nat. Commun.* 11 (1), 4204. doi:10.1038/s41467-020-17927-6

Guo, J., Wang, Y., Lai, J., Pan, C., Wang, S., Fu, H., et al. (2020). Spatiotemporal distribution of nitrogen biogeochemical processes in the coastal regions of northern Beibu Gulf, south China sea. *Chemosphere* 239, 124803. doi:10.1016/j.chemosphere.2019.124803

Heaton, T. J., Köhler, P., Butzin, M., Bard, E., Reimer, R. W., Austin, W. E. N., et al. (2020). Marine20—the marine radiocarbon age calibration curve (0–55,000 cal BP). *Radiocarbon* 62 (4), 779–820. doi:10.1017/RDC.2020.68

Hedges, J. I., and Keil, R. G. (1995). Sedimentary organic matter preservation: an assessment and speculative synthesis. *Mar. Chem.* 49, 137–139. doi:10.1016/0304-4203(95)00013-h

Higginson, M. J., Maxwell, J. R., and Altabet, M. A. (2003). Nitrogen isotope and chlorin paleoproductivity records from the Northern South China Sea: remote vs. local forcing of millennial- and orbital-scale variability. *Mar. Geol.* 201 (1–3), 223–250. doi:10.1016/S0025-3227(03)00218-4

Ho, P. C., Okuda, N., Yeh, C. F., Wang, P. L., Gong, G. C., and Hsieh, C. (2021). Carbon and nitrogen isoscape of particulate organic matter in the East China Sea. *Prog. Oceanogr.* 197, 102667. doi:10.1016/j.pocean.2021.102667

Hosoda, S., Inoue, R., Nonaka, M., Sasaki, H., Sasai, Y., and Hirano, M. (2021). Rapid water parcel transport across the Kuroshio Extension in the lower thermocline from dissolved oxygen measurements by Seaglider. *Prog. Earth Planet. Sci.* 8 (1), 16. doi:10.1186/s40645-021-00406-x

Hu, B., Li, J., Zhao, J., Wei, H., Yin, X., Li, G., et al. (2014). Late Holocene elemental and isotopic carbon and nitrogen records from the East China Sea inner shelf: implications for monsoon and upwelling. *Mar. Chem.* 162, 60–70. doi:10.1016/j.marchem.2014.03.008

Hu, L., Shi, X., Bai, Y., Qiao, S., Li, L., Yu, Y., et al. (2016). Recent organic carbon sequestration in the shelf sediments of the Bohai Sea and Yellow Sea, China. *J. Mar. Syst.* 155, 50–58. doi:10.1016/j.jmarsys.2015.10.018

Hu, L., Shi, X., Yu, Z., Lin, T., Wang, H., Ma, D., et al. (2012). Distribution of sedimentary organic matter in estuarine–inner shelf regions of the East China Sea: implications for hydrodynamic forces and anthropogenic impact. *Mar. Chem.* 142 (144), 29–40. doi:10.1016/j.marchem.2012.08.004

Huang, C., Kong, D., Chen, F., Hu, J., Wang, P., and Lin, J. (2021). Multi—proxy reconstructions of climate change and human impacts over the past 7000 Years from an archive of continental shelf sediments off eastern Hainan Island, China. *Front. Earth Sci.* 9, 663634. doi:10.3389/feart.2021.663634

Huang, C., Zeng, T., Ye, F., Xie, L., Wang, Z., Wei, G., et al. (2018). Natural and anthropogenic impacts on environmental changes over the past 7500 years based on the multi-proxy study of shelf sediments in the northern South China Sea. Quat. Sci. *Rev.* 197, 35–48. doi:10.1016/j.quascirev.2018.08.005

Huang, E., Tian, J., and Steinke, S. (2011). Millennial-scale dynamics of the winter cold tongue in the southern South China Sea over the past 26 ka and the East Asian winter monsoon. *Quat. Res.* 75 (1), 196–204. doi:10.1016/j.yqres.2010.08.014

Huang, J., Wan, S., Xiong, Z., Zhao, D., Liu, X., Li, A., et al. (2016). Geochemical records of Taiwan-sourced sediments in the South China Sea linked to Holocene climate changes. *Palaeogeogr. Palaeoclimatol. Palaeoecol.* 441, 871–881. doi:10.1016/j.palaeo.2015.10.036

Jian, Z., Wang, P., Saito, Y., Wang, J., Pflaumann, U., Oba, T., et al. (2000). Holocene variability of the Kuroshio current in the Okinawa Trough, northwestern Pacific Ocean. *Earth Planet. Sci. Lett.* 184, 305–319. doi:10.1016/s0012-821x(00)00321-6

Jing, Z., Qi, Y., Hua, Z., and Zhang, H. (2009). Numerical study on the summer upwelling system in the northern continental shelf of the South China Sea. *Cont. Shelf Res.* 29 (2), 467–478. doi:10.1016/j.csr.2008.11.008

Jurikova, H., Abe, O., Shiah, F. K., and Liang, M. C. (2022). New constraints on biological production and mixing processes in the South China Sea from triple isotope composition of dissolved oxygen. *Biogeosciences* 19 (7), 2043–2058. doi:10.5194/bg-19-2043-2022

Kienast, M., Higginson, M. J., Mollenhauer, G., Eglinton, T. I., Chen, M. T., and Calvert, S. E. (2005). On the sedimentological origin of down-core variations of bulk sedimentary nitrogen isotope ratios. *Paleoceanography* 20 (2). doi:10.1029/2004PA001081

Kienast, M. (2000). Unchanged nitrogen isotopic composition of organic matter in the South China Sea during the last climatic cycle: global implications. *Paleoceanography* 15 (2), 244–253. doi:10.1029/1999PA000407

Kohn, M. J. (2010). Carbon isotope compositions of terrestrial C3 plants as indicators of (paleo)ecology and (paleo)climate. *Proc. Natl. Acad. Sci.* 107 (46), 19691–19695. doi:10.1073/pnas.1004933107

Lamb, A. L., Wilson, G. P., and Leng, M. J. (2006). A review of coastal palaeoclimate and relative sea-level reconstructions using δ^{13}C and C/N ratios in organic material. *Earth-Science Rev.* 75 (1–4), 29–57. doi:10.1016/j.earscirev.2005.10.003

Lambeck, K., Rouby, H., Purcell, A., Sun, Y., and Sambridge, M. (2014). Sea level and global ice volumes from the last glacial maximum to the Holocene. *Proc. Natl. Acad. Sci.* 111 (43), 15296–15303. doi:10.1073/pnas.1411762111

Li, C., Jian, Z., Jia, G., Dang, H., and Wang, J. (2019). Nitrogen fixation changes regulated by upper water structure in the South China sea during the last two glacial cycles. *Glob. Biogeochem. Cycles* 33 (8), 1010–1025. doi:10.1029/2019GB006262

Li, J., Dodson, J., Yan, H., Wang, W., Innes, J. B., Zong, Y., et al. (2018). Quantitative Holocene climatic reconstructions for the lower Yangtze region of China. *Clim. Dyn.* 50 (3–4), 1101–1113. doi:10.1007/s00382-017-3664-3

Li, M., Ouyang, T., Zhu, Z., Tian, C., Peng, S., Tang, Z., et al. (2019). Rare earth element fractionations of the northwestern South China Sea sediments, and their implications for East Asian monsoon reconstruction during the last 36 kyr. *Quat. Int.* 525, 16–24. doi:10.1016/j.quaint.2019.09.007

Li, M., Ouyang, T., Zhu, Z., Tian, C., Peng, S., Zhong, H., et al. (2022a). Reconstruction of chemical weathering intensity and asian summer monsoon evolution in the Red River basin over the past 36 kyr. *Paleoceanogr. Paleoclimatology* 37 (5), 4397. doi:10.1029/2021PA004397

Li, X., Dodson, J., Zhou, J., and Zhou, X. (2009a). Increases of population and expansion of rice agriculture in Asia, and anthropogenic methane emissions since 5000 BP. *Quat. Int.* 202 (1–2), 41–50. doi:10.1016/j.quaint.2008.02.009

Li, Y., Pérez-Mejías, C., Zhao, J., Li, H., Zhang, H., Lu, J., et al. (2022b). Indian summer monsoon variations during the Younger Dryas as revealed by a laminated stalagmite record from the Tibetan Plateau. *Quat. Sci. Rev.* 278, 107375. doi:10.1016/j.quascirev.2022.107375

Li, Z., Pospelova, V., Liu, L., Francois, R., Wu, Y., Mertens, K. N., et al. (2021). High-resolution reconstructions of Holocene sea-surface conditions from dinoflagellate cyst assemblages in the northern South China Sea. *Mar. Geol.* 438, 106528. doi:10.1016/j.margeo.2021.106528

Li, Z., Saito, Y., Dang, P. X., Matsumoto, E., and Vu, Q. L. (2009b). Warfare rather than agriculture as a critical influence on fires in the late Holocene, inferred from northern Vietnam. *Proc. Natl. Acad. Sci.* 106 (28), 11490–11495. doi:10.1073/pnas.0813258106

Lin, D. C., Liu, C. H., Fang, T. H., Tsai, C. H., Murayama, M., and Chen, M. T. (2006). Millennial-scale changes in terrestrial sediment input and Holocene surface hydrography in the northern South China Sea (IMAGES MD972146). *Palaeogeogr. Palaeoclimatol. Palaeoecol.* 236 (1–2), 56–73. doi:10.1016/j.palaeo.2005.11.039

Lin, I. I., Lien, C. C., Wu, C. R., Wong, G. T. F., Huang, C. W., and Chiang, T. L. (2010). Enhanced primary production in the oligotrophic South China Sea by eddy injection in spring. *Geophys. Res. Lett.* 37 (16), L16602. doi:10.1029/2010GL043872

Liu, K. K., Chao, S. Y., Shaw, P. T., Gong, G. C., Chen, C. C., and Tang, T. Y. (2002). Monsoon-forced chlorophyll distribution and primary production in the South China Sea: observations and a numerical study. *Deep Sea Res. Part I Oceanogr. Res. Pap.* 49 (8), 1387–1412. doi:10.1016/S0967-0637(02)00035-3

Liu, M., Li, C., Zhang, F., Zhang, R., Yang, W., Chen, M., et al. (2020). A persistent increase in primary productivity east off Hainan Island (northwestern South China Sea) over the last decades as inferred from sediment records. *Mar. Pollut. Bull.* 158, 111428. doi:10.1016/j.marpolbul.2020.111428

Liu, S., Li, D. W., Xiang, R., Yu, M., Zhang, H., Li, L., et al. (2023). Intensification of the East Asian winter monsoon resulted in greater preservation of terrestrial organic carbon on the inner shelf of the East China Sea since the last 1400 years. *Palaeogeogr. Palaeoclimatol. Palaeoecol.* 615, 111454. doi:10.1016/j.palaeo.2023.111454

Liu, Z., Zhao, Y., Colin, C., Stattegger, K., Wiesner, M. G., Huh, C. A., et al. (2016). Source-to-sink transport processes of fluvial sediments in the South China Sea. *Earth-Science Rev.* 153, 238–273. doi:10.1016/j.earscirev.2015.08.005

Lougheed, B. C., and Obrochta, S. P. (2019). A rapid, deterministic age-depth modeling routine for geological sequences with inherent depth uncertainty. *Paleoceanogr. Paleoclimatology* 34 (1), 122–133. doi:10.1029/2018PA003457

Lu, X., Huang, C., Chen, F., Zhang, S., Lao, Q., Chen, C., et al. (2021). Carbon and nitrogen isotopic compositions of particulate organic matter in the upwelling zone off the east coast of Hainan Island, China. *Mar. Pollut. Bull.* 167, 112349. doi:10.1016/j.marpolbul.2021.112349

Mackensen, A., and Schmiedl, G. (2019). Stable carbon isotopes in paleoceanography: atmosphere, oceans, and sediments. *Earth-Science Rev.* 197, 102893. doi:10.1016/j.earscirev.2019.102893

Ren, H., Sigman, D. M., Chen, M. T., and Kao, S. J. (2012). Elevated foraminifera-bound nitrogen isotopic composition during the last ice age in the South China Sea and its global and regional implications. *Glob. Biogeochem. Cycles* 26 (1), 26. doi:10.1029/2010GB004020

Sandeep, K., Shankar, R., Warrier, A. K., Yadava, M. G., Ramesh, R., Jani, R. A., et al. (2017). A multi-proxy lake sediment record of Indian summer monsoon variability during the Holocene in southern India. *Palaeogeogr. Palaeoclimatol. Palaeoecol.* 476, 1–14. doi:10.1016/j.palaeo.2017.03.021

Selvaraj, K., Lee, T. Y., Yang, J. Y. T., Canuel, E. A., Huang, J. C., Dai, M., et al. (2015). Stable isotopic and biomarker evidence of terrigenous organic matter export to the deep sea during tropical storms. *Mar. Geol.* 364, 32–42. doi:10.1016/j.margeo.2015.03.005

Shen, J., Jones, R. T., Yang, X., Dearing, J. A., and Wang, S. (2006). The Holocene vegetation history of Lake Erhai, Yunnan province southwestern China: the role of climate and human forcings. *Holocene* 16 (2), 265–276. doi:10.1191/0959683606hl923rp

Steinke, S., Glatz, C., Mohtadi, M., Groeneveld, J., Li, Q., and Jian, Z. (2011). Past dynamics of the East asian monsoon: no inverse behaviour between the summer and winter monsoon during the Holocene. *Glob. Planet. Change* 78 (3–4), 170–177. doi:10.1016/j.gloplacha.2011.06.006

Steinke, S., Mohtadi, M., Groeneveld, J., Lin, L. C., Löwemark, L., Chen, M. T., et al. (2010). Reconstructing the southern south China sea upper water column structure since the last glacial maximum: implications for the East asian winter monsoon development. *Paleoceanography* 25 (2), 1850. doi:10.1029/2009PA001850)

Strong, D., Flecker, R., Valdes, P. J., Wilkinson, I. P., Rees, J. G., Michaelides, K., et al. (2013). A new regional, mid-Holocene palaeoprecipitation signal of the Asian Summer Monsoon. *Quat. Sci. Rev.* 78, 65–76. doi:10.1016/j.quascirev.2013.07.034

Takahashi, M., and Hori, T. (1984). Abundance of picophytoplankton in the subsurface chlorophyll maximum layer in subtropical and tropical waters. *Mar. Biol.* 79 (2), 177–186. doi:10.1007/BF00951826

Tesdal, J. E., Galbraith, E. D., and Kienast, M. (2013). Nitrogen isotopes in bulk marine sediment: linking seafloor observations with subseafloor records. *Biogeosciences* 10 (1), 101–118. doi:10.5194/bg-10-101-2013

Tue, N. T., Quan, D. M., Nguyen, P. T., Dung, L. V., Quy, T. D., and Nhuan, M. T. (2019). Holocene environmental changes in Red River delta, Vietnam as inferred from the stable carbon isotopes and C/N ratios. *J. Earth Syst. Sci.* 128 (1), 15. doi:10.1007/s12040-018-1041-1

Wan, S., Toucanne, S., Clift, P. D., Zhao, D., Bayon, G., Yu, Z., et al. (2015). Human impact overwhelms long-term climate control of weathering and erosion in southwest China. *Geology* 43 (5), 439–442. doi:10.1130/G36570.1

Wang, H., Kandasamy, S., Liu, Q., Lin, B., Lou, J. Y., Veeran, Y., et al. (2021). Roles of sediment supply, geochemical composition and monsoon on organic matter burial along the longitudinal mud belt in the East China Sea in modern times. *Geochim. Cosmochim. Acta*, 66–86. doi:10.1016/j.gca.2021.04.025

Wang, L., Sarnthein, M., Erlenkeuser, H., Grimalt, J., Grootes, P., Heilig, S., et al. (1999). East asian monsoon climate during the late pleistocene: high-resolution sediment records from the South China Sea. *Mar. Geol.* 156 (1–4), 245–284. doi:10.1016/S0025-3227(98)00182-0

Wang, L., Ye, F., Wei, G., Huang, C., Chen, F., Li, Z., et al. (2022). East Asian summer monsoon and human activity imprint on $\delta^{15}N_{org}$ records at the northern coast of the South China Sea over the last 7500 years. *Palaeogeogr. Palaeoclimatol. Palaeoecol.* 595, 110976. doi:10.1016/j.palaeo.2022.110976

Wang, M., Chen, X., Qin, L., Man, M., Su, M., and Jia, G. (2023a). Concomitant changes of lipid biomarker and water column mixing since mid-Holocene. *Chem. Geol.* 629, 121502. doi:10.1016/j.chemgeo.2023.121502

Wang, X., Zhong, Y., Clift, P. D., Feng, Y., Wilson, D. J., Kaboth-Bahr, S., et al. (2023b). Interactions between depositional regime and climate proxies in the northern South China sea since the last glacial maximum. *Paleoceanogr. Paleoclimatology* 38 (3), e2022PA004591. doi:10.1029/2022PA004591

Wang, Y., Cheng, H., Edwards, R. L., He, Y., Kong, X., An, Z., et al. (2005). The Holocene Asian monsoon: links to solar changes and North Atlantic climate. *Science* 308 (5723), 854–857. doi:10.1126/science.1106296

Wang, Y., Liu, X., and Herzschuh, U. (2010). Asynchronous evolution of the Indian and East asian summer monsoon indicated by Holocene moisture patterns in monsoonal central Asia. *Earth-Science Rev.* 103 (3–4), 135–153. doi:10.1016/j.earscirev.2010.09.004

Wu, J., Hong, Y., Wen, X., Li, Y., Wang, Y., and Chang, X. (2020). Activity, abundance, and community composition of anaerobic ammonia–oxidizing (anammox) bacteria in sediment cores of the Pearl River Estuary. *Estuaries Coasts* 43 (1), 73–85. doi:10.1007/s12237-019-00668-1

Wu, K., Shi, X., Lou, Z., Wu, B., Li, J., Zhang, H., et al. (2021). Sedimentary responses to climate changes and human activities over the past 7400 Years in the western Sunda shelf. *Front. Earth Sci.* 9, 631815. doi:10.3389/feart.2021.631815

Wu, M. S., Zong, Y., Mok, K. M., Cheung, K. M., Xiong, H., and Huang, G. (2017). Holocene hydrological and sea surface temperature changes in the northern coast of the South China Sea. *J. Asian Earth Sci.* 135, 268–280. doi:10.1016/j.jseaes.2017.01.004

Xia, X., Wu, Q., Zhu, B., Zhao, P., Zhang, S., and Yang, L. (2015). Analyzing the contribution of climate change to long-term variations in sediment nitrogen sources for reservoirs/lakes. *Sci. Total Environ.* 523, 64–73. doi:10.1016/j.scitotenv.2015.03.140

Xu, G., Liu, J., Liu, S., Wang, Z., Hu, G., and Kong, X. (2016). Modern muddy deposit along the Zhejiang coast in the East China Sea: response to large-scale human projects. *Cont. Shelf Res.* 130, 68–78. doi:10.1016/j.csr.2016.10.007

Xu, M. N., Zhang, W., Zhu, Y., Liu, L., Zheng, Z., Wan, X. S., et al. (2018). Enhanced ammonia oxidation caused by lateral Kuroshio intrusion in the boundary zone of the northern South China Sea. *Geophys. Res. Lett.* 45 (13), 6585–6593. doi:10.1029/2018GL077896

Yan, X., Yang, J. Y. T., Xu, M. N., Tan, E., Zheng, Z., Zou, W., et al. (2022). Isotope constraints on nitrogen dynamics in the upper water column of the South China Sea. *Front. Mar. Sci.* 9, 1104135. doi:10.3389/fmars.2022.1104135

Yang, B., Liu, S. M., and Zhang, G. L. (2018). Geochemical characteristics of phosphorus in surface sediments from the continental shelf region of the northern South China Sea. *Mar. Chem.* 198, 44–55. doi:10.1016/j.marchem.2017.11.001

Yang, J. Y. T., Kao, S. J., Dai, M., Yan, X., and Lin, H. L. (2017). Examining N cycling in the northern South China sea from N isotopic signals in nitrate and particulate phases: n cycling in the South China sea. *J. Geophys. Res. Biogeosciences* 122 (8), 2118–2136. doi:10.1002/2016JG003618

Yang, J. T., Tang, J., Kang, S., Dai, M., Kao, S., Yan, X., et al. (2022). Comparison of nitrate isotopes between the South China sea and western North Pacific ocean: insights into biogeochemical signals and water exchange. *J. Geophys. Res. Oceans* 127 (5), 18304. doi:10.1029/2021JC018304

Yang, S., Tang, M., Yim, W. W. S., Zong, Y., Huang, G., Switzer, A. D., et al. (2011). Burial of organic carbon in Holocene sediments of the Zhujiang (Pearl River) and Changjiang (Yangtze River) estuaries. *Mar. Chem.* 123 (1–4), 1–10. doi:10.1016/j.marchem.2010.07.001

Ye, F., Guo, W., Shi, Z., Jia, G., and Wei, G. (2017). Seasonal dynamics of particulate organic matter and its response to flooding in the Pearl River Estuary, China, revealed by stable isotope (δ^{13}C and δ^{15}N) analyses. *J. Geophys. Res. Oceans* 122 (8), 6835–6856. doi:10.1002/2017JC012931

Yu, M., Eglinton, T. I., Haghipour, N., Montluçon, D. B., Wacker, L., Hou, P., et al. (2021). Contrasting fates of terrestrial organic carbon pools in marginal sea sediments. *Geochimica Cosmochimica Acta* 309, 16–30. doi:10.1016/j.gca.2021.06.018

Zhang, M., Liu, X., Xu, F., Li, A., Gu, Y., Chang, X., et al. (2022). Organic carbon deposition on the inner shelf of the East China sea constrained by sea level and climatic changes since the last deglaciation. *J. Ocean Univ. China* 2022, 1–13. doi:10.1007/s11802-023-5476-x

Zheng, X., Kao, S., Chen, Z., Menviel, L., Chen, H., Du, Y., et al. (2016). Deepwater circulation variation in the South China sea since the last glacial maximum. *Geophys. Res. Lett.* 43 (16), 8590–8599. doi:10.1002/2016GL070342

Zhou, G., Cao, X., Xia, J., Wang, S., and Song, Z. (2022). A dramatic marine environment change in the Beibu Gulf of the South China Sea around 3.2 kyr BP. *Lithosphere* 2022, 2632112. doi:10.2113/2022/2632112

Zhu, X., Jia, G., Mao, S., Sun, Y., Wu, N., Tian, Y., et al. (2020). Long chain 1,14-diols as potential indicators for upper water stratification in the open South China Sea. *Ecol. Indic.* 110, 105900. doi:10.1016/j.ecolind.2019.105900

Zong, Y. (2004). Mid-Holocene sea-level highstand along the Southeast coast of China. *Quat. Int.* 117 (1), 55–67. doi:10.1016/S1040-6182(03)00116-2

frontiers | Frontiers in Earth Science

TYPE Original Research
PUBLISHED 04 January 2024
DOI 10.3389/feart.2023.1329921

OPEN ACCESS

EDITED BY
Nadia Solovieva,
University College London,
United Kingdom

REVIEWED BY
Liang Yi,
Tongji University, China
Jiawei Fan,
China Earthquake Administration, China

*CORRESPONDENCE
Shenghui Jiang,
✉ jsh254677@ouc.edu.cn
Jing Feng,
✉ fengjing200272@163.com

RECEIVED 30 October 2023
ACCEPTED 15 December 2023
PUBLISHED 04 January 2024

CITATION
Qiu J, Jiang S, Wang J, Feng J, Chen J, Dong C, Jiang Y and Zhang D (2024), Mechanism and genesis of Sanmen Bay as a sink of Holocene Yangtze River sediment, Zhejiang Province, China. *Front. Earth Sci.* 11:1329921. doi: 10.3389/feart.2023.1329921

Mechanism and genesis of Sanmen Bay as a sink of Holocene Yangtze River sediment, Zhejiang Province, China

Jiandong Qiu[1,2], Shenghui Jiang[3]*, Jianqiang Wang[4], Jing Feng[1]*, Junbing Chen[4], Chao Dong[4], Yunshui Jiang[1] and Daolai Zhang[1]

[1]Qingdao Institute of Marine Geology, China Geological Survey, Qingdao, China, [2]Laboratory for Marine Geology, Laoshan Laboratory for Marine Science and Technology, Qingdao, China, [3]Key Lab of Submarine Geosciences and Prospecting Techniques, MOE and College of Marine Geoscience, Ocean University of China, Qingdao, China, [4]Zhejiang Institute of Hydrogeology and Engineering Geology, Ningbo, China

Introduction: The Holocene mud deposits that extend from the Yangtze River mouth to the Taiwan Strait along the Zhejiang–Fujian coast, East China Sea (ECS), have attracted considerable research attention. However, there is a lack of consensus regarding the redistribution flux of Yangtze River sediment after it enters the sea. There are many bays along the Zhejiang and Fujian coasts, but their role in the source–sink process of Yangtze River sediment is not well-documented owing to limited data.

Methods: In this study, data from shallow seismic profiles, core samples, and surface sediment samples were analysed to assess the role of Sanmen Bay, the second largest bay in Zhejiang Province, in the source–sink process of Yangtze River sediments.

Results: The results showed that Sanmen Bay is an important sink for Yangtze River sediments. The characteristics of the clay minerals indicate that the fine-grained sediments in Sanmen Bay are mainly derived from Yangtze River sediments. The thickness of Holocene deposits in Sanmen Bay ranges from 8.2 to 32.0 m, with an average of 23.4 m and a total sediment volume of 5.06×10^4 Mt, accounting for 1% of Yangtze River sediment in this time period. The Bayesian age-depth model based on borehole accelerator mass spectrometry (AMS) ^{14}C dating shows that a high sedimentation rate occurred in the early and late Holocene but decreased significantly in the mid-Holocene, which is similar to that of the inner shelf of the East China Sea (ECS).

Conclusion: The variation in the Holocene sedimentation rate in Sanmen Bay is related to the southward transport process and mechanism of Yangtze River sediments. The results of this study provide a basis for understanding the source–sink process of sediment in large rivers.

KEYWORDS

Sanmen Bay, Holocene, Yangtze River, seismic profiles, sediment budget

1 Introduction

Since the Holocene, mud has accumulated on continental shelves under various environmental conditions, resulting in the formation of diverse mud depocenters (Hanebuth et al., 2015; Porz et al., 2021). Owing to their high deposition rate and the stable sedimentary environment, high-resolution environmental evolution information of the Holocene has been recorded and widely used to study climate change, source–sink processes, and sea–land interactions (Liu et al., 2020; Liu et al., 2023). Mud depocenters represent sinks of major offshore sediments on modern continental shelves. Mud deposits are not as stable and uniform as expected and require more detailed study (Gao and Collins, 2014; Porz et al., 2021).

Holocene mud deposited along the Zhejiang–Fujian coast has attracted considerable research attention. In the past decade, numerous studies have focused on its spatial distribution, sediment transport and provenance, paleoclimate reconstruction, and paleomonsoon evolution and formation mechanisms (Liu et al., 2006; 2007; Qiao et al., 2017; Dong et al., 2021). These studies made considerable contributions to understanding the mud belt.

The sediment flux of the Yangtze River into the sea is controlled by multiple factors, including precipitation in the Yangtze River Basin, the development of the Yangtze River Delta, and human activities (Feng et al., 2016; Dong et al., 2021). Sediment from the Yangtze River on the ECS shelf is characterised by a pattern of “summer storage and winter transport.” The summer monsoon contributes more than 80% of the annual precipitation (Wang et al., 2011), and sediment carried by river runoff is mainly deposited in estuaries during this period (Feng et al., 2016). The impact of the diluted water from the Yangtze River on the coasts of Zhejiang and Fujian is weak (Wu et al., 2013). From late September to April, following the summer monsoon, the winter monsoon drives coastal flow along Zhejiang and Fujian, carrying suspended material from the Yangtze River from north to south (Qin et al., 1987; Lee and Chao, 2003). Therefore, the sediment flux of the Yangtze River into the sea is unlikely to be the main factor controlling sedimentary evolution in the mud deposit area south of the Yangtze River Delta (Shi et al., 2022). Instead, coastal flow controlled by the East Asian winter monsoon is more likely to be the primary driving force for transporting nearshore sediments, and it plays a fundamental role in the formation of mud depocenters on the eastern China continental shelf (Shi et al., 2022). The strength of the winter monsoon directly

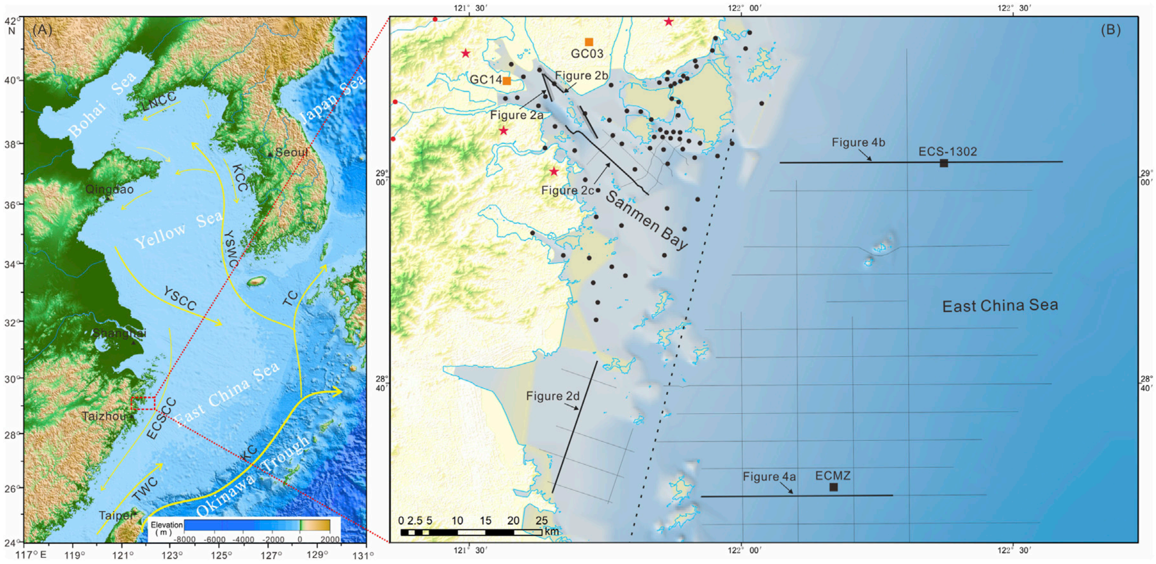

FIGURE 1
(A) Bathymetry, regional circulation pattern (in winter) and **(B)** locations of seismic profile (black lines), surface sediments of sea area (black circles), floodplain (red circles), mountain area (red stars), and boreholes (yellow squares) in Sanmen Bay, and boreholes on the inner shelf of East China Sea (black squares). The black dotted line separates Sanmen Bay and the inner shelf of the East China Sea. KC, Kuroshio Current; TC: Tsushima current; YSWC, Yellow Sea Warm Current; TWC, Taiwan Warm Current; YSCC, Yellow Sea Coastal Current; KCC, Korean Coastal Current; ECSCC, East China Sea Coastal Current). The base map was drawn using GMT software (Wessel and Smith, 1995), and elevation data was from http://www.ngdc.noaa.gov/mgg/global/global.html.

TABLE 1 Details of the sediment cores described in this study.

Core no.	Latitude	Longitude	Elevation (m)	Core length (m)	Data source
GC03	29.158°N	121.570°E	+3	80	This study
GC14	29.220°N	121.720°E	+1.88	105.5	This study
ECS-1302	29.025°N	122.371°E	−38.2	60.9	Liu et al. (2023)
ECMZ	28.5°N	122.17°E	−40	44.06	Dong (2018)

TABLE 2 Accelerator mass spectrometry (AMS)^{14}C ages for cores GC03 and GC14.

Core	Core depth (m)	Material	δ^{13}C (‰)	Conventional^{14}C age (^{14}C yr)	Calibrated age (cal yr BP)		Lab. No.
					Intercept	Range (1σ)	
GC03	3.34	Shell		780 ± 30	314	248–409	QNLMA 210192
	6.46	Shell	−0.3	1320 ± 30	772	689–840	Beta 562745
	7.20	Shell		2135 ± 30	1620	1538–1697	QNLMA 210193
	9.28	Oyster		6675 ± 35	7050	6964–7146	QNLMA 210194
	10.36	Shell	−1.7	7400 ± 30	7743	7666–7821	Beta 562746
	12.17	Gastropod		7740 ± 40	8088	8006–8168	QNLMA 210195
	22.27	Gastropod	−1.8	8300 ± 30	8730	8616–8835	Beta 562747
GC14	2.13	Shell		1890 ± 35	1352	1274–1419	QNLMA 210196
	3.33	Gastropod		2130 ± 35	1614	1532–1696	QNLMA 210197
	4.51	Shell	−2.1	6260 ± 30	6572	6482–6658	Beta 562748
	9.79	Oyster	1.1	6850 ± 30	7235	7157–7310	Beta 562749
	11.85	Oyster		6985 ± 40	7360	7278–7429	QNLMA 210198
	14.13	Gastropod	−1.4	7400 ± 30	7743	7666–7821	Beta 562750

TABLE 3 Optically stimulated luminescence (OSL) dating results for cores GC03 and GC14.

Core no.	Sample no.	Depth (m)	U (ppm)	Th (ppm)	K (%)	Water (%)	De (Gy)	Dose rate (Gy/ka)	Age (ka)
GC03	OSL-1	27.34	1.83	9.99	2.09	23.92	56.5 ± 8.3	2.77 ± 0.15	20.4 ± 1.4
	OSL-3	36.23	2.16	10.21	1.76	14.38	87.2 ± 9.2	2.60 ± 0.20	33.5 ± 4.5
	OSL-5	41.86	2.36	10.74	1.67	13.49	98.6 ± 10.2	1.71 ± 0.18	57.8 ± 2.5
	OSL-7	49.34	1.67	8.46	1.70	12.95	182.8 ± 10.5	2.49 ± 0.19	73.3 ± 3.1
	OSL-8	52.51	1.90	7.34	1.27	13.25	325.3 ± 12.4	2.85 ± 0.23	114.1 ± 12.8
GC14	OSL-1	21.45	1.78	8.57	1.93	17.26	85.9 ±8.2	2.73 ± 0.20	31.5 ± 1.3
	OSL-3	31.84	1.96	9.54	1.96	16.69	90.6 ± 10.1	1.67 ± 0.16	54.2 ± 5.0
	OSL-5	37.02	2.01	8.90	1.83	14.98	178.8 ± 11.7	2.55 ± 0.20	70.0 ± 4.3
	OSL-7	42.05	1.88	7.26	1.42	14.52	295.8± 12.5	3.41 ± 0.24	86.8 ± 3.5

determines the transport capacity of resuspended fine particles from the mouth of the Yangtze River southward (Zheng et al., 2014). The formation of the Zhejiang and Fujian coastal flows preceded the formation of the mud deposits during the mid-Holocene (Li and Zhang, 2020), indicating the existence of other decisive driving factors. In addition to coastal flow, the Taiwan Warm Current/Kuroshio branch plays a crucial role in the exchange of materials and energy in the ECS shelf (Hu et al., 2015). The intensity of the Kuroshio has changed significantly during the Holocene (Jian et al., 2020), and the combined effect of the Kuroshio branch and the Zhejiang and Fujian coastal flows is also likely to change, making it unclear what role they played in the migration of the mud depocenter. Furthermore, the redistribution flux of Yangtze River sediment after it enters the sea remains uncertain (Liu et al., 2007). The bay is an important sink for Yangtze River sediment in the nearshore area. There are many bays along the Zhejiang and Fujian coasts, including the Hangzhou, Xiangshan, Sanmen, Taizhou, and Wenzhou Bays. However, there is a lack of research on the sediment flux and capture mechanisms of nearshore bays during the transport process of Yangtze River sediment along the Zhejiang and Fujian coasts.

As the second largest bay in Zhejiang Province, Sanmen Bay has seen achievements in water quality, biology, ecology, hydrodynamics, and land reclamation (Dong and Cao, 1996; Peng, 2013); however, there are few reports on the evolution of sedimentary environments in this area. In this study, based on recent data from shallow seismic profiles, geological drilling, and surface sediment sampling in Sanmen Bay, we aimed to analyse the sedimentary stratigraphy, provenance, sediment flux, and sedimentary genesis mechanism since the beginning of the Holocene and explore the role of Sanmen Bay in the source–sink process of the Yangtze River sediment. The findings of this study

TABLE 4 Assemblages and percentage of clay minerals in Holocene sediments of core GC03 (unit:%).

Core	Depth	Smectite	Illite	Kaolinite	Chlorite
GC03	2.85	3.0	64.2	15.5	17.3
	4.68	5.4	59.2	16.2	19.3
	6.46	5.4	63.4	14.4	16.9
	8.38	5.5	58.0	16.7	19.9
	10.21	6.4	61.8	14.6	17.2
	12.03	3.3	67.2	13.6	15.9
	13.89	4.9	61.4	16.6	17.1
	15.97	5.5	65.0	12.6	16.8
	18.42	5.2	65.1	13.5	16.2
	20.19	6.3	62.0	15.0	16.7
	22.09	-	71.0	13.4	15.5
Min		-	58.0	12.6	15.5
Max		6.4	71.0	16.7	19.9
Average		5.1	63.5	14.7	17.2

reveal the sediment flux patterns of the source–sink process in Sanmen Bay and provide a basis for understanding sediment mechanisms in other large rivers.

2 Materials and methods

2.1 Geological setting

Sanmen Bay is the second largest bay in Zhejiang Province, located in the middle part of China's 'golden coastline' and in the centre of the national coastline, with a sea area of 775 km^2 (Editorial Board of Annals of Bays in China, 1992). It is a structural bay mainly influenced by its location in the Cathaysian fold belt of the South China fold system in the southeast of the Jiangshan-Shaoxing deep fault. Tectonic changes since the Mesozoic are mainly composed of fault deformation, and a fold structure has not developed. Mesozoic volcanic and pyroclastic rocks are widely distributed, and Middle and Upper Neozoic basalts are locally developed. Quaternary continental and coastal facies were the main deposits in the estuary and bay plains. Since the Quaternary, at least three large-scale transgressions have occurred in the study area. The transgression was the largest since the sea level reached its current level approximately 7000 years ago (Peng, 2013).

The landform around Sanmen Bay is mainly hilly, with a catchment area of 3160 km^2. The Jiao River Mountain in the southwest of Sanmen Bay is the highest in elevation, with its main peak Huangxi Liang reaching 882 m above sea level. More than 30 rivers entering the bay are short mountain streams with an annual average runoff of 26.8 × 10^8 m^3. Most sediment entering the sea is coarse-grained material that accumulates in the riverbed above the mouth of the river and gradually develops into small flood- and alluvial plains. Sanmen Bay has a wide sea area; the water depth is generally 5–10 m, and the underwater geomorphology mainly includes plains, scour troughs, and tidal channels. The sediment is composed mainly of clayey silt and silty sand. Clayey silt covers most of the bay and is mainly distributed on a broad tidal flat at the top of the bay. The sediment is coarser at the top of the inlet and gradually becomes finer in the bay owing to stream injection (Editorial Board of Annals of Bays in China, 1992).

Sanmen Bay is a typical semi-closed bay with strong tides and many backstreams, an average tidal range of 4.25 m, and a maximum tidal range of 7.75 m. The tide is a regular semidiurnal tide, and the tidal current reciprocates. Generally, ebb velocity is higher than flood velocity. The maximum flood and ebb velocities are 153 and 200 cm/s, respectively (Yang and Chen, 2007).

2.2 Shallow seismic profiles

In April 2019, 310 km of high-resolution shallow seismic profiles were acquired in Sanmen Bay using a seismic profiling system (CSP-D2400; Subsea Technologies, Aberdeen, United Kingdom) (Figure 1). Seismic reflection data were collected at a pulse energy of 750 J and a frequency band of 100–5000 Hz. High-resolution seismic profiles of 1100 km in the ECS were obtained using a seismic profiling system (SBP/AAE; Great Yarmouth, United Kingdom) in 2012 and 2013. Seismic data were collected at a pulse energy of 500 J and a frequency band of 500–5000 Hz. During the cruises, navigation was accomplished using several differential GPS devices, which were accurate to within 5 m, and the ship speed was generally less than 9 km/h (five knots).

Interpretation of the shallow seismic profile followed the principles of sequence and seismic stratigraphy. Depositional sequences and bounding surfaces (onlap, downlap, truncation, and toplap) were identified based on the reflector characteristics of the seismic data. For all time-depth conversions, an acoustic velocity of 1600 m/s was used for sedimentary successions.

2.3 Core data

Cores GC03 and GC14 were recovered from the tidal flat of Sanmen Bay using rotary drilling from May to June 2019 (Table 1). The study area was covered by ZJCORS. ZJCORS is the Zhejiang Continuous Operation Satellite Positioning Integrated Service System. Its goal is to establish a global navigation satellite system with high accuracy, high temporal and spatial resolution, high efficiency, and high coverage. This system provides convenient, fast, and accurate positioning of drilling locations and elevations. Core positioning and elevation measurements were carried out using a Zhonghaida C30 GPS with a positioning accuracy greater than 10 cm and an elevation measurement accuracy greater than 5 cm. Two cores were drilled consecutively into medium-weathered bedrock. Core GC03 was collected from Shepan Island at an elevation of 3 m, with a length of 80 m and an average recovery of 89%. Core GC14 was collected from Changjie Town at an elevation of 1.88 m, with a length of 105.5 m and an average recovery of 93.1%.

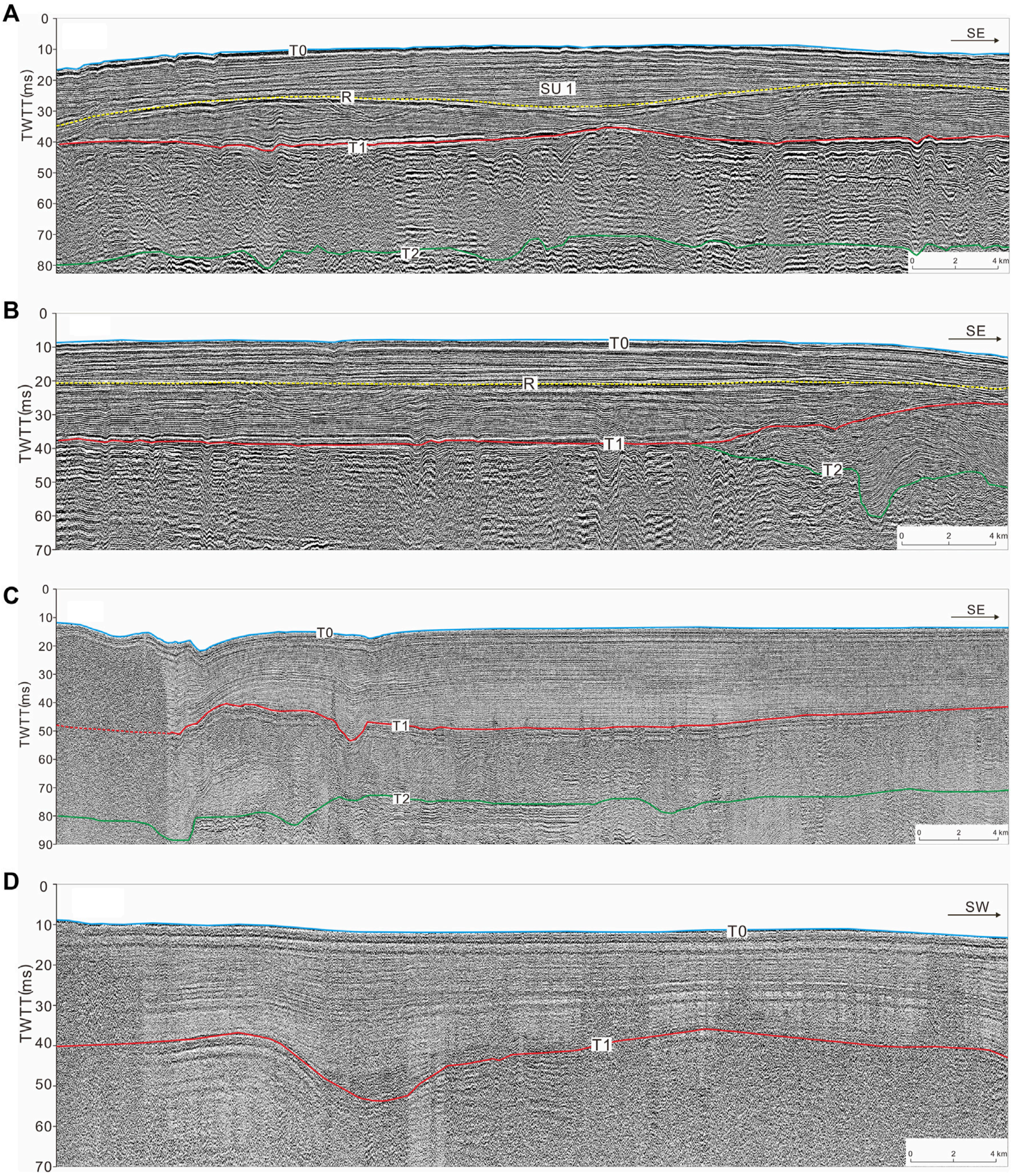

FIGURE 2
Part of the typical seismic profiles at the top **(A,B)** and mouth **(C,D)** of Sanmen Bay. R is an internal unconformity surface, which can be clearly recognised. Note: Figure 1 shows the location of the profile. TWTT, two-way travel time.

In the laboratory, the cores were split lengthwise, visually described, photographed, and subsampled. Gastropods and unbroken shells, including oyster shells, were selected and sent to Beta Analytic (Miami, FL, United States of America) and the Testing Centre of the Laoshan Laboratory (Qingdao, China) for accelerator mass spectrometry (AMS) ^{14}C dating (Table 2). Radiocarbon ages were corrected for fractionation by δ^{13}C values measured simultaneously and for the regional marine reservoir effect ($\triangle R = -66 \pm 30$ a), which was calculated according to the reservoir ages of mollusc shells from six samples from the northern coast of Taiwan Island (Yoneda et al., 2007). Calendar ages were calculated with the Calib rev. 8.1.2 program using the Marine20 curve (Stuiver et al., 2020) and are reported as calendar ^{14}C ages before 1950 CE with one standard deviation (1σ) uncertainty.

A total of nine samples from cores GC03 and GC14 were collected for optically stimulated luminescence (OSL) dating of quartz using a Daybreak 2200 thermoluminescence (TL)/OSL reader (Daybreak Nuclear and Medical Systems, Guilford, CT, United States of America) at the Testing Centre of the Qingdao

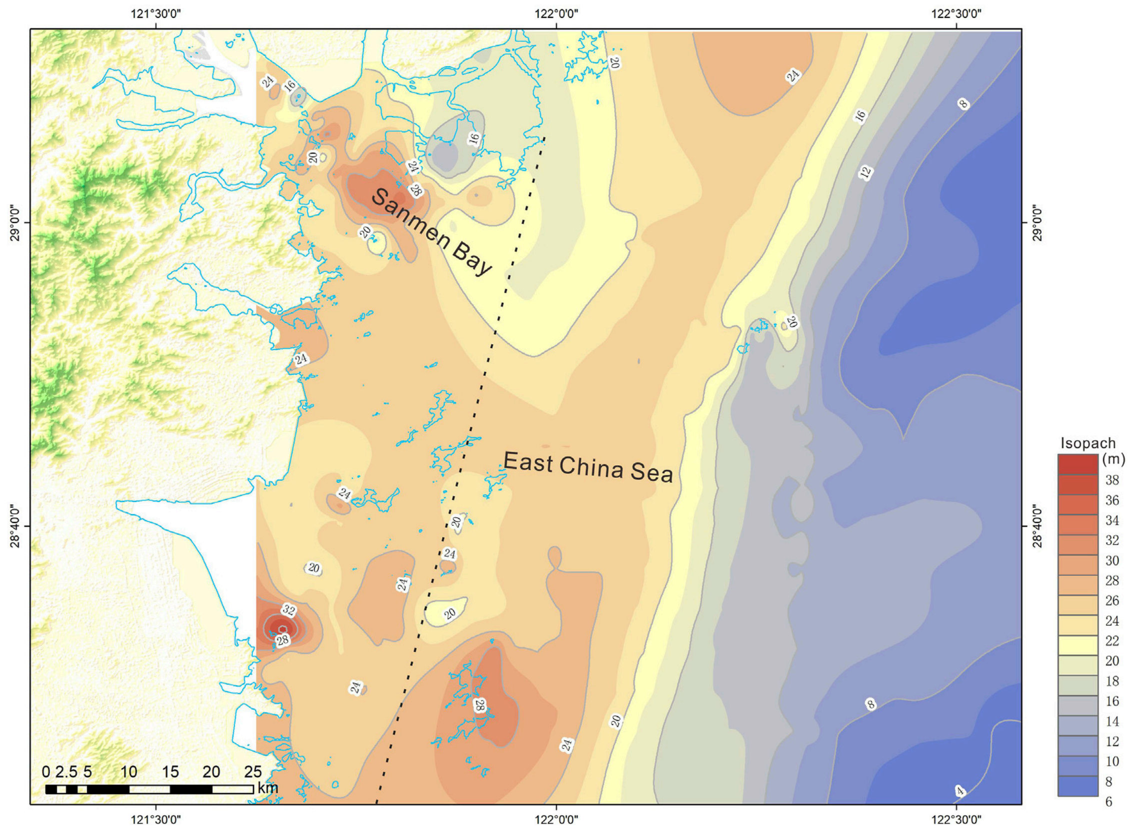

FIGURE 3
Isopach of the seismic unit between T0 and T1 (unit: m), divided into two parts (Sanmen Bay and the inner shelf of East China Sea).

Institute of Marine Geology (Table 3). To determine the equivalent dose (De), the medium-grainde (38–63 μm size) qutartz fraction was separated from all the samples (Lai and Brückner, 2008). The De was determind using the single aliquot regenerative (SAR) standardized growth curve (SGC) method (Roberts and Duller, 2004) with an automated Risø TL/OSL-DA-20 reader. All samples showed high OSL sensitivity and stable OSL signals. The concentrations of K, U, and Th were measured using inductively coupled plasma mass spectrometry (ICP-MS) and converted into dose rates based on data from Aitken (1998) and Marsh et al. (2002).

Subsamples in core GC03 were taken at 20-cm intervals for grain-size analysis and measured using a Malvern Mastersizer 2000 laser particle size analyser (Malvern Panalytical, Malvern, United Kingdom) at the Center of Testing, Qingdao Institute of Marine Geology, China. The upper 23-m sediments of core GC03 were taken at 180- to 200-cm intervals for clay minerals (Table 4) at the Center of Testing, Qingdao Institute of Marine Geology, using a D/Max-2500 X-ray diffractometer, see detail in Guang et al. (2022).

We referenced two well-studied cores from the ECS, ECS-1302 and ECMZ, for comparison (Dong, 2018; Liu et al., 2023).

2.4 Surface sediments

A total of 78 surface sediment samples were acquired from Sanmen Bay in September 2019, including 71 from sea areas, 3 from floodplains, and 4 from mountainous areas (Figure 1). Surface sediments (0–5 cm) were used for analyses of grain size and clay mineral content, which were conducted at the Testing Centre of the Qingdao Institute of Marine Geology using a Mastersizer-2000 laser particle analyser (Malvern Panalytical) and a D/Max-2500 X-ray diffractometer (Rigaku), respectively (Guang et al., 2022).

3 Results

3.1 Seismic stratigraphy (transgressive surface and holocene deposits) shallow seismic structure

Based on the identification of the shallow seismic profile interface, characteristics of the seismic reflection wave groups, and internal reflection structure, three reflection interfaces were recognised, denoted T0, R, and T1, in descending order (Figures 2, 4). Compared with previous geological and geophysical records from the Yangtze River deposits (Liu et al., 2006; Liu et al., 2007) and other similar deltaic deposits of the Yellow (Liu et al., 2004; Liu et al., 2007) and Po rivers (Cattaneo et al., 2003), the prominent acoustic reflector, T1, appears to be the base of the post-glacial transgressive surface, which apparently formed due to rapid landward transgression during rapid sea-level rise (Liu et al., 2004). Meanwhile, R is the internal interface, and T0 is the seafloor.

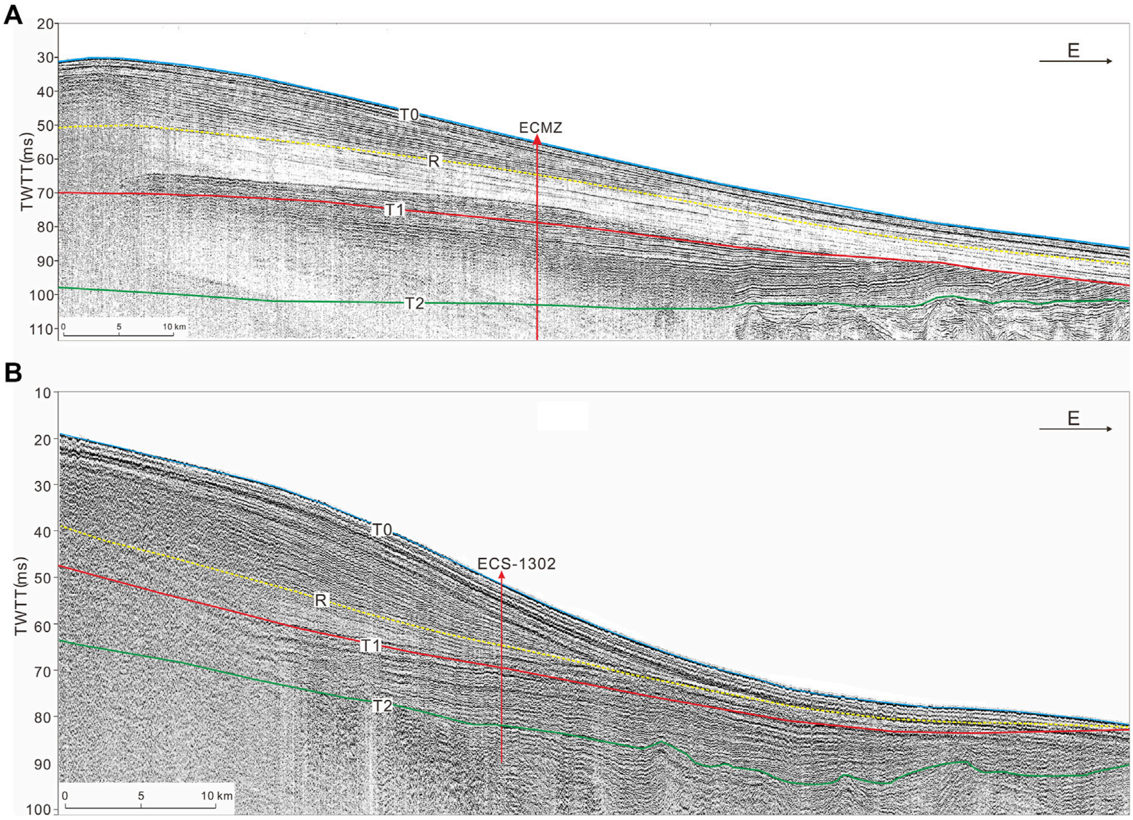

FIGURE 4
Part of the W–E seismic profiles passing through cores ECMZ **(A)** and ECS-1302 **(B)**. The internal angular unconformity surface R in core ECMZ **(A)** was formed at 2 ka (Dong, 2018). The internal unconformity surface R in core ECS-1302 **(B)** represents the maximum flooding surface (Liu et al., 2023). Note: Figure 1 shows the location of the profile. TWTT, two-way travel time.

Based on the internal reflection patterns, the deposits in the study area were divided into two parts: Sanmen Bay and the inner shelf of the ECS. In Sanmen Bay, the seismic unit above T1 is a set of reflection layers with a high frequency and amplitude. At the top of Sanmen Bay, an internal unconformity surface, R, can be identified with strong amplitude, medium and strong reflections, and good continuity; however, it cannot be traced continuously throughout the area and is difficult to correlate with the various seismic profiles. Locally, the strata exhibit a concave or divergent filling reflection structure below the R surface (Figures 2A, B). Reflector R was not easily identified at the entrance to Sanmen Bay (Figures 2C, D). The lack of a well-studied core penetrating these seismic profiles makes it difficult to determine the formation time of interface R or whether R is the Holocene maximum flooding surface (MFS). The thickness of the seismic unit between T1 and T0 ranges from 8.2 to 32.0 m, with an average of 23.4 m (Figure 3). In Sanmen Bay, there are two deposition areas with thicknesses of more than 28 m in the north and south. The unit below T1 mainly shows chaotic reflection (Figure 2) and parallel-to-subparallel or undulating reflection, which was not the focus of the present study.

On the inner shelf of the ECS, the seismic unit above T1 mainly shows predominant sigmoidal clinoform deposits (Figure 4), which have been well-studied in previous research (Liu et al., 2006; Liu et al., 2007; Xu et al., 2012). In this area, the clinoform thins offshore to the east, reaching a depocentre of more than 28 m to the south (Figure 4A). Close inspection of many clinoform profiles reveals a rather complex inner structure. In the south, an angular unconformity surface, R, separates the upper flatter and opaque layers from the lower relatively dipping and transparent layers (Liu et al., 2007; Xu et al., 2012). The AMS ^{14}C dates in the ECMZ core indicated that R was formed at 2 ka (Dong, 2018). In the north, the 2 ka angular unconformity surface is not easily recognised (Figure 4B), but another internal reflector, R, which represents the Holocene MFS, can be identified according to the AMS ^{14}C dates of ECS-1302 (Liu et al., 2023), with the upper strata downlapping onto the MFS.

3.2 Lithofacies associations and dating of cores

Based on the lithological facies, sediment colour, AMS ^{14}C, and OSL dating data, and the focus of the current study (Figure 5), cores GC03 and GC14 are mainly divided into Holocene deposits and pre-Holocene deposits (Figure 6), of which Holocene deposits are the focus of this study.

In core GC03, 0–2.8-m deposits were backfill soil. The 2.8–23.6-m deposits were mainly composed of deep grey clayey silt with uniform lithology and occasionally black carbonaceous spots, and they contained a large number of shell fragments and complete snail

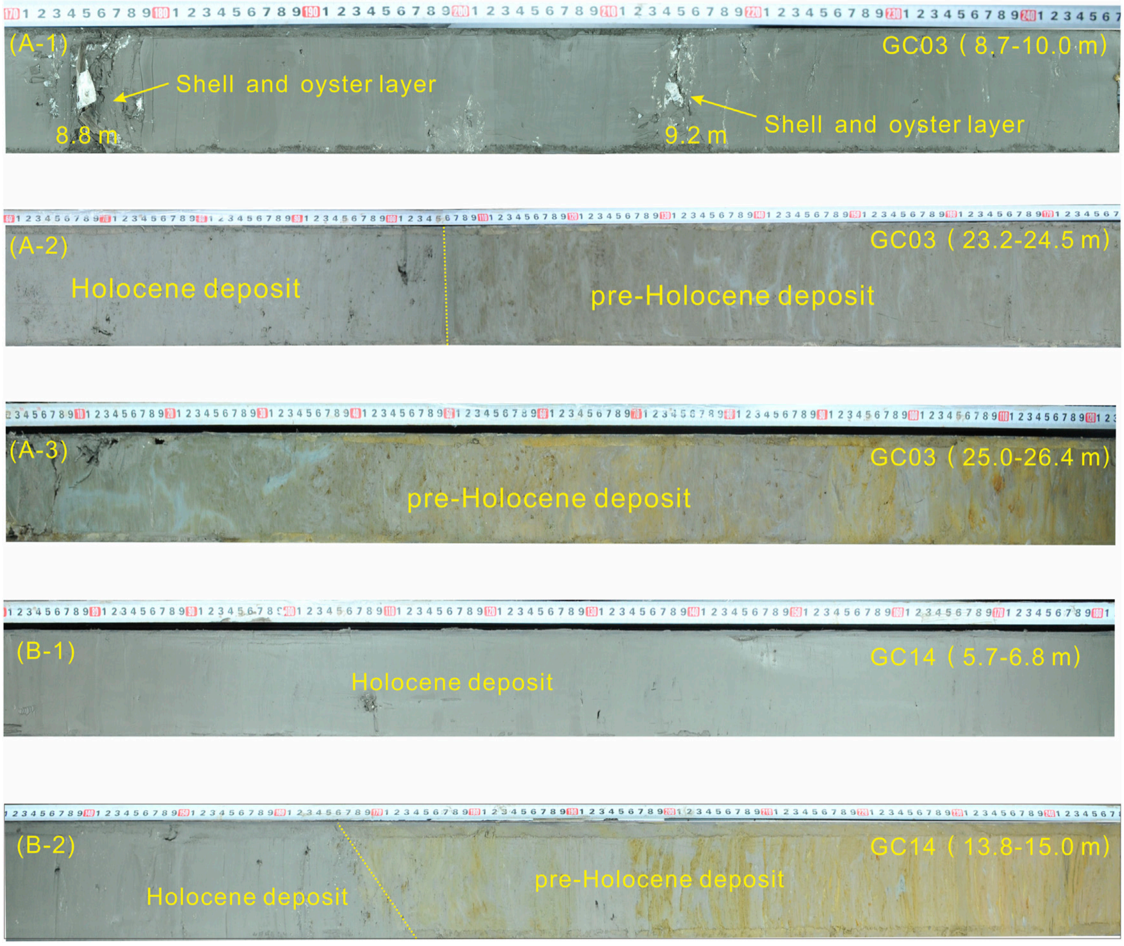

FIGURE 5
Core sediment in GC03 **(A)** and GC14 **(B)**; 8.8 and 9.2 m in core GC03 are shell and oyster layers, respectively. The yellow dotted line separates the Holocene and pre-Holocene deposits.

and oyster shells, especially in the 8.7–10.0-m depositional section of the core. The deposits between 8.8 and 9.2 m in core GC03 were shell and oyster layers (Figure 5A). There were seven AMS ^{14}C dating datasets with good sedimentary sequences, which were between 314 and 8712 cal a BP. Combined with the sedimentary facies and in comparison with the well-studied cores in the ECS, this section is recognised as a Holocene deposit. This section is separated from the underlying section by an erosional surface (Figure 5B). The underlying section (23.6–80 m) is mainly characterised by clayey silt, with the upper section being a deep yellow-grey and cyan-green hard clay layer, and the area 3–6 m below 49 m being composed of four coarse sand and gravel layers (Figure 6A). The OSL dating data in this section ranged from 20.4 ± 1.4 ka to 114.1 ± 12.8 ka, indicating that this section represents a pre-Holocene deposit.

In core GC14, the 0–2.0-m deposits were backfill soil. The 2.0–14.2-m deposits were deep grey clayey silt with uniform lithology, occasional black carbonaceous spots, many shell fragments, and relatively complete snails. There were six AMS ^{14}C dating datasets with good sedimentary sequences, which were between 1352 and 7743 cal a BP. Combined with the sedimentary facies and in comparison with the well-studied cores in the ECS, this section is recognised as a Holocene deposit. This section is separated from the underlying section by an erosional surface (Figure 5B). The underlying section (14.2–105.5 m) is mainly characterised by clayey silt, with the upper section being a deep yellow-grey and cyan-green hard clay layer, and the area 2–5 m below 60 m being composed of three coarse sand and gravel layers (Figure 6B). The OSL dating data in this section ranged from 31.5 ± 1.3 ka to 86.8 ± 3.5 ka, indicating that this section is a pre-Holocene deposit.

3.3 Holocene sedimentation rate in sanmen Bay

Accurate dating of sediments forms the fundamental basis of sedimentology in coastal settings. Dating sediments in coastal areas remain challenging due to the extremely complex sediment transport and deposition processes in fluvial-marine transition zones. A general stratigraphic framework of cores GC03 and GC14 was identified based on sedimentary structures and facies, grain size, and comparison with other well-studied cores from adjacent areas (Figure 6). Thirteen AMS ^{14}C datings are shown in Table 2, ranging from 314 to 8712 cal a BP in core GC03 and 1352–7743 cal a BP in core GC14, which were in good stratigraphic

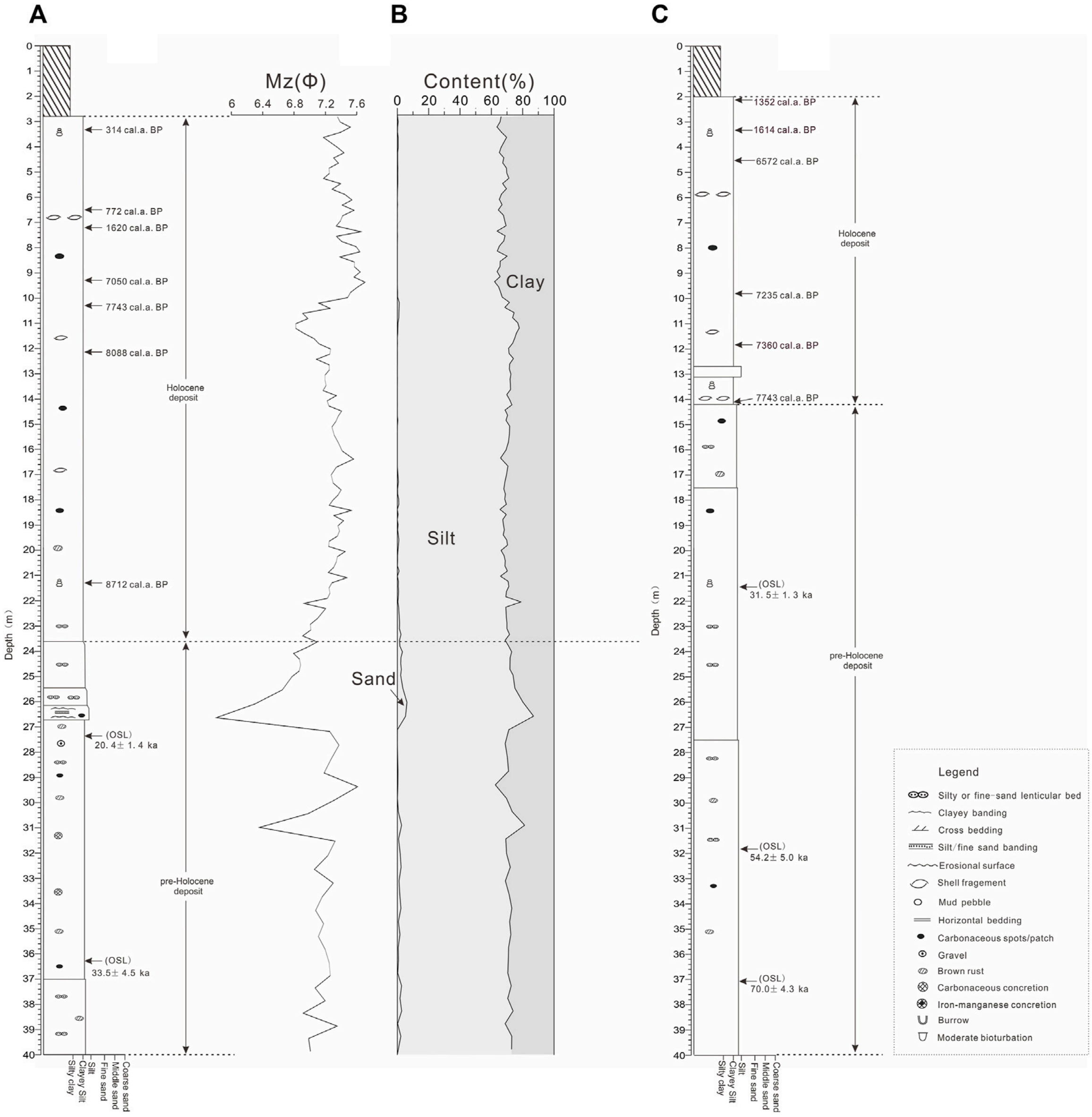

FIGURE 6
Geological column of cores GC03 **(A)** and GC14 **(C)** with accelerator mass spectrometry (AMS) ^{14}C and optically stimulated luminescence (OSL) dates and distribution of mean grain size (Mz) and sediment contents of core GC 03 **(B)**.

order and did not appear age-reversed. Nine OSL datings are shown in Table 3, ranging from 20.4 ± 1.4 ka to 114.1 ± 12.8 ka in core GC03 and 31.5 ± 1.3 ka to 86.8 ± 3.5 ka in core GC14, which were also in good sedimentary succession. The AMS ^{14}C dating and OSL dating in Sanmen Bay exhibited good stratigraphic order and did not occur age-reversed, which may be due to the relatively stable sedimentary environment in the bay.

The P sequence age-depth modelling (Bronk Ramsey, 2008; Bronk Ramsey, 2009) for Holocene sediments of cores GC03 and GC14 was performed using OxCal 4.4 (https://c14.arch.ox.ac.uk/), which uses a Bayesian approach in which sediment deposition is modelled as a Poisson process. Parameter (k) determines the extent to which the sedimentation rates (SR) are allowed to vary. For all the P-sequence models in this study, a uniformly distributed prior was used for k, such that $k_0 = 1$ and log10 $(k = K_0) \sim U(-2, 2)$. This age-depth method using Bayesian modelling has been widely applied to continental shelf marine sediment chronology. We chose this method because it can provide a more reliable chronology with wider applicability and offers the advantage of sensing small variations in the accumulation rate (Zhang et al., 2022; Yuan et al., 2023).

According to the age-depth relationship results (Figure 7), the SR of the Holocene can be divided into three phases: high SR in the early Holocene, up to 0.60–1.41 cm/yr in core GC03 and 0.62–1.20 cm/yr in core GC14, and high SR in the late Holocene, up to 0.66 and 0.45 cm/yr in the two cores, respectively. Low SR occurred during the mid-Holocene, approximately 0.04 and 0.03 cm/yr in cores GC03 and GC14, respectively. Although both

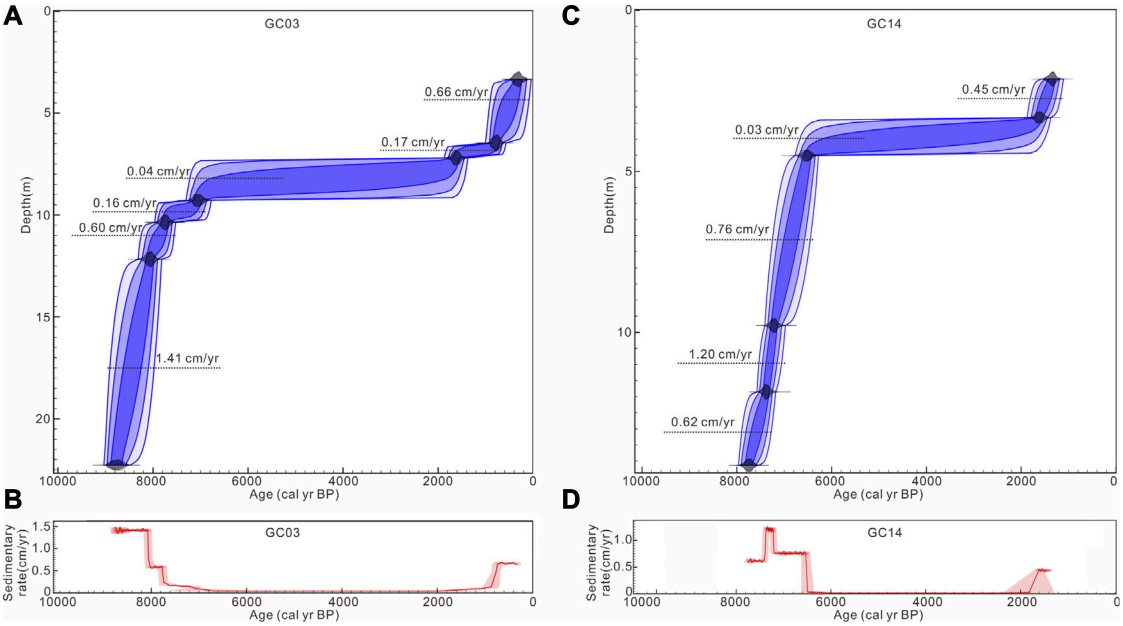

FIGURE 7
Bayesian age-depth model of cores GC03 **(A)** and GC14 **(C)** and the sedimentation rate for the two cores **(B,D)** of the Holocene sediment.

TABLE 5 Assemblages and percentage of clay minerals in Sanmen Bay surface sediments (unit: %) (Guang et al., 2022).

Location	Sample number		Smectite	Illite	Kaolinite	Chlorite
Sea area	71	min	1.86	54.01	12.39	16.23
		max	6.77	67.89	18.47	22.08
		avr	3.85	61.66	15.34	19.15
Floodplain	3	min	0	18.07	21.24	19.98
		max	2.74	55.75	45.89	36.03
		avr	1.22	41.26	32.16	25.36
Mountain area	4	min	0	11.38	26.58	5.35
		max	9.17	44.93	56.08	45.82
		avr	1.15	29.57	38.46	30.82

cores showed the same trend of sedimentary rate, the SRs of core GC03 were higher than those of core GC14.

4 Discussion

4.1 Sediment source analysis

The grain size of surface sediments in Sanmen Bay ranges from 5.6 to 7.6 Φ, with an average of 6.87 Φ (Guang et al., 2022), becoming gradually finer moving from the bay mouth to the bay top. The mean grain size of Holocene sediments in core GC03 ranges from 6.82 to 7.71 Φ, with an average of 7.30 Φ, indicating that the Holocene sediments in core GC03 were mainly composed of clayey silt and the lithology is relatively uniform.

The clay minerals in the Holocene sediments of core GC03 were mainly illite, ranging from 58% to 71%, with an average concentration of 63.5%, followed by chlorite, kaolinite, and smectite, with average concentrations of 17.2, 14.7, and 5.1%, respectively (Table 4). The clay mineral assemblage was illite-chlorite-kaolinite-smectite, which is consistent with that of Yangtze River sediments.

The clay minerals in the surface sediments of the Sanmen Bay sea area were mainly illite, with an average concentration of 61.66%, followed by chlorite, kaolinite, and smectite, with average concentrations of 19.15, 15.34, and 3.85%, respectively (Table 5). The clay mineral assemblage was illite-chlorite-kaolinite-smectite, which is consistent with that of the Yangtze River sediments. For comparison, the average concentration of illite in the surface sediments of the floodplain was 41.26%, which is much lower

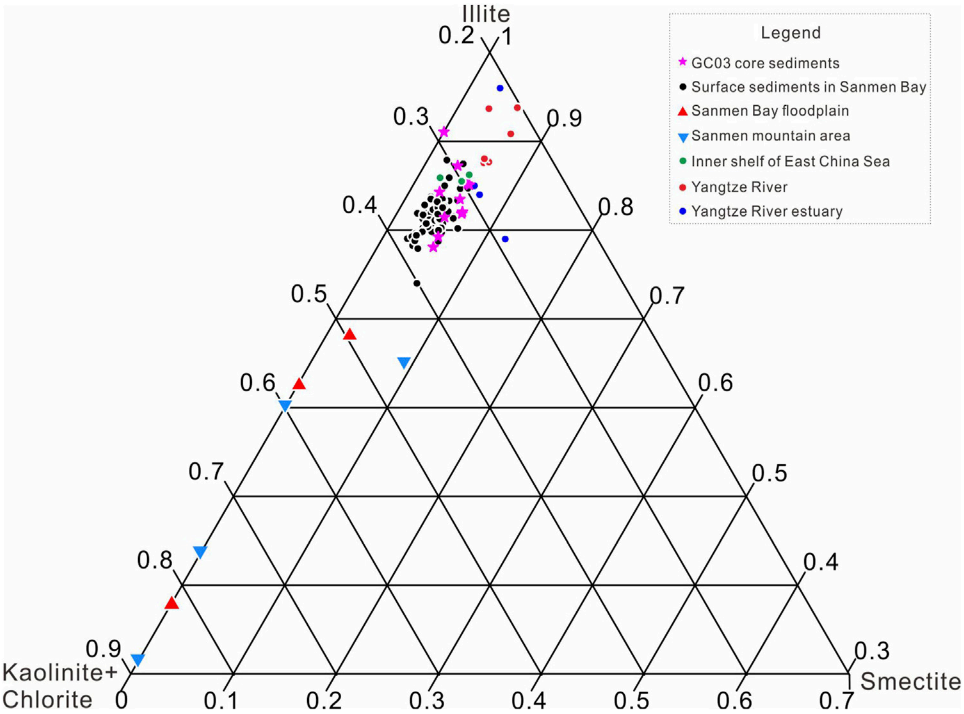

FIGURE 8
Ternary diagram of clay mineralogy of Sanmen Bay core sediments (pink stars), surface sediments (black circles), Sanmen Bay floodplain (red triangles), soil samples from the Sanmen mountain area (blue triangles) (Guang et al., 2022), inner shelf of East China Sea (blue circles) (Chen, 2008), Yangtze River estuary (green circles) (Liang et al., 2015), and Yangtze River (red circles) (Yang, 1988; He et al., 2011).

than that in the Sanmen Bay sea area. The average kaolinite, chlorite, and smectite concentrations in the floodplain were 32.16, 25.36, and 1.22%, respectively (Table 5). Therefore, the clay mineral assemblage in the floodplain is illite-kaolinite-chlorite-smectite. In contrast, the clay minerals in the soil samples from the mountainous areas were mainly kaolinite and chlorite, with average concentrations of 38.46% and 30.82%, respectively. The average concentrations of illite and smectite were 29.57% and 1.15%, respectively (Table 5). Thus, the clay mineral assemblage in the mountainous area was kaolinite-chlorite-illite-smectite.

A ternary diagram of smectite, chlorite + kaolinite, and illite concentrations shows that the concentrations of the samples collected from the Holocene sediments of core GC03 and the sea area of Sanmen Bay are quite similar to the clay concentrations derived from the Yangtze River estuary deposits but are very different from the floodplain and mountain area sediments (Figure 8). Clay minerals in the Holocene sediments of core GC03 overlap with the Yangtze River estuary deposits (Liang et al., 2015), therefore, it can be inferred that the Yangtze River sediments have significant contributions to the Sanmen Bay. The poor overlap between the sediments of core GC03 and the Yangtze River drainage sediments (Yang, 1988; He et al., 2011) may be due to the complex rock types and climate conditions of a large area of Yangtze River drainage system. The clay mineral in the upper stream of Yangtze river contains higher contents of illite and chlorite, while the mid- and lower streams constitute more smectite and kaolinite (Chen, 2008; He et al., 2011). In addition, grain size may also had a influence. For clay mineral analyses, less than 2 μm clay components were selected for Yangtze River sediments, while the bulk samples were measured for core GC03 sediments.The clay minerals in the surface sediments of Sanmen Bay varied by region. At the top of the bay, the concentrations of kaolinite and chlorite were high, similar to the characteristics of the clay mineral assemblage in the floodplain sediments of the inlet river, indicating that the coarse sediments of the estuary were affected by the input of the local river (Guang et al., 2022). In the Sanmen Bay sea area, the concentration of illite was higher than those of kaolinite and chlorite. The clay mineral assemblage characteristics were similar to those of the Yangtze River, indicating that the fine sediments from the Sanmen Bay sea area were mainly derived from the Yangtze River. Therefore, Sanmen Bay is a sink for Yangtze River sediment.

4.2 Sediment budget and origin of holocene sediment in Sanmen Bay

Based on the thickness of the Holocene sediment (Figure 3), the sediment volume in Sanmen Bay was calculated using the volume function of ArcMap 10.6, and it was found to be approximately 42.2 km^3 or 5.06 × 10^4 Mt, given an average sediment density of 1.2 t/m^3 (Xu et al., 2012). The rivers that empty into Sanmen Bay are short mountain streams with coarse sediments, which are mainly deposited in the riverbed above the estuary and gradually develop into flood- and alluvial plains. The annual average runoff of these rivers into Sanmen Bay is approximately 2.68 × 10^8 m^3 (85 m^3/s), which is equivalent to only one-fourteenth of the total runoff of the

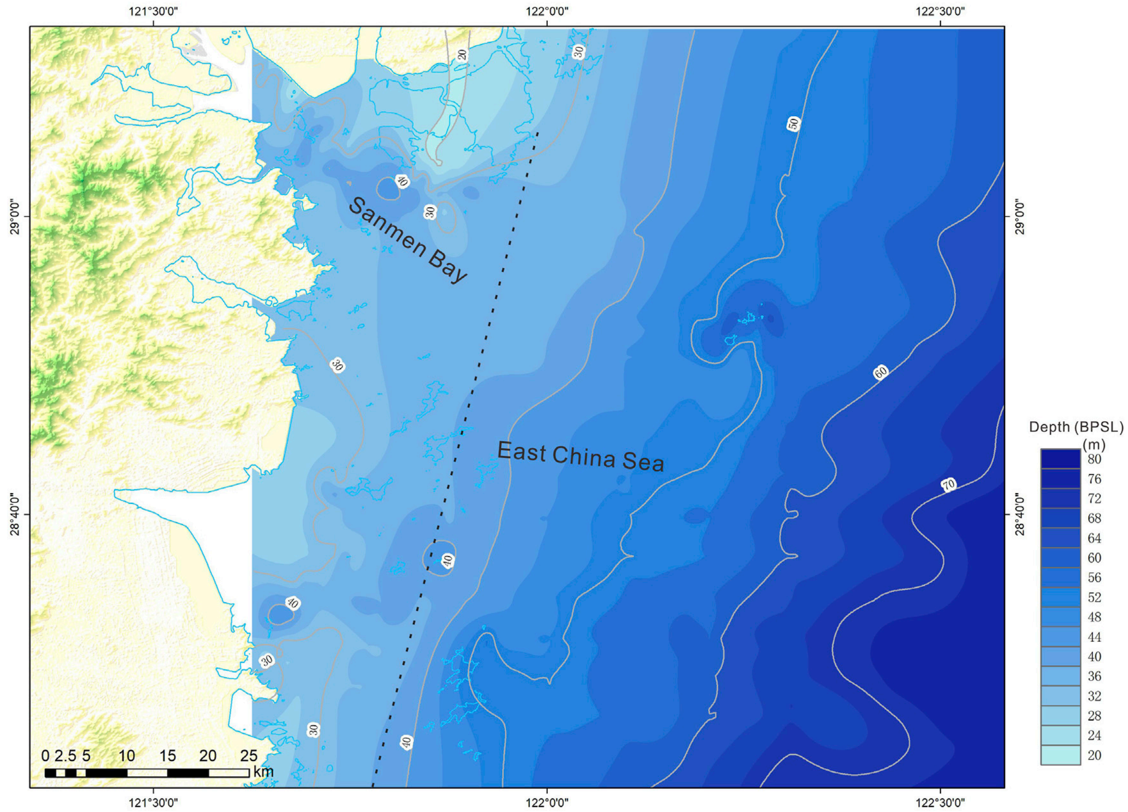

FIGURE 9
Depth distribution of seismic reflector, T1, below present sea level (BPSL) (unit: m).

Qiangtang River into the sea; therefore, it has little impact on the water exchange in Sanmen Bay (Yang and Chen, 2007). Sediments derived from local streams were considered negligible (Editorial Board of Annals of Bays in China, 1992). The clay mineral assemblage also indicates that the fine sediment in Sanmen Bay was mainly derived from the Yangtze River. Over the past million years, the Yangtze River has transferred 480 Mt/yr of sediment to the ECS (Xu et al., 2012), and during the Holocene, it discharged 480 × 10^4 Mt. Therefore, Sanmen Bay captured approximately 1% of Yangtze River sediments during the Holocene.

The tidal current plays an important role in transporting Yangtze River sediment into Sanmen Bay. Influenced by topography, the tidal current from the outer sea reciprocates after entering the bay. The duration of the flood and ebb tides are not equal, with the duration of the flood tide being greater than that of the ebb tide and the velocity of the ebb tide being greater than that of the flood tide (Yang and Chen, 2007). Northeast of Sanmen Bay, Yangtze River sediments are transported from north to south under the influence of the ECS Coastal Current. Near the mouth of the bay, sediments are transported from the outer sea to the bay under the influence of flood tides. The bay exhibits a wide tidal range and a high flood velocity, with maximums of up to 7.75 m and 153 cm/s (Editorial Board of Annals of Bays in China, 1992), respectively. The sediment carried in the seawater can enter the flood tide everywhere in the bay. When the tide reaches its highest or lowest point, the tide velocity reaches a minimum, resulting in a decrease in the capacity to carry sediment, and the sediment in the seawater can be deposited. Under the influence of ebb tidal currents, the sediment at the top of the bay is transported to the mouth of the bay, resulting in thicker Holocene sediments in the middle of Sanmen Bay (Figure 3). The formation of two depositional areas with a thickness of more than 28 m in the north and south of Sanmen Bay may also be related to the original topography (Figure 9), where the depth of T1 was more than 40 m below the present sea level, which is clearly deeper than the surrounding area.

The origin of Holocene sediment in Sanmen Bay and variation in the SR of cores GC03 and GC14 mainly depended on the southward transport of Yangtze River sediments Figure 10. Sea level changes and ocean currents strongly influence deposition (Yang et al., 2014; Gao et al., 2015). At approximately 8–7 ka, the sea level reached the present height (Xu et al., 2009; Zheng et al., 2015), and the modern current system in ECS was formed (Zheng et al., 2015). In addition, the ECS Coastal Current began to flow southward, transporting Yangtze River-derived sediment to the Zhejiang-Fujian coast. Since then, the inner shelf of the ECS and Sanmen Bay have been formed in a relatively stable environment (Li et al., 2014). Coastal flow controlled by the East Asian winter monsoon is undoubtedly the primary driving force for the transport of nearshore sediments and plays a fundamental role in the formation of mud depocenters on the continental shelf of eastern China (Shi et al., 2022). The strength of the winter monsoon directly determines the transport capacity of fine particles resuspended from the mouth of the Yangtze River southward (Zheng et al., 2014). In the early Holocene, the East Asian winter monsoon and the

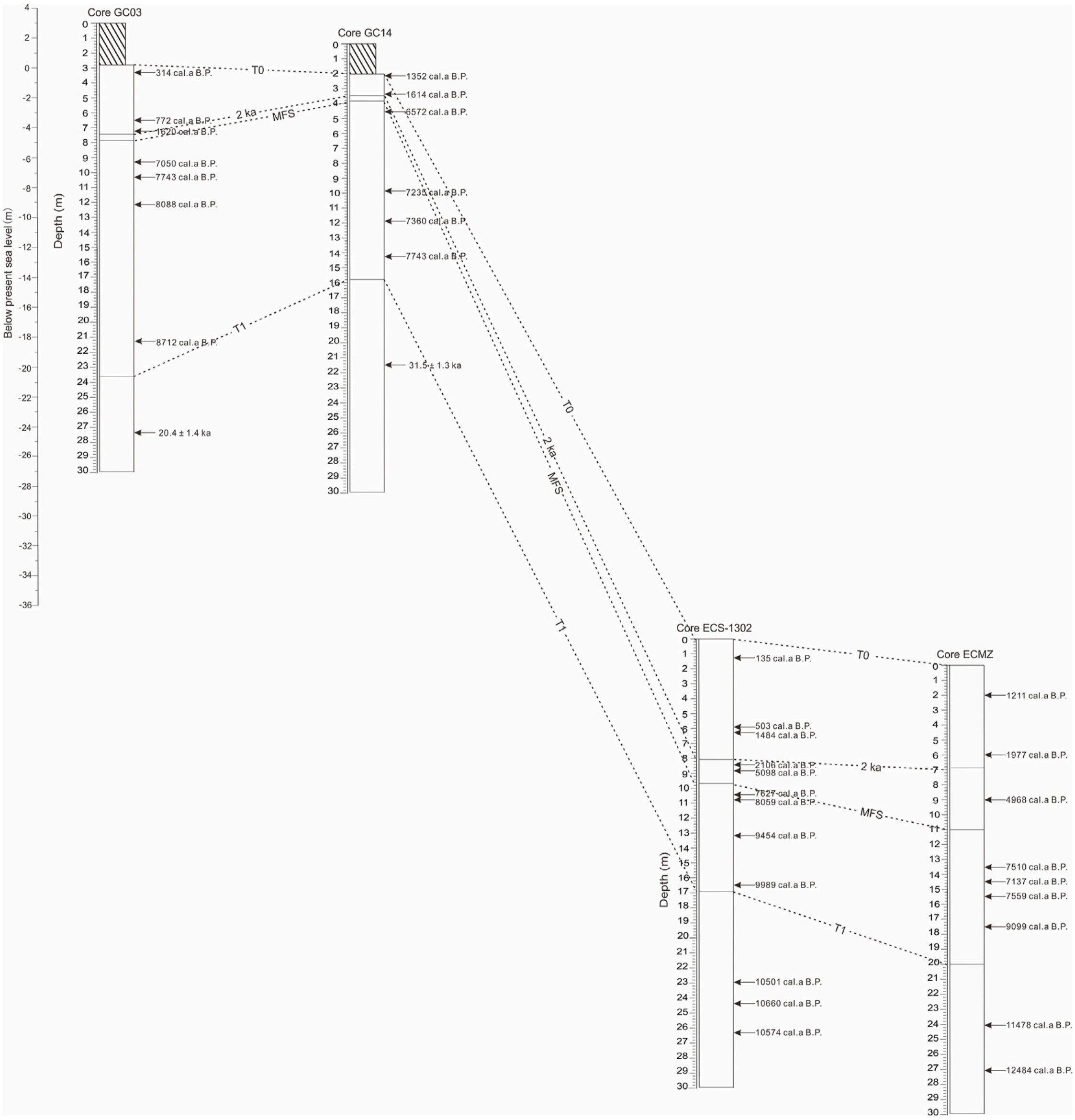

FIGURE 10
Stratigraphic correlations among boreholes in the study area. MFS: maximum flooding surface; ECS-1302 data from Liu et al., 2023; ECMZ data from (Dong, 2018).

transport capacity of the Zhejiang and Fujian coastal currents were strong, resulting in a large amount of Yangtze River sediment being transported to the nearshore area of Sanmen Bay and deposited in the bay by reciprocating flow at a high sedimentation rate. In the middle Holocene, the winter monsoon weakened, and the water column in the nearshore area of Sanmen Bay became stratified owing to the influence of the Taiwan Warm Current and the Kuroshio branch. Large amounts of sediment were trapped in the paleo-incised valley to fill the accommodation space (Song et al., 2013), resulting in a low sedimentation rate. After approximately 2 ka, the sediment from the Yangtze River mouth began to overflow (Song et al., 2013), and with the influence of human activities and the strengthening of the East Asian winter monsoon, the transport capacity of the Zhejiang and Fujian coastal currents increased, increasing the amount of sediment transported southward. A large amount of Yangtze River sediment was transported outside Sanmen Bay and deposited in the bay by reciprocating flow, resulting in an increase in the sedimentation rate.

5 Conclusion

Based on recent data from shallow seismic profiles, geological drilling, and surface sediment sampling in Sanmen Bay, we analysed the sedimentary stratigraphy, provenance, sediment flux, and sedimentary genesis mechanism during the Holocene and explored the role of Sanmen Bay in the source–sink process of Yangtze River sediment. The characteristics of the clay minerals indicate that the fine-grained sediments in Sanmen Bay are mainly derived from Yangtze River sediments. Sanmen Bay is an important sink for Yangtze River sediments, with the thickness of Holocene deposits ranging from 8.2 to 32.0 m, with an average of 23.4 m. The total sediment volume was 5.06×10^4 Mt, accounting for 1% of Yangtze River sediment during the Holocene. The Bayesian age-depth model based on borehole AMS ^{14}C dating shows that a high sedimentary rate occurred in the early and late Holocene but decreased significantly in the mid-Holocene, which is similar to the pattern on the inner shelf of the ECS. The variation in the Holocene sedimentation rate in Sanmen Bay is related to the southward transport process and mechanism of the Yangtze River sediments.

Data availability statement

The original contributions presented in the study are included in the article/Supplementary material, further inquiries can be directed to the corresponding authors.

Author contributions

JQ: Conceptualization, Investigation, Writing–original draft, Writing–review and editing, Methodology. SJ: Writing–original draft, Supervision, Writing–review and editing, Conceptualization, Methodology. JW: Investigation, Methodology, Writing–original draft. JF: Supervision, Writing–review and editing, Writing–original draft, Conceptualization, Methodology. JC: Investigation, Resources, Writing–original draft. CD: Writing–review and editing, Data curation, Formal Analysis. YJ: Writing–review and editing, Data curation, Formal Analysis. DZ: Data curation, Formal Analysis, Writing–review and editing.

Funding

The author(s) declare financial support was received for the research, authorship, and/or publication of this article. This study was funded by the China Geological Survey (Grant No. DD20230071, DD20230409 and DD20190276), Shandong Provincial Natural Science Foundation (No. ZR2020MD069 and ZR2021MD049), National Key Research and Development Program of China (No. 2021YFF0704000), and Science and Technology Innovation Project of Laoshan Laboratory (No. LSKJ202204400).

Acknowledgments

We are grateful to Drs. Su Guohui and Wang Zhao for their financial supports for sample testing and paper publication.

Conflict of interest

The authors declare that the research was conducted in the absence of any commercial or financial relationships that could be construed as a potential conflict of interest.

Publisher's note

References

Aitken, M. J. (1998). *An introduction to optical dating: the dating of quaternary sediments by the use of photon-stimulated luminescence.* Oxford: Oxford University Press.

Bronk Ramsey, C. (2008). Deposition models for chronological records. *Quat. Sci. Rev.* 27 (1–2), 42–60. doi:10.1016/j.quascirev.2007.01.019

Bronk Ramsey, C. (2009). Bayesian analysis of radiocarbon dates. *Radiocarbon* 51 (1), 337–360. doi:10.1017/s0033822200033865

Cattaneo, A., Correggiari, A., Langone, L., and Trincardi, F. (2003). The late-Holocene Gargano subaqueous delta, Adriatic shelf: sediment pathways and supply fluctuations. *Mar. Geol.* 193 (1–2), 61–91. doi:10.1016/s0025-3227(02)00614-x

Chen, L. (2008). *Sedimentary mineralogy of the China sea*. Beijing: China Ocean Press.

Dong, J. (2018). "Sediment provenance and environment records on the inner shelf of the East China Sea since the last glaciation maximum,". Doctor Dissertation (Qingdao: Qingdao University).

Dong, J., Li, A., Lu, Z., Liu, X., Wan, S., Yan, H., et al. (2021). Millennial-scale interaction between the East asian winter monsoon and el nino-related tropical pacific precipitation in the Holocene. *Palaeogeogr. Palaeoclimatol. Palaeoecol.* 573, 110442. doi:10.1016/j.palaeo.2021.110442

Dong, Y., and Cao, P. (1996). Sedimentary characteristics of the muddy bays in the Zhejiang and Fujian provinces. *J. East China Norm. Univ.* 2, 77–83.

Editorial Board of Annals of Bays in China (1992). *Annals of bays in China (series 5).* Beijing: China Ocean Press, 234–279.

Feng, Z., Liu, B., Zhao, Y., Li, X., Jiang, L., and Si, S. (2016). Spatial and temporal variations and controlling factors of sediment accumulation in the Yangtze River estuary and its adjacent sea area in the Holocene, especially in the Early Holocene. *Cont. Shelf Res.* 125, 1–17. doi:10.1016/j.csr.2016.06.007

Gao, S., and Collins, M. (2014). Holocene sedimentary systems on continental shelves. *Mar. Geol.* 352, 268–294. doi:10.1016/j.margeo.2014.03.021

Gao, S., Wang, D., Yang, Y., Zhou, L., Zhao, Y., Gao, W., et al. (2015). Holocene sedimentary systems on a broad continental shelf with abundant river input: process–product relationships. *Geol. Soc. Spec. Publ.* 429, 223–259. doi:10.1144/sp429.4

Guang, X., Tian, Y., Yin, P., Yang, S., Chu, Z., Cao, K., et al. (2022). Clay mineral assemblages and provenance in the surface sediment of the Sanmen Bay. *Mar. Geol. Front.* 38 (12), 40–46. doi:10.16028/j.1009-2722.2022.175

Hanebuth, T., Lantzsch, H., and Nizou, J. (2015). Mud depocenters on continental shelves-appearance, initiation times, and growth dynamics. *Geo-Mar. Lett.* 35, 487–503. doi:10.1007/s00367-015-0422-6

He, M., Zheng, H., Huang, X., Jia, J., and Li, L. (2011). Clay mineral assemblages in the Yangtze drainage and provenance implications. *Acta Sediment. Sin.* 29 (3), 544–551. doi:10.14027/j.cnki.cjxb.2011.03.006

Hu, D., Wu, L., Cai, W., Gupta, A., Ganachaud, A., Qiu, B., et al. (2015). Pacific western boundary currents and their roles in climate. *Nature* 522, 299–308. doi:10.1038/nature14504

Jian, Z., Wang, P., Saito, Y., Wang, J., Pflaumann, U., Oba, T., et al. (2020). Holocene variability of the Kuroshio current in the okinawa trough, northwestern pacific ocean. *Earth Planet. Sc. Lett.* 184, 305–319. doi:10.1016/s0012-821x(00)00321-6

Lai, Z. P., and Brückner, H. (2008). Effects of feldspar contamination on equivalent dose and the shape of growth curve for OSL of silt-sized quartz extracted from Chinese loess. *Geochronometria* 30 (1), 49–53. doi:10.2478/v10003-008-0010-0

Lee, H., and Chao, S. (2003). A climatological description of circulation in and around the East China Sea. *Top. Stud. Oceanogr.* 50, 1065–1084. doi:10.1016/s0967-0645(03)00010-9

Li, A., and Zhang, K. (2020). Research progress of mud wedge in the inner continental shelf of the East China Sea. *Oceanol. Limnol. Sin.* 51 (4), 705–727. doi:10.11693/hyhz20200500145

Li, G., Li, P., Liu, Y., Qiao, L., Ma, Y., Xu, J., et al. (2014). Sedimentary system response to the global sea level change in the East China Seas since the last glacial maximum. *Earth-Sci. Rev.* 139, 390–405. doi:10.1016/j.earscirev.2014.09.007

Liang, X., Yang, S., Yin, P., et al. (2015). Distribution of clay mineral assemblages in the rivers entering Yellow Sea and East China Sea and the muddy shelves deposits and control factors. *Mar. Geol. Quat. Geol.* 35 (6), 1–15. doi:10.16562/j.cnki.0256-1492.2015.06.001

Liu, J., Li, A., Xu, K., Veiozzi, D., Yang, Z., Milliman, J., et al. (2006). Sedimentary features of the Yangtze River-derived along-shelf clinoform deposit in the East China sea. *Cont. Shelf Res.* 26, 2141–2156. doi:10.1016/j.csr.2006.07.013

Liu, J., Milliman, J., Gao, S., and Cheng, P. (2004). Holocene development of the yellow river's subaqueous delta, north Yellow Sea. *Mar. Geol.* 209, 45–67. doi:10.1016/j.margeo.2004.06.009

Liu, J., Qiu, J., Saito, Y., Zhang, X., Niang, X., Wang, F., et al. (2020). Formation of the Yangtze Shoal in response to the post-glacial transgression of the paleo-Yangtze (Changjiang) estuary, China. *Mar. Geol.* 423, 106080. doi:10.1016/j.margeo.2019.106080

Liu, J., Qiu, J., Saito, Y., Zhang, X., Wang, H., Wang, F., et al. (2023). Late pleistocene to Holocene facies architecture and sedimentary evolution of the Zhejiang coast, east China sea. *Mar. Geol.* 423, 107027. doi:10.1016/j.margeo.2023.107027

Liu, J., Xu, K., Li, A., Milliman, J., Velozzi, D., Xiao, S., et al. (2007). Flux and fate of Yangtze River sediment delivered to the East China sea. *Geomorphology* 85, 208–224. doi:10.1016/j.geomorph.2006.03.023

Marsh, R., Prestwich, W., Rink, W., and Brennan, B. (2002). Monte Carlo determinations of the beta dose rate to tooth enamel. *Radiat. Meas.* 35, 609–616. doi:10.1016/S1350-4487(02)00065-3

Peng, W. (2013). "Response of hydrodynamic environment to reclamation in Sanmen Bay,". Master Dissertation (Zhejiang: Zhejiang University).

Porz, L., Zhang, W., Hanebuth, T., and Schrum, C. (2021). Physical processes controlling mud depocenter development on continental shelves-Geological, oceanographic, and modeling concepts. *Mar. Geol.* 432, 106402. doi:10.1016/j.margeo.2020.106402

Qiao, S., Shi, X., Wang, G., Zhou, L., Hu, B., Hu, Li., et al. (2017). Sediment accumulation and budget in the bohai sea, Yellow Sea and east China sea. *Mar. Geol.* 390, 270–281. doi:10.1016/j.margeo.2017.06.004

Qin, Y., Zhao, Y., Chen, L., and Zhao, S. (1987). *Geology of East China sea*. Beijing: Ocean Press.

Roberts, H. M., and Duller, G. A. (2004). Standardised growth curves for optical dating of sediment using multiple-grain aliquots. *Radiat. Meas.* 38 (2), 241–252. doi:10.1016/j.radmeas.2003.10.001

Shi, Y., Xu, X., Sheng, H., Lv, J., Zhang, S., and Gao, J. (2022). Neglected role of continental circulation in cross-shelf sediment transport: implications for paleoclimate reconstructions. *Mar. Geol.* 443, 106703. doi:10.1016/j.margeo.2021.106703

Song, B., Li, Z., Saito, Y., Okuno, J., Li, Z., Lu, A., et al. (2013). Initiation of the Changjiang (Yangtze) delta and its response to the mid-Holocene sea level change. *Palaeogeogr. Palaeoclimatol. Palaeoecol.* 388, 81–97. doi:10.1016/j.palaeo.2013.07.026

Stuiver, M., Reimer, P. J., and Reimer, R. W. (2020). *CALIB 8.2.* [WWW program] Available at: http://calib.org (Accessed August 14, 2020).

Wang, H., Saito, Y., Zhang, Y., Bi, N., and Yang, Z. (2011). Recent changes of sediment flux to the western Pacific Ocean from major rivers in East and Southeast Asia. *Earth-Sci. Rev.* 108 (1–2), 80–100. doi:10.1016/j.earscirev.2011.06.003

Wessel, P., and Smith, W. H. F. (1995). New version of the generic mapping tools. *Eos Trans. AGU.* 76, 329. doi:10.1029/95eo00198

Wu, H., Deng, B., Yuan, R., Hu, J., Gu, J., Shen, F., et al. (2013). Detiding measurement on transport of the Changjiang-derived buoyant coastal current. *J. Phys. Oceanogr.* 43 (11), 2388–2399. doi:10.1175/jpo-d-12-0158.1

Xu, F., Li, A., Xiao, S., Wan, S., Liu, J., and Zhang, Y. (2009). Paleoenvironmental evolution in the inner shelf of the East China Sea since the last deglaciation. *Acta Sediment. Sin.* 27, 118–127. doi:10.14027/j.cnki.cjxb.2009.01.009

Xu, K., Li, A., Liu, J., Million, J., Yang, Z., Liu, C., et al. (2012). Provenance, structure, and formation of the mud wedge along inner continental shelf of the East China Sea: a synthesis of the Yangtze dispersal system. *Mar. Geol.* 291-294, 176–191. doi:10.1016/j.margeo.2011.06.003

Yang, S., and Chen, B. (2007). The transportation characteristics of suspended load in Sanmen Bay. *Trans. Oceanol. Limnolo.* 4, 21–29. doi:10.13984/j.cnki.cn37-1141.2007.04.008

Yang, S. Y., Wang, Z. B., Dou, Y. G., and Shi, X. F. (2014). Chapter 21 A review of sedimentation since the Last Glacial Maximum on the continental shelf of eastern China. *Geol. Soc. Lond. Mem.* 41, 293–303. doi:10.1144/m41.21

Yang, Z. (1988). Mineralogical assemblages and chemical characteristics of clays from sediments of the Huanghe, Changjiang, Zhujiang Rivers and their relationship to the climate environment in their sediment source areas. *Oceanol. Limnologia Sinica* 19 (4), 336–346.

Yoneda, M., Uno, H., Shibata, Y., Suzuki, R., Kumamoto, Y., Yoshida, K., et al. (2007). Radiocarbon marine reservoir ages in the western Pacific estimated by pre-bomb molluscan shells. *Nucl. Instrum. Methods Phys. Res. Sect. B* 259, 432–437. doi:10.1016/j.nimb.2007.01.184

Yuan, X., Hu, R., Feng, X., Qiu, J., Wang, N., Yao, Z., et al. (2023). Sedimentary records and implications for the evolution of sedimentary environments inferred from BH1302 during the late Quaternary in the Bohai Sea, China. *Mar. Geol.* 456, 106986. doi:10.1016/j.margeo.2022.106986

Zhang, S., Liu, S., Shu, Z., Xu, X., Lv, J., Shi, Y., et al. (2022). Climate-driven provenance variation and sedimentary system evolution at the Changjiang distal mud since the mid-Holocene. *Mar. Geol.* 452, 106902. doi:10.1016/j.margeo.2022.106902

Zheng, X., Li, A., Wan, S., Jiang, F., and Johnson, C. (2014). ITCZ and ENSO pacing on East Asian winter monsoon variation during the Holocene: sedimentological evidence from the Okinawa trough. *J. Geophys. Res. Oceans* 119, 4410–4429. doi:10.1002/2013jc009603

Zheng, X., Li, A., Wan, S., Jiang, F., Yin, X., and Lu, J. (2015). Formation of the modern current system in the East China Sea since the early Holocene and its relationship with sea level and the monsoon system. *Chin. J. Oceanol. Limnol.* 33, 1062–1071. doi:10.1007/s00343-015-4089-7

Frontiers in
Earth Science

Investigates the processes operating within the major spheres of our planet

Advances our understanding across the earth sciences, providing a theoretical background for better use of our planet's resources and equipping us to face major environmental challenges.

Discover the latest Research Topics

See more →

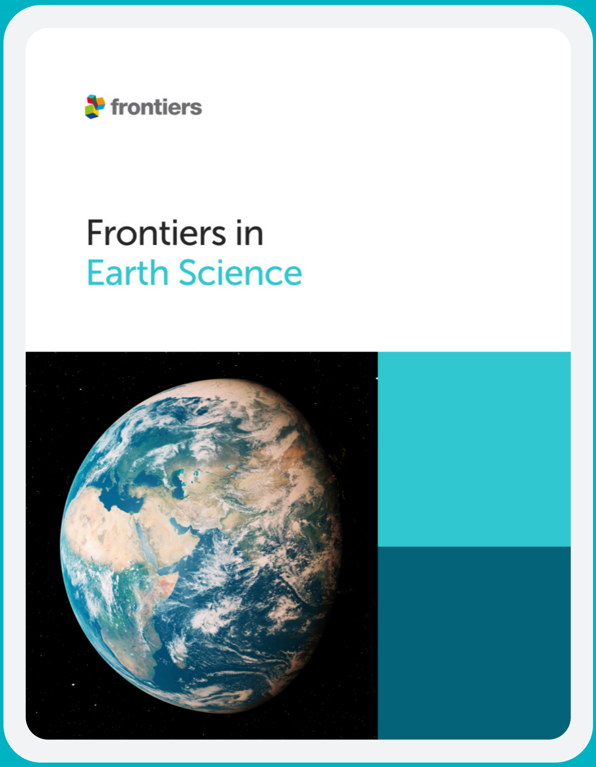
frontiers

Frontiers in
Earth Science

Frontiers

Avenue du Tribunal-Fédéral 34
1005 Lausanne, Switzerland
frontiersin.org

Contact us

+41 (0)21 510 17 00
frontiersin.org/about/contact